

Development of Simultaneous Multi-Radionuclide Imaging with a Novel
SiPM-based Preclinical SPECT Scanner

by

Matthew Strugari

Submitted in partial fulfilment of the requirements
for the degree of Doctor of Philosophy

at

Dalhousie University
Halifax, Nova Scotia
December 2023

Dalhousie University is located in Mi'kma'ki, the
ancestral and unceded territory of the Mi'kmaq.
We are all Treaty people.

Table of Contents

List of Tables	vi
List of Figures	vii
Abstract	x
List of Abbreviations and Symbols Used	xi
Acknowledgements	xv
Chapter 1 Introduction	1
1.1 Production of Radiopharmaceuticals	4
1.2 Molecular Imaging	7
1.2.1 Emission Tomography Image Acquisition	10
1.2.2 Preclinical and Translational Imaging	15
1.3 Performance Measurements of Gamma Cameras	17
1.4 Monte Carlo in Nuclear Medicine Imaging	18
1.5 Implementations of Multi-Radionuclide SPECT	19
1.5.1 Crosstalk Corrections Pre-Reconstruction	21
1.5.2 Crosstalk Corrections During Reconstruction	24
1.5.3 Crosstalk Corrections Post-Reconstruction	26
1.5.4 Summary of Insights	27
1.6 Research Objectives	27
1.6.1 Hypotheses	28
Chapter 2 Theory	29
2.1 Prologue	29
2.2 Radioactivity	29
2.2.1 Alpha Emission	30
2.2.2 Isobaric Transition	31
2.2.3 Isomeric Transition	32
2.3 Interactions of Radiation with Matter	32
2.3.1 Charged Particle Interactions	33

2.3.2	Electromagnetic Interactions	37
2.4	Radiation Detection and Measurement	42
2.4.1	Modes of Detector Operation	42
2.4.2	Dead Time	45
2.4.3	Detection Efficiency	45
2.4.4	Counting Statistics	47
2.4.5	Types of Radiation Detectors	48
2.5	Nuclear Medicine Imaging	53
2.5.1	Gamma Camera	54
2.5.2	Positron Emission Tomography	55
2.6	Tomographic Image Reconstruction	55
2.6.1	Analytical Reconstruction	56
2.6.2	Iterative Reconstruction	58
2.6.3	Artificial Intelligence Reconstruction	62
2.7	Summary	62
Chapter 3 NEMA NU 1-2018 Performance Characterization and Monte Carlo Model Validation of the Cubresa Spark SiPM-based Preclinical SPECT Scanner		63
3.1	Prologue	63
3.2	Abstract	64
3.3	Introduction	65
3.4	Methods and Materials	67
3.4.1	Equipment Description	67
3.4.2	Simulation Description	69
3.4.3	NEMA Performance Characterization and SPECT Model Validation	71
3.4.4	Tests of Intrinsic Gamma Camera Detector Characteristics	72
3.4.5	Tests of Gamma Camera Detectors with Collimators	75
3.4.6	Tests Specific to Tomographic Camera Systems	76
3.5	Results	79
3.5.1	Tests of Intrinsic Gamma Camera Detector Characteristics	79

3.5.2	Tests of Gamma Camera Detectors with Collimators	83
3.5.3	Tests Specific to Tomographic Camera Systems	85
3.6	Discussion	88
3.7	Conclusion	92
Chapter 4 Integration of Advanced 3D SPECT Modelling for Pinhole Collimators into the Open-Source STIR Framework		93
4.1	Prologue	93
4.2	Abstract	94
4.3	Introduction	94
4.4	Technical Description	95
4.5	Materials and Methods	97
4.5.1	Quantitative Assessment of Reconstructed Data	99
4.5.2	Qualitative Assessment of Reconstructed <i>In Vivo</i> Data	103
4.6	Results	105
4.6.1	Quantitative Assessment of Reconstructed Data	105
4.6.2	Qualitative Assessment of Reconstructed <i>In Vivo</i> Data	108
4.7	Discussion	109
4.8	Conclusion	112
Chapter 5 Spectral Unmixing of Multi-Radionuclide SPECT Acquisitions using the Open-Source SIRF and CIL Frameworks		113
5.1	Prologue	113
5.2	Abstract	114
5.3	Introduction	115
5.4	Methods and Materials	118
5.4.1	Description of Hardware and Software	119
5.4.2	Objective Function Defined with the Core Imaging Library	120
5.4.3	Determination of Equation Parameters	123
5.4.4	Experimental Test of Crosstalk Correction Efficacy	125
5.5	Results	129

5.5.1	Determination of Equation Parameters	129
5.5.2	Experimental Test of Crosstalk Correction Efficacy using $^{99m}\text{Tc}/^{123}\text{I}$	131
5.5.3	Experimental Test of Crosstalk Correction Efficacy using $^{99m}\text{Tc}/^{111}\text{In}$	136
5.6	Discussion	141
5.7	Conclusion	145
Chapter 6	Conclusion	146
	Bibliography	152
Appendix A	STIR Parameter Files	172
Appendix B	Copyright License Agreements	174

List of Tables

1.1	Physical characteristics of commonly used radionuclides in nuclear medicine.	5
1.2	Typical performance of clinical and preclinical gamma cameras.	18
3.1	Geometric specifications of pinhole collimators.	69
3.2	Intrinsic spatial resolution and linearity.	79
3.3	Flood field uniformity.	80
3.4	SPECT reconstructed spatial resolution without scatter.	86
3.5	SPECT reconstructed spatial resolution with scatter.	86
3.6	SPECT volume sensitivity, uniformity, and variability.	88
3.7	Performance comparisons of commercial preclinical SPECT cameras validated with GATE using ^{99m}Tc	91
4.1	Summary of simulated ^{99m}Tc phantom acquisitions and reconstructions.	100
4.2	Summary of <i>in vivo</i> ^{123}I acquisition and reconstruction.	104
4.3	Computation cost in single-pinhole SPECT OSEM reconstruction with 120 projections, eight subsets, and 40 subiterations.	106
5.1	Energy window characteristics for $^{99m}\text{Tc}/^{123}\text{I}$	123
5.2	Sensitivity mixing weights for $^{99m}\text{Tc}/^{123}\text{I}$ in measurement and simulation.	130
5.3	Sensitivity mixing weights for $^{99m}\text{Tc}/^{111}\text{In}$ in simulation.	130
5.4	Quantitative accuracy of $^{99m}\text{Tc}/^{123}\text{I}$ using RMSE in measurement and simulation.	133
5.5	Contrast of $^{99m}\text{Tc}/^{123}\text{I}$ using RMSE in measurement and simulation.	135
5.6	Image noise of $^{99m}\text{Tc}/^{123}\text{I}$ using CV in measurement and simulation.	135
5.7	Quantitative accuracy of $^{99m}\text{Tc}/^{111}\text{In}$ using RMSE in simulation.	140
5.8	Contrast of $^{99m}\text{Tc}/^{111}\text{In}$ using RMSE in simulation.	140
5.9	Image noise of $^{99m}\text{Tc}/^{111}\text{In}$ using CV in simulation.	141

List of Figures

1.1	Multi-radionuclide energy spectrum of ^{57}Co , $^{99\text{m}}\text{Tc}$, ^{123}I , and ^{111}In acquired with a high-purity germanium detector.	2
1.2	Window characteristics in the triple energy window method.	3
1.3	Periodic table highlighting elements with radionuclides having applications in nuclear medicine.	4
1.4	Fused SPECT/CT images allow for correct anatomical localization of SPECT findings.	8
1.5	Illustration of types of events in nuclear medicine imaging observed with a gamma camera and PET scanner.	11
1.6	Basic types of SPECT collimators.	13
1.7	GATE Monte Carlo simulation of a hypothetical clinical brain SPECT acquisition illustrating the detailed analysis of photon interactions.	20
2.1	Stopping power of water for various charged particles.	34
2.2	Parameters of charged-particle collisions with atoms.	34
2.3	Electromagnetic interactions and associated attenuation.	38
2.4	Elastic scattering of a photon with an electron at rest.	40
2.5	Photon interactions in varying detector sizes with associated pulse height spectra.	44
2.6	Paralyzable and non-paralyzable system dead time.	46
2.7	Basic principles of gas-filled detectors.	49
2.8	Basic principles of a photomultiplier tube.	52
2.9	The Anger camera.	54
2.10	Acquisition of raw SPECT data stored in a sinogram.	57
2.11	Illustration of simple backprojection.	57
2.12	Illustration of filtered backprojection.	58
2.13	Acquisition model describing the transformation operation between detector and image space.	59

3.1	The Cubresa Spark preclinical SPECT scanner and mouse-sized scatter phantom, illustrated in a photograph of the system and a GATE model rendering.	68
3.2	Digitizer signal processing model of the Spark's readout electronics used in GATE.	71
3.3	Intrinsic spatial resolution and linearity illustrated in planar mask projection images.	80
3.4	Intrinsic count rate performance in air.	82
3.5	Intrinsic energy resolution.	82
3.6	System spatial resolution without scatter.	83
3.7	System spatial resolution with scatter.	84
3.8	System planar sensitivity.	85
3.9	SPECT reconstructed spatial resolution with scatter.	87
3.10	SPECT volume sensitivity, uniformity, and variability.	88
4.1	PinholeSPECTUB projection matrix system of reference and sign criteria.	97
4.2	Comparative sinograms of the IQ phantom hot rods from GATE simulation and STIR forward projection.	101
4.3	Axial sums of OSEM reconstructed images from phantom simulations, illustrating reconstruction accuracy and radioactive source distributions used in analysis.	105
4.4	SPECT IQ phantom hot rod CNR for different reconstruction algorithms available in STIR.	107
4.5	SPECT spatial resolution with scatter in the mouse-sized scatter phantom reconstructed with OSEM and different projection matrix corrections.	108
4.6	SPECT uniformity and variability in the volumetric cylinder reconstructed with OSEM and different projection matrix corrections.	108
4.7	Slices of the volumetric cylinder reconstructed with OSEM illustrating the DOI correction software bug.	109
4.8	Fused SPECT/CT image of a mouse used in assessing qualitative <i>in vivo</i> image quality.	110
5.1	Illustration of ROIs used in the analysis of crosstalk correction performance.	128

5.2	System planar sensitivity projection images and energy spectra measured with ^{99m}Tc and ^{123}I	130
5.3	Reconstructed images demonstrating crosstalk correction in measurement and simulation of $^{99m}\text{Tc}/^{123}\text{I}$	132
5.4	Gold standard reconstructed images of $^{99m}\text{Tc}/^{123}\text{I}$ demonstrating perfect crosstalk correction.	133
5.5	Relative activity of reconstructed $^{99m}\text{Tc}/^{123}\text{I}$ line sources.	134
5.6	Contrast of reconstructed $^{99m}\text{Tc}/^{123}\text{I}$ line sources.	135
5.7	Reconstructed images demonstrating crosstalk correction in simulation of $^{99m}\text{Tc}/^{111}\text{In}$	137
5.8	Gold standard reconstructed images of $^{99m}\text{Tc}/^{111}\text{In}$ demonstrating perfect crosstalk correction.	138
5.9	Relative activity of reconstructed $^{99m}\text{Tc}/^{111}\text{In}$ line sources.	139
5.10	Contrast of reconstructed $^{99m}\text{Tc}/^{111}\text{In}$ line sources.	141

Abstract

Multi-radionuclide single-photon emission computed tomography (SPECT) is becoming increasingly important in nuclear medicine investigations for radiopharmaceutical drug development and procedural advancement. Crosstalk is the primary challenge, where γ -rays from one radionuclide become incorrectly attributed to the competing radionuclide(s), leading to a mixing of acquired signals. This degrades image quality and accuracy, and can negatively impact interpretation of nuclear medicine images and studies. This work presents the development of a novel crosstalk correction technique, referred to as “spectral unmixing”, that separates radiopharmaceutical distributions into their respective images using spectral information during reconstruction. It was implemented at the Biomedical MRI Research Laboratory (BMRL) using the Cubresa Spark silicon photomultiplier (SiPM)-based preclinical SPECT scanner.

First, the Spark’s performance was characterized with one radionuclide, namely ^{99m}Tc . This work was published in the article “NEMA NU 1-2018 performance characterization and Monte Carlo model validation of the Cubresa Spark SiPM-based preclinical SPECT scanner” in *EJNMMI Physics*. In tandem, open-source pinhole-SPECT reconstruction software was developed and integrated into the Software for Tomographic Image Reconstruction (STIR). The software, as demonstrated in the publication “Integration of advanced 3D SPECT modelling for pinhole collimators into the open-source STIR framework” in *Front. Nucl. Med.*, was licensed to University College London (UCL) and is the first configurable platform for pinhole collimators. The extension of the pinhole-SPECT library from STIR to the Synergistic Image Reconstruction Framework (SIRF) established the basis for spectral unmixing. The final manuscript, “Spectral unmixing of multi-radionuclide SPECT acquisitions using the open-source SIRF and CIL frameworks”, was developed in collaboration with researchers at UCL. Complex multi-radionuclide SPECT acquisitions using $^{99m}\text{Tc}/^{123}\text{I}$ and $^{99m}\text{Tc}/^{111}\text{In}$ were measured and simulated, and spectral unmixing was found to have superior image quality and quantitative accuracy compared to conventional crosstalk correction methods.

The spectral unmixing crosstalk correction methodology can be readily implemented with different SPECT systems, and its modular construction is suitable for more versatile advancements. Spectral unmixing crosstalk correction has the potential to lead to novel molecular imaging abilities and technologies, as well as accelerated studies offering unprecedented insight into the complexities of human physiology and disease progression.

List of Abbreviations and Symbols Used

μ CT	micro computed tomography
^{111}In	indium-111
^{123}I	iodine-123
^{125}I	iodine-125
^{131}I	iodine-131
^{133}Xe	xenon-133
^{15}O	oxygen-15
^{18}F	fluorine-18
^{201}Tl	thallium-201
^{235}U	uranium-235
^{236}U	uranium-236
^{32}P	phosphorus-32
^{57}Co	cobalt-57
^{67}Ga	gallium-67
$^{81\text{m}}\text{Kr}$	krypton-81m
^{82}Rb	rubidium-82
^{90}Y	yttrium-90
$^{99\text{m}}\text{Tc}$	technetium-99m
^{99}Mo	molybdenum-99
2D	two-dimensional
3D	three-dimensional
AI	artificial intelligence
APD	avalanche photodiode
ATT-C	attenuation correction
BChE	butyrylcholinesterase
BMRL	Biomedical MRI Research Laboratory
CDRF	collimator-detector response function
CFOV	central field of view
CIL	Core Imaging Library
CNR	contrast-to-noise ratio
CSDA	continuous slowing-down approximation
CsI	cesium iodide
CsI(Na)	sodium-activated cesium iodide
CsI(Tl)	thallium-activated cesium iodide
CT	computed tomography
CV	coefficient of variation

CZT	cadmium zinc telluride
DOI	depth of interaction
DOI-C	DOI correction
EC	electron capture
EGS	Electron Gamma Shower
EM	expectation maximization
ESSE	effective source scatter estimate
FBP	filtered back projection
FDG	¹⁸ F-fluorodeoxyglucose
FOV	field of view
FT	Fourier transformation
FWHM	full width at half maximum
FWTM	full width at tenth maximum
GATE	Geant4 Application for Tomographic Emission
Geant4	Geometry and Tracking
GM	Geiger-Müller
HPGe	high-purity germanium
IC	internal conversion
ICA	independent component analysis
ICR	input count rate
ID	identification
K-L	Kullback-Leibler
K-N	Klein-Nishina
LET	linear energy transfer
LOR	line-of-response
LORs	lines-of-response
LROC	localization receiver operating characteristic
LSF	line spread function
LTS	long term support
MAA	macroaggregated albumin
MAP	maximum a posteriori
MCNP	Monte Carlo N-Particle
meas	measurement
MLEM	maximum likelihood expectation maximization
MPH	multi-pinhole
MR	magnetic resonance

MRI	magnetic resonance imaging
MSV	mean square voltage
MWSR	multiple window spatial registration
N-C	no corrections
NaI	sodium iodide
NaI(Tl)	thallium-activated sodium iodide
NEMA	National Electrical Manufacturers Association
NIST	National Institute of Standards and Technology
NM	nuclear medicine
OCR	observed count rate
OS-OSL-MRP	ordered subsets one step late with median root prior
OS-SPS-QP	ordered subsets separable paraboloidal surrogate with quadratic prior
OSEM	ordered subsets expectation maximization
PDHG	primal dual-hybrid gradient
PET	positron emission tomography
PF	penalization factor
PH	parallel-hole
PMT	photomultiplier tube
PPGD	preconditioned projected gradient descent
proj	projection
PSF	point spread function
PSF-C	PSF correction
PSFATDOI-C	all corrections
PSFATDOIM-C	all corrections with masking
PSPMT	position-sensitive photomultiplier tube
px	pixels
RAM	random access memory
RMSE	root-mean-square error
ROI	region of interest
ROOT	Rapid Object-Oriented Technology
sim	simulation
SiPM	silicon photomultiplier
SIRF	Synergistic Image Reconstruction Framework
SNR	signal-to-noise ratio
SPAD	single photon avalanche photodiode
SPECT	single-photon emission computed tomography
SPH	single-pinhole
STIR	Software for Tomographic Image Reconstruction
STL	standard tessellation language

SVS	system volume sensitivity
TcO_4^-	technetium pertechnetate
TEW	triple energy window
TV	total variation
UCL	University College London
UCT	uniformity correction table
UFOV	useful field of view
UV	ultraviolet
VOI	volume of interest
VSAC	volume sensitivity per axial centimeter
vx	voxels

Acknowledgements

This thesis would not have been possible without the encouragement, collaboration, assistance, and contribution from numerous individuals. I extend a heartfelt thank you to everyone involved, including those unmentioned here.

First and foremost, I would like to thank my co-supervisors Dr. Kimberly Brewer and Dr. Steven Beyea for their trusting support, patience, and mentorship. Their guidance promoted independent learning, and for that I am extremely grateful. Secondly, I would like to thank my committee members, Dr. Alasdair Syme and Dr. Chris Bowen, for their thoughtful and invaluable input during the course of this project. Their discussions provided clarity and focus that kept me on track toward attainable outcomes. Altogether, this work was achieved with financial support from the Nova Scotia Graduate Scholarship Program—thank you.

Next, I am forever indebted to the nuclear medicine technologists at the IWK Health Centre, namely Sandra MacDonald, Sandra Ellis, and Nicole Mroz, whose assistance was instrumental in all work involving radionuclides. I commend machinist Ian Conrod from the Nova Scotia Health Medical Physics Team, who fabricated components fundamental to the project. My appreciation is also expressed to Bob Schellenberg and Ryan Sparkes at Cubresa Inc. for their willingness to educate me on the inner workings of the vital equipment upon which this thesis was built.

I would especially like to thank Professor Kris Thielemans from the Institute of Nuclear Medicine at University College London. His mentorship was paramount to the success of this project, and my appreciation cannot be overstated. I am honoured to have been introduced into his network and given the opportunity to share in the important work that extends throughout the medical imaging research community.

Thank you to my medical physics colleagues and labmates who were always available and willing to discuss research ideas and provide crucial feedback. It has truly been a pleasure to work with every one of you.

To my beloved parents Darrell and Debbie, sisters Brittany and Caitlin, partner Breagh, and closest friends who endured my time as a student—your encouragement and support have been pillars of strength in my becoming as a medical physicist.

Chapter 1

Introduction

Nuclear medicine imaging utilizes small amounts of radioactive substances to detect, diagnose, stage, or treat a variety of ailments such as cancer, heart disease, gastrointestinal, endocrine, and neurological disorders [1]. The functions of specific organs can be assessed through the intake of a radiopharmaceutical into the body, and the physiologic interactions of the agent give rise to information portrayed in the acquired images. Nuclear medicine investigations are traditionally performed with one radiopharmaceutical, but multi-agent investigations are becoming increasingly important for drug development and procedural advancement.

The ability to utilize multiple radiopharmaceuticals in a single acquisition provides immense potential for enhancing the accuracy and effectiveness of medical care. For example, advanced diagnosis can derive significant benefits from multiple procedures performed in concert, allowing for more accurate and comprehensive assessments of medical conditions. In addition, multi-radionuclide treatment planning and monitoring play a pivotal role in the identification and optimization of tailored patient interventions. This fosters the practice of precision medicine, encompassing various aspects of disease pathology that are vital for patient-specific treatments. Multi-radionuclide imaging offers a range of additional benefits, such as improved patient outcomes, minimized patient discomfort, reduced acquisition time, the production of perfectly co-registered images in space and time, and higher throughput of subjects and studies [2]. More importantly, it has the potential to offer unprecedented insight into the complexities of physiology and disease progression. Preclinical multi-radionuclide imaging presents a wealth of opportunities to deepen our comprehension of physiological processes and establish novel imaging techniques and therapies.

During the preclinical stage of radiopharmaceutical development, a new agent is investigated to examine its safety, pharmacokinetics and pharmacodynamics, dosimetry, and potential usefulness in a nuclear medicine procedure [3]. This is typically performed by evaluating the effects first in small animals, and by extension in humans, since human and animal health are closely intertwined [4]. Whether imaging

small animals or humans, nuclear medicine investigations are carried out with radiation detectors that localize ionizing radiation emitted from the subject. Positron (β^+) and gamma-ray (γ -ray) emitters are the primary radionuclides of interest, producing readily detectable signals outside the body. In the case of positron emission tomography (PET), annihilation photons carry no information regarding the radionuclide from which they ultimately originated, hindering their use in multi-radionuclide imaging. On the other hand, in single-photon emission computed tomography (SPECT), gamma cameras can readily distinguish radionuclides by their γ -ray energies, and are therefore more suitable for multi-radionuclide imaging.

Crosstalk is the primary challenge in multi-radionuclide SPECT, defined as signal contamination in one radionuclide's energy window from photons of the competing radionuclide(s). This can occur through:

1. Downscatter from higher energy photons, or
2. Overlap of photopeaks in an energy window.

Scatter and crosstalk lead to blurred projection images and increased noise, reduced image contrast and resolution, and a loss in quantification accuracy [5–7]. As illustrated in Fig. 1.1 for a high-purity germanium (HPGe) detector exhibiting extraordinary energy resolution [8], relatively narrow energy windows aid in selecting primary events associated with a given radionuclide. Although the energy windows aim to exclude unwanted events, the scatter continuum indicates a small degree of crosstalk for lower-energy radionuclides. For gamma cameras with less-favourable energy resolution, photopeak overlap can also become a serious problem.

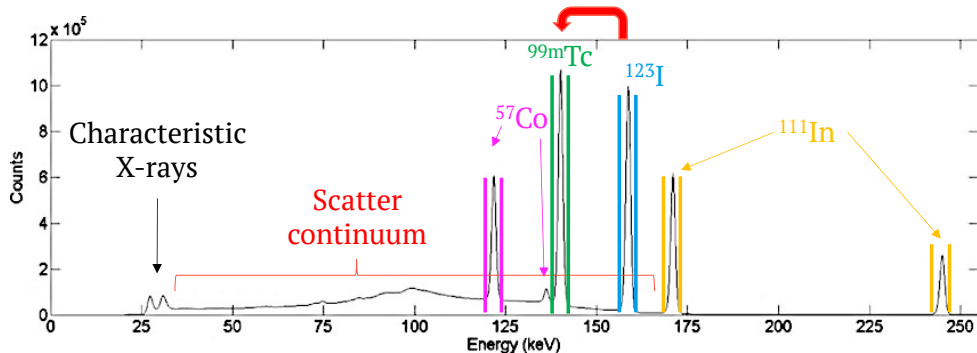


Figure 1.1: Multi-radionuclide energy spectrum of cobalt-57 (^{57}Co), technetium-99m ($^{99\text{m}}\text{Tc}$), iodine-123 (^{123}I), and indium-111 (^{111}In) acquired with a HPGe detector. The energy resolution is on the order of 1%, which provides sharp and distinguishable photopeaks for radionuclide selection using primary energy windows as indicated. A red arrow emphasizes downscatter crosstalk from a higher-energy radionuclide. Adapted from [8] by adding labels and annotations, used with permission.

The most common approach to multi-radionuclide SPECT crosstalk correction is the triple energy window (TEW) method developed by Ogawa et al. [9]. It estimates crosstalk from the scatter continuum extending above and below the primary energy window (see Fig. 1.2), then subtracts the result from the primary window. The TEW approach is generally successful so long as photopeaks are individually resolved, and each pixel in the image contains sufficient counts to accurately estimate the scatter continuum. When those conditions are not met, detected counts are incorrectly subtracted from the data, and image quality and quantitative accuracy are degraded. It is important to note that crosstalk subtraction compromises the Poisson distribution of detected events, which directly impacts the accuracy of statistical reconstruction algorithms. Despite this fact, the TEW method continues to be the clinically accepted method due to its simplicity and effectiveness in a number of complex situations [2].

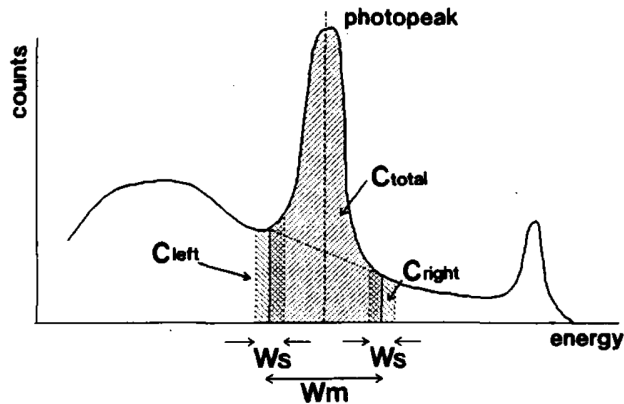


Figure 1.2: Window characteristics in the TEW method. The main window is located at the photopeak and subwindows are centered on the limits of the main window. The crosstalk component in the main window is estimated from a trapezoidal area using photon counts from the two subwindows, where C refers to the counts in the window of width W . From [9], used with permission.

State-of-the-art SPECT systems with enhanced spatial resolution are becoming increasingly accessible in both preclinical and clinical domains. Their primary emphasis is directed towards improving spatial resolution, with less emphasis on energy resolution, which is typically on the order of 10–15%. Given the resolution constraints of current and emerging technology, preclinical and clinical multi-radionuclide SPECT would benefit from a crosstalk correction technique that is not limited by a system’s energy or spatial resolution, nor uses subtractive methods. Therefore, this work aims to establish an improvement in multi-radionuclide recognition suitable for all SPECT systems, and its implementation was tested with a novel silicon photomultiplier (SiPM)-based preclinical SPECT scanner.

1.1 Production of Radiopharmaceuticals

To become oriented with the intricacies of multi-radionuclide SPECT, it is imperative to understand the fundamentals of nuclear medicine. Despite radioactive elements occurring naturally in the world, the majority of radionuclides used in nuclear medicine are produced by particle accelerators, nuclear reactors, or radionuclide generators. Particle accelerators, such as the cyclotron, accelerate relatively light ions to high energies ranging from a few MeV to several hundred MeV [1]. The high-energy ions bombard target nuclei to generate nuclear reactions that leave the target nuclei in an excited state. A cyclotron can bombard a target with protons to leave it in an excited state before undergoing β^+ -decay. In some cases, the excited state decays to a clinically useful radionuclide for PET or SPECT applications (see Fig. 1.3 and Table 1.1) [1, 10–12]. Since many of these radionuclides have half-lives on the order of minutes, cyclotrons are often installed in a hospital to prevent excess decay before transportation to their final destination.

1 H																	2 He
3 Li	4 Be											5 B	6 C β^+	7 N β^+	8 O β^+	9 F β^+	10 Ne
11 Na	12 Mg											13 Al	14 Si	15 P T	16 S	17 Cl	18 Ar
19 K	20 Ca	21 Sc β^+T	22 Ti	23 V	24 Cr	25 M β^+	26 Fe β^+	27 Co β^+	28 Ni β^+	29 Cu β^+T	30 Zn	31 Ga $\gamma\beta^+T$	32 Ge	33 As β^+	34 Se γ	35 Br β^+T	36 Kr γ
37 Rb β^+	38 Sr β^+T	39 Y β^+T	40 Zr β^+	41 Nb β^+	42 Mo	43 Tc $\gamma\beta^+$	44 Ru γ	45 Rh T	46 Pd	47 Ag T	48 Cd	49 In γ	50 Sn T	51 Sb	52 Te	53 I $\gamma\beta^+T$	54 Xe γ
55 Cs	56 Ba	57 La	72 Hf	73 Ta γ	74 W	75 Re T	76 Os	77 Ir	78 Pt γT	79 Au T	80 Hg T	81 Tl γ	82 Pb T	83 Bi T	84 Po	85 At T	86 Rn
87 Fr	88 Ra T	89 Ac T															
lanthanides		58 Ce	59 Pr	60 Nd	61 Pm	62 Sm T	63 Eu	64 Gd	65 Tb T	66 Dy	67 Ho T	68 Er	69 Tm	70 Yb	71 Lu T		
actinides		90 Th T	91 Pa	92 U	93 Np	94 Pu	95 Am	96 Cm	97 Bk	98 Cf	99 Es	100 Fm	101 Md	102 No	103 Lr		

Figure 1.3: Periodic table highlighting elements with radionuclides having applications in nuclear medicine. The applications are identified by symbols, where γ is for planar scintigraphy/SPECT, β^+ is for PET, and T is for theranostics using β^- , α , or Auger-emitting radioisotopes. From [12], used with permission.

Similar to the approach of target bombardment in particle accelerators, nuclear reactors bombard heavy nuclei with neutrons to produce useful radionuclides. When a heavy nucleus, such as uranium-235 (^{235}U), absorbs a neutron to become uranium-236

Table 1.1: Physical characteristics of commonly used radionuclides in nuclear medicine.

Radionuclide	Emission(s) ¹	Energy E (keV) ²	Abundance (%)	Half-life $T_{1/2}$	Specific activity A_S (MBq/nmol)	Comments and applications
PET radionuclides						
Oxygen-15 (¹⁵ O)	β^+	1735	99.9	122 s	3.4	Measure blood flow in heart, brain, and tumours with ¹⁵ O-water.
Fluorine-18 (¹⁸ F)	β^+	634	97	110 min	0.063	> 70–80% of all clinical PET studies, typically in ¹⁸ F-fluorodeoxyglucose (FDG).
Rubidium-82 (⁸² Rb)	β^+	2605 3381	13 82	75 s	n.d.	Myocardial perfusion imaging.
SPECT radionuclides						
Technetium-99m (^{99m} Tc)	γ	140	88	6.01 h	20,000 - 50,000	> 70% of all imaging studies.
Indium-111 (¹¹¹ In)	γ	171 245	90 94	2.8 d	60	Used when kinetics require imaging > 24 h post-injection.
Iodine-123 (¹²³ I)	γ	159	83	13.2 h	123 - 4,300	Diagnosis of thyroid cancer.
Therapeutic radionuclides						
Phosphorus-32 (³² P)	β^-	1711	100	14.3 d	n.d.	Treatment of myeloproliferative blood disorders.
Yttrium-90 (⁹⁰ Y)	β^-	2279	99.9	2.67 d	n.d.	Radioembolization treatment for nonresectable liver cancer.
Iodine-131 (¹³¹ I)	β^- γ	606 364	89 83	8.02 d	222 - 327	Detection and treatment of thyroid cancer and hyperthyroidism.

¹Emission(s) of interest

²Maximum energy of β decay

n.d.: no data

(^{236}U), the extremely unstable nucleus undergoes spontaneous fission, splitting the nucleus into fragments that can be chemically separated from other fission products. Common fragments useful in nuclear medicine include molybdenum-99 (^{99}Mo), iodine-131 (^{131}I), and xenon-133 (^{133}Xe). If a less massive nucleus is used as the target, then neutron activation can occur. In this case, the product of the reaction is an isotope with excess neutrons sharing the same chemical properties as the target. This makes chemical separation infeasible, although the activation products may decay to a desired radioisotope that can then be chemically separated for clinical use.

Radionuclide generators produce useful radionuclides by holding a parent in such a way that the daughter can be easily extracted or eluted for clinical use. The parent radionuclide is one with a relatively long half-life that decays to a more desirable radionuclide with a shorter half-life. An example of such a radionuclide pertains to arguably the most important γ -ray emitter in nuclear medicine—technetium-99m ($^{99\text{m}}\text{Tc}$). In a ^{99}Mo generator, ammonium molybdenate is attached to a porous column containing alumina resin. As ^{99}Mo decays to $^{99\text{m}}\text{Tc}$, the column is periodically eluted with saline to remove the loosely bound daughter. The extracted technetium pertechnetate (TcO_4^-) can then be used as the starting material for radiochemistry.

The ideal radionuclide in nuclear medicine has a half-life that matches the intended application—shorter half-lives minimize radiation exposure during imaging, and longer half-lives maximize therapeutic dose to the patient. In PET, the ideal radionuclide emits low-energy β^+ -particles that annihilate near the decay site, while in SPECT, the γ -ray energy should be high enough to penetrate tissue and leave the body, but low enough to be detected with a gamma camera. It is not simply a matter of choosing which radionuclide has ideal characteristics, then placing it within the organ of interest. Typically, a biomolecule is chosen based on its affinity for a specific organ or bodily function, then the biomolecule is labelled with a suitable radionuclide. Once labelled, it is important for radiopharmaceuticals to have a high specific activity, defined as the quantity of radioactivity per unit of substance (see Table 1.1). The maximum attainable specific activity is contingent on the molar mass and half-life of a radionuclide. Samples having 100% radioisotope abundance with no contamination are referred to as carrier-free, and are preferred in radiopharmaceutical preparations to increase labelling efficiency and minimize the mass and volume of the administered material [1]. Although PET radionuclides typically have higher carrier-free specific activities, their short half-lives and associated radiochemistry result in radiotracers with much lower specific activities than SPECT compounds [11].

Many biomolecules are composed primarily of hydrogen, carbon, and oxygen, allowing for a radioactive counterpart to be attached while maintaining the biomolecule's properties. This is the common approach for PET tracers utilizing radionuclides with low atomic numbers. Naturally, radiolabelling depends on the number of valence electrons and the resulting chemical bonds. For this reason, ^{99m}Tc is used in ~85% of SPECT procedures since it has seven outer electrons, offering a variety of opportunities for labelling molecules for different uses [13]. The resulting radiopharmaceuticals are analogue molecules mimicking those already found within the body. Many clinically used SPECT agents can be readily obtained from nuclear medicine departments, and if a desired SPECT radiopharmaceutical is not commercially available, a relatively simple laboratory setup often suffices since radiolabelling chemistry is usually simpler for SPECT than for PET [11]. Furthermore, the available SPECT radionuclides with a range of photon energies and half-lives make possible the simultaneous acquisition of multiple radiotracers capable of assessing distinct biological processes at the same time, from the same subject.

Carrier-free radionuclides that are readily usable without pharmaceutical labelling include ^{131}I and oxygen-15 (^{15}O). For those radionuclides that do require labelling to a biomolecule, the procedure is often as simple as aseptically injecting a known quantity of the radionuclide precursor into a sterile "cold kit" or vial containing the lyophilized (freeze-dried) pharmaceutical precursor [1]. The radionuclide becomes chemically attached to the pharmaceutical and the resulting kit is typically a multidose vial ready for use, although additional preparation steps may be required such as boiling, heating, filtration, and/or buffering. Taking everything into consideration, the ideal radiopharmaceutical possesses a high target affinity; is safe, convenient, cost-effective, and available; deposits a low radiation dose to healthy tissue inside the body, and in the case of therapeutics, deposits a large radiation dose inside the target.

1.2 Molecular Imaging

Functional and structural imaging have been central to the development and advancement of nuclear medicine and overall healthcare. Both imaging domains exploit the interactions of electromagnetic radiation to form images, although the resulting images contain highly differentiated information due to the sources of radiation. When an external source of ionizing radiation uniformly irradiates the body, detailed visualization of anatomical structure is possible due to differences in attenuation within the body. For example, calcium concentrated in bone makes up the most abundant high-

atomic number element in the body, which readily attenuates X-rays. This causes bones to appear with great contrast to soft tissues in X-ray or computed tomography (CT) images. Not only are structural images useful for localizing anatomical features, they can also enhance PET and SPECT data quality through attenuation correction and synergistic image reconstruction [14].

Functional imaging has clear diagnostic strength over anatomical techniques, since biochemical changes always occur before visible anatomical changes in the progression of disease [15]. By administering an internal source of ionizing radiation to a subject, the resulting distribution of a radiopharmaceutical can be reconstructed to visualize functional information. When fused with a structural image as demonstrated in Fig. 1.4 for an indium-111 (^{111}In)-labelled radiotracer [16], even more useful information can be extracted, as multiple modalities aid in localizing and staging disease while providing specificity and differentiation from normal tissue. This provides a means of studying dynamic and temporal biological processes of disease through an understanding of the physical and physiological phenomena of radiopharmaceuticals.

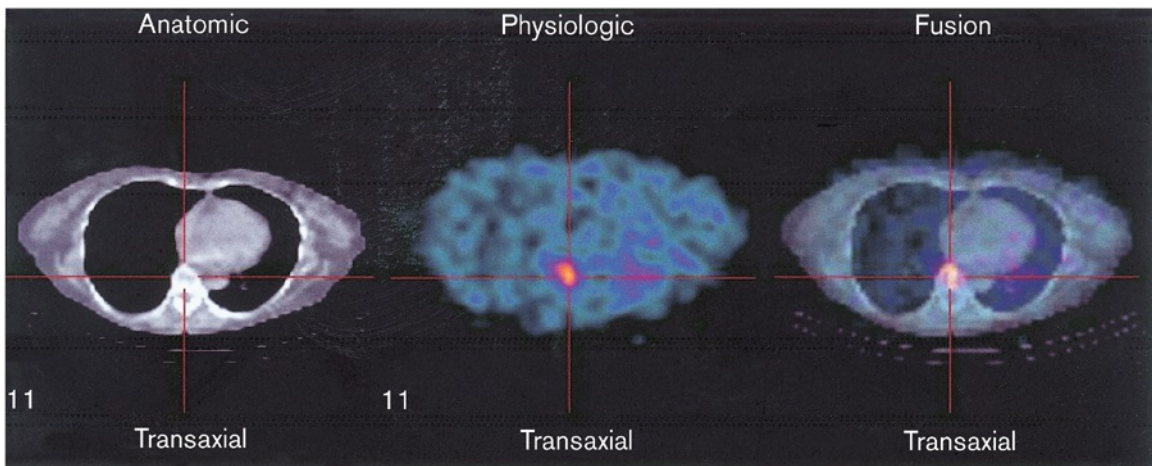


Figure 1.4: ^{111}In pentetreotide chest SPECT/CT in a 62-year-old female patient with a previously resected carcinoid tumour. SPECT shows a focal uptake, and the fused SPECT/CT image precisely localizes it in the T8 vertebrae. A bone scan did not show abnormalities, and magnetic resonance imaging confirmed the SPECT/CT findings. From [16], used with permission.

Nuclear medicine image contrast depends on the tissue's ability to concentrate a radiopharmaceutical in the body according to pharmacological interactions between radiopharmaceuticals and biochemical markers released during the disease process [17]. Bioactive molecules labelled with a radioactive isotope are ideally taken-up by a cellular target, resulting in a high target-to-background activity ratio. By ob-

servicing the uptake over time and where radiation is emitted from, a radiologist can monitor both the pharmacokinetics indicating the movement and transformation of a drug within the body, along with the pharmacodynamics indicating how the drug exerts its effects on the body. Radiopharmaceuticals can be categorized by the following classes of uptake mechanisms: active, passive, and combined intracellular uptake, and extracellular uptake. Comprehension of these mechanisms can aid the radiologist in selecting the appropriate radiopharmaceutical(s) to use for a given indication. It can also aid in minimizing false positives and false negatives when interpreting nuclear medicine studies through an understanding of the underlying reasons for both normal and abnormal physiologic radiopharmaceutical distributions.

The ability to visualize cellular function parameters enables a variety of choices from potential biomarker targets, including cellular metabolism, proliferation, gene expression, peptide and membrane biosynthesis, receptor expression, hypoxia, angiogenesis, and apoptosis [3]. Knowledge of these cellular functions continues to advance, along with nuclear medicine procedures and associated technology to visualize and target specific functions at the molecular level. What's more, separate protocols previously requiring two or more drugs can now be combined into a single procedure, offering identical physiological conditions during simultaneous acquisition.

Multi-radionuclide SPECT is becoming increasingly prevalent in modern nuclear medicine. Numerous preclinical and clinical studies have explored its applications in various fields, including cardiac imaging [18–25], neuroimaging [26–33], lung function assessment [34, 35], and hyperparathyroidism [36–39]. For example, in cardiac SPECT, a combination of ^{99m}Tc sestamibi and thallium-201 (^{201}Tl) assesses myocardial perfusion and heart muscle viability, aiding in coronary artery disease management. In the evaluation of pulmonary embolism or other lung conditions, ^{99m}Tc macroaggregated albumin (MAA) is used for perfusion imaging, while krypton-81m (^{81m}Kr) or ^{133}Xe are used for ventilation studies. For hyperparathyroidism and thyroid cancer, ^{99m}Tc sestamibi targets parathyroid adenomas, while ^{201}Tl or iodine-123 (^{123}I) delineates and assesses thyroid function. Additionally, in the context of cancer imaging, multi-radionuclide SPECT is valuable for assessing organ function while localizing and characterizing tumours [40, 41]. These applications demonstrate how combinations of functional imaging techniques can examine different aspects of physiology in unison. Furthermore, multi-radionuclide SPECT in theranostics can play a pivotal role in patient selection for targeted radionuclide therapy by determining whether a tumour exhibits specific receptor expression or biomarker targets [42].

Expanding the scope of multi-radionuclide SPECT, neuroimaging plays a crucial role in assessing and diagnosing conditions like Alzheimer’s disease and epilepsy, offering a comprehensive evaluation of brain function [41]. For dementia differentiation, the combination of cerebral perfusion imaging with dopamine transporter imaging aids in distinguishing between Alzheimer’s disease and other forms of dementia, such as Lewy body dementia [43]. In epilepsy management, precise localization of epileptogenic foci is vital for effective treatment planning and potential surgical intervention [44]. Cerebral perfusion imaging identifies regions with compromised blood flow, often linked with epileptic activity, and benzodiazepine receptor imaging offers insights into receptor distribution and binding. Together, these techniques can pinpoint the specific brain regions responsible for seizures. In addition to epilepsy and Alzheimer’s disease, a wide range of conditions can affect the central nervous system, including Parkinson’s, multiple sclerosis, Huntington’s disease, cerebral palsy, neurodegenerative diseases, brain tumours, and psychiatric disorders, among others. The versatility of multi-radionuclide SPECT makes it a valuable tool for addressing a wide spectrum of diseases and conditions throughout the body. It holds substantial untapped potential for enhancing our comprehension of underlying pathophysiology while facilitating the development of novel and personalized treatment strategies.

1.2.1 Emission Tomography Image Acquisition

Molecular images are most commonly produced with ionizing radiation detected outside the body using individual γ -ray emissions, or β^+ emissions yielding back-to-back annihilation photons detected in coincidence. The emitted photons are most likely to interact with a radiation detector via photoelectric absorption and Compton scattering as they impart a signal in the detector through ionization and excitation.

1.2.1.1 Positron Emission Tomography

In the case of β^+ -emitting radiopharmaceuticals, polyenergetic β^+ -emissions ultimately annihilate with an electron to produce back-to-back coincident 511 keV photons. As illustrated in Fig. 1.5, the annihilation photons are detected with opposing detectors in a PET scanner to localize the radiopharmaceutical distribution in a three-dimensional (3D) image [45]. In this fashion, a typical PET scanner consists of a large ring of scintillation crystals optically coupled to photosensitive photomultiplier tubes (PMTs). By combining multiple scintillation crystal rings along a PET scanner’s axis, excellent sensitivity can be achieved.

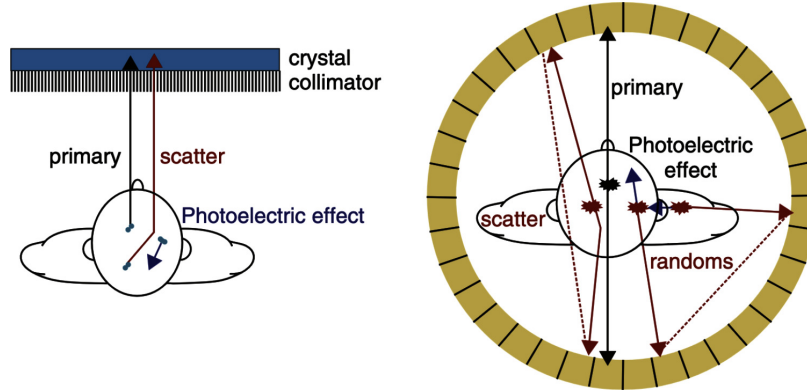


Figure 1.5: Illustration of types of events in nuclear medicine imaging observed with a gamma camera (left) and PET scanner (right). From [45], provided courtesy of Dr. Georges El Fakhri, used with permission.

After the atoms of the crystal have been excited by ionizing radiation, scintillation light is emitted as the atoms return to their relaxed state. This isotropically emitted scintillation light is subsequently detected by an array of PMTs whose signals are processed by a computer to determine the position, energy deposited, and time of interaction. A coincidence timing window begins once a 511 keV photon is detected, and if a second event is detected within that timing window, the events are registered as a coincident event. Qualified events are selected from true coincidences with the goal of eliminating any signal arising from random and scatter coincidences. Qualified coincident events determine the lines-of-response (LORs) along which radioactive decay events are presumed to have occurred. Modern PET detectors calculate the time-of-flight from subsequent events to better localize the radiotracer along the observed LOR and improve spatial resolution. By reconstructing qualified coincident events, the radiopharmaceutical distribution can be quantified in 3D.

A common misconception is that PET offers superior spatial resolution over SPECT. In general, PET spatial resolution is primarily limited by three factors [1]:

1. The intrinsic spatial resolution of the detectors,
2. The distance travelled by positrons before annihilation, and
3. The non-collinearity of annihilation photons.

This can be expressed through the equation for the system resolution R_S using

$$R_S^2 = R_I^2 + R_{\beta^+}^2 + R_{180^\circ}^2 \quad (1.1)$$

where R_I is the intrinsic resolution, and R_{β^+} and R_{180° quantify resolution loss due

to the positron range and non-collinearity of photons, respectively. Non-collinearity is caused by any residual momentum of the β^+ particle, which is conserved through ejection of annihilation photons separated by less than 180° . The loss of resolution from non-collinearity is worse for clinical PET than preclinical PET due to the scanner's larger bore diameter. While SPECT does not inherently suffer from factors 2 and 3, it does offer improved intrinsic resolution since the scintillation crystal used in SPECT scanners can be much thinner than in PET. This is because SPECT systems are optimized to detect photons primarily in the energy range of 100–200 keV while PET photons are primarily around 511 keV and hence more penetrating.

1.2.1.2 Single-Photon Emission Computed Tomography

Contrary to polyenergetic β -emitting radionuclides, γ -ray emitting radionuclides emit monoenergetic photons with a specific energy. As illustrated in Fig. 1.5, individual photons emitted directly from the nucleus can be detected with a radiation detector in a gamma camera. While a gamma camera can be used for two-dimensional (2D) planar scintigraphy, SPECT creates 3D images by rotating the camera around the subject to acquire then reconstruct multiple projection images into a radiopharmaceutical distribution.

In order to identify the LOR between the gamma camera and radionuclide of origin, a collimator with one or more apertures is placed in front of the scintillation crystal to define the direction of detected γ -rays. As illustrated in Fig. 1.6 [46], collimators come in a variety of geometries including parallel hole, pinhole, divergent, and convergent, with each serving a different purpose [47]. The aperture arrangement directly affects SPECT spatial resolution and sensitivity. In the absence of photon scatter, the limiting spatial resolution of a projection image depends on two factors [1]:

1. The intrinsic spatial resolution of the detector, and
2. The collimator's geometric resolution.

These factors can be related through the equation for the system resolution using

$$R_S^2 = R_I^2 + R_C^2 \tag{1.2}$$

where R_C is the collimator resolution determined by the aperture diameter. These factors can be corrected for magnification to account for distances in the object rather than distances in the detector. For this reason, well-designed converging or pinhole collimators are able to magnify images to enhance the collimator's geometric reso-

lution while overcoming the camera’s intrinsic spatial resolution, ultimately leading to higher-resolution images in comparison to non-magnifying or minifying collimators [48]. There is usually a tradeoff between system resolution and sensitivity, however, it has been shown that pinhole collimation offers distinct advantages over other collimators in terms of high-resolution imaging with improved sensitivity [49].

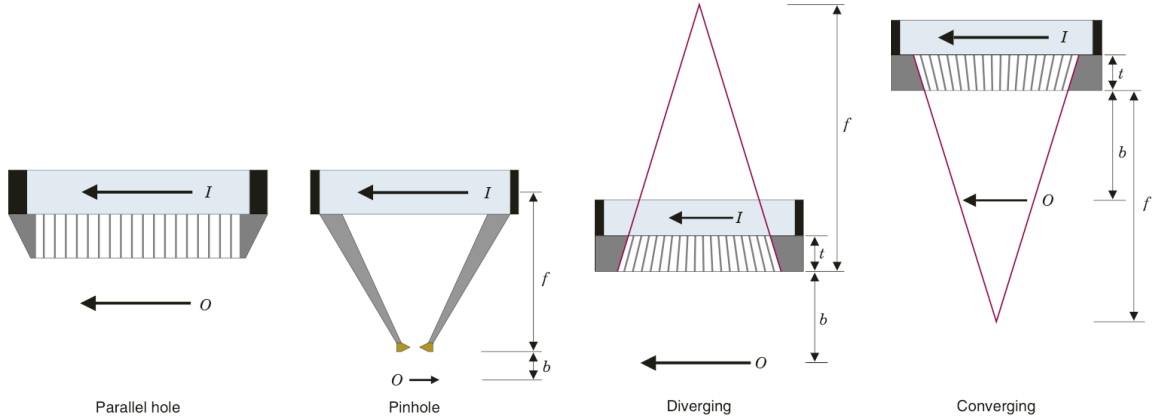


Figure 1.6: Basic types of SPECT collimators illustrating the effect of aperture design on magnification and image orientation. Symbols are as follows: radioactive source O , projected image I , source-to-aperture distance b , pinhole aperture-to-detector distance or collimator-to-convergence point distance f , and collimator thickness t . Adapted from [46] by cropping and modifying layout, used with permission.

Behind the collimator, photon detection remains as described for PET: photons interact in a scintillation crystal to produce optical photons which are readily detected by PMTs, and computer electronics calculate the (x, y) positions and deposited energy for each interaction within the crystal. Gamma cameras acquire 2D planar images, and by rotating the camera around the subject, viewing the subject with multiple cameras, and/or viewing the subject through multiple pinholes, numerous projection images can be obtained to reconstruct the radiopharmaceutical distribution.

The desired single-photon events used in tomographic image reconstruction are the primary unscattered photons present in the photopeak. In reality, photons can scatter multiple times before their energy is deposited in the detector and integrated into an energy spectrum. Although an energy spectrum does not identify primary versus scattered photons, their presence introduces distinguishable features, such as the photopeak and scatter continuum. With the aid of Monte Carlo simulations, detailed information about photon scatter can be recorded, including the scatter site, energy following scatter, and number of times scattered. Without Monte Carlo, the identification of scattered photon events relies primarily on energy discrimination.

In most clinical SPECT situations, scattered photons account for 30–40% of the photons detected in the photopeak energy window [2]. This results in mispositioned counts leading to blurred projection images, reduced image contrast, a loss of spatial resolution, and a significant decrease in quantification accuracy in the underlying activity distribution [5–7]. The degradation of image quality is attributable to the inability to identify the exact location of scatter events. At best, a collimator can aid in identifying the direction from which a detected photon entered the camera. To emphasize the effects of degraded image quality, consider the study of ^{201}Tl cardiac perfusion SPECT by Floyd et al. in [50], where major changes in image contrast and quantification were revealed by applying a Monte Carlo-based scatter correction to ten patient-cases. In nearly every patient-case, a greater defect was revealed in the left anterior descending and right coronary arteries than what was initially estimated with conventional energy windows, with the total average defect increasing from 12.4% to 20.2%. This resulted in three cases overturned from normal to abnormal and nine patients receiving coronary angiography to assess blockage.

Radiation detectors used in nuclear medicine imaging have recently seen improvements in the limiting intrinsic spatial resolution through the development of solid-state photodetectors such as cadmium zinc telluride (CZT) and silicon photomultipliers (SiPMs) [51]. Their advancement is owed to the continual refinement in semiconductor fabrication processes which has matured over the past 30 years. One of the key differences between CZT and SiPM technology is that SiPM's require a scintillator to convert γ -rays into visible light, whereas CZT detectors directly convert γ -rays into electrical signal. Furthermore, SiPM arrays are considered to be more compact with simpler readout electronics requiring a lower operating voltage than CZT technology.

In nuclear medicine applications, SiPMs outperform traditional PMTs in terms of their superior timing resolution, small form factor offering improved spatial resolution, thermal stability due to reduced operating current, and their insensitivity to magnetic fields. This has led to the direct incorporation of PET into magnetic resonance imaging (MRI). Thick metal collimators used with SPECT are generally limited to operation in environments free of magnetic fields, although SPECT/MRI scanners have recently been developed in side-by-side and in-line systems [52], in addition to SPECT inserts for clinical and preclinical MRI [53–55]. Nonetheless, SiPM technology is still in its infancy and has yet to be seen in widespread clinical implementation, while their preclinical implementation is yielding immense benefits, primarily in the realms of radiopharmaceutical drug development and procedural advancement.

1.2.2 Preclinical and Translational Imaging

Procedures that were once developed in the clinic are now being designed and tested at the preclinical level, where successful drug development and application is translated cyclically from bench to bedside and back as information is gathered and built upon [11]. This approach to translational research is shaping the practice of modern medicine to become more sustainable by incorporating knowledge from multidisciplinary, multiphase, and multisectoral projects to arrive at solutions for complex health-related problems. Before a radiopharmaceutical becomes clinically implemented, there are five development stages involving multidisciplinary contributions, which can span over 10 to 15 years [56]. The stages are:

1. Discovery and development,
2. Preclinical research,
3. Clinical research involving phases I–IV,
4. Review from regulatory agencies, and
5. Post safety monitoring from regulatory agencies.

It is difficult to pinpoint where drug development begins in nuclear medicine, but in almost every case, it starts with an unmet clinical need where a non-invasive approach is required. Examples include target identification, characterization of drug pharmacological, pharmacokinetic, and pharmacodynamic profiles, and organ function and metabolism in a variety of pathological contexts [11]. To satisfy this need, researchers turn to preclinical settings to discover, develop, and validate safe and effective radiopharmaceuticals using small-animal models.

In early studies, clinical SPECT systems were retrofitted with pinhole collimators positioned close to the animal to achieve high-resolution images with a large magnification factor [49]. With a high magnification factor, the image-degrading effect of the camera’s intrinsic resolution is minimized. Combining this knowledge of pinhole collimation with a paralleled interest in understanding biochemical processes has sped up the development of dedicated high-resolution molecular imaging systems for small animals [57]. The superior resolution-sensitivity tradeoff of pinhole collimators in SPECT make them appealing in the construction of novel preclinical scanners. More recently, Cubresa Inc. developed a SiPM-based pinhole-SPECT system—the Spark—which has already proven itself useful by imaging ^{123}I for targeting butyrylcholinesterase (BChE) for diagnosis of Alzheimer’s disease [58].

During the preclinical stage of drug development research, *in vitro* and *in vivo*

testing supports a drug's safe application in humans prior to translation into clinical trials. While *in vitro* studies offer valuable information on cellular function and response to novel drug developments, the environment in which these studies are performed outside the living organism does not necessarily encapsulate the behaviour of the cells *in vivo*. Therefore, small-animal models bearing human cell-lines permit the study of complex interactions occurring in relevant biological systems with variables related to immunological, nutritional, or hormonal aspects, as well as systemic responses. The use of small-animal models represents a bridge between discoveries at the molecular level and clinical implementation. By introducing non-invasive molecular imaging techniques in a preclinical context, longitudinal studies are possible, making it feasible to repeatedly screen the entire disease spectrum from onset and progression to therapy monitoring [11]. For these reasons, small-animal imaging techniques continue to drive their increasing use by pharmaceutical companies, contract research organizations, and research institutions.

Preclinical imaging techniques are typically designed with small-animal homologs, such as mice, bearing human similarities and cell-lines to allow results to be easily translated to humans [59]. To facilitate this translation, it is important to consider the mass and associated volume of the administered radiopharmaceutical. In preclinical imaging, the maximum injected volume should not exceed 10% of the total blood volume [11]. Therefore, a 20 g mouse with a blood-volume of 2 ml should not receive an intravenous injection exceeding 200 μ l. Due to labelling efficiency, concentration, and specific activity, this puts a limit on the amount of radioactivity that can be administered, which is typically on the order of tens of MBq for small-animal SPECT. When translating between humans and small animals, the amount of injected radioactivity does not scale with the subject size since high-resolution preclinical systems require a greater concentration of injected tracer per gram of tissue, with a ratio of 20 \times that in humans [11]. This illustrates that as the size of the regions to be quantified is reduced, and/or the sensitivity of the scanner is reduced, the amount of radiopharmaceutical administered is typically increased to achieve adequate count statistics. This elevated amount of chemical compound per unit mass can threaten the validity of the tracer principle in the event where receptor occupancy becomes saturated [60].

PET and SPECT scanner designs aim to optimize both resolution and sensitivity, but experimental scanners are increasingly pursuing resolution at the expense of sensitivity. High doses of radioactivity and/or long scan times are often required to achieve adequate count statistics in high-resolution systems. This can lead to the

administration of a significant mass of radiopharmaceutical in the case of low-specific-activity radionuclides, such as those used in PET. For these reasons, brain imaging in small animals remains as a challenging application due to the small sizes of brain structures, the complex kinetics, and the relatively low tracer uptake [61]. Therefore, high-specific-activity radionuclides are crucial for the validity of preclinical and translational molecular imaging. The improved sensitivity of PET compared to SPECT does not always compensate for low specific activities [11]. The use of multi-pinhole collimation has become the standard in most preclinical SPECT systems, as it offers high spatial resolution with increased system sensitivity over single-pinhole SPECT, although single-pinhole collimators can offer a larger field of view (FOV) with comparable resolution. These factors must be taken into consideration when designing imaging studies. Furthermore, imaging systems and their associated software usually have multiple options for generating data, which are often overlooked but essential when reporting the methods used to create and analyze data [62]. Therefore, it is important to understand the performance aspects of an imaging system, as they have a direct impact on data quality and possible uncertainties.

1.3 Performance Measurements of Gamma Cameras

The accepted approach to measuring spatial resolution, sensitivity, and other performance metrics of medical imaging devices is based on protocols defined by the National Electrical Manufacturers Association (NEMA). Founded in 1926, NEMA is a standards-developing organization associated with electrical equipment and medical imaging manufacturers. The products used in medical imaging demand refined standards for assessing their performance to ensure patient safety, inform decision-making, drive research and innovation, and provide comparative performance evaluation.

Prior to the coming of NEMA standards, manufacturers measured the performance of their cameras in a variety of ways, making it difficult to objectively compare manufacturer's specifications for different cameras. With the introduction of NEMA protocols, manufacturers can now publish important performance parameters, and customers can reproduce these tests to verify whether a newly purchased camera meets the published specifications. The ability to directly compare performance parameters can influence purchase decisions, as well as the types and designs of studies permitted within a nuclear medicine or research department. Researchers can use the NEMA protocol to gain knowledge of these performance parameters, providing insight into what can be expected in a reconstructed image, minimum detectable limits, and

amounts of administrable radioactivity, for example, all of which are important for designing imaging studies.

The protocols published by NEMA define quantitative measurements of performance characteristics and reporting techniques for the specification of a number of parameters. These performance parameters can be broken down into subcategories depending on the type of camera being tested, i.e., CT, MRI, PET, or SPECT. Table 1.2 presents typical performance characteristics of modern clinical [1] and pre-clinical gamma cameras [63–67]. Although NEMA has not yet published a dedicated protocol for preclinical SPECT, the clinical standard can be reasonably adapted to test preclinical systems. These modifications generally involve the use of smaller pixel sizes and smaller radioactive source distributions, which deviate from the specified standard to reflect the high-resolution capabilities of preclinical SPECT.

Table 1.2: Typical performance of clinical and preclinical gamma cameras.

Performance parameter	Clinical SPECT	Preclinical SPECT
Intrinsic spatial resolution	2.7–4.2 mm	1.5–4.0 mm
Intrinsic flood field uniformity	2–5%	1–5%
Intrinsic energy resolution	9–11%	5–20%
SPECT spatial resolution	~10 mm	0.4–1.75 mm

1.4 Monte Carlo in Nuclear Medicine Imaging

Despite the continual refinement of gamma camera performance parameters, the acquisition of nuclear medicine images can be deficient of useful or key information. Some performance parameters simply cannot be measured or depend on factors difficult to measure. Simulations using the Monte Carlo technique are therefore an important tool in evaluating a range of medical physics related topics pertaining to the interactions of radiation with matter, detector geometry and material designs, and the impact of various factors on image quality.

One of the most important applications of the Monte Carlo method is to simulate realistic images from imaging systems. This requires an accurate model of the imaging system, which further depends on accurate physics models. This can be difficult to configure when one considers the number of adjustable parameters that can affect image quality. To assist in this adjustment, various Monte Carlo software packages offer modules to simulate the behaviour of radiation detectors and the signal processing chain in an imaging system. For example, the Geant4 Application for Tomographic Emission (GATE) uses the Geometry and Tracking (Geant4) toolkit to generate and

transport particles through the materials of modelled geometries. This mimics physical phenomena between particles and matter by simulating numerous random events or interactions based on known probabilities and statistical distributions.

To illustrate the generation of simulated data, consider the detection of a γ -ray in a scintillation crystal. If the γ -ray interacts and deposits energy in the scintillation crystal, GATE processes this information to simulate detector pulses, which correspond to observed data. The associated pulse can be tuned such that the output simulation data resembles measured data. This is done with the digitizer in GATE, which consists of several modules that collectively filter data to account for aspects of camera performance. Many of these modules in GATE require the input of a reference value. Therefore, the NEMA standards offer a useful approach to determining the required input values while also enabling model validation through direct comparison of simulated and measured results.

Once a Monte Carlo model has been validated, a number of previously inaccessible stages of image formation can be investigated in detail, as illustrated in Fig. 1.7. This allows for multiple scattering of photons to be evaluated, attenuation properties investigated, detector interaction points determined, and parent sources identified [68]. This investigation can be aided by the generation of gold standard data. In nuclear medicine imaging, gold standard images typically refer to those that are free of scatter or photon crosstalk. The formation of these types of images are indispensable in assessing crosstalk correction performance in multi-radionuclide SPECT.

1.5 Implementations of Multi-Radionuclide SPECT

The primary challenge in multi-radionuclide SPECT is photon crosstalk. This causes incorrect reconstruction of the radiopharmaceutical distribution and incorrect quantification of the absolute activity, resulting in a loss of specificity and contrast of the true radiotracer distribution. Energy discrimination by simply filtering the primary events with a primary energy window generally does not suffice to correct for crosstalk due to a gamma camera's energy resolution. The deleterious effect of energy resolution is minimized in HPGe detectors which exhibit an energy resolution near 1% and offer precise identification and discrimination of γ -ray energies [8]. However, HPGe detectors require cryogenic cooling for low-noise operation and are expensive and complex, making them less desirable for nuclear medicine imaging applications than commonly used scintillation crystals like cesium iodide (CsI) and sodium iodide

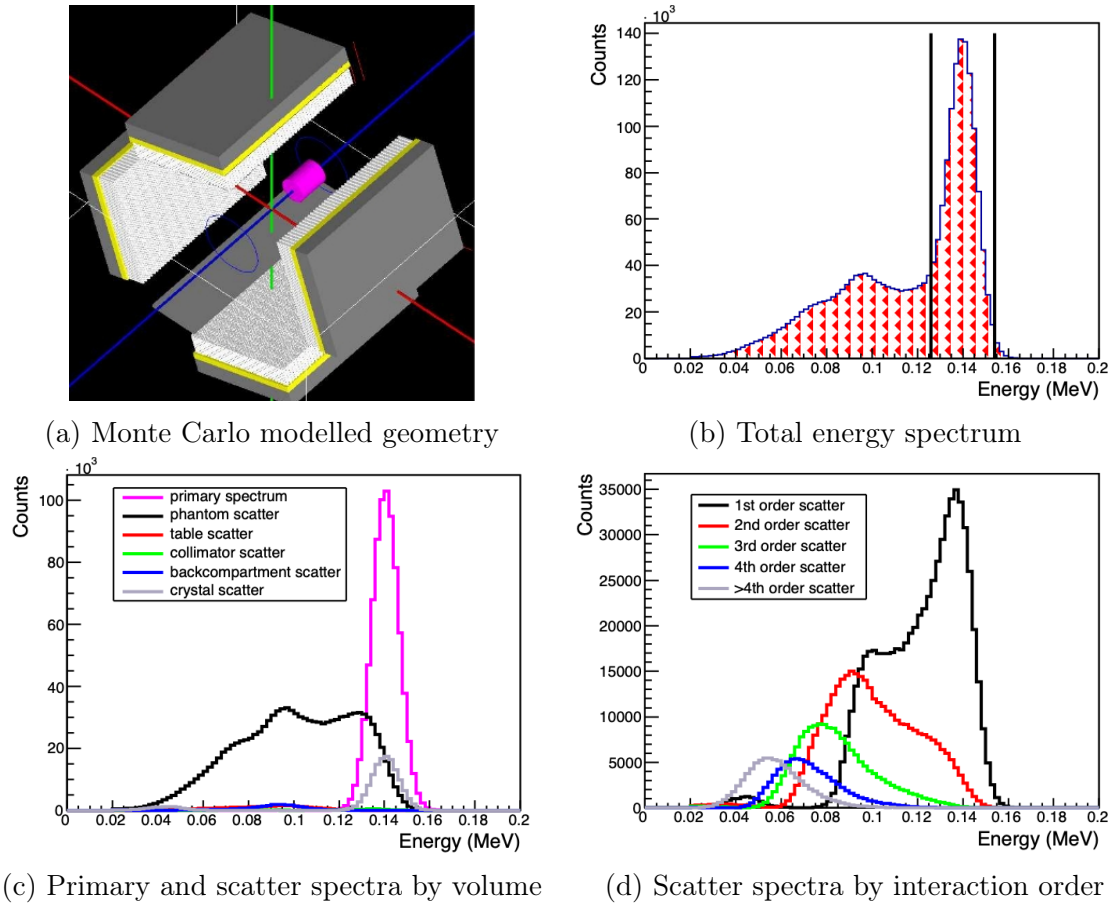


Figure 1.7: GATE Monte Carlo simulation of a hypothetical clinical SPECT acquisition using ^{99m}Tc . (a) The modelled SPECT system features four gamma cameras rotating about a cylindrical brain phantom. (b) The total energy spectrum of detected events is illustrated with a 20% energy window centered on the photopeak. Note that experimental SPECT detectors are only capable of measuring a photon’s energy, not the number of times scattered, which contributes to the total summed energy spectrum. (c) Energy spectra illustrate the decomposed contributions from photons scattering in different components of the SPECT system. Note the scatter contributions overlapping with the primary photopeak. (d) Scatter spectra show that the peak shifts to lower energies depending on the number of scatter events.

(NaI). Fortunately for common SPECT systems, crosstalk can be corrected to some degree through accurate modelling of the SPECT system matrix, photon energy discrimination, and/or implementation of physics-based models to allow simultaneous identification of two or more radionuclides.

The wide range of approaches adopted by different researchers for estimating crosstalk adds to the general confusion as to which method is best to adopt. The most successful techniques focus on spectral-based measurement, modelling, or a

combination of both in order to estimate the crosstalk present in acquired images. These methods are generally based on the equation

$$P = T - S \tag{1.3}$$

where P represents the primary emissions of interest for a given radionuclide, T is the total acquired data, and S gives the estimated crosstalk component. Subtractive methods risk compromising the Poisson distribution of data, which can negatively impact the quality of reconstructed images. Spectral-based corrections utilize the energy spectrum to estimate, then subtract the crosstalk events from acquired data prior to reconstruction to prevent crosstalk from influencing the reconstructed distribution. In the case of model-based corrections, the correction is typically applied post-reconstruction using a model to estimate then subtract the 3D distribution of crosstalk events from the tomographic image reconstructed from all events. This section addresses some pearls and pitfalls of existing crosstalk correction methods.

1.5.1 Crosstalk Corrections Pre-Reconstruction

1.5.1.1 Dual Energy Window Method

Crosstalk corrections made prior to tomographic reconstruction utilize the energy spectrum and multiple energy windows to estimate scatter and crosstalk events. Note the interchangeable use of scatter and crosstalk due to the application of scatter correction methods for crosstalk correction. One of the earliest approaches of scatter correction was developed in 1984 by Jaszczak et al. using a dual energy window approach [69]. In this method, crosstalk is estimated as

$$S = kS_{sw} \tag{1.4}$$

where k is the fraction of scatter or photon crosstalk in the primary window and S_{sw} are the scatter or crosstalk events in the secondary window. Thus, a fraction of secondary window events are subtracted directly from the primary window.

There are issues faced with estimating the scaling factor or fraction of scattered events solely from the energy spectrum, since the spatial distribution of scatter differs as a function of energy loss and number of scattering events. In other words, the primary window contains photons with small deflection angles, i.e., first-order scatter, while the secondary window contains photons with larger deflection angles

and higher-order scatter. Thus, the dual energy window method effectively removes too many photons far from the true source location and not enough at the source location [2]. Although this method is suitable for scatter estimation using counts below one photopeak, it is not suitable in multi-radionuclide (or multi-energy) SPECT where spectral information exists across multiple photopeaks.

1.5.1.2 Triple Energy Window Method

A similar energy window approach was developed by Ogawa et al. in 1991 that addresses the difficulty in estimating the fraction of scatter or crosstalk events found in the primary window. This approach, known as the triple energy window (TEW) method, uses secondary energy windows overlapping the limits of the primary energy window to estimate the scatter continuum found directly in the primary window. The secondary windows determine the number of detected events with energies above and below the photopeak, and the resulting trapezoidal area between the secondary windows is assumed to correlate to the scatter continuum in the absence of the photopeak using the equation

$$S = \left(\frac{C_l}{w_l} + \frac{C_u}{w_u} \right) \times \frac{w_p}{2}. \quad (1.5)$$

Here, w denotes the energy window width and C denotes the counts in the corresponding lower l , upper u , and primary p windows. The calculation is applied pixel-by-pixel for the entire set of projection images. This method offers an approach that is conceptually simpler than dual energy windows and is extendable to multi-radionuclide SPECT, so long as photopeaks are individually resolved.

The pixel-by-pixel calculation requires sufficient count statistics to reliably estimate the scatter or crosstalk continuum, and this issue can be mitigated to some degree in clinical applications where large pixels are used. However, in preclinical applications where high-resolution detectors have small pixels, the count deprivation issue is exacerbated. Nonetheless, Cot et al. applied the TEW method with attenuation correction in preclinical SPECT to determine whether corrections were necessary, given the limited attenuation in small animals [70]. Without any correction, an error of -30% was observed in quantitative accuracy. This result improved with attenuation correction, leading to a quantitative overestimation of nearly 13% . When attenuation and crosstalk correction were combined, Cot found excellent agreement between the true and reconstructed activity concentration, as indicated by an error of 1.2% .

1.5.1.3 Independent Component Analysis

Independent component analysis (ICA) is a computational method for separating multivariate signal into additive subcomponents [71]. It aims to find a linear transformation using a mixing matrix that decomposes the signal into independent components to uncover the original sources in the observed data. Chang et al. [72] and later Yang et al. [73] explored the use of spectral unmixing with ICA using several energy windows. Their formalisms solved for mixing matrix values that equated the acquired energy spectrum to a weighted linear combination of independent components associated with $^{99\text{m}}\text{Tc}$ and ^{123}I . Both groups reported that radionuclide images could be well-separated, for which Chang et al. used 26 energy windows and Yang et al. used seven energy windows. Xu et al. also formulated an unmixing strategy based on the makeup of signals in each energy window [74]. Their work relied on the calculation of crosstalk contamination factors and detector efficiencies for iodine-125 (^{125}I) and ^{111}In to scale linear combinations of projection images.

1.5.1.4 Other Energy Window Methods

Numerous energy window approaches for scatter and crosstalk estimation have been studied in a variety of configurations. King et al. [75] and Pretorius et al. [76] analyzed the use of a dual photopeak window to split the primary window in two, with only marginal benefits observed. Vija et al. attempted to linearly combine images from different energy windows to estimate a scatter image [77]. More recently, Hapdey et al. used spectral factor analysis by modelling the energy spectrum in a given pixel as a linear combination of basis spectra, including a spectrum for each of the L photopeaks and $L+1$ scatter spectra surrounding the photopeaks [30]. Thus, by solving the linear combination to extract a photopeak component, images could be generated from the primary counts for a given radionuclide. Substantial biases in absolute quantification have been reported in spectral factor analysis due to the difficulty in separating unscattered photons from photon crosstalk or photons scattered by a small angle [30, 78].

Other researchers compared dual energy window, TEW, and spectral factor analysis methods in single-radionuclide SPECT and found that scatter correction significantly improved contrast and absolute quantitation but did not have noticeable effects on uniformity or spatial resolution, although the signal-to-noise ratio was reduced [79]. Similarly, Ljungberg et al. compared activity quantitation of dual-energy, dual-photopeak, and TEW methods in $^{99\text{m}}\text{Tc}$ brain perfusion imaging and found min-

imal differences, stating that “a user may select a correction method that is easy to implement on a particular system.” [80]. Therefore, despite the admirable attempts of past researchers to apply spectral-based crosstalk and scatter corrections, the TEW method continues to be the clinically adopted method due to its simplicity and effectiveness in a variety of complex scatter and crosstalk scenarios.

1.5.2 Crosstalk Corrections During Reconstruction

An appealing approach to crosstalk correction is to include a mathematical model during iterative reconstruction in order to modify, rather than subtract, the distribution of photon crosstalk. Unfortunately, interjecting information into a reconstruction algorithm or modelling the system matrix is not commonly available to researchers, since scanner geometry and reconstruction algorithms are often proprietary pieces of information protected by the manufacturer. This has led to limited implementations of crosstalk correction techniques during iterative image reconstruction. Nonetheless, crosstalk correction algorithms that do interject into the iterative reconstruction process typically incorporate an additional computation step to utilize information from the TEW or other appropriate methods [20].

1.5.2.1 Energy Window Methods

Studies by King et al. found improved image quality after adding a scatter term to the forward projection estimate during iterative reconstruction [75]. Their original work used a dual window approach, which required estimation of a scatter fraction to scale the total number of events detected in a given pixel. However, their later work in [81] used a TEW estimate for the scatter term added during forward projection, resulting in a lower error compared to the conventional TEW method.

1.5.2.2 Klein-Nishina Method

A complex approach to crosstalk correction presented by Shcherbinin et al. employed the Klein-Nishina (K–N) differential cross-section of photon scatter to analytically model the scattered photon distribution [82]. When applied to high-energy photons, the analytic K–N formula describes Compton scattering and allows for an exact calculation of scattering angles. In this analytic approach, CT data must be available for subject decomposition. By considering the material of the subject, the applied K–N formula modelled the probability of a photon scattering in a voxel before being detected in a specific detector dixel. Considering that 30–40% of detected pho-

tons have scattered in a clinical acquisition, and photons can scatter multiple times before detection, an analytical calculation for so many possible scatter and detection combinations quickly becomes computationally expensive, especially when considering the number of scatter events that must occur to cause crosstalk in lower-energy windows. Nonetheless, by combining the analytical formulae into their iterative reconstruction algorithm, Shcherbinin et al. found that reconstructed images demonstrate significant improvement in data quantitation [39].

1.5.2.3 Dual System Matrices

Another practical approach was explored by Kamphuis et al. known as the dual matrix method [83]. In this work, the individual SPECT system matrix was replaced with a backprojection matrix to account for crosstalk, attenuation, and detector response, and a forward-projection matrix to account only for attenuation and detector response. Zeng and Gullberg [84] later commented on the inclusion of crosstalk events during iterative reconstruction and stated that, "... [iterative] algorithms demonstrate first a short convergent trend then diverge from the desired solution, no matter if a valid or invalid projection/backprojector pair is used. Therefore, choosing a valid backprojector may not be a very critical factor in a practical image reconstruction problem." Thus, multi-radionuclide SPECT may not benefit from reconstruction with unmatched forward/backward projectors in an attempt to correct for crosstalk.

1.5.2.4 Monte Carlo Methods

Monte Carlo techniques are the tool of choice for developing and testing crosstalk corrections, and some of the most advanced methods derive detailed information from simulations for direct incorporation into their formalism. The approach to crosstalk correction proposed by Du and Frey implemented the effective source scatter estimate (ESSE) to model crosstalk [31]. This was supplemented with Monte Carlo calculated point-source response functions to model the collimator-detector response function (CDRF) describing the effects of collimation, interactions in the collimator and detector, and detector energy resolution. The model-based information was combined with iterative reconstruction to reduce crosstalk. The ESSE method estimates an effective scatter source for each projection by convolving the activity distribution with scatter kernels. The effective scatter source is attenuated according to the subject geometry, blurred with the CDRF, and added to the forward projection through iterative reconstruction to form an estimate of the scatter in the projection data.

In a simultaneous brain SPECT study using ^{99m}Tc and ^{123}I , the effects of crosstalk contamination reduced image contrast and overestimated absolute activity in all structures by up to 66% [32]. After applying the Monte Carlo-based ESSE-CDRF approach, image contrast was improved and the errors in absolute activity quantitation were reduced to less than $\pm 5\%$. Farncombe et al. also explored the use of the ESSE method in comparison to perfect scatter rejection, TEW scatter estimation, and no correction for gallium-67 (^{67}Ga) multi-energy SPECT studies [85]. Through an analysis of a localization receiver operating characteristic (LROC) curve, the area under the curve A_{LROC} with no scatter compensation was 0.67. The results for the ESSE and TEW methods were significantly better, yielding A_{LROC} values of 0.73 and 0.75, respectively, while perfect scatter compensation had a value of $A_{\text{LROC}} = 0.84$. This indicates that crosstalk and scatter correction are beneficial for image quality, although a complex model may not be superior to simpler correction methods.

1.5.3 Crosstalk Corrections Post-Reconstruction

1.5.3.1 Convolution Kernel Subtraction

Correction methods that make use of physical models for scatter or crosstalk correction can be applied following image reconstruction with data that has already been filtered by energy windows. Such examples include convolution subtraction, where a scatter response function is convolved with the source distribution [86–88]. The scatter response function is defined as the spatial variation of scattered γ -rays about an origin corresponding to a given strength of unscattered γ -rays at that origin:

$$S = k(P' * G) \tag{1.6}$$

where S and k are as previously defined, P' represents the primary events from the competing radionuclide, and G is a Gaussian convolution kernel containing the localized crosstalk distribution. Thus, by convolving the kernel with the primary events reconstructed in the competing image, the resulting crosstalk distribution can be subtracted directly from the dataset of interest to obtain the primary image for one radionuclide. This of course requires estimation of k in order to appropriately scale the number of crosstalk events based on the specific subject. Not only does this method require tuning a parameter specific to the acquisition, it also assumes the subject is a homogeneous medium due to the kernel's spatial invariance. Therefore, this method may not be suitable in complex multi-radionuclide SPECT acquisitions.

1.5.4 Summary of Insights

A notable point through past attempts of scatter and crosstalk correction is that a general pitfall arises when a scalable or tunable parameter is present in the equation. The presence of an adjustable parameter yields a fragile method that is ineffective at blindly processing a myriad of SPECT acquisitions ranging from simple to complex. This is evidenced by the wide-spread library of crosstalk correction techniques that have not been clinically adopted, which further demonstrates that scatter and crosstalk problems have not been adequately solved. Additionally, crosstalk correction performance differs when considering the type of gamma camera being used and its inherent energy resolution and spatial resolution, so caution must be exercised when interpreting past reports of quantitative accuracy and image quality. Therefore, this thesis aims to develop a novel and robust method for multi-radionuclide SPECT with superior quantitative accuracy and image quality.

1.6 Research Objectives

The overarching aim of this thesis was to implement a simultaneous multi-radionuclide imaging protocol using a novel SiPM-based preclinical SPECT scanner—the Cubresa Spark. Through the challenges identified in the previous sections, the approach to crosstalk correction was presumed to be limited to pre- and post-reconstruction methods due to restricted information surrounding the Spark, namely the unknown multi-pinhole collimator geometry and inaccessible image reconstruction software. Therefore, the widespread acceptance of the TEW method made it appealing for ease of implementation. However, while initial development focused on the TEW method, a serendipitous opportunity led to the development of a novel crosstalk correction technique applied during reconstruction.

Objective 1. The first thesis objective was to characterize the Spark according to the NEMA standards, since there were no published Spark performance parameters. This work is presented in Chapter 3. A GATE Monte Carlo model was developed and validated against NEMA measurements to aid in characterizing the Spark when imaging ^{99m}Tc . With a validated simulation model, crosstalk correction efficacy could be tested against gold standard data.

Objective 2. The second thesis objective was to integrate and test open-source pinhole-SPECT reconstruction software in the Software for Tomographic Image Reconstruction (STIR). This work is presented in Chapter 4. To elaborate on this

serendipitous opportunity, the exploration of STIR’s TEW implementation ultimately led to an opportunity to integrate a pinhole-SPECT library into STIR. This enabled advanced testing of crosstalk efficacy using the Spark’s single-pinhole collimator after testing the software for functionality and quantitative and qualitative image quality.

Objective 3. The final thesis objective was to develop a crosstalk correction technique that would overcome TEW’s shortcomings in low-energy-resolution, high-spatial-resolution, and count-deprived settings. As described in Chapter 5, the pinhole-SPECT library was extended to the Synergistic Image Reconstruction Framework (SIRF), and its interoperability with the Core Imaging Library (CIL) provided the advanced optimization and regularization methods used in this work. The novel method uses a mixing matrix to exploit the gamma camera’s sensitivity to each radionuclide, which aids in iteratively optimizing detected events between each image during synergistic reconstruction.

1.6.1 Hypotheses

The work of Objective 3 provided a basis for the following hypotheses:

1. **Spectral unmixing can be applied to multi-radionuclide SPECT acquisitions, so long as the γ -ray emissions are unique, and the gamma camera sensitivity is known for the primary emissions.**
2. **Spectral unmixing can allow for any multi-radionuclide SPECT acquisition to be reconstructed with a considerable improvement in quantitative accuracy and image quality compared to conventional primary and triple energy window methods.**

Successful evaluation of the Spark’s performance in single- and multi-radionuclide SPECT will be key to its utilization in developing novel radiopharmaceuticals and imaging techniques aimed at improving our understanding of human physiology and disease progression. The novel multi-radionuclide SPECT technique developed in this thesis holds substantial potential to positively impact preclinical and clinical investigations within the realm of nuclear medicine. This advancement could potentially bring about significant transformations in the way interventions are approached and managed for cardiac, neurological, and cancer-related conditions, among others. The following chapter describes the theoretical physics concepts in relation to this work, subsequent chapters focus on the research objectives, and the final chapter concludes the thesis by summarizing the key findings while hypothesizing on future work.

Chapter 2

Theory

2.1 Prologue

This chapter forms the basis and theoretical foundation for understanding the inner workings of multi-radionuclide single-photon emission computed tomography (SPECT). It begins with the definition of radioactivity and the types of radiation used in nuclear medicine, how radiation interacts with matter, and how those interactions can be exploited to detect radiation. This establishes the fundamental cornerstone upon which nuclear medicine imaging is built. An overview is then given on nuclear medicine image acquisition and tomographic reconstruction.

2.2 Radioactivity

The nature of radioactive emanations was a primary area of research for Nobel laureates Henri Becquerel, Ernest Rutherford, and Pierre and Marie Curie at the end of the 1800s. Three years after the 1896 discovery of natural radioactivity by Henri Becquerel, Ernest Rutherford began classifying radioactivity according to its ability to penetrate matter and to ionize air. Around the same time (1898), radium was discovered by Pierre and Marie Curie, and Marie coined the term radioactivity to describe the phenomenon of radiation emitted through atomic decay. Following the letters in the Greek alphabet, alpha α , beta β , gamma γ , etc., radioactivity was classified by three particulate emissions:

- **α -rays:** Least penetrating and most ionizing,
- **β -rays:** Moderately penetrating and ionizing, and
- **γ -rays:** Most penetrating and least ionizing.

Through a variety of experiments, it was concluded that α -rays are identical to helium nuclei, β -rays are electrons and positrons, and γ -rays are photons, all of which are produced within the nuclei of radioactive elements. Additional experiments conducted by Irene Curie and Pierre Joliot revealed that radionuclides could be man-made after observing positrons emanating from aluminium foil bombarded with α -rays.

Whether man-made or naturally occurring, radioactive transformations that occur in atomic nuclei can be categorized as alpha emissions, isobaric transitions, or isomeric transitions. To mathematically describe radioactive transformations, consider the activity or rate of decay A of a sample of N radioactive nuclei present at time t . If no new nuclei are introduced into the sample, then the number dN decaying in a time dt is proportional to N :

$$A = \lambda N = -\frac{dN}{dt}. \quad (2.1)$$

Here, λ is the decay constant of proportionality. Integrating Eq. 2.1 yields the law of radioactive decay,

$$N(t) = N_0 e^{-\lambda t} \quad \text{or} \quad A(t) = A_0 e^{-\lambda t} \quad (2.2)$$

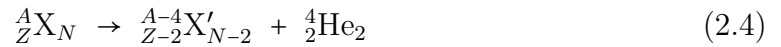
where the subscript “0” indicates the initial quantity present at $t = 0$. It then follows that the half-life gives the time necessary for half of the present nuclei to decay ($N = N_0/2$) which can be calculated from Eq. 2.2 to obtain

$$t_{1/2} = \frac{\ln(2)}{\lambda}. \quad (2.3)$$

As indicated by its name, λ is constant for a specific radionuclide. Today, the International System of Units defines the unit of radioactivity as the Becquerel (Bq) where $1 \text{ Bq} = 1 \text{ decay/s}$.

2.2.1 Alpha Emission

Within the nucleus of an atom, protons repel via Coulombic interactions, while the strong nuclear force competes to hold the neutrons and protons together. When the proton-to-neutron ratio of an atomic nucleus is too large, such is the case for heavy nuclei, the atom is considered unstable and α emission is favoured. The decay process is given by



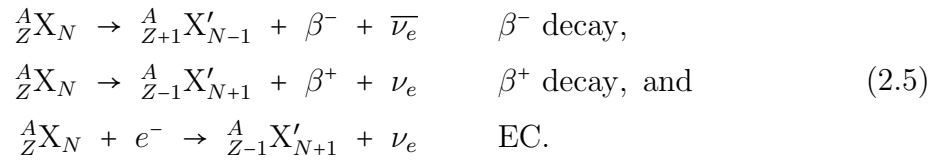
where $A = Z + N$ is the mass number, Z and N are the number of protons and neutrons, respectively, and X and X' represent the chemical symbols of the initial and final nuclei. The daughter nucleus may not be stable following α emission, and can further decay through a series of radioactive emissions until stable.

Due to the relatively large charge and mass of α particles and despite their several MeVs of energy, they are readily stopped in matter because of their high linear energy transfer (LET). Thus, α particles deposit all of their energy in a very short

distance, about 2–10 cell diameters [89]. This does not pose a problem outside the human body, where the dead layer of skin cells is sufficiently thick to absorb all α particles. However, the shielding effect from dead tissue is absent inside the body and α radiation dissipates a large amount of energy directly in living tissue, which can cause adverse health effects. Therefore, although their use is becoming increasingly popular in targeted radionuclide therapy, α -rays are not commonly used in nuclear medicine since it is difficult to safely transport α -emitters to the target site, and they cannot be detected outside the body to aid in localization.

2.2.2 Isobaric Transition

Isobaric transitions are governed by the weak nuclear force in a mode of radioactive decay where the mass number A remains unchanged while Z and N change by ± 1 . Nuclei which are neutron-rich tend to decay by converting a neutron into a proton through the emission of an electron (β^-) and an accompanying electron antineutrino $\bar{\nu}_e$. Conversely, nuclei which are proton-rich can decay in one of two ways: by converting a proton into a neutron through the emission of a positron (β^+) and an electron neutrino ν_e , or by capturing an electron from an innermost shell in the electron cloud then emitting a neutrino. Thus, β^- decay, β^+ decay, and electron capture (EC) can be expressed in the following respective decay equations:



The energies of β -emissions range continuously from very low to a maximum on the order of hundreds or thousands of keVs, corresponding to the energy difference between the parent and daughter nuclear states. Wolfgang Pauli hypothesized the existence of the neutrino in 1930 when he postulated its existence to account for the energy spectrum of β -particles according to the laws of conservation [90]. Despite the relatively high energies of β -emissions, they are significantly less massive than α particles and are considered to be low-LET radiation. Isobaric transitions are important processes in the creation of radionuclides, such as fluorine-18 (^{18}F) for nuclear medicine imaging applications and iodine-131 (^{131}I) for targeted radionuclide therapy.

2.2.3 Isomeric Transition

Typically, following α or β decay, nuclei are left in a metastable or isomeric excited state where they may remain excited for a long period of time spanning nanoseconds to hours, or years in a few cases [90]. Metastable states, such as ^{99m}Tc , are denoted by the letter “m” following the mass number when the half-life is longer than a microsecond [3]. In order to return to the ground state, there are two competing decay modes, in which the atom de-excites by transferring tens to hundreds of keVs of energy out of the nucleus. Gamma decay occurs when one or more photons are emitted directly from the nucleus,



Since Z and N remain unchanged following decay, there is no transmutation of one element to another. The other competing decay mode for isomeric transitions is internal conversion (IC), in which the nucleus de-excites by transferring its energy directly to an atomic electron that becomes ejected from the atom. The emissions from isomeric transitions are considered to be low-LET radiations.

The most important isomeric transition in nuclear medicine involves technetium-99m (^{99m}Tc) which possesses desirable characteristics such as a modest half-life ($t_{1/2} = 6.01$ h), a readily detectable γ -ray energy ($E_\gamma = 140.5$ keV), absence of α or β emissions, and valence electrons that permit labelling with a variety of biomolecules. It is important to understand and consider all the possible radiation decay types and particle interactions in nuclear medicine due to the wide variety of radionuclides, their associated decay schemes, and the potential combinations that can be used clinically and preclinically.

2.3 Interactions of Radiation with Matter

In order to understand how nuclear medicine images are acquired, it is imperative to understand the mechanisms by which radiation interacts with matter. These interactions involve a transfer of energy from the radiation to the matter, and in all instances, excitation or ionization results in the interacting medium. The probability of interaction depends on a number of characteristics including the charge, mass, and energy of the radiation as well as the nature of the attenuating medium, such as the atomic number, atomic weight, and density of the stopping material. These factors greatly influence the range of charged particles in motion and the probabilities of photon interactions. In this section, interaction mechanisms will be discussed in relation

to charged particles and electromagnetic radiation. Note that nuclear interactions by heavy charged particles, such as α particles and larger, are often ignored in the context of radiological physics and dosimetry (see Sec. 2.2.1) [91].

2.3.1 Charged Particle Interactions

The passage of charged particles through matter is governed by electromagnetic interactions due to the Coulomb field surrounding a charged particle. Thus, a charged particle interacts with the atomic electrons or nuclei of practically every atom it passes. Each interaction occurs through a collision where a minute amount of the particle's kinetic energy is transferred, which can result in thousands of collisions for a 5-MeV α particle (typical of those emitted in radioactive decay) [91]. The loss of kinetic energy occurs gradually in a process referred to as the continuous slowing-down approximation (CSDA), and can be characterized by a common or mean range R calculated from the stopping power of the medium as

$$R = \int_T^0 \left(-\frac{dE}{dx} \right)^{-1} dE. \quad (2.7)$$

Here, T refers to the kinetic energy of the charged particle, and the stopping power ($-dE/dx$) describes the magnitude of the energy loss (dE) per unit length (dx). The stopping power, and hence the range, is determined by the particle type, the energy of the particle, and the medium being traversed. Figure 2.1 plots the stopping power for various charged particles in water [92].

The total stopping power can be considered from the additive energy losses of collisions and radiation

$$\left(\frac{dE}{dx} \right) = \left(\frac{dE}{dx} \right)_c + \left(\frac{dE}{dx} \right)_r. \quad (2.8)$$

Collisional losses can be further divided into hard and soft collisions and are the dominant energy loss mechanism for heavy, moderately relativistic charged particles. Conversely, radiative losses are dominant for highly relativistic charged particles. Soft collisions describe Coulomb scattering of charged particles with atomic electrons in the medium, whereas hard collisions describe Coulomb scattering with nuclei. Therefore, the stopping power, namely collisional, relates directly to the absorbed dose deposited in a medium which plays a critical role in radiopharmaceutical dosimetry. Figure 2.2 illustrates the parameters for characterizing charged-particle Coulomb-force interactions based on the impact parameter b and the atomic radius a .

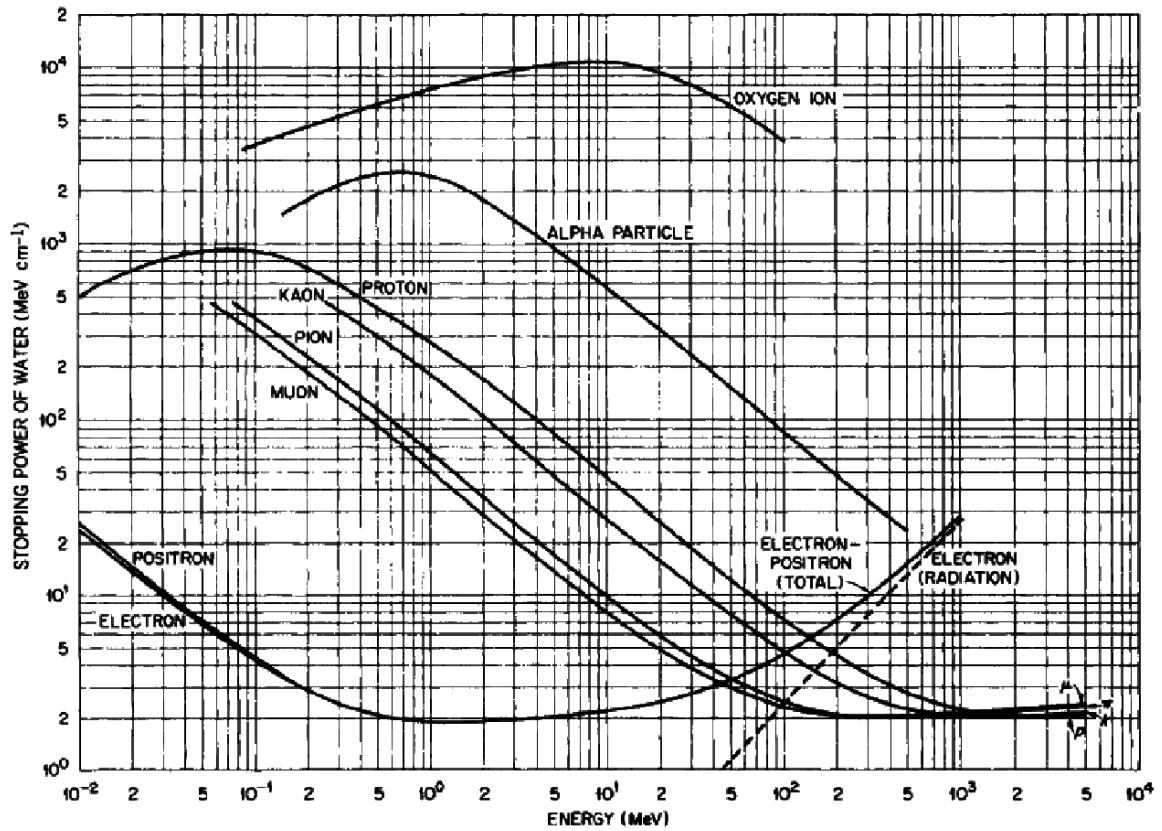


Figure 2.1: Stopping power of water in units of MeV/cm for various heavy charged particles and electrons. From [92], used with permission.

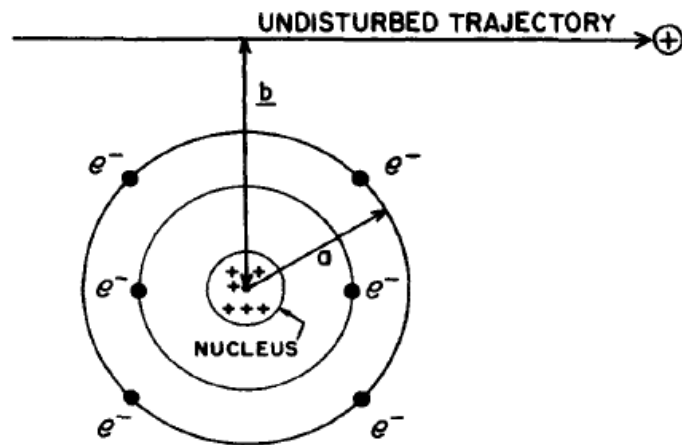


Figure 2.2: Parameters of charged-particle collisions with atoms: a is the classical atomic radius and b is the classical impact parameter. From [91], used with permission.

2.3.1.1 “Soft” Collisions ($b \gg a$)

Any charged particle in motion is surrounded by an electromagnetic field which extends out into space. Therefore, when a charged particle passes by an atom, even at a considerable distance, the particle’s Coulomb force field is felt by the atom as a whole due to the atomic charges present in the interaction. This Coulomb field can cause one or more electrons to become excited to a higher energy level, or the atom may become ionized if any valence-shell electrons are ejected. An ejected electron, called a delta-ray (δ -ray), that receives a sufficient amount of energy can go on to cause further excitation and ionization. Furthermore, due to the vast emptiness of space, a charged particle traversing a medium is most likely to experience soft collisions, which accounts for the majority of energy loss through excitation and ionization.

2.3.1.2 “Hard” (Knock-on) Collisions ($b \approx a$)

As the impact parameter approaches the order of the atomic radius, the probability of a charged particle interacting with and ejecting a single atomic electron significantly increases. The resulting δ -rays may again go on to induce further excitation and ionization. If the incident charged particle imparts sufficient energy for inner-shell electrons to overcome their binding energy and become ejected, then characteristic X-rays and/or Auger electrons will be emitted as the inner-shell vacancy becomes filled. Therefore, some energy transferred to the medium may be transported away from the interaction site by the δ -rays, X-rays, and/or Auger electrons. Although hard collisions account for fewer interactions than soft collisions, the amount of energy transferred by a knock-on collision is significantly greater than a soft collision. Therefore, the total energy spent by a charged particle traversing a material is comparable for soft and hard collisions [91].

2.3.1.3 Nuclear Interactions ($b \ll a$)

Previously, charged particle interactions were generalized to treat both heavy and light charged particles alike. However, nuclear interactions are significantly different between heavy and light charged particles, which requires separate consideration of their interaction mechanisms.

2.3.1.3.1 Heavy Charged Particles

Heavy charged particles refer to those with a mass significantly greater than the electron, i.e., muons and ions. A heavy charged particle with sufficiently high kinetic

energy on the order of ~ 100 MeV may interact inelastically with the nucleus to split individual nucleons from the nucleus, which can induce further interactions. Fortunately, such energetic particles are only used in nuclear reactors and the production of radiopharmaceuticals, and their radiative interactions need not be considered further in the definition of stopping power [1]. Since large particles do not accelerate rapidly when traversing a medium, they do not produce significant amounts of radiation or bremsstrahlung—German for “braking radiation”. The total stopping power for heavy charged particles was derived by Hans Bethe in 1930 based on the quantum mechanical calculation of the collision process,

$$\frac{dE}{dx} = \left(\frac{e^2}{4\pi\epsilon_0} \right)^2 \frac{4\pi z^2 N_0 Z \rho}{m_0 c^2 \beta^2 A} \left[\ln \left(\frac{2m_0 c^2 \beta^2}{I(1-\beta^2)} \right) - \beta^2 \right] \quad (2.9)$$

where $\beta = v/c$ is the speed of the particle v relative to the speed of light c in vacuum, z is its electric charge in multiples of electron charge, Z , A , and ρ are the atomic number, atomic weight, and density of the stopping material, N_0 is Avogadro’s number, $m_0 c^2$ is the electron rest mass, and I is the mean excitation energy of the atomic electrons [93].

2.3.1.3.2 Electrons

Electrons (either $+$ or $-$) interact through Coulomb scattering from atomic electrons, similar to heavy charged particles. However, electrons suffer large deflections in collisions with other electrons, and therefore follow tortuous paths. In a head-on collision, a large fraction of the electron’s initial energy may be transferred to the knocked-on electron. Furthermore, electrons are subject to large accelerations, in which case the electron may convert a significant fraction of its kinetic energy (up to 100%) into a bremsstrahlung photon [93]. The resulting photon is carried away and may interact with the medium through electromagnetic interactions. Bethe also derived the terms for electron energy loss due to collisional and radiative losses as

$$\left(\frac{dE}{dx} \right)_c = \left(\frac{e^2}{4\pi\epsilon_0} \right)^2 \frac{2\pi N_0 Z \rho}{m_0 c^2 \beta^2 A} \left[\ln \left(\frac{T(T + m_0 c^2)^2 \beta^2}{2I^2 m_0 c^2} \right) + (1 - \beta^2) - (2\sqrt{1 - \beta^2} - 1 + \beta^2) \ln 2 + \frac{1}{8} (1 - \sqrt{1 - \beta^2})^2 \right] \quad (2.10)$$

$$\left(\frac{dE}{dx} \right)_r = \left(\frac{e^2}{4\pi\epsilon_0} \right)^2 \frac{Z^2 N_0 (T + m_0 c^2) \rho}{137 m_0^2 c^4 A} \left[4 \ln \left(\frac{2(T + m_0 c^2)}{m_0 c^2} \right) - \frac{4}{3} \right] \quad (2.11)$$

where T is the electron kinetic energy [93].

Before discussing electromagnetic interactions and in addition to the aforementioned modes of kinetic energy dissipation (soft, hard, and radiative interactions), a fourth mode of interaction can be considered exclusive to antimatter (i.e., positrons). As positrons scatter and impart energy along their tortuous paths, they slow down and eventually encounter an electron. The positron and electron annihilate by converting their rest mass energies into back-to-back 511 keV photons. Any residual momentum of the system is transferred to one or both of the photons, causing a slight acollinearity and/or energy discrepancy between the resultant annihilation photons. Again, the resulting photons may go on to interact with the medium through electromagnetic interactions. This mode of interaction is most important in positron emission tomography (PET).

2.3.2 Electromagnetic Interactions

Analogous to the law of radioactive decay which describes the number of radioactive nuclei remaining after some time, the law of exponential attenuation describes the remaining intensity I of a photon beam after traversing a medium,

$$I = I_0 e^{-\mu x} = I_0 e^{-\left(\frac{\mu}{\rho}\right)(\rho x)}. \quad (2.12)$$

Here, x refers to the thickness of material traversed, ρ is the material density, and μ denotes the total linear attenuation coefficient which is the summed contribution from the photoelectric effect τ , Compton scattering σ , and pair production κ :

$$\frac{\mu}{\rho} = \frac{\tau}{\rho} + \frac{\sigma}{\rho} + \frac{\kappa}{\rho}. \quad (2.13)$$

When characterizing the type of interaction by photon energy, it is instructive to remove the material dependency by considering the mass attenuation coefficient (μ/ρ) and mass thickness (ρx). The relative importance of the photoelectric effect, Compton scattering, and pair production depends both on the atomic number Z of the medium and the photon energy $E_\gamma = h\nu$, where h is Planck's constant and ν is the photon frequency. Other photon processes such as Rayleigh scattering and photonuclear interactions have insignificantly small attenuation coefficients and can be completely ignored in the context of nuclear medicine [94].

The mass attenuation coefficient describes the interaction cross-section, which defines the effective target area seen by the photon per unit mass rather than per atom [93]. Although the probabilities of interactions are difficult to calculate, exper-

imental studies have provided empirical values. An example of the mass attenuation coefficient for lead is shown in Fig. 2.3a. Also shown in Fig. 2.3 is a plot of the dominant interaction regions and the mean range for γ -rays in comparison to α - and β -rays based on the attenuation of radiation in a slab of material.

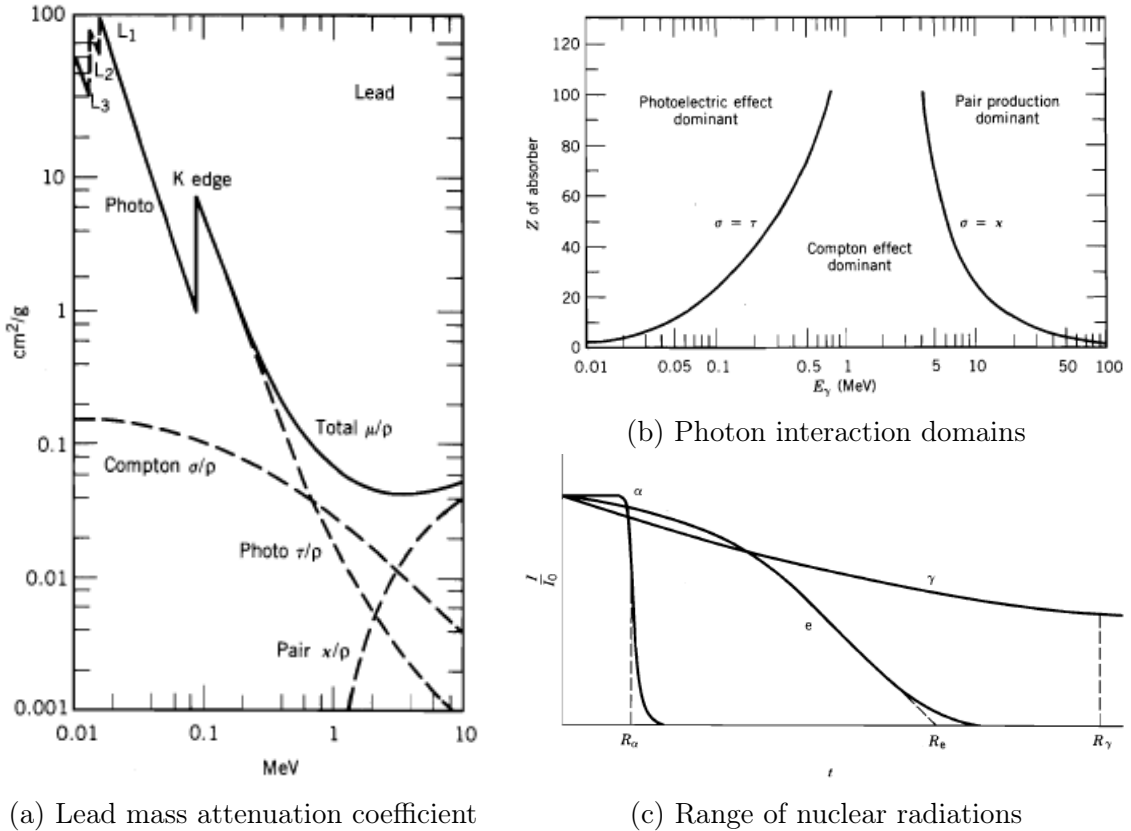


Figure 2.3: (a) Total mass attenuation coefficient of lead ($Z = 82$) with illustrated contributions from photon interactions: the photoelectric effect τ/ρ , Compton scattering σ/ρ , pair production κ/ρ , and their sum μ/ρ . The discontinuity of the photoelectric effect is due to the K-edge of the innermost K-shell atomic electrons. (b) Relative importance of the three major types of photon interactions. The curves illustrate the values of Z and E_γ for which the mass attenuation coefficient for two types of interactions are equal. (c) Transmitted intensity of α -, β -, and γ -rays through a material of thickness t . For γ -rays and α -rays, the mean range is the material thickness resulting in a 50% loss in intensity ($I/I_0 = 0.5$), and for electrons, the mean range is defined by the extrapolated range where the linear region is extrapolated to intersect the horizontal axis. The range of γ -rays may be $10^4 \times$ that of α -rays. From [93], subfigure (a) adapted by cropping out left half of image, used with permission.

2.3.2.1 Photoelectric Effect

In the photoelectric effect, a photon is absorbed by an atomic electron and the resulting photoelectron is released from the atom where it can impart energy through excitation and ionization in the medium. It is also the primary and desired mode of photon detection in nuclear medicine imaging. As illustrated in Fig. 2.3b, the photoelectric effect dominates over all other interactions for low energy photons ($h\nu \lesssim 100$ keV). It is convenient to remember that the probability of photoelectric interactions is proportional to the atomic number cubed and inversely proportional to the cube of the photon energy,

$$\frac{\tau}{\rho} \propto \left(\frac{Z}{h\nu} \right)^3. \quad (2.14)$$

There are discontinuities in the photoelectric cross-section, called absorption edges, due to increasing binding energies of electron orbital levels closer to the nucleus. Thus, as the photon energy increases, inner-shell electrons become capable of partaking in photoelectric interactions, which appears as a sudden increase in the interaction cross-section at a characteristic energy (see Fig. 2.3). In other words, the photoelectric effect is significantly more probable for photon energies just above an absorption edge.

2.3.2.2 Photon Scattering

The relative importance of Rayleigh scattering is negligible in comparison to the competing interactions of the photoelectric effect and Compton scattering. Nonetheless, Rayleigh scattering by the entire atom is still possible, in which case the photon elastically scatters and changes direction by a small angle without imparting energy.

Inelastic scattering occurs when a photon collides and transfers some of its energy and momentum to an electron that recoils. This was first described by Arthur Compton in 1923 and is illustrated in the kinematic diagram shown in Fig. 2.4 [95]. Using conservation of energy and momentum, and assuming an unbound electron, it can be shown that the final energy $h\nu'$ of the scattered photon is

$$h\nu' = \frac{h\nu}{1 + (h\nu/m_0c^2)(1 - \cos\theta)} \quad (2.15)$$

where $h\nu$ is the incident photon energy, $m_0c^2 = 511$ keV is the electron rest mass energy, and θ is the angle of the scattered photon with respect to its initial direction.

The recoil electron will then continue with kinetic energy

$$T = h\nu - h\nu' = h\nu \left(\frac{(h\nu/m_0c^2)(1 - \cos\theta)}{1 + (h\nu/m_0c^2)(1 - \cos\theta)} \right) \quad (2.16)$$

and undergo charged particle interactions with the surrounding medium (see Sec. 2.3.1). The Compton scattered photon may exit the medium without further interactions or undergo subsequent electromagnetic interactions.

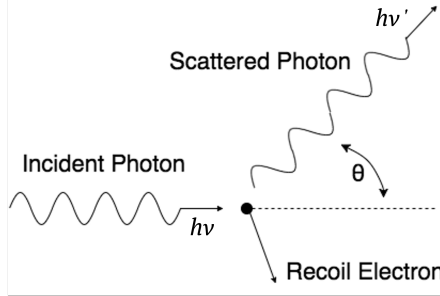


Figure 2.4: Elastic scattering of a photon with an electron at rest.

The incident photon energy must be significantly greater than the electron binding energy for a Compton interaction to occur. As illustrated in Fig. 2.3b, the Compton effect becomes dominant at medium photon energies ranging from approximately 30 keV to 30 MeV, although this range decreases with increasing atomic number. Therefore, the probability of Compton scattering increases relative to the probability of photoelectric interactions with increasing incident photon energy. In 1928, Klein and Nishina derived the Compton mass attenuation coefficient σ/ρ in relation to the cross-section of the electron σ_e ,

$$\frac{\sigma}{\rho} = \frac{N_A Z}{A} \sigma_e \quad (2.17)$$

where N_A and Z are as previously defined, A is the molecular weight, and $N_A Z/A$ is the number of electrons per unit mass of material [91]. The electron cross-section can be expressed as

$$\sigma_e = 2\pi r_0^2 \left(\frac{1 + \alpha}{\alpha^2} \left[\frac{2(1 + \alpha)}{1 + 2\alpha} - \frac{\ln(1 + 2\alpha)}{\alpha} \right] + \frac{\ln(1 + 2\alpha)}{2\alpha} - \frac{1 + 3\alpha}{(1 + 2\alpha)^2} \right) \quad (2.18)$$

where r_0 is the classical electron radius and $\alpha = h\nu/m_0c^2$ [91]. It is important and convenient to note that from Eq. 2.17, Z/A is approximately constant for all elements except hydrogen, so the mass attenuation coefficient is nearly independent of Z , and from Eq. 2.18, the electron cross-section is inversely proportional to the incident

photon energy. It therefore follows that

$$\frac{\sigma}{\rho} \propto \frac{Z^0}{h\nu}. \quad (2.19)$$

In general, photon scatter can be problematic in nuclear medicine imaging. Scattered photons contribute noise in emission tomography due to the difficulty in localizing scatter interaction sites and distinguishing them from emission sites. The effects from Compton scatter can be mitigated to some extent by discriminating photons by their energy and disregarding scattered photons. However, in the context of multi-radionuclide imaging where two or more radionuclides have comparable energies, the loss of energy may cause higher energy photons to be downscattered into the energy range of a competing radionuclide. This can result in signal interference and crosstalk between radionuclide data when reconstructing tomographic images. This will be discussed further in Ch. 5.

2.3.2.3 Pair Production

Photons with sufficiently high energy are capable of interacting in an atom's Coulomb force field to give rise to an electron and positron. More specifically, if a photon possesses energy greater than twice the rest mass energy of the electron ($2m_0c^2 = 1.022 \text{ MeV}$), then pair production is possible in the nuclear field. The photon's energy is converted to matter, and any residual energy will be transferred to the pair as kinetic energy. The resulting particles may then go on to excite and ionize the medium through charged particle interactions. If a photon possesses energy greater than $4m_0c^2 = 2.044 \text{ MeV}$, then triplet production is possible in the field of an atomic electron. Altogether, the probability of pair production exhibits a logarithmic photon energy dependence at relatively low energies which becomes independent at higher energies, but is directly related to the atomic number of the medium [91], that is

$$\frac{\kappa}{\rho} \propto Z. \quad (2.20)$$

Due to the high photon energy required for pair production, this interaction mechanism is of less importance in nuclear medicine.

2.4 Radiation Detection and Measurement

The detection of particles is based on an understanding of the physical phenomena by which radiation interacts and loses its energy in matter. Most radiation detectors exploit these interaction mechanisms to detect nuclear radiations using similar principles: the radiation enters the detector, interacts with the atoms of the detector medium and loses a fraction or all of its energy, and releases numerous relatively low-energy electrons from their atomic orbits. The liberated electrons are collected with an electric field applied within the detector to form a voltage or current pulse that can be analyzed by electronic circuitry.

2.4.1 Modes of Detector Operation

2.4.1.1 Current Mode

Radiation detectors operate between two fundamental modes of operation—pulse mode and current mode. In current mode, the interaction of each quantum of radiation is effectively averaged together to form a net current signal. The measured current linearly reflects charges contributed by each type of radiation. The average current I is given by the product

$$I = rQ \tag{2.21}$$

where r is the event rate and Q is the average charge produced per event [96]. The electronic signal from the detector is measured with an ammeter, whose response time is typically longer than the time between individual detection events. This averages out the signal fluctuations in the intervals between interactions. Current mode is typically used in environments with very high interaction rates to avoid dead-time losses where individual pulses may be indistinguishable, such as for radiation dosimetry.

Due to the random nature of radiation interactions in the detector, the variance or mean square voltage (MSV) may be used to characterize the statistical uncertainty in the detected signal. The signal variance $\overline{\sigma_I^2(t)}$ obtained in MSV mode is,

$$\overline{\sigma_I^2(t)} = \frac{rQ^2}{T}, \tag{2.22}$$

which gives the time average of the current fluctuations for a detector with response time T [96]. Equation 2.22 shows that the variance is proportional to the square of the charge per event, which therefore weights the detector response in favour of the type

of radiation giving the larger average charge per event. This can be useful in nuclear reactor instrumentation, for example, to enhance the neutron signal compared to smaller-amplitude γ -ray events [96]. In general, MSV mode is uncommon in nuclear medicine applications due to its limited use in specialized applications, such as when making measurements in mixed radiation environments when the charge produced by one type of radiation differs from the other type(s).

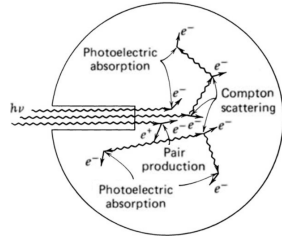
2.4.1.2 Pulse Mode

In pulse mode, the detector is designed to record the interaction of each individual quantum of radiation. This requires a separate electrical pulse to be generated for each quantum that interacts in the detector. The amplitude of the signal pulse V is directly proportional to the charge generated within the detector Q due to each individual interaction,

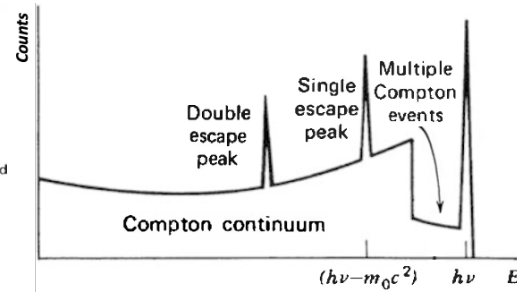
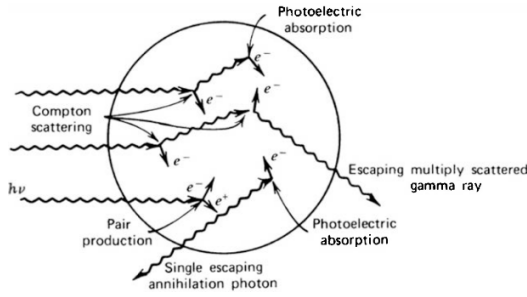
$$V = \frac{Q}{C} \quad (2.23)$$

where C is the capacitance of the detector and measuring circuit. The electronic signal from the detector usually goes to a preamplifier to convert the charge pulse to a voltage pulse, which is then amplified for ease of processing. The amplifier must be linear for the output to be proportional to the input, in order to relate the radiation energy to the pulse height. If the resulting pulse is larger than the threshold imposed on the single- or multichannel analyzer, the pulse will be counted in its corresponding energy bin. A single-channel analyzer counts the events that occur with a pulse height in a given energy range, whereas a multichannel analyzer counts the pulses across several energy ranges and bins them in a histogram with an analog to digital converter.

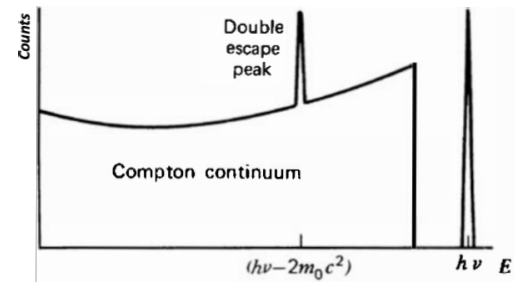
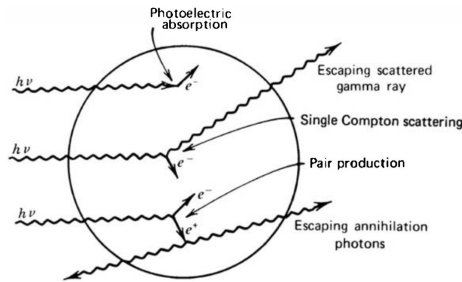
The resulting pulse-height spectrum reflects the corresponding distribution in energy of radiation incident on the detector, along with the relative intensity of radiation detected. Examples of idealized pulse-height spectra are shown in Fig. 2.5 for scintillation detectors, which are discussed in detail in Sec. 2.4.5.3. Applications that utilize the pulse-height spectrum are categorized as radiation spectroscopy. At high event rates, pulse mode is impractical or even impossible due to an inadequate time interval between events or an overlap of events in time. In such cases, current mode may be considered.



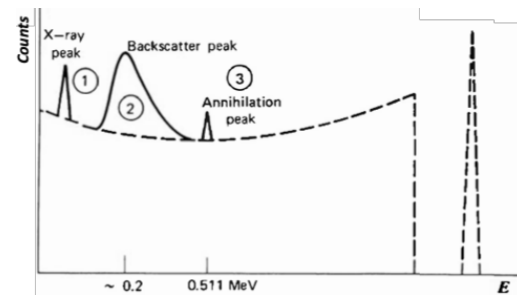
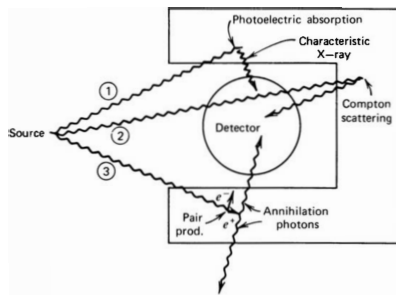
(a) Photon interactions in a large detector



(b) Photon interactions in an intermediate sized detector



(c) Photon interactions in a small detector



(d) Photon interactions in a medium surrounding the detector

Figure 2.5: Photon interactions in detectors (left), and associated idealized pulse height spectra (right). (a) The photoelectric effect and total containment of all subsequent interactions yield a photopeak at the incident photon energy $E = h\nu$. (b, c) Escaping Compton scattered photons produce a continuum across lower energies, and annihilation photons may escape the detector when incident photon energies exceed the pair production threshold ($2m_0c^2$). (d) In addition to the expected spectrum (dashed lines), the surrounding medium may contribute signal in the detector (solid lines) due to backscattered photons, characteristic X-rays, and annihilation photons. Adapted from [96] by adding labels and modifying layout, used with permission.

2.4.2 Dead Time

In pulse-mode operation, subsequent interactions must be separated by a finite amount of time to produce distinct signals. This is due to the system dead time, which describes the time required to process an individual detection event. The pulses produced by a radiation detector have a finite duration, and if a second pulse arises during the system dead time, its signal will be lost. If the second pulse occurs close enough in time to the first interaction, it may overlap to form a single distorted pulse. Two models exist to describe dead time behaviour based on non-paralyzable and paralyzable response. In a non-paralyzable system, an interaction that occurs during the dead time is ignored. Conversely, in a paralyzable system, an interaction that occurs during the dead time restarts the dead time interval. Fig. 2.6a shows the effect of dead time on the recorded interaction rate. The recorded count rate m for a non-paralyzable system can be mathematically described as

$$m = \frac{n}{1 + n\tau} \quad (2.24)$$

where n is the input interaction rate and τ is the system dead time [96]. A paralyzable system expresses a recorded count rate of

$$m = ne^{-n\tau}. \quad (2.25)$$

These equations are plotted in Fig. 2.6b. The two models describe the extremes of ideal dead time behaviour, whereas real systems may yield count rates between these two extremes.

2.4.3 Detection Efficiency

The efficiency or sensitivity of a detector describes the probability that a quantum of radiation will be detected. In a detector, charged particles readily interact with the active medium through ionization and excitation. The ion pairs formed can be easily collected with an electric field to form a signal, giving the detector a high intrinsic efficiency. Uncharged radiations have a considerably lower interaction probability than charged particles and can travel large distances between interactions. Thus, the intrinsic efficiency for detectors of neutral particles is often less than 100%. When a detector is less than 100% efficient, it is necessary to relate the number of particles

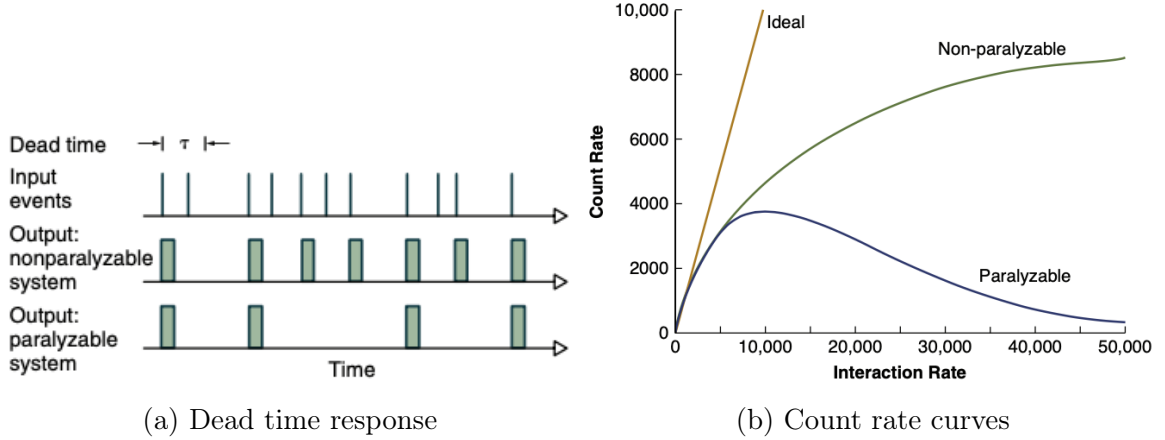


Figure 2.6: System dead time τ for a detector with a paralyzable or non-paralyzable response to radiation. (a) The recorded signal for an interaction event depends on the dead time response. For a paralyzable system, an input interaction event occurring during the dead time after a previous interaction restarts the dead time interval, while the event is simply ignored in a non-paralyzable system. The subfigure shows 11 input events, from which 4 are detected with a paralyzable system while 7 are detected with a non-paralyzable system. (b) The count rate curves for paralyzable and non-paralyzable detector systems show that the paralyzable system reaches a maximum and then decreases due to the lack of an event-free dead time intervals, whereas a non-paralyzable system plateaus at a count rate of $1/\tau$. Subfigure (a) from [46], subfigure (b) from [1], used with permission.

detected to the number emitted:

$$\epsilon_{\text{abs}} = \frac{\text{Number detected}}{\text{Number emitted}}. \quad (2.26)$$

Here, ϵ_{abs} is the absolute efficiency, which can be rewritten as

$$\begin{aligned} \epsilon_{\text{abs}} &= \frac{\text{Number detected}}{\text{Number incident on detector}} \frac{\text{Number incident on detector}}{\text{Number emitted}} \\ &= \epsilon_{\text{int}} \epsilon_{\text{geom}} \end{aligned} \quad (2.27)$$

where ϵ_{int} and ϵ_{geom} are implicitly defined as the intrinsic and geometric efficiencies, respectively. Recalling the law of exponential attenuation from Eq. 2.12, the intrinsic efficiency of the detector is $\epsilon_{\text{int}} = 1 - e^{-(\mu/\rho)\rho x}$. For an isotropic source of radiation, the geometric efficiency of the detector is $\epsilon_{\text{geom}} = 4\pi/\Omega$ where Ω is the solid angle of the detector seen from the source position. Therefore, the detection of radiation is application specific according to the particle of interest, which requires careful consideration of the detector medium and geometry.

2.4.4 Counting Statistics

The detection of radiation is a random phenomenon independent of the time since the previous event. This can be described as a Poisson process where the average time between events is known and constant, but the exact timing of events is random. The Poisson process can be considered in terms of space or time. The probability P of detecting N events in the interval can be calculated with the Poisson probability distribution function,

$$P(N|\langle N \rangle) = \frac{\langle N \rangle^N e^{-\langle N \rangle}}{N!} \quad (2.28)$$

where $\langle N \rangle$ is the expectation value or rate parameter in a fixed interval of time or space. The dispersion of the distribution can be quantified with the variance σ^2 . A unique property of the Poisson distribution is that the variance is equal to the mean:

$$\sigma^2 = \langle N \rangle. \quad (2.29)$$

When the variance is small, the measured result lies closely to the mean, and when the variance is large, the results are more widely spread around the mean. A useful measure of a distribution function's dispersion is the coefficient of variation CV which can be calculated as

$$\text{CV} = \frac{\sigma}{\langle N \rangle}. \quad (2.30)$$

Thus, the variance provides insight into the statistical noise or uncertainty associated with radiation detection where the uncertainty is given by the standard deviation σ .

Due to the random nature of radioactive decay and the statistical distribution of detected radiation, there is inherent noise or uncertainty associated with measured data that affects the quality and accuracy of measurements. The signal-to-noise ratio (SNR) is a measure of the quality of acquired data and is calculated using

$$\text{SNR} = \frac{\langle N \rangle}{\sigma}. \quad (2.31)$$

It represents the ratio of the measured mean (i.e., counts from radiation emitted by a source of interest) to the statistical noise, and a higher SNR indicates better data quality and improved accuracy. In addition to the statistical noise of radiation, there are several sources of random and systematic noise in radiation detection systems, including electrical noise (e.g., dark noise and voltage fluctuations), environmental noise (e.g., background radiation and electromagnetic interference), and instrumen-

tation noise (e.g., detector instabilities and variations in response over time). Signal processing techniques, such as filtering, background subtraction, and statistical analysis can often be employed to reduce noise and enhance data quality.

2.4.5 Types of Radiation Detectors

For α -rays and heavy charged particles with energies on the order of a few MeV, the maximum range in a solid is typically less than $100\ \mu\text{m}$, so very thin detectors with a solid medium provide sufficient stopping power [93]. The detection of β emissions requires a detector thickness of approximately 0.1 to 1 mm, and a 5 cm-thick detector, for example, may be sufficient to induce γ -ray interactions that can produce a viable electronic pulse. Furthermore, the specific detector application may only require particles to be counted to show the presence of radiation, in which case a Geiger counter may be used.

If information regarding a particle's energy is required, then a suitable material must be chosen in which the number of liberated electrons is large enough to accurately relate the collected charge to the incident energy. To measure unusually high count rates, a detector must be chosen that can recover quickly between interaction events; and for very low counting rates, the detector design must be sensitive to every interaction event while reducing the influence of background radiation. Lastly (and most importantly for nuclear medicine imaging), if reconstructing the trajectory of the detected radiation is of interest, then the detector must be position sensitive with respect to where the incident radiation entered the detector and the location of the interaction in the detector. Due to the comprehensive nature of radiation, no single detector can satisfy all applications. Therefore, the subsections that follow focus on the detection of particles likely to be encountered in nuclear medicine.

2.4.5.1 Gas-Filled Detectors

A gas-filled detector contains a volume of gas between two electrodes to exploit the ionization phenomenon that occurs when ionizing radiation passes through the detector. The ionization energy of most detector gases is 30–35 eV [96]. A potential difference or voltage is applied across two electrodes to create an electric field that separates the ions and liberated electrons, and an electrometer measures the signal by integrating the charges collected during the response time of the detector. As illustrated in Fig. 2.7, the applied voltage affects the pulse height produced in a gas-filled chamber, from which several well-defined regions may be identified. Within these

regions, ionization counters are commonly used in nuclear medicine for measuring radioactivity with a dose calibrator, proportional counters are inefficient for detecting X- and γ -rays and have limited use in nuclear medicine, and Geiger counters are effective in portable radiation survey meters for detecting small amounts of radiation.

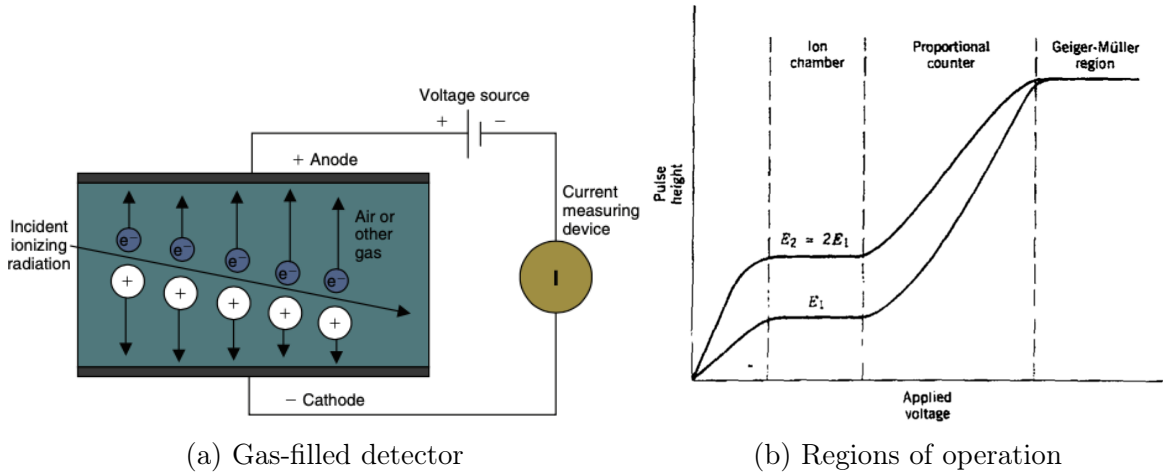


Figure 2.7: Basic principles of gas-filled detectors. (a) Electrons and ions produced by ionizing radiation in a gas-filled detector are collected by applying a potential difference across an anode and cathode. An electrometer measures the signal by integrating the charges collected during the detector response time. (b) The voltage applied across the electrodes affects the detector behaviour, in which distinct regions of pulse height exist. The pulse heights for two radiations differing in energy by a factor of two are shown. In the ionization chamber and proportional counter regions, the pulse height is proportional to the energy deposited by primary ionizing radiation, while all interactions produce the same signal in the Geiger-Müller region. Subfigure (a) from [46], subfigure (b) from [93], used with permission.

At very low voltages, recombination of the ions and liberated electrons (δ -rays) is likely to occur in the gas before electrodes can collect the charges. As the voltage is increased toward the ionization chamber region, more charges are collected, and so the signal increases before reaching a plateau as shown in Fig. 2.7. In the ionization chamber region, almost all ion pairs generated by the incident radiation are collected by the electrodes. Thus, the signal remains nearly constant and largely independent of variations in voltage. At intermediate voltages, i.e., in the proportional counter region, the electric field becomes capable of accelerating δ -rays to high enough energies that produce further ionization events in a single avalanche process. The gas amplification factor describes the avalanche charge multiplication that increases with voltage, and the output pulse is proportional to the total energy deposited by the incident ionizing particle. Similar to a proportional counter, a Geiger-Müller (GM)

counter operates on the gas amplification principle at high voltages. However, the δ -rays can cause excitation of the gas molecules that de-excite by emitting ultraviolet (UV) photons that may undergo photoelectric absorption in the detector, thereby producing electrons that cause additional avalanches [46]. Within the GM voltage region, all incident ionizing particles produce the same output pulse regardless of the amount of ionization, particle energy, or applied voltage. Beyond the GM region, spontaneous ionization may occur in the detector medium due to excessive electric field strength.

2.4.5.2 Semiconductor Detectors

Semiconductor detectors are the solid-state analogue to ionization chambers [96]. The use of a solid detection medium is advantageous in radiation detection due to the increased density leading to increased stopping power and attenuation, which further enhances the detection efficiency. Upon ionization, semiconductor detectors provide the greatest number of information carriers per pulse compared to all types of radiation detectors. The fundamental information carriers are electron-hole pairs created along the path traversed by the ionizing particle. They are analogous to the ion pair created in a gas-filled detector, and their influence in an electric field generates the basic electrical signal from the detector. It should be noted that the ions do not move in a solid; rather, the hole is filled by the sharing of electrons amongst covalent bonded atoms.

Semiconductors are crystalline materials, such as silicon, germanium, or more recently cadmium zinc telluride (CZT), with an electrical conductivity between insulators and conductors. They have a well-defined band gap of approximately 1 eV which defines the energy required to promote an atomic electron from the valence band to the conduction band [93]. When a voltage is applied to the semiconductor, a current is induced that can mask the radiation-induced current. Therefore, small amounts of dopants are added to the crystal to spoil the semiconductor's electrical conductivity. If the atoms of the added impurity have more valence electrons than those of the semiconductor, the material is called n-type due to excessive negative charge carriers in the valence band. Conversely, impurity atoms with fewer valence electrons than the semiconductor make the material p-type due to excess positively-charged holes in the valence band. The materials are brought into contact and a reverse bias voltage is applied across the p-n junction to separate the free charge carriers and form a depletion region. When ionizing radiation interacts in the deple-

tion region, electron-hole pairs are created. The electric field created by the reverse bias voltage separates the electron-hole pairs, and an electric pulse is imparted on the electrodes by the charge carriers. The measured current pulse is proportional to the energy deposited by the incident radiation, which makes semiconductor detectors useful for radiation spectroscopy.

2.4.5.3 Scintillation Detectors

As opposed to semiconductor detectors which directly detect ionizing radiation, scintillation detectors indirectly detect radiation by converting radiation into optical light that can be detected with a photosensor. In the scintillation process, incident ionizing radiation interacts with the scintillator and excites the atoms. The atoms undergo fluorescence (prompt decay) and phosphorescence (afterglow) to return to the ground state by emitting visible or UV light (3–4 eV) that can be readily detected. Organic and inorganic scintillators come in many physical forms including solid, liquid, gas, crystal, and plastic to name just a few, which provide widespread application in medical imaging. Inorganic scintillation crystals like cesium iodide (CsI) and sodium iodide (NaI) are most commonly used in nuclear medicine imaging due to their larger average atomic numbers and higher densities than organic scintillators. Activators such as sodium or thallium are often added to increase the probability for photon emission and reduce the self-absorption of optical light.

According to Bushberg [1] and Knoll [96], the ideal scintillation material should possess the following properties:

1. It should convert charged particle kinetic energy into detectable light with a high scintillation efficiency and a light yield proportional to the deposited energy over a wide range of radiation energies and particle types.
2. If used for X- and γ -ray detection, the attenuation coefficient should be large for a high detection efficiency.
3. The decay time of the induced luminescence should be short so that fast signal pulses can be generated.
4. The medium should be transparent to its own emissions for good light collection.
5. The emission spectrum should match the spectral sensitivity of the light receptor (photomultiplier tube (PMT), photodiode, or film).
6. The material should be rugged, unaffected by moisture, and inexpensive to manufacture.

The coupling of a scintillation crystal to a photosensor is typically done with optical grease to match the index of refraction between interfaces, and a light guide may be used to better match the geometry between the scintillator and photosensor. The photosensor is an electronic device, such as a PMT, semiconductor detector (photodiode), or image-intensifier tube, that converts light into an electrical signal. The construction of a PMT is illustrated in Fig. 2.8. Visible or UV light incident on the PMT's photocathode is converted into photoelectrons via the photoelectric effect. The photoelectrons are focused onto a dynode where they strike the surface and eject several secondary electrons. Each subsequent dynode is maintained at a higher potential, which multiplies the electrons and attracts them toward the anode. The current that is produced is proportional to the intensity of the light signal incident on the photocathode and thus the energy of the incident radiation event in the crystal.

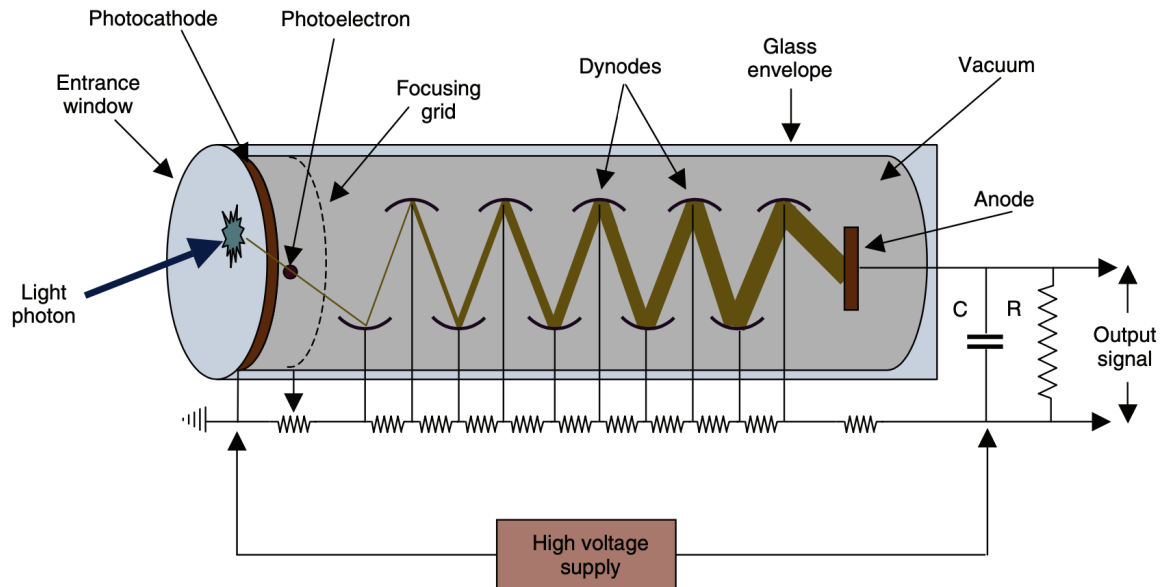


Figure 2.8: Basic principles of a photomultiplier tube showing the main components (photocathode, focusing electrode, dynodes, and anode) with an illustration of electron multiplication. Actual PMTs may use upwards of 12 dynodes with voltage increments from 100 V to 1200 V. From [46], used with permission

The construction of a PMT makes it bulky and sensitive to vibrations and magnetic fields, and its operation requires a high-voltage power supply. Photodiodes are light-sensitive semiconductor detectors that inherently avoid these problems, and have therefore undergone decades of development for scintillation detectors. Photodiodes are significantly smaller and less temperamental than PMTs, but they produce more electrical noise and do not amplify the output signal. Photodiodes behave analogous to gas-filled detectors, such that increasing the applied voltage enables an electron to

initiate an avalanche in an avalanche photodiode (APD). APDs can be operated in Geiger mode at even higher bias voltages, which creates a self-sustaining avalanche that must be quenched by a large resistor to return the photodiode to its quiescent state. In order to relate the amount of light from a scintillation event to the ionizing particle's energy, a number of APDs must be assembled to collect numerous photons over a small area. Thus, single-celled APDs or single photon avalanche photodiodes (SPADs) have been developed with dimensions of tens of microns to increase the probability that each microcell has only one photon incident on it. An example of an array of SPADs is the silicon photomultiplier (SiPM).

By assembling an array of photosensors, the position of the interaction in the detector can be localized from an analysis of the individual photosensor pulses. Scintillation light that is shared across multiple sensors can be analyzed with a center of mass formalism to determine the interaction site, and the total light collected can be related to the incident particle's energy. Semiconductor and scintillation detectors form the basis of radiation detection in modern nuclear medicine imaging devices, which will be described further in Sec. 2.5.

2.4.5.4 Performance Characteristics

The performance characteristics of radiation detectors can be generalized across detector types. Many of these characteristics, such as energy resolution, spatial resolution, and count rate performance are described in Ch. 3 in relation to nuclear medicine imaging devices and will not be included here.

2.5 Nuclear Medicine Imaging

In nuclear medicine imaging, two types of scanners are commonly used to form images of a radiopharmaceutical distribution in a subject—the gamma camera and the PET scanner. These scanners utilize the previously discussed principles of radiation detection to visualize single-photons produced by γ -emitting radionuclides or back-to-back annihilation photons produced by β^+ -emitting radionuclides. Gamma cameras are primarily used for planar scintigraphy and tomographic applications, whereas the PET scanner is used for tomographic imaging. Hybrid imaging systems commonly combine gamma cameras or PET scanners with computed tomography (CT) or magnetic resonance imaging (MRI) systems to obtain a fusion of functional and structural information that improves the accuracy and interpretation of images.

2.5.1 Gamma Camera

In 1958, Hal Anger introduced a scintillation detector for the production of images related to the biodistribution of radiopharmaceuticals [97]. The prototype of the gamma camera, referred to as the scintillation camera or the Anger camera, is presented in Fig. 2.9 [98]. Its design consisted of a shielded scintillation detector coupled with PMTs, a pinhole collimator, a single matrix circuit, a pulse-height selector, and a cathode-ray oscilloscope. Similar to the image formation process of modern gamma cameras, γ -rays entered the camera through the aperture along well-defined paths, then interacted with the scintillation crystal to produce flashes of light. The PMTs detected the flashes of light, and the single matrix circuit collected the electrical signal to determine the (x, y) position of events within the crystal based on the relative strengths of the electrical signal from each PMT. The pulse-height selector would then discriminate events based on the signal intensity to accept certain events, such as the photopeak scintillations from a γ -ray emitting radionuclide. Accepted events were then displayed with a long exposure on the oscilloscope's cathode-ray screen at the same relative positions as in the crystal, thereby forming a two-dimensional (2D) γ -ray image of the subject.

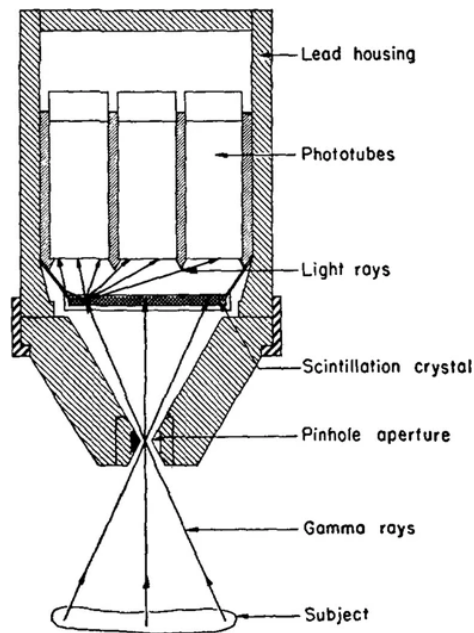


Figure 2.9: Original Anger camera developed by Hal Anger in 1958. The camera utilized a scintillation detector with seven PMTs to produce a 2D image of γ -rays that entered the camera through the pinhole aperture. From [98], Copyright 1958, AIP Publishing LLC, used in accordance with Dalhousie University's Fair Dealing Policy.

Although all Anger cameras are gamma cameras, not all gamma cameras are Anger cameras. Anger cameras specifically utilize scintillation crystals, whereas modern gamma cameras may use scintillation or semiconductor detectors with widely varying component designs. However, the image formation principles are the same as previously described for the Anger camera, with the added difference that modern cameras store the information from detected events in a computer for subsequent analysis. The collimator is a critical piece of equipment on a gamma camera for image formation. It permits the passage of γ -rays from specific directions, and the pattern of photon interactions in the radiation detector forms a 2D projection image of the radiopharmaceutical distribution in the subject. Multiple gamma cameras can be assembled on a gantry to simultaneously acquire images from multiple angles, and data acquired from multiple angles can be used to reconstruct three-dimensional (3D) tomographic images. This forms the basis for SPECT.

2.5.2 Positron Emission Tomography

Positron emission tomographs also use scintillation or semiconductor detectors, however, their construction is fundamentally different from gamma cameras due to the nature of the radiation being detected. Instead of using a physical collimator, PET scanners use opposing detectors to record back-to-back photons produced by positron annihilation. In a process known as electronic collimation, a timing window identifies photons arriving in coincidence, and the electronics calculate the line-of-response (LOR) along which the annihilation event is presumed to have occurred. By assembling rings of detectors, PET scanners can be made with a high geometric detection efficiency that significantly improves the sensitivity compared to gamma cameras. While increasing the number of detectors in a PET scanner and/or increasing the radioactivity in the field of view (FOV) can lead to an increase in the number of coincidence events, only true coincidence events are desired. False events, such as scattered or random coincidence, are incorrectly assigned an LOR that adds statistical noise to the reconstructed image. Qualified coincidences are reconstructed to form a tomographic image depicting the radiopharmaceutical distribution within the subject.

2.6 Tomographic Image Reconstruction

In principle, γ -rays detected from one particular direction can generate an image depicting the radioactive distribution with a subject. In practice, this can lead to an

overlap of structures affecting the interpretation of the radiopharmaceutical distribution. To remove the overlap, data acquired from several LORs can be reconstructed to form a 3D discretized image depicting the continuous distribution of radioactivity. The reconstructed image can be viewed in different planes and directions to remove overlap, increase contrast, and quantify uptake in specific tissues. This provides immense benefit in the study of biological processes. The following subsections describe the mathematical background necessary for tomographic image reconstruction as it relates to emission computed tomography.

2.6.1 Analytical Reconstruction

The simplest approach to reconstructing an image is to backproject detected events along their respective LORs. As illustrated in Fig. 2.10a, a distribution of radioactivity is localized in the (x, y) coordinate system, and a projection image is acquired from some angle in a coordinate system (r, s) stationary with respect to the gamma camera [46]. The two coordinate systems are related by the transformations

$$r = x \cos \phi + y \sin \phi \quad (2.32)$$

$$s = y \cos \phi - x \sin \phi \quad (2.33)$$

where ϕ is the angle of rotation of the gamma camera and corresponding angle between coordinate systems. By storing the 2D intensity profiles $p(r, \phi)$ from all angles and LORs in a matrix, a sinogram is formed as shown in Fig. 2.10b. This provides a convenient way of representing PET and SPECT data.

In simple backprojection, sinogram data is effectively smeared or painted back in the (x, y) image space along the direction from which it was acquired. The backprojections from all sinogram line profiles are added together, and an approximation of the radioactive distribution is obtained in an image as illustrated in Fig. 2.11. This is described with the equation

$$f'(x, y) = \frac{1}{N} \sum_{i=1}^N p(x \cos \phi_i + y \sin \phi_i, \phi_i) \quad (2.34)$$

where $f'(x, y)$ denotes an approximation to the true radioactive distribution and ϕ_i denotes the i^{th} projection from a total of N angles. The summation of backprojections creates a spoke or star artifact that results in blurring of the reconstructed object. Since the blurring decreases with distance from the source, this effect is described

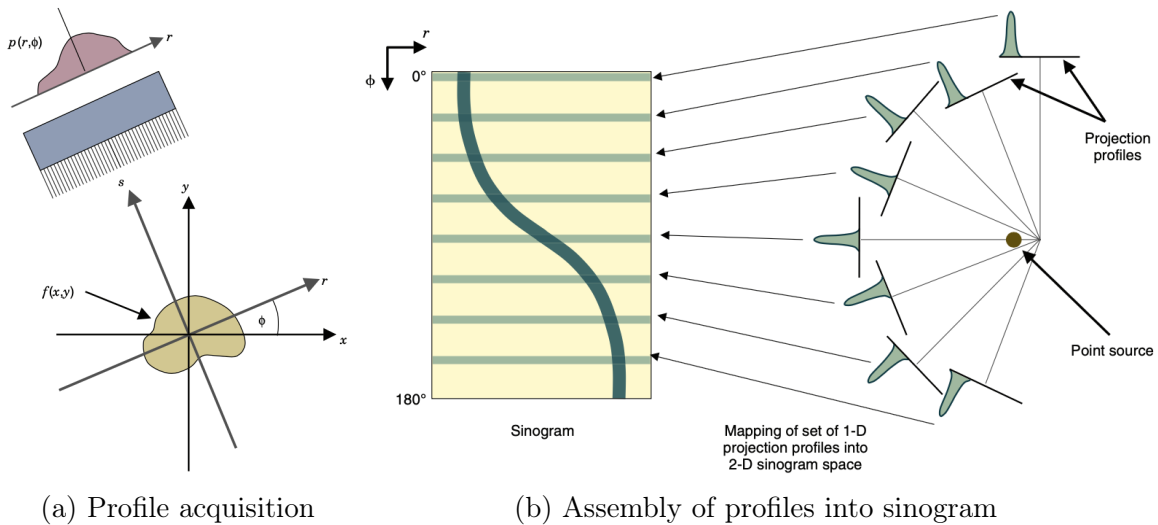


Figure 2.10: Acquisition of raw SPECT data stored in a sinogram. (a) Intensity profiles of a radioactive distribution are acquired with a gamma camera from different angles around a subject. (b) The intensity profiles from all angles are conveniently stored and visualized in a sinogram. Each row corresponds to an individual projection profile. A point source of radioactivity traces out a sinusoidal path. From [46], used with permission.

by an inverse $1/r$ relation. Image quality can be improved by increasing the number of projection angles and the number of samples along the profile. However, blurring remains to some degree. Therefore, sinograms can be filtered prior to backprojection to further improve image quality.

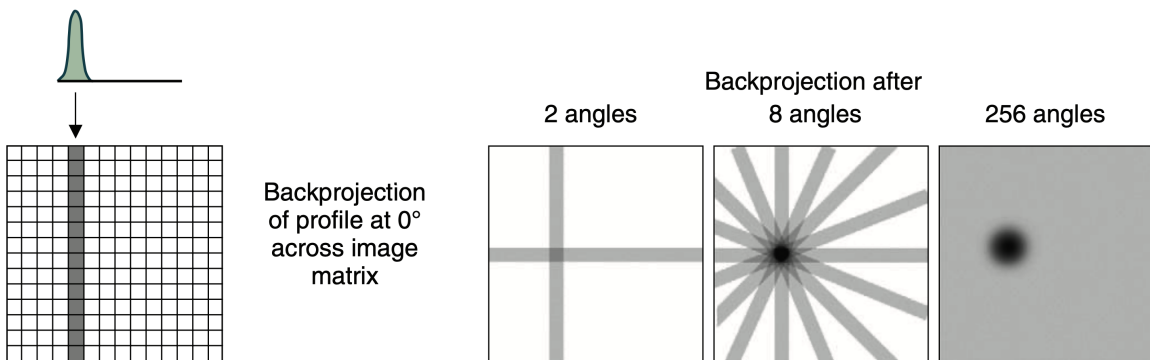


Figure 2.11: In simple backprojection, intensity profiles are projected along the direction from which they were acquired (left). A greater number of angles reduces the spoke artifact, which results in a $1/r$ blurring effect (right). Adapted from [46] by cropping and modifying layout, used with permission.

In filtered back projection (FBP), the sinogram line profiles are filtered in the frequency domain prior to backprojection. This is achieved with the Fourier transform

mation (FT) and inverse FT which convert data between the spatial and frequency domains. In the frequency domain, the FT of each line profile is multiplied by an appropriate filter to suppress the $1/r$ blurring effect. Filters are selected based on image quality requirements, noise characteristics, and the desired balance between resolution and noise suppression. After filtering, the inverse FT is calculated then backprojected to obtain the reconstructed image as illustrated in Fig. 2.12.

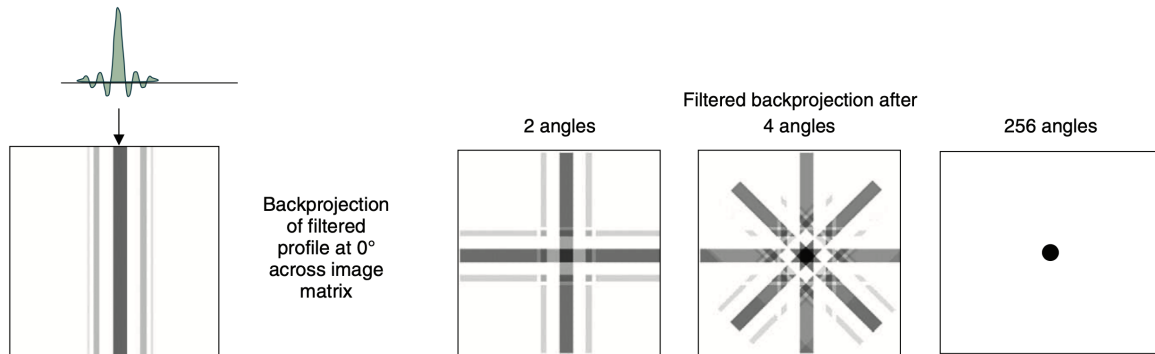


Figure 2.12: In filtered backprojection, intensity profiles are filtered in the frequency domain before being backprojected along the direction from which they were acquired (left). Filtering in the frequency suppresses the $1/r$ blurring, which becomes increasingly apparent with more projection angles (right). Adapted from [46] by modifying layout, used with permission.

Under idealized acquisition conditions where data is noise-free and completely sampled, the FBP method produces an accurate representation of the radioactive distribution. This is often not the case in nuclear medicine imaging due to the discrete size of radiation detectors and poor count statistics of acquired data. Furthermore, the FBP algorithm does not readily account for physical aspects of the image acquisition, such as spatial resolution in the detector or attenuation in the subject. Therefore, iterative reconstruction methods are increasingly being used instead of FBP in nuclear medicine.

2.6.2 Iterative Reconstruction

Iterative reconstruction is computationally more expensive than FBP. The process of iteratively reconstructing tomographic data from acquired data is based on the solution of the system of equations represented by

$$\mathbf{Ax} = \mathbf{b} \tag{2.35}$$

where \mathbf{A} is an operator referred to as the system matrix or acquisition model, \mathbf{x} is the image to reconstruct, and \mathbf{b} is the acquired data. In other words, given acquired data \mathbf{b} , the reconstruction process aims to find a tomographic image \mathbf{x} that best explains the acquired data using an acquisition model \mathbf{A} .

The acquisition model describes how data is translated from detector space to image space by mathematically modelling the data acquisition process. Thus, \mathbf{A} describes the probability of an emission from a given voxel in \mathbf{x} being detected in a given dixel in \mathbf{b} . The model depends heavily on imaging modality and can account for physical effects such as scanner geometry, detector efficiency, attenuation in the subject, and background noise. As illustrated in Fig. 2.13, the transformation process from image to detector space is described as the forward projection \mathbf{Ax} , and the transformation from detector space to image space is the backward projection $\mathbf{A}^T \mathbf{Ax}$, where \mathbf{A}^T is the adjoint of the system matrix.

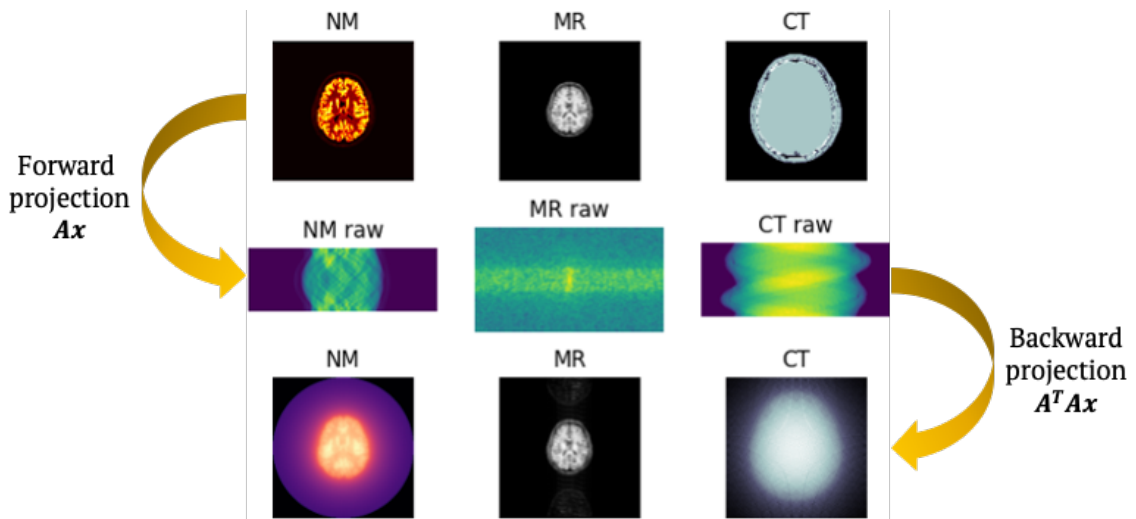


Figure 2.13: The acquisition model \mathbf{A} describes the transformation operation from image to detector space, and the backward projection $\mathbf{A}^T \mathbf{Ax}$ describes the transformation from detector to image space. The top row presents an object from which the acquired data were created. The middle row shows the representation of raw data in the form of a sinogram for nuclear medicine (NM) data (left) and CT data (right), and as a k-space map for magnetic resonance (MR) data (middle). The bottom row displays the backward projected data where the image quality has degraded since the adjoint operation does not equal the inverse operation.

In reality, Eq. 2.35 represents an ill-posed inverse problem since it is impossible to find an exact solution \mathbf{x} such that \mathbf{Ax} perfectly matches the measured data \mathbf{b} , i.e., $\mathbf{Ax} \neq \mathbf{b}$. Instead, the goal of iterative reconstruction is to minimize the difference or

residual ($\boldsymbol{\delta}$) between the forward projection and the acquired data,

$$\mathbf{Ax} - \mathbf{b} = \boldsymbol{\delta}. \quad (2.36)$$

One of the most basic approaches when minimizing the difference is to sum the terms of $\boldsymbol{\delta}$ according to the L^2 -norm which yields the least-squares objective function,

$$\|\mathbf{Ax} - \mathbf{b}\|_2^2 = \|\boldsymbol{\delta}\|_2^2. \quad (2.37)$$

Thus, the image $\hat{\mathbf{x}}$ that minimizes the least-squares objective function is

$$\hat{\mathbf{x}} = \arg \min_{\mathbf{x}} \|\mathbf{Ax} - \mathbf{b}\|_2^2. \quad (2.38)$$

There are many possible convergence algorithms that can minimize the objective function to deliver the reconstructed image, such as gradient descent and statistical algorithms like maximum likelihood expectation maximization (MLEM) and maximum a posteriori (MAP) estimation [99]. The reconstruction is initiated with an initial image estimate that typically contains ones in every voxel, and the algorithm updates the image estimate until a convergence condition has been reached or a specified number of iterations have occurred.

2.6.2.1 Gradient Descent

For a given estimate of the image \mathbf{x}^k at iteration k , the gradient of the objective function can be calculated at \mathbf{x}^k . By subtracting the gradient image from the image estimate, the resulting image \mathbf{x}^{k+1} is closer to a minimum of the objective function. This algorithm can be expressed as

$$\mathbf{x}^{k+1} = \mathbf{x}^k - \lambda^k \mathbf{A}^\top (\mathbf{Ax}^k - \mathbf{b}) \quad (2.39)$$

where λ^k is the scalar step size taken when subtracting the gradient image $\mathbf{A}^\top (\mathbf{Ax}^k - \mathbf{b})$. A small step size could require numerous iterations before arriving at the minimum, and a large step size can result in large oscillations of the objective function value without converging toward a stable solution. Gradient descent is considered relatively inefficient, but it is a fundamental and elementary optimization algorithm capable of reconstructing challenging datasets in nuclear medicine imaging.

2.6.2.2 Maximum Likelihood Expectation Maximization

In statistical image reconstruction, a probability function is required to maximize the probability that the reconstructed image is representative of the acquired data. As described by Shepp and Vardi in [100] and similar to Eq. 2.28, the probability P of observing the acquired data \mathbf{b} given the underlying object or image \mathbf{x} can be modelled with the Poisson probability distribution function using \mathbf{Ax} as the model of the mean:

$$P(\mathbf{b}|\mathbf{x}) = \frac{\mathbf{Ax}^{\mathbf{b}} e^{-\mathbf{Ax}}}{\mathbf{b}!}. \quad (2.40)$$

To simplify the mathematical calculations and optimize computation cost, the likelihood is used instead of probability to estimate the most likely image that generated the acquired data. In other words, an image is sought that maximizes the function $L(\mathbf{x}|\mathbf{b}) = P(\mathbf{b}|\mathbf{x})$. This is achieved in essence by calculating the gradient of the log-likelihood, equating the result to zero, and solving for the maximum likelihood estimate of the image. This depends on the current image estimate \mathbf{x}^k which is iteratively updated with the equation

$$\mathbf{x}^{k+1} = \frac{\mathbf{x}^k}{\mathbf{A}^\top \mathbf{1}} \mathbf{A}^\top \left(\frac{\mathbf{b}}{\mathbf{Ax}^k + \boldsymbol{\eta}} \right). \quad (2.41)$$

Here, $\boldsymbol{\eta}$ represents a scatter or background term added following forward projection.

In the iterative calculation, the current image estimate is forward projected, then a scatter or background noise term may be added before comparing the ratio with the acquired data. This ratio serves as a correction factor used to update the current image estimate following back projection, multiplication, and normalization. To speed up the calculation, the acquired data is often subdivided over subsets [101]. In general, advanced iterative reconstruction algorithms are an active area of research, and open-source software packages such as the Synergistic Image Reconstruction Framework (SIRF) [14] and the Core Imaging Library (CIL) [102] aim to provide a collaborative platform for the development and sharing of novel algorithms. These advancements continue to drive the technical application of nuclear medicine imaging devices, enhancing precision and detail in images that provide increased diagnostic accuracy and improved patient outcomes.

2.6.3 Artificial Intelligence Reconstruction

Artificial intelligence (AI) in nuclear medicine imaging encompasses a broad range of applications such as disease prediction and diagnosis, image reconstruction, pre- and post-reconstruction processing, and attenuation map generation [103]. The theoretical foundations of AI are beyond the scope of this thesis, however, AI represents an advanced area of research in nuclear medicine image formation that should not be overlooked. AI involves the simulation of human intelligence processes by machines. Machine learning is a subset of AI that focuses on learning from data to automatically recognize patterns and make predictions or decisions based on that learning, and deep learning is a subset of machine learning that uses multi-layered neural networks to mimic the learning process of the human brain to automatically learn hierarchical representations from raw data [104]. Algorithms have been developed to address deficiencies in PET and SPECT projection data due to photon interactions, detector response, and collimator penetration; and end-to-end algorithms aim to solve complex inverse problems to reconstruct images directly from raw data with superior noise suppression, resolution modelling, motion correction, and dose reduction compared to conventional methods. While the inclusion of AI in nuclear medicine proposes many opportunities and challenges [105], Reader and Pan [106] have highlighted concerns including false positive and negative findings which require uncertainty estimation, as well as a need for widely accepted benchmark datasets and tests. The reliability of AI in image reconstruction and broader nuclear medicine applications has not been definitively established as a robust tool within a readily implementable package, and this limitation constrains its further consideration in this thesis.

2.7 Summary

This chapter provided a foundational background for the theoretical and methodological tools employed throughout this thesis. The concept of radioactivity was introduced with an overview of radiation interactions in matter. Various types of radiation detectors were discussed while emphasizing their importance in nuclear medicine imaging. This laid the foundation for the description of PET and SPECT in nuclear medicine imaging, along with the basis of image reconstruction techniques. Together, these concepts are essential in the interpretation and understanding of the remainder of this thesis.

Chapter 3

NEMA NU 1-2018 Performance Characterization and Monte Carlo Model Validation of the Cubresa Spark SiPM-based Preclinical SPECT Scanner

3.1 Prologue

The theoretical background of radiation detector performance characteristics was deferred from the previous chapter due to its extensive presence in the current chapter. This chapter describes gamma camera performance as outlined by the National Electrical Manufacturers Association (NEMA). In tandem to the NEMA study presented here, single-photon emission computed tomography (SPECT) acquisition modelling software for pinhole collimators was developed for tomographic image reconstruction with the Software for Tomographic Image Reconstruction (STIR). A detailed description of the pinhole-SPECT software is given in the next chapter.

Recalling the first research objective, this chapter characterizes the Spark and validates its Monte Carlo model using the NEMA standards. Not only does this establish the imaging performance of the Spark, it also demonstrates the performance of silicon photomultipliers (SiPMs) in SPECT, for which published results are scarce. The NEMA standard provides a robust approach to characterization and validation, which ensures that measured and simulated data are accurate, reliable, and consistent. This is integral to the success and credibility of single- and multi-radionuclide SPECT studies with the Spark in subsequent chapters and future studies.

Publication: Strugari ME, DeBay DR, Beyea SD, and Brewer KD. “NEMA NU 1-2018 performance characterization and Monte Carlo model validation of the Cubresa Spark SiPM-based preclinical SPECT scanner”. In: *EJNMMI Physics* 10.1 (June 1, 2023), p. 35. ISSN: 2197-7364. DOI: 10.1186/s40658-023-00555-6

3.2 Abstract

Background: The Cubresa Spark is a novel benchtop silicon photomultiplier (SiPM)-based preclinical single-photon emission computed tomography (SPECT) system. SiPMs in SPECT significantly improve resolution and reduce detector size compared to preclinical cameras with photomultiplier tubes requiring highly magnifying collimators. The National Electrical Manufacturers Association (NEMA) NU 1 Standard for Performance Measurements of Gamma Cameras provides methods that can be readily applied or extended to characterize preclinical cameras with minor modifications. The primary objective of this study is to characterize the Spark according to the NEMA NU 1-2018 standard to gain insight into its nuclear medicine imaging capabilities. The secondary objective is to validate a Geant4 Application for Tomographic Emission (GATE) Monte Carlo simulation model of the Spark for use in preclinical SPECT studies.

Methods: NEMA NU 1-2018 guidelines were applied to characterize the Spark's intrinsic, system, and tomographic performance with single- and multi-pinhole collimators. Phantoms were fabricated according to NEMA specifications, with deviations involving high-resolution modifications. GATE was utilized to model the detector head with the single-pinhole collimator, and NEMA measurements were employed to tune and validate the model. Single-pinhole and multi-pinhole SPECT data were reconstructed with the Software for Tomographic Image Reconstruction (STIR) and HiSPECT, respectively.

Results: The limiting intrinsic resolution was measured as 0.85 mm, owing to a high-resolution SiPM-array combined with a 3 mm-thick scintillation crystal. The average limiting tomographic resolution was 1.37 mm and 1.19 mm for the single- and multi-pinhole collimators, respectively, which have magnification factors near unity at the center of rotation. The maximum observed count rate was 15,400 cps, and planar sensitivities of 34 cps/MBq and 150 cps/MBq were measured at the center of rotation for the single- and multi-pinhole collimators, respectively. All simulated tests agreed well with measurement, where the most considerable deviations were below 7%.

Conclusions: NEMA NU 1-2018 standards determined that a SiPM detector mitigates the need for highly magnifying pinhole collimators while preserving detailed information in projection images. Measured and simulated NEMA results were highly comparable with differences on the order of a few percent, confirming simulation accuracy and validating the GATE model. Of the collimators initially provided with the

Spark, the multi-pinhole collimator offers high resolution and sensitivity for organ-specific imaging of small animals, and the single-pinhole collimator enables high-resolution whole-body imaging of small animals.

3.3 Introduction

Functional imaging in nuclear medicine extensively employs positron emission tomography (PET) and single-photon emission computed tomography (SPECT) for disease diagnosis and staging, therapy planning, dosimetry, and monitoring of treatment response [108, 109]. These nuclear medicine techniques are based on radiopharmaceutical uptake within the body, yielding critical diagnostic information that can readily translate to developing theranostic strategies for managing various diseases [110, 111]. Such investigations are commonly performed in the preclinical setting to evaluate the effects of novel drugs and therapies in small animals, which requires that small animals be the appropriate surrogate for humans [4]. Mice are one of the preferred species for biomedical research because of their anatomical, physiological, and genetic similarity to humans [59]. Furthermore, preclinical imaging with mice demands high-resolution technology due to the study of relatively small organs that are approximately 3,000 times smaller in mice than humans [112]. Recent advancements in imaging technology have promoted widespread adoption of small-animal imaging, and the availability of dedicated preclinical scanners has increased to satisfy this demand. Some advantages of SPECT over PET include superior spatial resolution, simultaneous multi-energy and multi-radionuclide signature detection, increased accessibility to radionuclides with a range of physical half-lives, relatively simple and stable radiochemistry with increased specific activities, and reduced production costs [11, 57]. Therefore, developing sensitive and accurate preclinical SPECT systems is of growing importance.

Monte Carlo simulations are also essential in emission tomography investigations to model, develop, and evaluate nuclear-based imaging systems [113]. The Monte Carlo method is considered the gold standard for designing new medical imaging devices, offering an effective means to assess performance, optimize acquisition protocols, and evaluate new image reconstruction algorithms and correction techniques. Several Monte Carlo packages exist including Geometry and Tracking (Geant4) [114], Electron Gamma Shower (EGS) [115], and Monte Carlo N-Particle (MCNP) [116], all of which provide well-validated physics models and geometry modelling tools. These toolkits focus on radiation transport simulations, and tuning the code to model PET

and SPECT devices can be challenging. The Geant4 Application for Tomographic Emission (GATE) aims to simplify the modelling process while accommodating complex scanner geometries and imaging configurations using geometric definitions, time-dependent phenomena, radioactive source definitions, detector electronics modelling, and data output [113].

Several commercially available preclinical SPECT detectors have been investigated with GATE, including X-SPECT (TriFoil Imaging, Chatsworth, USA) [117], Inveon (Siemens, Munich, Germany) [118], HiReSPECT (Parto Negar Persia, Tehran, Iran) [119], and NanoSPECT/CT^{PLUS} (Mediso, Budapest, Hungary) [120] scanners. These systems, like all SPECT systems, are constructed with varying component designs, including but not limited to pinhole or parallel-hole collimators, monolithic or pixelated scintillation crystals, and solid-state or vacuum tube detector technologies. Cameras that use photomultiplier tubes (PMTs) for high-resolution preclinical SPECT are large and bulky and require highly magnifying pinhole collimators to overcome the limiting intrinsic spatial resolution of PMTs. While position-sensitive photomultiplier tubes (PSPMTs) offer a smaller form factor than PMTs with improved resolution, their combination with scintillation crystals to detect γ - and X-rays yields a detector that is also several centimeters thick, and the camera size is further increased when attaching pinhole or parallel-hole collimators. Recent advancements in solid-state technology, such as cadmium zinc telluride (CZT) for direct detection or silicon photomultipliers (SiPMs) coupled with scintillation crystals for indirect detection, provide advantages over PMT-based technology, including a smaller form factor for design flexibility, superior intrinsic spatial resolution, reduced power consumption, and insensitivity to magnetic fields and vibrations [51]. The use of SiPMs in SPECT is becoming more established, as demonstrated in the literature by a large area clinical SPECT detector [121] and SPECT inserts for clinical and preclinical magnetic resonance imaging [53–55]. An example of a novel SiPM-based preclinical SPECT scanner is the Spark (Cubresa Inc., Winnipeg, Canada) [122, 123].

Cubresa’s implementation of SiPMs in a pinhole-SPECT system with a magnification factor near unity and a form factor small enough for benchtop use is a novel application of SiPMs in SPECT evaluated in the current study. The Spark is a small-animal benchtop SPECT system optimized for *in vivo* mouse imaging and can be configured with up to two detector heads. Its current configuration features one detector head, single- and multi-pinhole collimators, a sodium-activated cesium iodide (CsI(Na)) scintillation crystal, and a SiPM array to achieve high-resolution planar

and tomographic imaging. Altogether, the detector head is less than 6 cm-thick from the face of the collimator to the exterior of the back compartment housing the electronics. This allows the Spark to be attached to preclinical computed tomography (CT) scanners for multi-modal disease study, translational research, and drug discovery applications. For example, it was recently utilized in developing diagnostic radiopharmaceuticals for Alzheimer’s disease [58]. Due to the limited yet increasing use of SiPMs in SPECT, the performance characteristics of a preclinical SiPM SPECT scanner have not been established or compared to other scanners in the literature.

To compare different gamma cameras, the National Electrical Manufacturers Association (NEMA) has published the NEMA NU 1-2018 Standard for Performance Measurements of Gamma Cameras [124]. This standard provides a uniform and consistent method for measuring and reporting performance parameters for various camera designs. Although NEMA has published a *clinical* and *preclinical* standard for PET scanners, a preclinical SPECT standard is currently unavailable. However, the NEMA NU 1-2018 clinical standard can be readily applied or extended to preclinical SPECT cameras with minor modifications. NEMA standards also provide a rigorous and thorough approach to validating Monte Carlo models, unlike some previously modelled systems in GATE that used widely varying, incomplete, or untraceable validation approaches.

The primary objective of this study is to evaluate the performance characteristics of a high-resolution SiPM-based preclinical SPECT scanner—the Cubresa Spark—according to the NEMA NU 1 Standard for Performance Measurements of Gamma Cameras. A secondary objective is to configure and validate a GATE simulation model of the Spark using the measured NEMA results. Collectively, this study aims to accurately establish the imaging performance of a SiPM SPECT system in planar and tomographic acquisitions, offering critical insight into its utility in supporting the development of novel molecular imaging agents and techniques.

3.4 Methods and Materials

3.4.1 Equipment Description

The Spark (Fig. 3.1) was affixed to the benchtop of a Triumph LabPET4/CT dual-modality system (TriFoil Imaging, Chatsworth, USA), and although the Triumph’s imaging systems were unused in this study, the animal bed was used for positioning radioactive sources in SPECT tests. The Spark’s detector housing, detector cover, and

collimator were manufactured from tungsten that yield an overall length, width, and height of $150.4 \times 138.1 \times 56.4 \text{ mm}^3$ when assembled. The detector housing accepts an aluminium scintillator housing assembled with a $102 \times 102 \times 3 \text{ mm}^3$ monolithic CsI(Na) scintillation crystal (Saint-Gobain Crystals, Hiram, USA) and a 2 mm-thick glass light guide. Saint-Gobain BC-631 silicone grease was used to optically couple the light guide to a 14×14 SensL C-series SiPM array comprised of 6 mm sensors with a 7.2 mm pitch on a printed circuit board (ON Semiconductor, Phoenix, USA). The SiPM array operates at room temperature without a cooling system. Further information regarding the construction of the Spark may be obtained from the manufacturer.

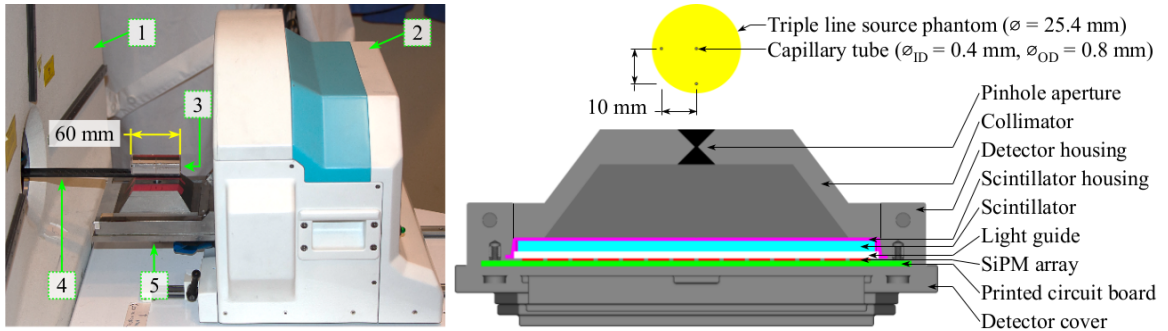


Figure 3.1: The Cubresa Spark preclinical SPECT scanner and the mouse-sized NEMA triple line source scatter phantom, illustrated in a photograph of the system (left) and an axial cutaway view of the detector head modelled in GATE (right). The labelled components in the photograph are the Triumph LabPET4/CT (1), Cubresa Spark gantry (2), mouse-sized NEMA triple line source scatter phantom (3), the animal bed (4), and the SPECT detector head (5). The triple line source phantom dimensions are included for scale.

As outlined in Table 3.1, the Spark performance was assessed with two interchangeable tungsten collimators (Scivis GmbH, Göttingen, Germany): a single-pinhole (SPH) collimator for high-resolution planar and tomographic imaging, and a multiplexing multi-pinhole (MPH) collimator for high-resolution tomography with increased sensitivity. The SPH collimator has a non-focusing right-circular double-cone pinhole, and the MPH collimator uses a 5×5 array of focusing right-circular double-cone pinholes, where each row focuses on a different volume of interest (VOI) in the tomographic field of view (FOV) [125]. The area of the detector used for imaging γ - and X-rays has a useful field of view (UFOV) and central field of view (CFOV) of 84.5 mm and 63.4 mm, respectively.

The Spark was delivered with Scivis' HiSPECT reconstruction software, which was preconfigured solely for the MPH collimator. Precise information regarding the

Table 3.1: Geometric specifications of pinhole collimators.

Aperture ¹	SPH	MPH
Pinhole diameter (mm)	1.0	1.0
Pinhole acceptance angle (°)	90.0	25.0
Number of pinholes	1	25
Thickness (mm)	10.0	10.0
Radius of rotation (mm)	28.0	28.0
Aperture-to-detector distance ² (mm)	26.75	26.75
Reconstructed axial FOV (mm)	57.0	14.0
Reconstructed transaxial FOV (mm)	46.0	30.0

¹SPH: single-pinhole, MPH: multi-pinhole

²Measured to face of scintillation crystal

MPH collimator geometry was not readily available, and as a result, this restricted the simulation model to the SPH collimator only. Measured and simulated SPH SPECT images were reconstructed with the Software for Tomographic Image Reconstruction (STIR) v5.1.0 using the pinhole-SPECT acquisition matrix [126–128].

Prior to measurement, the SPECT system was calibrated for gain, linearity, uniformity, center of rotation, and aperture-to-detector distance [129, 130]. A SiPM dixel-based gain correction table was applied to relate collected light signals to the energy of γ -rays, a linearity correction table compensated for distortions of γ -ray interaction sites in the detector, and a pixel-based uniformity correction table addressed variations in response across the detector. Correction tables were created with manufacturer-provided software, and additional details about the system calibration may be obtained directly from the manufacturer. Radionuclide activity measurements were performed with a Capintec CRC-55tR dose calibrator (Mirion Technologies, Florham Park, USA). Various phantoms and source holders were fabricated in-house to adhere to the NEMA protocol, and each required device is described in the following sections.

3.4.2 Simulation Description

A model of the Spark detector head (Fig. 3.1) was created using the SPECThead system in the GATE v9.0 Monte Carlo toolkit [113] compiled with Geant4 10.06.p01 [114] and Rapid Object-Oriented Technology (ROOT) 6.14.04 [131]. Simulations were distributed over 12 cores on an HP Z820 workstation operating Ubuntu 18.04.5 LTS with two Intel Xeon E5-2630 2.3 GHz hexa-core CPUs and 64 GB of 1600 MHz DDR3 memory. ROOT output was combined into one file and then converted to Cubresa’s list mode format for further processing.

Complex detector geometry was modelled with standard tessellation language (STL) files provided by Cubresa, and simple geometric volumes such as the scintillator, light guide, SiPM array, printed circuit board, and phantoms were modelled with predefined shapes available in GATE. Material properties were assigned to their respective volumes using the Geant4 and GATE materials database. More specifically, the modelled collimator, detector housing, and detector cover materials were tungsten, the scintillator housing was aluminium, the scintillation crystal was cesium iodide (CsI), the light guide was glass, the SiPM array was silicon, and the printed circuit board was epoxy. The scintillation process, optical photon transport, and light detection were not simulated to save computing time. Therefore, the silicone optical grease was negated from the simulation model. Other excluded components were the 3.5 mm-thick carbon fiber animal bed due to its application in only two NEMA tests with minimal attenuation in SPECT acquisitions, and the MPH collimator due to restricted knowledge of the pinhole geometry. For reasons detailed in the Discussion, the SPH collimator was modelled with a 0.85 mm diameter pinhole to better match the simulated collimator-detector response function to measurement.

Physics processes were initialized with the Geant4 standard electromagnetic physics package option 4 (`emstandard_opt4`) [114]. Particle production cuts were set at the default value of 1 mm corresponding to a few keV in most materials, except the scintillation crystal and pinhole knife-edge where the threshold was set to 1 keV. Radioactive sources were defined as an isotropic UserSpectrum source of γ -rays with emissions defined from the Table of Radionuclides [10]. The Spark’s electronics, i.e., signal processing chain, were modelled using the following GATE digitizer modules: the adder, readout, energy blurring, spatial blurring, pile-up, dead time, and efficiency. Figure 3.2 presents the digitizer chain with the values set for parameters of interest. Digitizer parameters were determined empirically from measurement by simulating a range of values for a given digitizer parameter, fitting a cubic spline to the simulated results, then interpolating the digitizer parameter at the measured result. However, the pile-up timing resolution t_{\min} was calculated as

$$t_{\min} = \frac{P_1}{R_T(P_0 + 2P_1)} \quad (3.1)$$

where P_0 and P_1 are the counts in the primary and first order pile-up peaks, respectively, and R_T is the true input count rate [132].

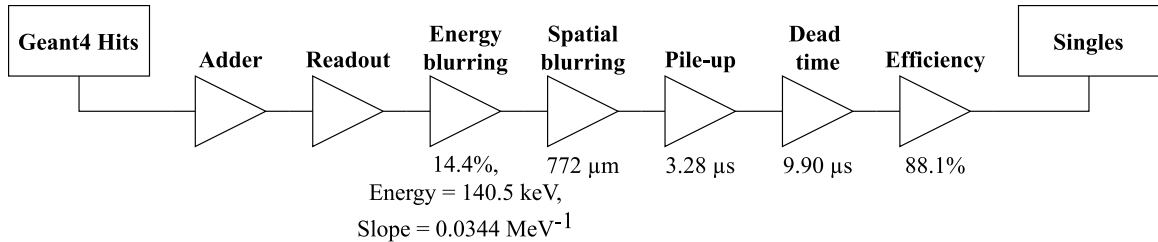


Figure 3.2: Digitizer signal processing model of the Spark’s readout electronics used in GATE. Interactions in the scintillation crystal were recorded as hits following Geant4 particle generation and transport through modelled materials. Hits were subsequently filtered through the digitizer modules to obtain singles corresponding to the detected signal after processing by the front-end electronics. Digitizer parameters were determined empirically from measurement by simulating a range of values for a given digitizer parameter, fitting a cubic spline to the simulated results, then interpolating the digitizer parameter at the measured result, except for the pile-up timing resolution which was calculated with Eq. 3.1.

3.4.3 NEMA Performance Characterization and SPECT Model Validation

Performance characterization of the Spark was made according to the NEMA NU 1-2018 protocol, with tests briefly described in the following sections. The radionuclide for all tests was technetium-99m (^{99m}Tc) except for the multiple window spatial registration test which used gallium-67 (^{67}Ga). An energy window width of 30% was centered on the reference photopeak(s) when generating projection images for all tests. The UFOV and CFOV were defined with electronic masking and images had 0.1 mm isotropic pixels unless stated otherwise. Measured data were acquired according to total acquisition time or counts through an open energy window. Note that acquired counts refers to the computer’s unprocessed estimate of counts determined from the optical light produced in the scintillation crystal, and Cubresa’s proprietary data processing software converts the optical light to detected/observed counts stored in list mode data in terms of position, energy, and time. Simulations were then configured based on measurements of data acquisition time, radioactivity, radioactive source distribution, and system geometry, except for the SPH collimator pinhole diameter. No corrections were applied to the simulated data at any stage. Validation of the GATE model was based on reporting parameter comparisons between measured and simulated NEMA results.

3.4.4 Tests of Intrinsic Gamma Camera Detector Characteristics

3.4.4.1 Intrinsic Spatial Resolution and Linearity

Intrinsic spatial resolution refers to the gamma camera's ability to localize an ionizing photon's interaction site within the detector, and intrinsic linearity reflects the distortion of those interaction sites throughout the detector's FOV. This test was performed with a 2.5 mm-thick tungsten planar mask comprised of a 3×3 grid of 0.8 mm-wide and 26.5 mm-long parallel slits having adjacent slit centers separated by 31.5 mm, and a Derenzo pattern with $\{0.7, 0.8, 0.9, 1.0, 1.2, 1.4\}$ mm diameter holes. An Eppendorf tube containing a 50 MBq point source was centered 65 cm above the face of the detector, and 15 million counts were acquired. Intrinsic resolution and linearity were assessed from line spread functions (LSFs) and analyzed according to the procedures defined by the NEMA NU 1-2018 protocol. A millimeters-per-pixel calibration factor was also calculated using line profile spacing to convert relevant image dimensions to physical units in relevant NEMA tests.

Normally, the mask-slit geometry would yield the limiting intrinsic spatial resolution. However, due to the spatial resolution performance of the SiPM detector, the mask-slit geometry described above produced LSFs that were wider than the intrinsic spatial resolution. Therefore, a secondary test was performed using a non-NEMA source geometry to extract the limiting resolution. A point spread function (PSF) was created with a pencil beam emitted from a tungsten line-source holder with a tunnel 0.4 mm in diameter, 10.0 mm in length, and centered 1.0 mm above the detector with a 1.0 cm-thick aluminium plate. A total of 100,000 counts were acquired from a 170 MBq line source established in a capillary tube (inner diameter $\varnothing_{ID} = 1.15$ mm, outer diameter $\varnothing_{OD} = 1.50$ mm, length $L = 75$ mm) and secured in the line-source holder. The PSF was then analyzed following the methods applied to the LSFs produced with the mask-slit geometry.

3.4.4.2 Intrinsic Flood Field Uniformity

The intrinsic uniformity quantifies the gamma camera's response to a uniform radiation flux. An 8 MBq point source was centered 65 cm above the face of the detector and 100 million counts were acquired. The measured and simulated flood field projection images with 1 mm pixels were smoothed once by convolution with the NEMA smoothing filter, and measured data were corrected for uniformity. The

integral uniformity was calculated using

$$\text{Uniformity (\%)} = \frac{\max - \min}{\max + \min} \times 100 \quad (3.2)$$

where max and min refer to the maximum and minimum pixel values within the FOV. Similarly, the differential uniformity was calculated with Eq. 3.2 from the max and min in a set of five contiguous pixels in a row or column.

3.4.4.3 Multiple Window Spatial Registration

The multiple window spatial registration (MWSR) test was performed with 11 MBq of ^{67}Ga to assess the Spark's ability to accurately localize photons of different energies when imaged through different energy windows. The previously described pencil beam source holder (see Sec. 3.4.4.1) was positioned in a 1.0 cm-thick aluminium plate at nine locations along the detector axes, including the center of the detector, $0.4\times$, and $0.8\times$ the distance to the edge of the UFOV. A total of 4 million counts were acquired at each position, and projection images were generated from each photopeak. The maximum axial and transaxial displacements of PSF centroids were then calculated. Overall spatial registration accuracy was also assessed according to the mean Euclidean distance between each centroid and the average centroid location.

3.4.4.4 Intrinsic Count Rate Performance in Air: Decaying Source Method

The count rate performance describes the gamma camera's ability to process one detection event before moving on to another, and the number of detected counts may be fewer than input events because of dead time and/or pile-up. Two models exist to describe idealized dead time behaviour: paralyzable and non-paralyzable dead time [96]. The Spark's behaviour is well-described with a paralyzable model using the equation

$$\text{OCR} = \text{ICR} e^{-\text{OCR}\tau} \quad (3.3)$$

where OCR is the observed count rate, ICR is the input count rate, and τ is the system dead time. Furthermore, OCR can be affected by pile-up, which occurs when a true event at time $t = 0$ is followed by subsequent events in the interval $0 < t < \tau$, followed by an event-free interval of length τ . Using the decaying source method, the

dead time was calculated from the intercept and slope of Eq. 3.4:

$$\lambda t + \ln \text{OCR} = -\text{ICR}_0 \tau e^{-\lambda t} + \ln \text{ICR}_0 \quad (3.4)$$

where λ is the decay constant, t is the time, ICR_0 is the true input rate at the beginning of measurement, $e^{-\lambda t}$ is the abscissa, and $\lambda t + \ln \text{OCR}$ is the ordinate [96].

Care was taken to minimize scatter during count rate performance assessment by securing an Eppendorf tube containing 235 MBq in a tungsten Capintec 511 Dose Drawing Syringe Shield. The shield was capped with a lead lid, and a 6.0 mm-thick copper plate covered the open side of the source holder. The source was placed at a distance of $5 \times \text{UFOV}$ above the detector face to produce a uniform radiation field. Counts were measured for 60 s and simulated for 10 s in 60 min intervals, and the last data point was acquired when the observed count rate dropped below 600 cps to determine ICR_0 accurately. All data were corrected for radioactive decay, and the measured data were corrected for background noise and uniformity. Measured count rate data were utilized to configure the digitizer pile-up, dead time, and efficiency modules in the simulation model. Following the NEMA protocol, the intrinsic count rate performance was analyzed in terms of the maximum OCR and 20% loss OCR.

3.4.4.5 Intrinsic Energy Resolution

The energy resolution characterizes a radiation detector's response to a monoenergetic radiation source and describes its ability to distinguish between different energies of that radiation. The formal definition is

$$\text{Energy resolution (\%)} = \frac{\text{FWHM}}{\text{Photopeak location}} \times 100 \quad (3.5)$$

where FWHM is the full width at half maximum of the photopeak calculated according to NEMA's resolution methodology in this context. The Spark's intrinsic energy resolution was assessed with 0.6 keV bins using the count rate data point immediately below the 20% loss OCR introduced in the previous section (Sec. 3.4.4.4). This data point satisfies all NEMA conditions while offering count rate traceability. The simulated data point below the 20% loss OCR was re-simulated with a 60 s acquisition time to obtain count statistics comparable to the measurement. Note that a keV-per-channel calibration factor was not calculated with cobalt-57 (^{57}Co) since a vendor-specific energy calibration is automatically applied to list mode data.

3.4.5 Tests of Gamma Camera Detectors with Collimators

In this study, system or *extrinsic* measurements primarily involved the SPH collimator due to its applicability in planar scintigraphy, yielding unambiguous projection images. Measurements with the experimental MPH were included where applicable.

3.4.5.1 System Spatial Resolution without Scatter

The system spatial resolution without scatter represents the gamma camera's limiting ability to localize a photon interaction site in the detector when combining collimator and intrinsic factors. Acquisitions were performed in the axial and transaxial directions using a precision glass capillary tube ($\varnothing_{ID} = 0.4$ mm, $\varnothing_{OD} = 0.8$ mm, $L = 75$ mm). The capillary tube contained 10 MBq of radioactivity, and 100,000 counts were acquired at positions of {0.4, 25.0, 50.0, 75.0, 100.0} mm from the face of the SPH collimator. NEMA's resolution methodology was applied to calculate resolution from LSFs. Results were corrected for magnification to compare resolution in the object rather than the detector. A plot of the average system resolution as a function of source-to-collimator distance was generated with a linear least squares fit to characterize the system resolution.

3.4.5.2 System Spatial Resolution with Scatter

The presence of a scattering medium degrades image quality in terms of projection image blurring, reduced contrast in reconstructed images, and decreased quantitative accuracy [2]. Thus, the system spatial resolution with scatter was assessed with a mouse-sized NEMA triple line source scatter phantom fabricated from an acrylic cylinder ($\varnothing = 25.4$ mm, $L = 60$ mm) with three 0.8 mm-diameter bores for precision capillary tubes: one at the center and two separated by 90° with a 10 mm radial offset. One precision capillary tube containing 10 MBq was inserted into the central bore of the scatter phantom, and 100,000 counts were acquired axially and transaxially at capillary tube positions of {12.7, 25.0, 50.0, 75.0, 100.0} mm from the face of the collimator. Analysis of the resulting projection images followed the methods outlined in Sec. 3.4.5.1.

3.4.5.3 System Planar Sensitivity

The system planar sensitivity characterizes the number of detected counts per unit activity to evaluate a collimator's count rate performance. A 35.0 mm diameter petri dish was filled with a solution of 2 ml of water and injected with a calibrated activity

of $A_{\text{cal}} = 210$ MBq for the SPH dataset and $A_{\text{cal}} = 25$ MBq for the MPH dataset. The internal base of the radioactive solution was placed at source-to-collimator distances of $D = \{10.0, 20.0, 28.0, 50.0, 100.0\}$ mm, and 4 million counts were acquired at each position in measurement. In contrast, counts were acquired for 100 s at each position in simulation to save on computing time. Data were acquired from the largest to the smallest distance with activity levels ranging from A_{cal} to ~ 15 MBq to minimize pile-up and dead time effects, namely in the SPH acquisition. Measured data were corrected for uniformity, and then the decay-corrected count rate R was calculated for each acquisition i as

$$R_i = \lambda C_i e^{\lambda(T_i - T_{\text{cal}})} \times (1 - e^{-\lambda T_{\text{acq},i}})^{-1} \quad (3.6)$$

where C_i is the summed counts from the projection image, T_i is the acquisition start time, $T_{\text{acq},i}$ is the acquisition duration, and T_{cal} is the time of activity calibration. Using a standard Levenberg-Marquardt non-linear least squares fit technique, the decay-corrected count rate and source-to-collimator distance for each SPH acquisition were fit with the function

$$R_i = c_0 + c_1 e^{(-c_2 D_i)} \quad (3.7)$$

where c_0 , c_1 , and c_2 are fitting parameters. The total system sensitivity S_{TOT} was then calculated as

$$S_{\text{TOT},i} = \frac{R_i}{A_{\text{cal}}} \quad (3.8)$$

and plotted against the source-to-collimator distance to characterize the sensitivity. Note that NEMA's protocol utilizes fit parameters from Eq. 3.7 to compute collimator penetration factors for detected counts in a given region of interest (ROI). This analysis was excluded as it does not apply to pinhole collimators. Furthermore, Eq. 3.7 does not apply to the MPH collimator due to the focusing orientation of pinholes.

3.4.6 Tests Specific to Tomographic Camera Systems

SPECT projection data were acquired from 0° to 270° in a 208×208 matrix with 0.5 mm isotropic pixels, then reconstructed with nine iterations of the maximum likelihood expectation maximization (MLEM) algorithm in 0.25 mm isotropic voxels. SPH SPECT data were acquired in 3° increments then reconstructed with STIR in a $230 \times 184 \times 184$ matrix, and MPH SPECT data were acquired in 90° increments then reconstructed with HiSPECT in an $80 \times 144 \times 144$ matrix. HiSPECT software only supports the MLEM algorithm, whereas STIR's pinhole-SPECT software permits

access to STIR’s extensive library of algorithms and corrections for the spatially variant collimator-detector response and attenuation. Thus, SPH SPECT data were also reconstructed with the filtered back projection (FBP) algorithm using a ramp filter to adhere to the NEMA protocol.

3.4.6.1 SPECT Reconstructed Spatial Resolution without Scatter

The reconstructed spatial resolution without scatter reflects the limiting size of a radioactive distribution that can be observed with the gamma camera. Three point sources in air were established in precision capillary tubes with a mean activity of 0.274 ± 0.007 MBq and an axial extent of ~ 0.4 mm. To conform to the small reconstructed FOV of the MPH collimator (see Table 3.1), one point source was centered on the axis of rotation, and the two remaining point sources were positioned at $\pm 75\%$ of the distance to the edge of the FOV, i.e., ± 5.25 mm axially and ± 11.25 mm transversally. The point sources were set in place, and 300,000 counts were acquired across all projections in the SPH and MPH acquisitions to directly compare tomographic resolution. Cubic ROIs were centered around each reconstructed point source and summed along each axis to calculate the radial, tangential, and axial resolution without scatter according to the NEMA protocol.

3.4.6.2 SPECT Reconstructed Spatial Resolution with Scatter

The reconstructed spatial resolution with scatter was assessed with the mouse-sized NEMA triple line source scatter phantom described in Sec. 3.4.5.2. Three capillary tubes containing a mean activity of 9.4 ± 0.1 MBq were inserted into the phantom and centered axially in the FOV, with peripheral line sources placed at 0° and 270° to maximize the amount of scatter contributing to projection images over the extent of rotation. The line sources in the scatter phantom were set in place, and 5 million counts were acquired across all projections in the SPH and MPH acquisitions to directly compare tomographic resolution. The reconstructed images were summed axially to obtain three 3.5 mm-thick transverse slices: one at the center of the FOV and two at $\pm 75\%$ the distance to the edge of the respective axial FOV. A square ROI was centered on each resulting PSF to calculate the central, radial, and tangential resolution with scatter according to the NEMA protocol.

3.4.6.3 SPECT Volume Sensitivity, Uniformity, and Variability

The system volume sensitivity (SVS) reports the total system sensitivity to a uniform activity concentration in a cylindrical phantom. An acrylic phantom ($\varnothing_{\text{ID}} = 26$ mm, $\varnothing_{\text{OD}} = 28$ mm, $L_{\text{inner}} = 21$ mm) was filled with water containing 1.75 MBq/ml then centered along the axis of rotation in the gamma camera's image space. The phantom was set in place, and SPH and MPH SPECT acquisitions were obtained with 10 s and 60 s projections, respectively. The measured data were corrected for uniformity, and then the SVS was calculated as

$$\text{SVS} = \frac{A}{B_c} \quad (3.9)$$

where A is the average count rate (total detected counts divided by total elapsed time including time for rotation) and B_c is the activity concentration halfway through the acquisition. By normalizing the SVS by the axial extent L of the cylindrical phantom in the reconstructed image, the volume sensitivity per axial centimeter (VSAC) was calculated as

$$\text{VSAC} = \frac{\text{SVS}}{L}. \quad (3.10)$$

The VSAC was then multiplied by the reconstructed axial FOV of the collimator to obtain a useful approximation of the total system response to a broad distribution of radioactivity.

Although it is not a defined NEMA test, the volume uniformity was evaluated from images of the cylindrical phantom reconstructed with the MLEM algorithm. Integral uniformity was calculated with Eq. 3.2 from a VOI covering 75% of the phantom's imaged length and 60% of the phantom's inner diameter. Within this VOI, the variability was determined from the coefficient of variation (CV):

$$\text{CV (\%)} = \frac{\sigma}{\mu} \times 100 \quad (3.11)$$

where σ is the standard deviation and μ is the mean voxel value within the VOI.

3.5 Results

3.5.1 Tests of Intrinsic Gamma Camera Detector Characteristics

3.5.1.1 Intrinsic Spatial Resolution and Linearity

Representative planar mask projection images from measured and simulated acquisitions are presented in Fig. 3.3, and Table 3.2 gives the intrinsic spatial resolution determined from the pencil beam PSF and planar mask LSFs in terms of the FWHM and full width at tenth maximum (FWTM). The pencil beam produced a measured and simulated limiting intrinsic spatial resolution of 0.85 mm, which was $\sim 7\%$ below that predicted by the planar mask slits. Table 3.2 also presents the differential and absolute intrinsic spatial linearity results, which were found to be $\lesssim 0.1$ mm in measurement and simulation. The measured and simulated linearity results calculated a calibration factor of 0.099 mm/pixel. Altogether, good agreement was observed between measurement and simulation, and measured results indicated highly accurate positioning and minimal distortion of detected photons with the SiPM array.

Table 3.2: Intrinsic spatial resolution and linearity.

Reporting parameter	Region of interest	Measurement	Simulation
Resolution PSF FWHM (mm)	Middle of FOV	0.851 ± 0.010	0.850 ± 0.003
Resolution PSF FWTM (mm)	Middle of FOV	1.559 ± 0.014	1.591 ± 0.007
Resolution LSF FWHM (mm)	UFOV	0.912 ± 0.098	0.916 ± 0.026
	CFOV	0.953 ± 0.091	0.924 ± 0.029
Resolution LSF FWTM (mm)	UFOV	1.73 ± 0.15	1.66 ± 0.03
	CFOV	1.80 ± 0.14	1.68 ± 0.03
Differential linearity (mm)	UFOV	0.023	0.001
	CFOV	0.024	0.002
Absolute linearity (mm)	UFOV	0.102	0.003
	CFOV	0.055	0.003

3.5.1.2 Intrinsic Flood Field Uniformity

Integral and differential uniformity calculated from the UFOV and CFOV of flood field images are presented in Table 3.3. The measured and simulated uniformity results were $< 3\%$ and $< 2\%$, respectively, showing good agreement and uniform response to radiation. While the absolute differences between measurement and simulation were on the order of 1%, the relative differences were as high as 53%. This could be due to a variety of reasons affecting the Spark’s detector response in measurement, including scintillation crystal material properties, sources of photon scatter, background and electronic noise, or Cubresa’s event positioning and gain/uniformity correction algorithms, which differ from simulation and can be cumbersome to model.

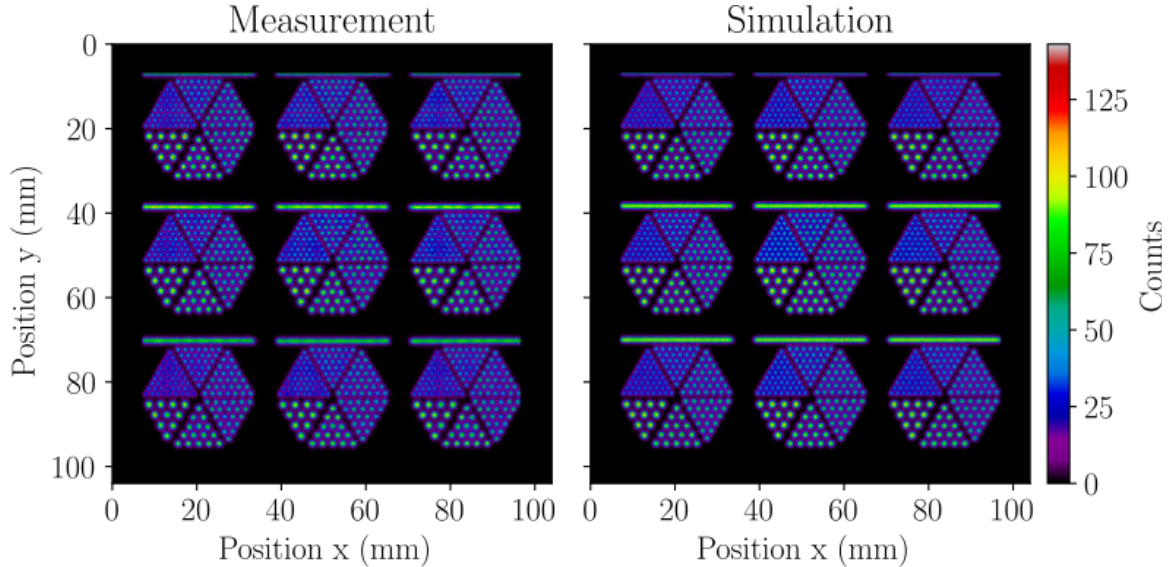


Figure 3.3: Representative planar mask projection images from measurement (left) and simulation (right) with 0.1 mm isotropic pixels and without uniformity correction. The measured image agrees well with the simulation and demonstrates the minimal distortion and superior resolution of SiPMs. The Derenzo patterns are fully resolved, and the FWHM of PSFs produced by the 0.7 mm diameter holes were consistent with a limiting intrinsic resolution of 0.85 mm. The images shown are for demonstrative purposes, as the detector’s FOV is not large enough to include the full extent of all line profiles and Derenzo patterns, which resulted in clipping of the line profiles shown at $y = 7$ mm. Therefore, when analyzing the intrinsic spatial resolution and linearity from all line profiles, the central line profiles were placed across the center of the detector as instructed by the NEMA protocol, thereby clipping the Derenzo pattern at $y = 97$ mm (not shown).

Table 3.3: Flood field uniformity.

Reporting parameter	Region of interest	Measurement	Simulation
Integral uniformity (%)	UFOV	2.96	1.72
	CFOV	2.79	1.96
Row differential uniformity (%)	UFOV	2.75	1.69
	CFOV	2.52	1.77
Column differential uniformity (%)	UFOV	2.75	1.67
	CFOV	2.11	1.67

3.5.1.3 Multiple Window Spatial Registration

The higher energy γ -rays from ^{67}Ga were observed to penetrate the walls of the tungsten pencil beam holder and produce noisy projection images, resulting in a significant fraction of total counts detected outside the pencil beam PSF. Nonetheless, the measured (simulated) MWSR was found to have maximum PSF centroid displacements in the axial and transaxial directions of 0.192 mm (0.095 mm) and 0.259 mm

(0.149 mm), respectively, which reflects the worst-case-scenarios of misregistration. The mean Euclidean distance between each centroid and the average centroid location for a given pencil beam location was 0.050 ± 0.023 mm and 0.044 ± 0.022 mm in measurement and simulation, respectively. In other words, photons of different energies were accurately localized, and centroids from different energy windows were found within one pixel of each other on average.

3.5.1.4 Intrinsic Count Rate Performance in Air: Decaying Source Method

Figure 3.4 presents the $^{99\text{m}}\text{Tc}$ count rate performance curve where the measured (simulated) maximum and 20% loss OCRs were 15,410 cps (15,500 cps) and 7,520 (7,440 cps), respectively. The measured data were corrected for uniformity and a background count rate of 11.6 cps to directly compare with the simulation, for which no corrections were necessary. The measured and simulated results were comparable at input count rates below the maximum. However, the experimental detector did not behave like an idealized paralyzable system at relatively large count rates. Unexpected behaviour was observed through photopeak shifting in addition to pulse pile-up and dead time effects at count rates beyond the maximum—a count rate range unlikely to be encountered with typical *in vivo* usage of the Spark. The measured (simulated) dead time was found to be $23.9 \mu\text{s}$ ($23.8 \mu\text{s}$) using Eq. 3.4.

3.5.1.5 Intrinsic Energy Resolution

Energy spectra are presented in Fig. 3.5 where the intrinsic energy resolution was 14.7% in measurement and simulation. Minute differences can be observed in the energy spectra at energies above the photopeak due to incomplete scintillation light collection during pile-up in the experimental system. Aside from the differences in pile-up energy distribution, a 3.1% difference was found in the number of pile-up events detected in an energy window extending above 150 keV.

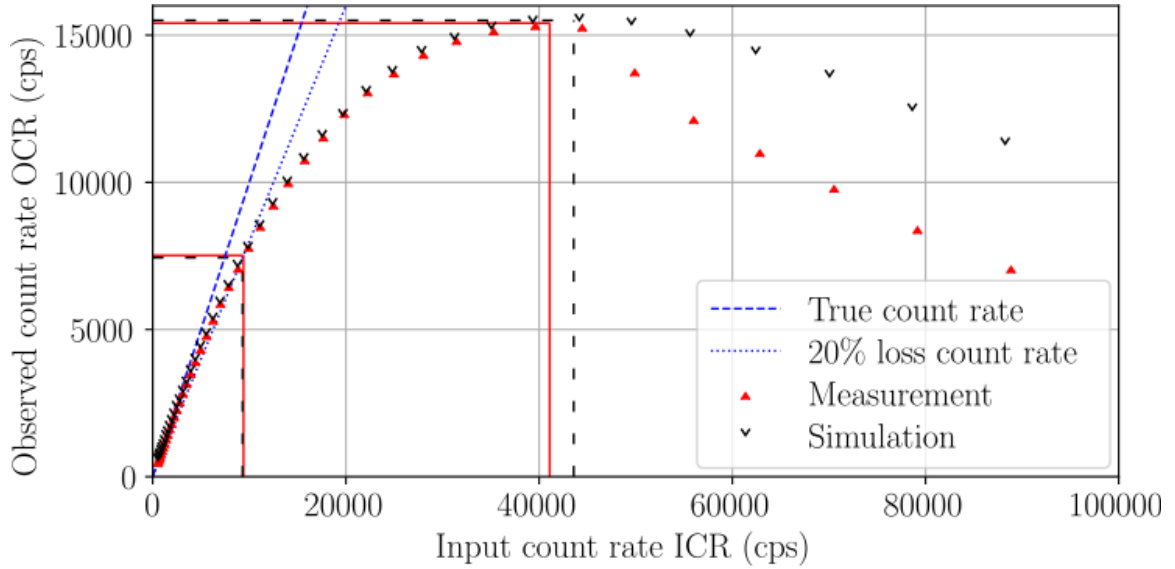


Figure 3.4: Intrinsic count rate performance in air. Measured results are shown with red solid carets and simulated results with black empty carets. Additional lines illustrate the maximum OCR and 20% loss OCR for measurement (solid lines) and simulation (dashed lines). The count rates are in agreement below the maximum OCR while above the maximum, the measured OCR falls off the trend line as the photopeak shifted to lower energies.

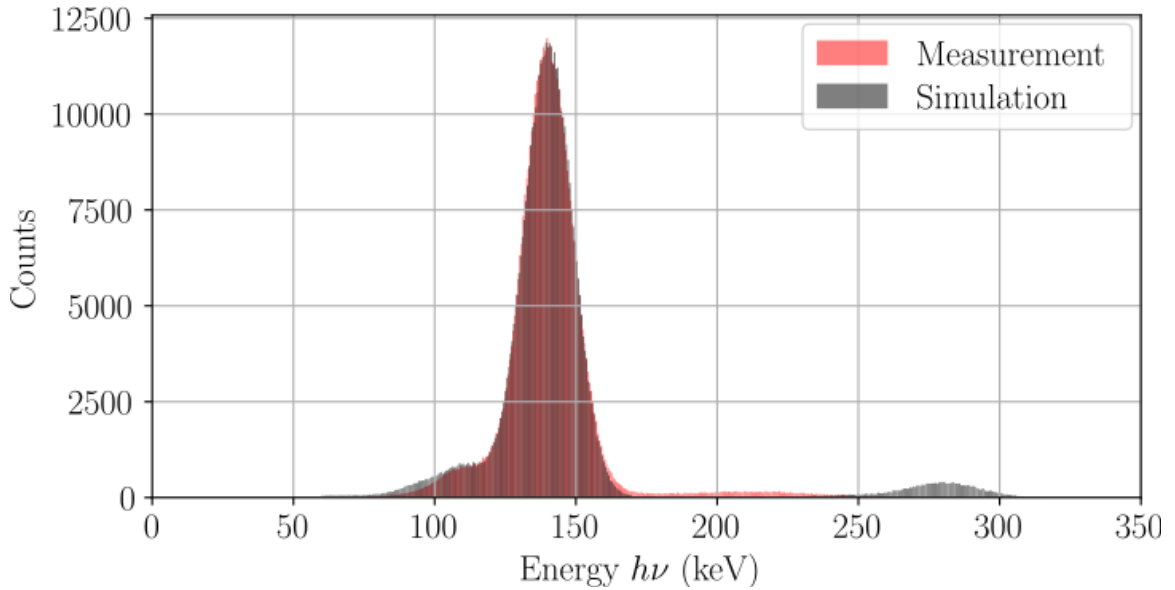


Figure 3.5: Measured and simulated $^{99\text{m}}\text{Tc}$ energy spectra acquired at a count rate loss below 20%. The intrinsic resolution was 14.7% in both cases. Differences can be observed in the pile-up energy distribution due to partial scintillation light collection of the SiPM array, which was not modelled with GATE.

3.5.2 Tests of Gamma Camera Detectors with Collimators

3.5.2.1 System Spatial Resolution without Scatter

The system spatial resolution without scatter is shown in Fig. 3.6. A linear least squares fit to measured and simulated data calculated a coefficient of determination of $r^2 = 1.0$ and similar FWHM line equations. The equations predicted a measured (simulated) limiting system spatial resolution of 1.87 mm (1.80 mm) at the center of rotation ($D = 23.0$ mm). Overall, the FWHM differences between measurement and simulation varied from 4.8% to 3.2% over source-to-collimator distances from 0 mm to 100 mm, respectively. A discrepancy can be observed in the FWTM best-fit lines.

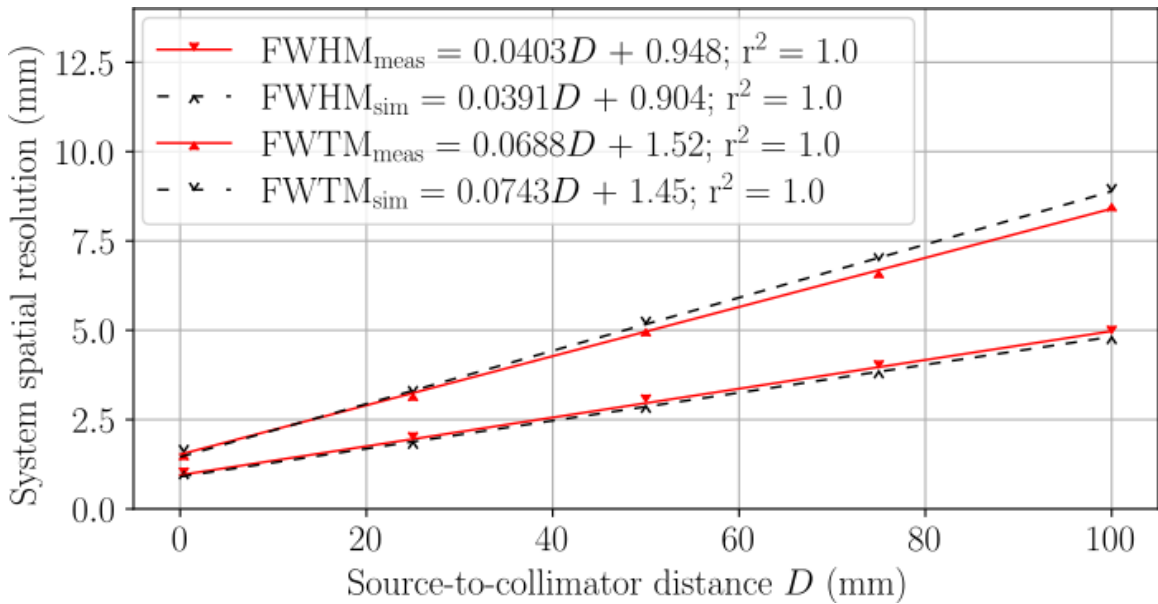


Figure 3.6: System spatial resolution without scatter, presented in terms of FWHM and FWTM for the SPH collimator. Measured results are shown with solid red carets and solid lines of best fit, and simulated results are shown with empty black carets and dashed lines of best fit. Equations for lines of best fit are distinguished in the legend with abbreviated subscripts for measurement (meas) and simulation (sim). The measured (simulated) system resolution without scatter at the center of rotation was 1.87 mm (1.80 mm).

3.5.2.2 System Spatial Resolution with Scatter

The system spatial resolution with scatter in the mouse-sized NEMA triple line source scatter phantom is presented in Fig. 3.7. Linear least squares fits calculated a coefficient of determination of $r^2 = 1.0$ and comparable FWHM and FWTM fit equations between measurement and simulation. The FWHM equations predicted a

measured (simulated) system spatial resolution with scatter of 1.98 mm (1.88 mm) at the center of rotation. Here, the FWHM differences between measurement and simulation varied from 7.1% to 2.9% over source-to-collimator distances from 0 mm to 100 mm, respectively. Interestingly, the FWTM best-fit lines have a higher degree of correspondence between measurement and simulation with scatter than without.

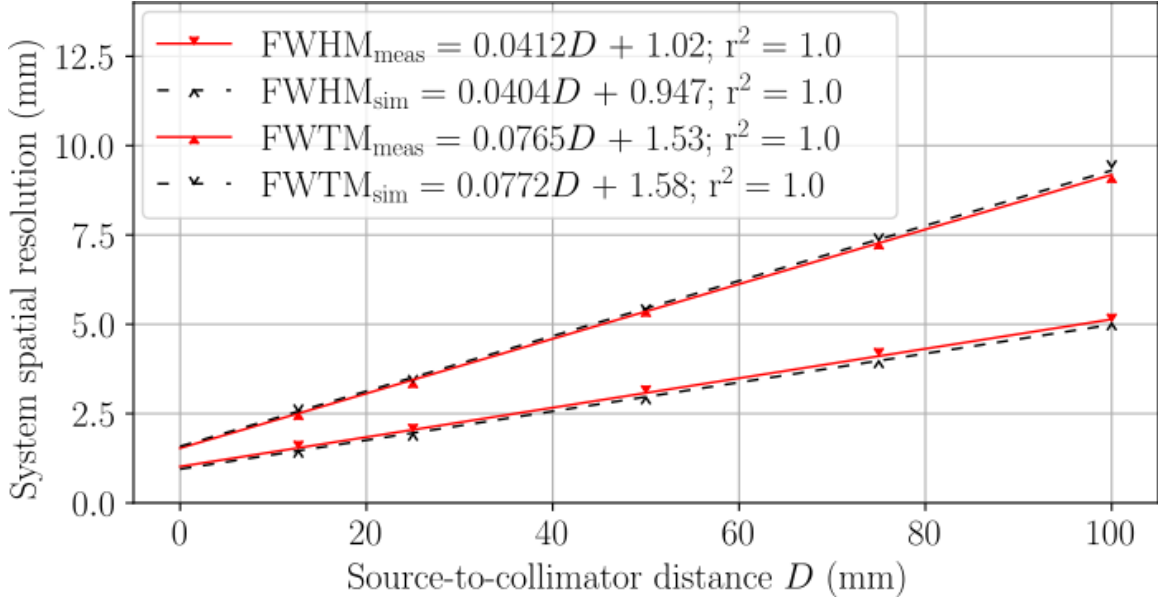


Figure 3.7: System spatial resolution with scatter in a mouse-sized NEMA triple line source scatter phantom presented in terms of FWHM and FWTM for the SPH collimator. Measured results are shown with solid red carets and solid lines of best fit, and simulated results are shown with empty black carets and dashed lines of best fit. Equations for lines of best fit are distinguished in the legend with abbreviated subscripts. The measured (simulated) system resolution with scatter at the center of rotation was 1.97 mm (1.88 mm).

3.5.2.3 System Planar Sensitivity

The total system planar sensitivity is presented in Fig. 3.8 for the SPH and MPH collimators. For the SPH collimator, the exponential fit calculated a measured (simulated) planar sensitivity of 33.8 cps/MBq (35.2 cps/MBq) at the center of rotation, reflecting a 4.0% difference. The difference increased to 14.2% at the face of the collimator, which could be partly due to limitations in modelling the collimator with a 0.85 mm pinhole. For the MPH collimator, sensitivity is optimized within the tomographic FOV due to the focusing nature of the pinholes. Therefore, the three largest values were fit with a quadratic function, and interpolation at the center of rotation calculated a planar sensitivity of 150 cps/MBq.

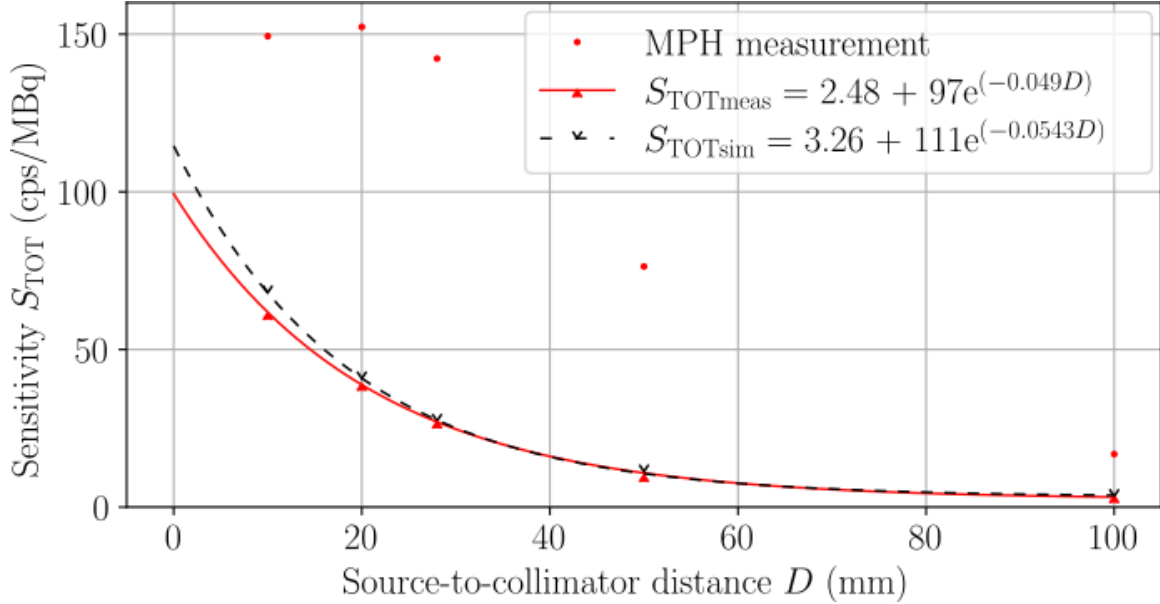


Figure 3.8: Planar sensitivity as a function of source-to-collimator distance. For the SPH collimator, measured results are shown with solid red carets, and a solid line of best fit and simulated results are shown with black with empty carets and a dashed line of best fit. MPH collimator results are shown as red dots. Fit equations for the SPH collimator measurement and simulation are distinguished in the legend with abbreviated subscripts. The MPH collimator geometry is optimized for increased sensitivity in the tomographic FOV, whereas the SPH collimator sensitivity increases when approaching the pinhole.

3.5.3 Tests Specific to Tomographic Camera Systems

3.5.3.1 SPECT Reconstructed Spatial Resolution without Scatter

Table 3.4 details the three-dimensional (3D) resolution from all reconstructed point source images. Acquisitions with the SPH collimator calculated a measured (simulated) limiting 3D resolution of 1.37 ± 0.15 mm (1.30 ± 0.15 mm). The MPH collimator yielded a 13% improvement in the limiting resolution with a value of 1.19 ± 0.20 mm and a submillimeter tangential resolution due to the lateral focusing pinholes. Note that leaching of radioactivity into the capillary tube sealing clay was observed in measurement. A closer inspection of Table 3.4 confirms that the axial resolutions were overestimated in measurement when considering that all other FWHM were nearly identical between SPH collimator measurement and simulation.

Table 3.4: SPECT reconstructed spatial resolution without scatter.

Reporting parameter	Measurement			Simulation	
	MPH	SPH	SPH	SPH	SPH
Collimator	MPH	SPH	SPH	SPH	SPH
Reconstruction algorithm	MLEM	MLEM	FBP	MLEM	FBP
Central transaxial FWHM (x, y) (mm)	1.29 ± 0.04	1.45 ± 0.01	2.26 ± 0.01	1.50 ± 0.01	2.26 ± 0.01
Central axial FWHM (z) (mm)	1.56 ± 0.01	1.58 ± 0.01	2.45 ± 0.01	1.31 ± 0.01	2.26 ± 0.01
Peripheral radial FWHM (x) (mm)	1.13 ± 0.08	1.25 ± 0.06	2.03 ± 0.10	1.30 ± 0.09	2.11 ± 0.25
Peripheral tangential FWHM (y) (mm)	0.91 ± 0.05	1.23 ± 0.11	1.94 ± 0.14	1.26 ± 0.13	1.93 ± 0.10
Peripheral axial FWHM (z) (mm)	1.24 ± 0.04	1.45 ± 0.16	2.70 ± 0.04	1.12 ± 0.06	2.48 ± 0.05
Average 3D FWHM (mm)	1.19 ± 0.20	1.37 ± 0.15	2.26 ± 0.30	1.30 ± 0.15	2.20 ± 0.23

3.5.3.2 SPECT Reconstructed Spatial Resolution with Scatter

Figure 3.9 presents the central 3.5 mm-thick slice of the mouse-sized NEMA triple line source scatter phantom from the MLEM reconstructions, and Table 3.5 gives a breakdown of in-plane resolution values from reconstructed mouse phantom images. Acquisitions with the SPH collimator produced a measured (simulated) average in-plane resolution of 1.44 ± 0.07 mm (1.46 ± 0.07 mm), and the MPH collimator yielded a 17% improvement with an average FWHM of 1.18 ± 0.15 mm. Measurement and simulation were found to have excellent agreement in tomographic resolution, with differences below 2%. Although the MPH collimator is capable of higher resolution than the SPH collimator, the reduced standard deviation of the SPH resolution indicates that its in-plane resolution is more symmetric throughout the tomographic FOV.

Table 3.5: SPECT reconstructed spatial resolution with scatter.

Reporting parameter	Measurement			Simulation	
	MPH	SPH	SPH	SPH	SPH
Collimator	MPH	SPH	SPH	SPH	SPH
Reconstruction algorithm	MLEM	MLEM	FBP	MLEM	FBP
Central FWHM (mm)	1.29 ± 0.05	1.52 ± 0.04	2.23 ± 0.07	1.54 ± 0.05	2.21 ± 0.08
Radial FWHM (mm)	1.27 ± 0.06	1.39 ± 0.06	2.34 ± 0.11	1.40 ± 0.04	2.30 ± 0.06
Tangential FWHM (mm)	0.99 ± 0.07	1.41 ± 0.03	2.03 ± 0.11	1.43 ± 0.03	2.06 ± 0.10
Average in-plane FWHM (mm)	1.18 ± 0.15	1.44 ± 0.07	2.20 ± 0.16	1.46 ± 0.07	2.19 ± 0.12

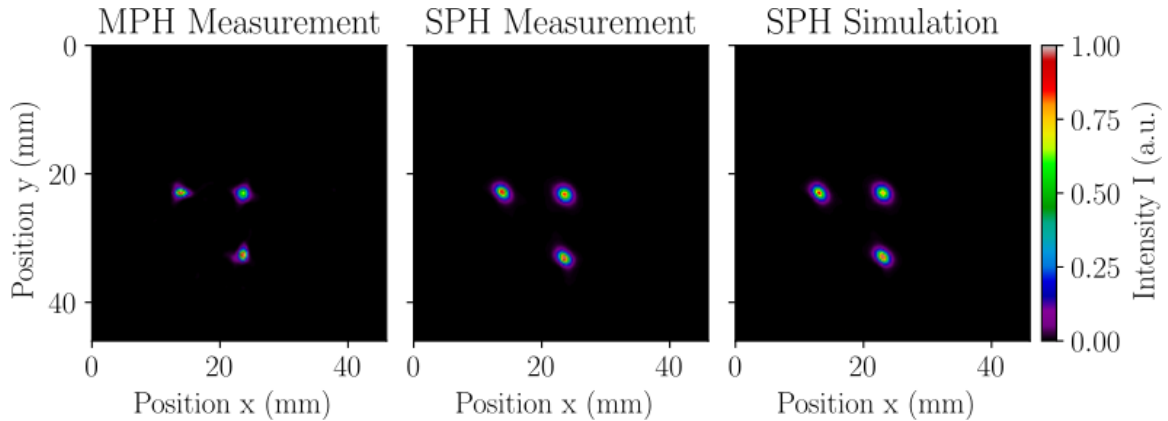


Figure 3.9: SPECT reconstructed spatial resolution with scatter evaluated with a mouse-sized NEMA triple line source scatter phantom in MPH collimator measurement (left), SPH collimator measurement (middle), and SPH collimator simulation (right). The images present the central 3.5 mm-thick transverse slice from the MLEM reconstruction used in calculating the radial, tangential, and central resolution. Images were normalized by the maximum displayed pixel value, resulting in intensity values with arbitrary units (a.u.). The MPH collimator offers superior tomographic resolution compared to the SPH collimator when scanning relatively small radioactivity distributions.

3.5.3.3 SPECT Volume Sensitivity, Uniformity, and Variability

Tomographic images of the cylindrical phantom reconstructed with the MLEM algorithm are presented in Fig. 3.10, and the corresponding volume sensitivity, uniformity, and variability results are given in Table 3.6. When comparing the measurement to simulation, the SPH volume sensitivity had the largest discrepancy observed across all NEMA tests, with a difference of 7.3%. This can be attributed to the slight overestimation in simulated sensitivity, an air bubble in the phantom during measurement that increased the source-to-collimator distance on average, and the exclusion of the animal bed from the simulation model. Although the SPH collimator has fewer pinholes than the MPH collimator and utilizes a smaller area of the UFOV, its increased tomographic FOV and total system response compensate for the relatively low sensitivity. Furthermore, tomographic images produced with the SPH collimator are considerably more uniform with less variability than those made with the MPH collimator.

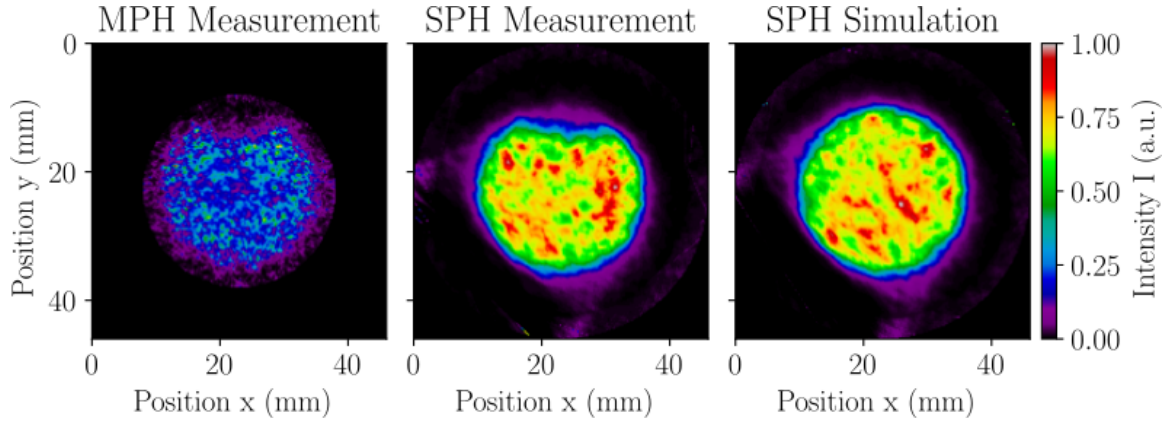


Figure 3.10: SPECT volume sensitivity, uniformity, and variability evaluated with a cylindrical phantom in MPH collimator measurement (left), SPH collimator measurement (middle), and SPH collimator simulation (right). The images present the central 0.25 mm-thick transverse slice from the MLEM reconstruction used in calculating volume uniformity and variability. Images were normalized by the maximum displayed pixel value, resulting in intensity values with arbitrary units (a.u.). A bubble can be seen in the measured data that was not modelled in the simulation. The SPH collimator offers a larger FOV with superior uniformity and noise characteristics compared to the MPH collimator when scanning relatively large radioactivity distributions.

Table 3.6: SPECT volume sensitivity, uniformity, and variability.

Reporting parameter	Measurement		Simulation
Collimator	MPH	SPH	SPH
SVS (cps/(MBq/cm ³))	2,200	329	354
VSAC (cps/(MBq/cm ²))	1,570	157	169
Total system response (cps/(MBq/cm ³))	2,200	901	970
Uniformity (%)	96.5	48.2	38.2
CV (%)	38.7	11.6	10.2

3.6 Discussion

The performance characteristics of a high-resolution SiPM-based preclinical SPECT system—the Cubresa Spark—have been evaluated for the first time according to the NEMA NU 1-2018 Standard for Performance Measurements of Gamma Cameras. The primary challenge in applying the NEMA NU 1 standard in a preclinical setting with a small-area detector was satisfying count-related specifications in the MWSR and SPECT reconstructed spatial resolution tests. Despite the relatively low count statistics associated with the SPH collimator and pencil beam apertures, practical count-starved acquisitions were obtained in favour of timely measurements because adherence to count criteria was inherently so time-consuming that it was

considered unduly burdensome. One test that exceeded the count criteria was the intrinsic count rate performance in air, which specifies that the final data point should be measured when the observed count rate drops below 4,000 cps because the dead time is only a fraction of a percent. Adherence to this specification would have yielded an overestimated 20% loss count rate of 10,000 cps due to a failure to extract the true input count rate from the linear response region of the detector.

Upon comparison with available reference values from Cubresa, the measured intrinsic spatial resolution of 0.851 ± 0.010 mm was in excellent agreement with the reference value of 0.85 mm. To our knowledge, this is the highest reported intrinsic resolution of any gamma camera evaluated with the NEMA NU 1 standard to date. When comparing the system planar sensitivities, measured results of 33.8 cps/MBq for the SPH collimator and 150 cps/MBq for the MPH collimator were not in agreement with the respective reference values of 50 cps/MBq and 467 cps/MBq. The discrepancy is likely due to differences in source geometry, for which a planar source was used in this study while Cubresa likely used a point source. In general, pinhole collimator sensitivity is greatest along the pinhole axis and decreases when moving orthogonally off-axis. Therefore, the measured and simulated SPH collimator sensitivity represents the average sensitivity in a 35 mm-diameter plane located 23 mm from the face of the collimator. Furthermore, the sensitivity profiles shown in Fig. 3.8 underestimate the sensitivity for source positions near the face of the collimator due to the extent of radioactivity lying outside the conic pinhole FOV. Regarding the MPH collimator and recalling that each row of pinholes focuses on a different VOI, accurate measurement of the MPH collimator sensitivity would require optimal placement of separate sources centered at the focal point of each VOI to ensure that all emissions occur inside the conic FOVs of all pinholes. This could be done with detailed knowledge of pinhole geometry.

When comparing internal results between measurement and simulation, the intrinsic performance parameters were very similar, and measured results were accurately simulated, which primarily validates the GATE detector head and digitizer settings. The parameters set in the digitizer differ from the corresponding observables, highlighting the importance of tuning the digitizer—a complex achievement with the Spark since it is not a conventional gamma camera. This process was made simpler and more accurate by applying NEMA’s methodology. Comparisons of the system and SPECT performance also showed excellent agreement between measurement and simulation, with the most considerable differences amounting to $\lesssim 7\%$. Altogether,

these results confirm the accuracy of the Monte Carlo simulation results and satisfy the secondary objective of validating the GATE simulation model of the Spark for use in preclinical SPECT studies, such as validating STIR’s pinhole-SPECT image reconstruction capabilities [123, 126].

When tuning the GATE model for the system and tomographic simulations, a 0.85 mm diameter pinhole was defined with a 90° acceptance angle for the SPH collimator to better match the measured and simulated collimator-detector response functions in terms of resolution and sensitivity. This diameter was obtained following the methodology for calculating digitizer parameters as described in Sec. 3.4.2. When simulating a 1.0 mm-diameter pinhole, the simulated system resolution without scatter was characterized as $\text{FWHM} = 0.0424D + 1.12$ (mm), which agrees well with theoretical equations from Van Audenhaege et al. [48], but predicts a limiting resolution of 2.10 mm at the center of rotation that does not correspond with the measured result of 1.87 mm. This discrepancy can be attributed to a vendor-specific event positioning algorithm that improves the Spark’s resolution, which could not be accounted for using the digitizer. Similarly, the simulated 1.0 mm pinhole system planar sensitivity was characterized as $S_{\text{TOT}} = 4.33 + 148e^{(-0.0563D)}$ (cps/MBq), which predicts a sensitivity of 44.9 cps/MBq at the center of rotation which is much greater than the measured result of 33.8 cps/MBq. This discrepancy could relate to the choice of CsI as the scintillation crystal material. This predefined material describes unactivated CsI and has the same physical characteristics as CsI(Na) and thallium-activated cesium iodide (CsI(Tl)), but differs in terms of optical properties such as scintillation light yield, de-excitation time, refractive index, and peak emission wavelength [133, 134]. The introduction of optical properties into the simulation could allow for simulation of the entire SiPM readout logic to improve sensitivity and overall simulation accuracy. However, it would significantly increase computation time. Current efforts are ongoing to incorporate SiPM-specific software into GATE’s digitizer to reproduce signals from SiPMs [135, 136].

Several commercially available preclinical SPECT systems have been validated with GATE using $^{99\text{m}}\text{Tc}$ and are compared in Table 3.7. Comparisons with pinhole collimators are made against 1.0 mm-diameter pinholes where data were available, except for the NanoSPECT/CT^{PLUS} which uses 1.5 mm pinholes. System and SPECT parameters are cited at the radius of rotation. These tabulated studies not only demonstrate the flexibility and reliability of GATE for accurately modelling various detector designs but also illustrate the potential of SiPMs in molecular imaging.

Comparisons of gamma camera performance for different imaging systems are best performed according to the NEMA NU 1 standard, as it provides a uniform and consistent method for measuring and reporting performance parameters for various camera designs. Unfortunately, most tabulated systems were not evaluated with NEMA standards, perhaps due to the absence of a dedicated preclinical SPECT standard from NEMA, a shortage of required resources, or a restriction from essential scanner data. Therefore, direct comparisons are limited due to inconsistent reporting parameters from different researchers and organizations. Nonetheless, this study has demonstrated competitive performance characteristics of the novel SiPM-based SPECT system, including the highest intrinsic spatial resolution of the tabulated gamma cameras, the smallest form factor, good energy resolution, and comparable sensitivity and tomographic resolution to the top-performing preclinical systems.

Table 3.7: Performance comparisons of commercial preclinical SPECT cameras validated with GATE using ^{99m}Tc .

Reporting parameter	Spark	X-SPECT	Inveon	HiReSPECT	NanoSPECT
Detection method	SiPM	CZT	PSPMT	PSPMT	PMT
Scintillation crystal ¹	CsI(Na)	N/A	NaI(Tl)	CsI(Na)	NaI(Tl)
Collimator ²	SPH/MPH	SPH/MPH	SPH/MPH	PH	SPH/MPH
Radius of rotation (mm)	28	25	25	25	45
Magnification factor	$\sim 1\times$	$\sim 4\times$	$\sim 4\times$	$1\times$	$\sim 3.5\times$
Energy window width	30%	20%	20%	N/A	20%
Aperture size (mm)	1.0	1.0	1.0	1.2	1.5
Intrinsic spatial resolution (mm)	0.85	1.5	N/A	N/A	3.2
Intrinsic energy resolution (%)	14.7	5	12.4	19.15	8.7
System resolution (mm)	SPH: 1.87	SPH: 1.02	N/A	2.79	N/A
Sensitivity (cps/MBq)	SPH: 34 MPH: 150	MPH: 155	SPH: 38 MPH: 286	36–42	SPH: 42 MPH: 191
SPECT resolution (mm)	SPH: 1.37 MPH: 1.19	MPH: 0.58	SPH: 1.25	1.7	SPH: 1.27 MPH: 1.24
References	N/A	[64, 117, 137]	[65, 118, 138, 139]	[119, 140, 141]	[120, 142]

¹CsI(Na): sodium-activated cesium iodide, NaI(Tl): thallium-activated sodium iodide

²SPH: single-pinhole, MPH: multi-pinhole, PH: parallel-hole

N/A: not applicable or not available

3.7 Conclusion

The performance of a novel preclinical SiPM-based SPECT scanner has been characterized according to the NEMA NU 1-2018 Standard for Performance Measurements of Gamma Cameras. Measured and simulated NEMA tests were highly comparable, where the most considerable differences were below 7%, and overall differences were a few percent. This confirms simulation accuracy and satisfies the secondary objective of validating the GATE Monte Carlo model. Of the collimators initially provided with the Spark, the multi-pinhole collimator investigated in this study offers increased spatial resolution and sensitivity for organ-specific imaging of small animals, and the single-pinhole collimator enables high-resolution whole-body imaging of small animals. This work demonstrates that a SiPM detector mitigates the need for highly magnifying collimators while preserving detailed information in projection images.

Chapter 4

Integration of Advanced 3D SPECT Modelling for Pinhole Collimators into the Open-Source STIR Framework

4.1 Prologue

The second research objective was to integrate and test open-source reconstruction software for single-photon emission computed tomography (SPECT) systems with pinhole collimators in the Software for Tomographic Image Reconstruction (STIR). Previously, open-source software was unavailable for pinhole-SPECT systems. This work established the first open-source platform configurable for complex pinhole-SPECT geometries. The open-source nature of this project promotes further collaboration and reproducibility of research, which has significant potential to positively impact preclinical and clinical nuclear medicine practice, medical research, patient outcomes, and gamma camera design. It also provides the critical foundation for the novel multi-radionuclide SPECT technique established in the next chapter.

The open-source pinhole-SPECT software was licensed to University College London (UCL), London, UK, and is maintained in part by the Collaborative Computation Project in Synergistic Reconstruction for Biomedical Imaging (CCP SyneRBI). It included a set of C++ classes, member functions, and test files developed to reconstruct images for pinhole-SPECT cameras. The software integrated code written by Carles Falcon for calculating the system matrix for single- and multi-pinhole collimators. Its integration was finalized during a student exchange with UCL’s Institute of Nuclear Medicine with support from CCP SyneRBI.

Publication: Strugari M, Falcon C, Erlandsson K, Hutton BF, Brewer K, and Thielemans K. “Integration of advanced 3D SPECT modelling for pinhole collimators into the open-source STIR framework”. In: *Frontiers in Nuclear Medicine* 3 (Apr. 18, 2023), p. 1134774. ISSN: 2673-8880. DOI: 10.3389/fnume.2023.1134774

4.2 Abstract

Single-photon emission computed tomography (SPECT) systems with pinhole collimators are becoming increasingly important in clinical and preclinical nuclear medicine investigations, as they can provide a superior resolution-sensitivity trade-off compared to conventional parallel-hole and fanbeam collimators. Previously, open-source software did not exist for reconstructing tomographic images from pinhole-SPECT datasets. A 3D SPECT system matrix modelling library specific for pinhole collimators has recently been integrated into STIR—an open-source software package for tomographic image reconstruction. The pinhole-SPECT library enables corrections for attenuation and the spatially variant collimator-detector response by incorporating their effects into the system matrix. Attenuation correction can be calculated with a simple single line-of-response or a full model. The spatially variant collimator-detector response can be modelled with point spread function and depth of interaction corrections for increased system matrix accuracy. In addition, improvements to computational speed and memory requirements can be made with image masking. This work demonstrates the flexibility and accuracy of STIR’s support for pinhole-SPECT datasets using measured and simulated single-pinhole SPECT data, from which reconstructed images were analyzed quantitatively and qualitatively. The extension of the open-source STIR project with advanced pinhole-SPECT modelling will enable the research community to study the impact of pinhole collimators in several SPECT imaging scenarios and with different scanners.

4.3 Introduction

Single-photon emission computed tomography (SPECT) is based on the detection of individual γ -rays emitted from a radiotracer distribution within a subject. An Anger camera detects the γ -rays with a scintillation crystal and associated electronics after passing through a collimator [97]. The collimator aperture permits the passage of γ -rays from specific directions, and the pattern of photon interactions in the scintillation crystal forms a two-dimensional (2D) projection image of the tracer distribution in the subject. A series of projection images acquired from different angles can be subsequently used to reconstruct the three-dimensional (3D) radiotracer distribution in a tomographic image.

The design of the collimator in terms of hole size, material, and overall geometry, among other factors, affects the spatial resolution and sensitivity of a SPECT system.

Several designs exist, including but not limited to parallel-hole, slant-hole, converging and diverging, fanbeam, and pinhole collimators [47]. Therefore, the choice of collimator design is application dependent for channelling photons of different energies, magnifying or minifying images, or selecting between image quality and imaging speed. Although parallel-hole and fanbeam collimators are conventionally used when imaging small fields-of-view (FOVs), pinhole collimators can provide a superior resolution-sensitivity trade-off [143]. Besides the successful application of pinhole-SPECT systems in small-animal imaging, there has been a resurgence in the use of pinhole collimators for clinical cardiac and brain studies, and when imaging small FOVs [144].

While pinhole-SPECT has regained popularity in clinical and preclinical investigations of molecular imaging agents, no open-source software solutions are available for reconstructing pinhole-SPECT datasets. However, recent efforts have led to the integration of a 3D SPECT system matrix modelling library for pinhole collimators into the open-source Software for Tomographic Image Reconstruction (STIR). The STIR package is an object-oriented library implemented in C++ that provides a framework for research in the processing and reconstruction of emission tomography studies [127]. Initially written to support positron emission tomography (PET) data, STIR was previously extended to handle SPECT data with parallel- and converging-hole collimators [128, 145]. This was achieved by integrating parts of the SPECT Reconstruction Library developed at the University of Barcelona into STIR [70, 146–148]. The expansion of STIR’s support for pinhole collimators marks the first open-source platform for reconstructing pinhole-SPECT datasets, which is important for advancing molecular imaging techniques and technologies.

This work aims to demonstrate the capabilities of STIR’s support for pinhole-SPECT datasets. The pinhole code uses a similar implementation strategy as the previously integrated SPECT collimator modelling. The library enables corrections for attenuation and the spatially variant collimator-detector response by incorporating their effects into the system matrix.

4.4 Technical Description

Similar to the original SPECTUB implementation, the new pinhole-SPECT implementation is referred to as `PinholeSPECTUB` and includes a dedicated reader for pinhole-SPECT projection data in Interfile format [149], with some adaptations as

pinhole collimators are not supported in Interfile. The pinhole-SPECT Interfile reader utilizes the projection matrix size, pixel scaling factor, and detector radius defined at the face of the scintillation crystal. System matrix calculation is executed with the `ProjMatrixByBinPinholeSPECTUB` projector class derived from the existing STIR `ProjMatrixByBin` class, and detector and collimator parameter files are utilized in addition to the usual STIR parameter file. The parameter files are text files that use an Interfile-like syntax. They are composed of keywords corresponding to the names of the various reconstruction and matrix parameters, with the values entered next to them. Sample parameter files for configuring the `PinholeSPECTUB` projector can be found in App. A, and a detailed description of all parameters can be found in STIR’s documentation.

The detector file defines the intrinsic resolution for point spread function (PSF) correction, scintillation crystal attributes for depth of interaction (DOI) correction, and orbit information for the acquisition (i.e., number of orbits, number of angles, initial angle, angular increment—positive for counterclockwise and negative for clockwise rotation, and axial position with respect to the reconstructed volume). Note that only circular camera orbits are supported at this time. The collimator file defines the radius of rotation and geometry for cylindrical or polygonal collimators (i.e., the detector element exposed by the pinhole, hole position, shape—rectangular or round, size, tilt, and acceptance angle). An illustration of the pinhole-SPECT system matrix geometry for a polygonal collimator setup is shown in Fig. 4.1.

The system matrix weights the contribution of each image voxel along the line-of-response (LOR) to each detector element. Corrections can be made for increased system matrix accuracy by modelling the effects of intrinsic PSF, DOI, and attenuation when configuring the STIR parameter file. When PSF correction is disabled, a geometrical approach is applied by considering the projection of the pinhole on the detector. This provides higher computational speed and reduced memory requirement compared to the PSF approach, but is less accurate. When PSF correction is enabled, the projection of the hole is convolved with the PSF in detector space to account for the blurring effects of the camera. Values parsed from the parameter file define the number of standard deviations to consider in the PSF along with the subsampling factor to temporally reduce PSF resolution for increased calculation accuracy before downsampling the final PSF to the bin size. Furthermore, when PSF or DOI corrections are enabled, an additional parsed parameter sets the spatial sampling interval for PSF and DOI distributions.

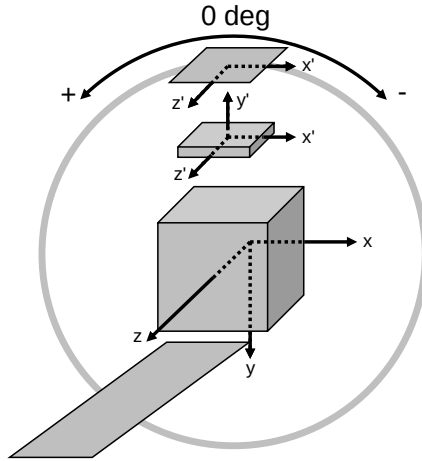


Figure 4.1: PinholeSPECTUB system of reference and sign criteria illustrated for a polygonal collimator setup. Note that the projection matrix adheres to STIR’s coordinate system as indicated by the x , y , and z axes. The detector and collimator use a rotating frame of reference where the transaxial x' and axial z' axes coincide with STIR’s axes when the detector is at 0° . The collimator uses a right-handed coordinate system as indicated by the y' axis, which points toward the detector. Further information is given in the text and STIR’s documentation.

Enabling DOI correction subdivides the scintillation crystal using Bresenham’s line algorithm [150] to calculate the crystal attenuation and DOI along the LOR. If DOI correction is disabled, half the crystal thickness is added to the detector radius. When attenuation correction is enabled, a simple correction can be applied where the same attenuation factor is applied for the whole PSF, or a full correction can be applied where different attenuation factors are applied for each bin of the PSF [145]. Further improvements to speed and memory can be made with image masking using the default cylinder, an attenuation map, or a mask file. The default cylinder is based on the object radius in the image volume. It is essential to set the object radius greater than or equal to the size of the object in the attenuation map or mask file when masking, as the matrix weights are calculated according to this value. Failure to do so will result in an error. The projection matrix can be kept in memory or calculated per projection angle. In the latter case, the memory is released before starting calculations on a new angle, reducing memory requirements but increasing computation time for iterative reconstruction algorithms.

4.5 Materials and Methods

To test the pinhole-SPECT implementation in STIR, the Spark silicon photomultiplier (SiPM)-based preclinical SPECT system was used with a single-pinhole

(SPH) collimator (Cubresa Inc., Winnipeg, Canada). Previous work characterized the system with the National Electrical Manufacturers Association (NEMA) NU 1-2018 Standards for Performance Measurements of Gamma Cameras, and a corresponding Geant4 Application for Tomographic Emission (GATE) Monte Carlo model was validated [107]. Excellent agreement was found between measurement and simulation with differences on the order of a few percent, supporting the accuracy and detailed analysis of simulated data in this study.

The Spark has a fixed rotation range of 270° from a starting angle of 180° . Angular increments of 3° were used for data acquisition based on NEMA's specification [124]. GATE simulation results [113] were output to Rapid Object-Oriented Technology (ROOT) format [131] and converted to Cubresa's list mode format. Projection data with 0.5 mm bins were generated from measured and simulated list mode data using a 30%-wide energy window centered on the photopeak. Projection images were then converted from Cubresa's format to Interfile format for use with STIR. Parameter files were configured as necessary with a full attenuation correction model, a PSF subsampling factor of 1, a maximum number of PSF standard deviations of 2, and a spatial resolution of 0.1 mm when sampling distributions in PSF or DOI corrections. Unless explicitly stated, images were reconstructed in the entire FOV using an object radius of $r = 23.0$ mm.

Simulations and image reconstructions were performed on an HP Z820 workstation operating Ubuntu 18.04.5 LTS with two Intel Xeon E5-2630 2.3 GHz hexa-core CPUs and 64 GB of 1600 MHz DDR3 memory. The SPH-SPECT data for quantitative image assessment were simulated with GATE v9.0, while qualitative image assessment used *in vivo* data. Tomographic images were reconstructed with STIR v5.1.0 on a single CPU core as the `PinholeSPECTUB` projector class has not yet been configured to use the OpenMP nor Message Passing Interface capabilities of STIR, which would allow it to perform several computations in parallel. Note that pre-corrected projection data are expected as input into the projection matrix. Therefore, measured data were corrected with energy, linearity, and uniformity calibrations, while simulated data required no calibration.

4.5.1 Quantitative Assessment of Reconstructed Data

4.5.1.1 Phantom Simulations and Data Generation

Phantom data were simulated with three different subjects containing technetium-99m ($^{99\text{m}}\text{Tc}$): a NEMA Micro-PET IQ phantom, a mouse-sized NEMA triple line source scatter phantom, and a volumetric cylinder. The IQ phantom (outer diameter $\varnothing_{\text{OD}} = 33.5$ mm, length $L = 63.0$ mm) was made from polymethyl methacrylate containing three different sections: a spillover section with water and air, a uniform section (inner diameter $\varnothing_{\text{ID}} = 30.0$ mm, $L = 15.0$ mm), and a section with five hot rods ($\varnothing_{\text{ID}} = \{1, 2, 3, 4, 5\}$ mm, $L = 20.0$ mm). The triple line source scatter phantom ($\varnothing_{\text{OD}} = 25.4$ mm, $L = 60.0$ mm) was made from acrylic to house three precision glass capillary tubes ($\varnothing_{\text{OD}} = 0.8$ mm, $\varnothing_{\text{ID}} = 0.4$ mm) with one located at the center and two with a 10.0 mm radial offset separated by 90° . The volumetric cylinder ($\varnothing_{\text{OD}} = 28.0$ mm, $L = 55.0$ mm) was made from acrylic with a uniform section of radioactivity ($\varnothing_{\text{ID}} = 26.0$ mm, $L = 21.0$ mm). Attenuation maps were produced with GATE to delineate regions of interest (ROIs) and correct for attenuation in the triple line source phantom and volumetric cylinder.

Table 4.1 summarizes the simulated phantom acquisitions, projection and reconstruction matrices, reconstruction algorithms, and applied analyses which are further described in the proceeding subsections. Iterative reconstruction algorithms and matrix corrections were used to assess figures of merit in terms of computation cost, contrast-to-noise ratio (CNR), resolution, uniformity, and variability.

Table 4.1: Summary of simulated ^{99m}Tc phantom acquisitions and reconstructions.

Subject	Activity	Acquisition	Projections	Projection matrix	Reconstruction matrix	Algorithm ¹	Analysis ²
IQ phantom	50 MBq	Forward proj	120 (8 subsets)	90×90 px, 1.0 mm	120×92×92 vx, 0.5 mm	OSEM	Computation cost
IQ phantom	50 MBq	3600 s	91 (7 subsets)	208×208 px, 0.5 mm	230×184×184 vx, 0.25 mm	OSEM, OS-OSL-MRP, OS-SPS-QP	Hot rod CNR
Line source	30 MBq	5460 s	91 (7 subsets)	208×208 px, 0.5 mm	230×184×184 vx, 0.25 mm	OSEM	Resolution
Cylinder	20 MBq	910 s	91 (7 subsets)	208×208 px, 0.5 mm	230×184×184 vx, 0.25 mm	OSEM	Uniformity & CV

¹ OSEM: ordered subsets expectation maximization, OS-OSL-MRP: ordered subsets one step late with median root prior (penalization factor, PF = 1.0), OS-SPS-QP: ordered subsets separable paraboloidal surrogate with quadratic prior (PF = 0.3)

² CNR: contrast-to-noise ratio, CV: coefficient of variation

4.5.1.2 Computation Cost with Different Matrix Corrections

To compare computation costs for different types of matrix corrections, a forward projection of the IQ phantom was made with 120 views over 360° using a reduced matrix size (see Table 4.1). Images with different matrix configurations were reconstructed with the ordered subsets expectation maximization (OSEM) algorithm [101] using eight subsets and 40 subiterations. Matrices were configured for no corrections (N-C), attenuation correction (ATT-C), DOI correction (DOI-C), PSF correction (PSF-C), all corrections (PSFATTDI-C), and all corrections with masking (PSFATTDI-M-C) using the default cylindrical mask ($r = 17.0$ mm). Maximum RAM and CPU time were recorded with Ubuntu's `/usr/bin/time -v` command when calling STIR's `OSMAPOS` program from the command line. Memory and CPU time requirements were compared between storing the matrix in memory and calculating it per projection angle.

4.5.1.3 Contrast-to-Noise Ratios in the IQ Phantom

Sample sinograms of the IQ phantom hot rods are shown in Fig. 4.2 from the GATE simulation and the STIR forward projection, including attenuation, DOI, and PSF effects. Despite the relatively low count statistics associated with the SPH-SPECT simulation, the visual agreement between these sinograms supports that the implementation of the `PinholeSPECTUB` projector matrix in STIR is suitable for pinhole-SPECT datasets.

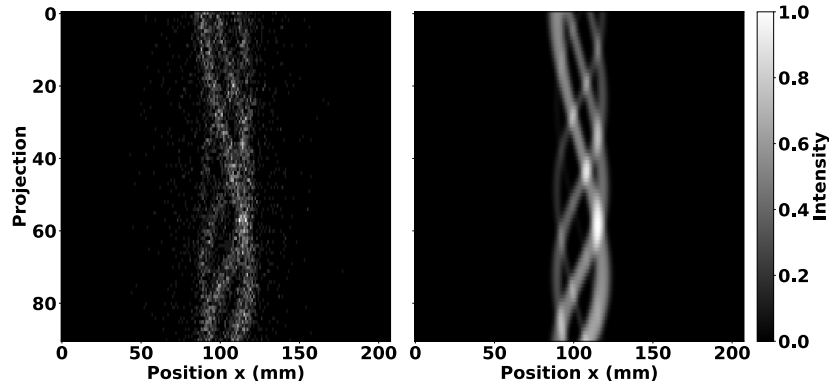


Figure 4.2: Projection of the IQ phantom hot rod region displayed in a 2D sinogram arrangement showing the GATE simulated data (left) and the STIR forward projection of the radioactive source distribution adding attenuation, DOI, and PSF degradation (right). Sinograms were normalized by the maximum pixel count. The sinograms show good agreement despite the relatively low count statistics associated with the SPH-SPECT simulation.

To compare different reconstruction algorithms, the CNR for each hot rod i in the IQ phantom was assessed using

$$\text{CNR}_i = \frac{|I_i - I_r|/(I_i + I_r)}{\sigma/\mu}. \quad (4.1)$$

Here, I_i is the mean intensity of the i^{th} hot rod delineated by the attenuation map, I_r is the mean intensity of the reference ROI central to the hot rods ($\varnothing = 5.4$ mm, $L = 15.0$ mm), and σ and μ are the standard deviation and mean intensity, respectively, in an ROI central to the uniform volume ($\varnothing = 18.0$ mm, $L = 11.25$ mm). To elaborate, the cylindrical ROIs covered 60% of the active diameter and 75% of the active length based on NEMA's methodology, except for hot rod ROIs, which used the entire diameter and length in analysis. Note that the coefficient of variation (CV) is expressed in the denominator of Eq. 4.1:

$$\text{CV} = \frac{\sigma}{\mu}. \quad (4.2)$$

The reconstruction algorithms chosen for CNR comparisons were OSEM, ordered subsets one step late with median root prior (OS-OSL-MRP) using a penalization factor of $\text{PF} = 1.0$ [151], and ordered subsets separable paraboloidal surrogate with quadratic prior (OS-SPS-QP) using $\text{PF} = 0.3$ and relaxation parameters of $\alpha = 1.0$ and $\gamma = 0.1$ [152]. The OS-SPS-QP algorithm was initialized with the OSEM image after 21 subiterations. Hot rod CNR was calculated for each algorithm and plotted over the number of subiterations.

4.5.1.4 Resolution in the Scatter Phantom

To compare resolution with different types of corrections available in the PinholeSPECTUB projector, the triple line source scatter phantom was reconstructed with the OSEM algorithm in the following configurations: N-C, ATT-C, DOI-C, PSF-C, and PSFATTDUI-C. The in-plane resolution was calculated according to NEMA's methodology from the average full width at half maximum (FWHM) in x and y directions in three 3.5 mm-thick transverse slices: one at the center and two at ± 14.5 mm. The average of all x and y FWHM results was calculated for each matrix configuration and plotted over the number of subiterations.

4.5.1.5 Uniformity and Variability in the Volumetric Cylinder

To compare uniformity and variability with different types of corrections available in the PinholeSPECTUB projector, the volumetric cylinder was reconstructed with the OSEM algorithm in the following configurations: N-C, ATT-C, DOI-C, PSF-C, and PSFATDOI-C. Variability was assessed from the coefficient of variation using Eq. 4.2, and uniformity U was calculated as

$$U = \frac{I_{\max} - I_{\min}}{I_{\max} + I_{\min}} \quad (4.3)$$

where I_{\max} and I_{\min} refer to the maximum and minimum intensities in the ROI central to the uniform volume ($\varnothing = 15.6$ mm, $L = 15.75$ mm). Smaller values of uniformity and variability correspond to better image quality. The uniformity and variability results were separately plotted over the number of subiterations for each matrix configuration.

4.5.2 Qualitative Assessment of Reconstructed *In Vivo* Data

A previously acquired *in vivo* dataset was chosen to demonstrate qualitative image results from an investigation of novel radiotracers for Alzheimer’s disease diagnosis [58, 153]. As summarized in Table 4.2 and [123], a B6SJLF1/J mouse was administered an intravenous tail-vein injection with a 28 MBq iodine-123 (^{123}I)-labelled cholinesterase agent. The SPH-SPECT acquisition commenced 2 h post-injection, and acquired data were reconstructed with the maximum likelihood expectation maximization (MLEM) algorithm in nine iterations [100]. A subsequent micro computed tomography (μCT) scan was acquired with a Triumph LabPET4/CT (TriFoil Imaging, California, United States) using an X-ray tube potential of 70 kVp and exposure of 17.8 mAs over 512 projections. The μCT image was reconstructed with filtered back projection (FBP) and a ramp filter in a $512 \times 512 \times 512$ matrix having 0.1 mm isotropic voxels. The fused SPECT/CT image was visually inspected for uptake in different organs and any notable features.

Table 4.2: Summary of *in vivo* ^{123}I acquisition and reconstruction.

Subject	Activity	Acquisition	Projections	Projection matrix	Reconstruction matrix	Algorithm	Analysis
<i>In vivo</i> mouse	28 MBq	3600 s	91 (1 subset)	208×208 px, 0.5 mm	230×184×184 vx, 0.25 mm	MLEM	Qualitative review

4.6 Results

4.6.1 Quantitative Assessment of Reconstructed Data

Axial sums of OSEM reconstructed images from phantom simulations are shown without matrix corrections in Fig. 4.3. These images illustrate the radioactive ^{99m}Tc source distributions analyzed in the preceding subsections. Furthermore, they demonstrate appreciable image quality characteristics with source distributions true to their physical geometry.

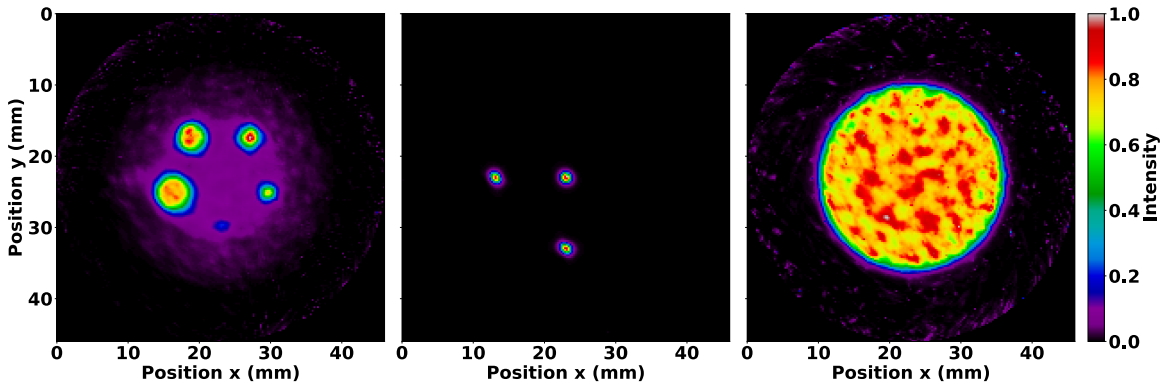


Figure 4.3: Normalized axial sum of OSEM images after 35 subiterations with seven subsets and no matrix corrections. Images are shown for the IQ phantom hot rods (left), mouse-sized NEMA line source phantom (middle), and volumetric cylinder (right). The IQ phantom image was summed over the length of the hot rods, whereas the other images were summed over the entire length of the reconstructed image. Note the expected distributions of ^{99m}Tc .

4.6.1.1 Computation Cost with Different Matrix Corrections

Table 4.3 summarizes the time and memory requirements for OSEM reconstruction of SPH-SPECT data with different matrix corrections while keeping the matrix in memory or (re)calculating it for every projection angle. As expected, storing the matrix in memory required more memory but less CPU time than calculating it per projection angle. Comparing calculations where matrix corrections were applied independently, PSF correction required the greatest memory and the least computation time. In contrast, attenuation correction required no additional memory and DOI correction required the greatest computation time. The combined usage of DOI and PSF corrections required even greater memory and time due to PSF correction applied at different depths in the crystal, while the inclusion of attenuation modelling further increased CPU time.

Table 4.3: Computation cost in SPH-SPECT OSEM reconstruction with 120 projections, eight subsets, and 40 subiterations.

Correction type ¹	Matrix in memory		Matrix per projection	
	Max RAM (MB)	CPU time (s)	Max RAM (MB)	CPU time (s)
N-C	8,344	114	175	310
ATT-C	8,353	414	184	2,154
DOI-C	14,624	1,236	228	6,610
PSF-C	22,388	265	304	783
PSFATTDROI-C	31,689	2,677	380	16,421
PSFATTDROI-C	18,368	1,495	267	8,211

¹ N-C: no corrections, ATT-C: attenuation correction, DOI-C: DOI correction, PSF-C: PSF correction, PSFATTDROI-C: all corrections, and PSFATTDROI-C: all corrections with masking using the default cylindrical mask ($r = 17.0$ mm).

4.6.1.2 Contrast-to-Noise Ratios in the IQ Phantom

Image quality was assessed from hot rod CNR in the IQ phantom for different reconstruction algorithms available in STIR, including OSEM, OS-OSL-MRP, and OS-SPS-QP. Fig. 4.4 presents the performance of these algorithms based on plots of hot rod CNR over 200 subiterations. In OSEM reconstruction, the CNR reached a maximum following one complete iteration and then continually decreased with increasing subiterations due to an amplification of the variability in the uniform ROI. In OS-OSL-MRP and OS-SPS-QP reconstructions, the CNR converged to a stable value while preserving spatial detail. However, OS-OSL-MRP reached a maximum CNR following one complete iteration and then decreased toward a stable value with increasing subiterations, and OS-SPS-QP converged toward a maximum and stable value with increasing subiterations. The increase in CNR for the OS-SPS-QP algorithm can be attributed to its effectiveness in noise reduction, particularly in the uniform ROI.

4.6.1.3 Resolution in the Scatter Phantom

Fig. 4.5 shows a plot of the average in-plane resolution of precision line sources in the mouse-sized NEMA triple line source scatter phantom reconstructed with the OSEM algorithm. In all cases, the resolution improved as the number of subiterations increases. When comparing resolution with and without matrix corrections by averaging the FWHM across all 200 subiterations, it can be seen that attenuation correction resulted in a negligible 0.4% improvement to resolution due to its present

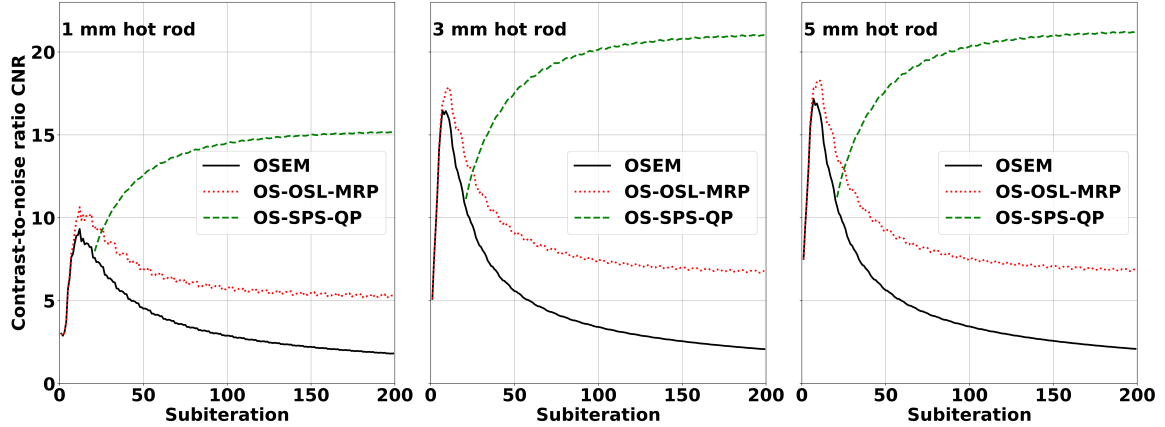


Figure 4.4: SPECT IQ phantom hot rod CNR plots for the 1 mm (left), 3 mm (middle), and 5 mm (right) hot rods. Images were reconstructed using OSEM (solid line), OS-OSL with median root prior (dotted line), and OS-SPS with quadratic prior (dashed line). All images were reconstructed with seven subsets and no matrix corrections, and the OS-SPS-QP reconstruction was initialized with the OSEM image after 21 subiterations. Hot rod contrast was calculated relative to the central inter-rod region void of ^{99m}Tc , and CV was calculated in the uniform ^{99m}Tc region. The OS-SPS-QP algorithm preserved spatial detail and effectively reduced noise while converging to a stable value.

application in a preclinical setting where attenuation effects were minimal. DOI correction provided a 4% improvement in resolution, and PSF correction provided a 16% improvement in resolution. Combining matrix corrections yielded the greatest 19% improvement in resolution.

4.6.1.4 Uniformity and Variability in the Volumetric Cylinder

Fig. 4.6 presents uniformity and variability plots in the volumetric cylinder reconstructed with the OSEM algorithm. As expected, uniformity and variability worsened with increasing subiterations in OSEM reconstruction. PSF correction improved uniformity and variability amongst all independently applied matrix corrections, and attenuation correction provided no appreciable change in this preclinical application. DOI correction degraded uniformity and variability as illustrated in Fig. 4.7 due to a bug affecting voxels within a small angle from the pinhole axis. This was reflected by a uniformity value that quickly reached 100% within five complete OSEM iterations, and a CV with the largest slope and intercept compared to all other matrix calculations.

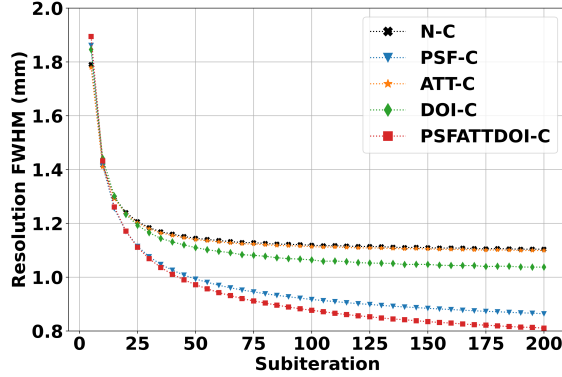


Figure 4.5: SPECT spatial resolution with scatter in the mouse-sized NEMA triple line source scatter phantom. Images were reconstructed using the OSEM algorithm with seven subsets and various matrix corrections. Resolution was calculated from the average x and y FWHM in three 3.5 mm-thick transverse slices. As expected, resolution improved with increasing subiterations in OSEM reconstruction. PSF correction provided the greatest resolution improvement compared to other independently applied matrix corrections.

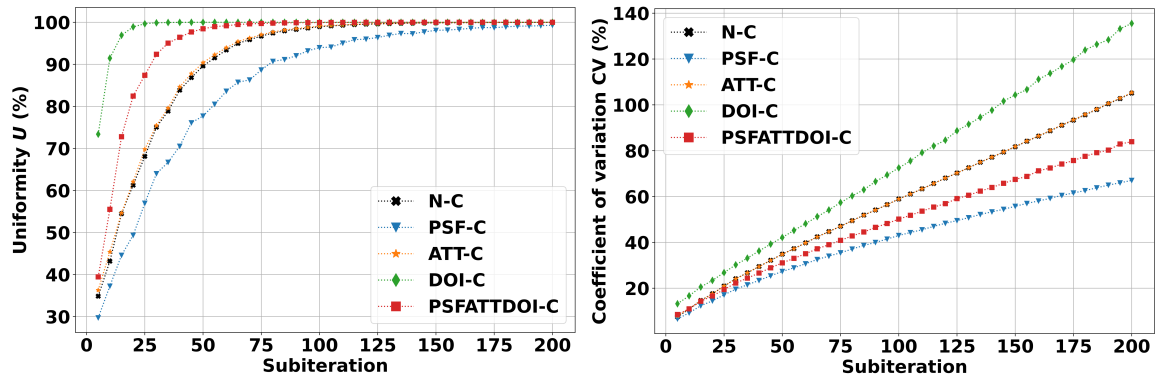


Figure 4.6: SPECT uniformity (left) and variability (right) in the volumetric cylinder. Images were reconstructed using the OSEM algorithm with seven subsets and various matrix corrections. As expected, uniformity and variability increased with increasing subiterations in OSEM reconstruction. PSF correction improved uniformity and variability, while DOI correction degraded image quality due to a bug affecting voxels within a small angle from the pinhole axis.

4.6.2 Qualitative Assessment of Reconstructed *In Vivo* Data

A fused SPECT/CT image of the *in vivo* mouse acquisition is shown in Fig. 4.8 where the reconstructed radiotracer distribution was clearly localized within the bounds of the body and other organs. For example, the novel ^{123}I -labelled tracer under investigation was observed in the olfactory bulb, eyes, salivary glands, and heart, with limited uptake in the brain. The conic bounds of the fully sampled FOV can

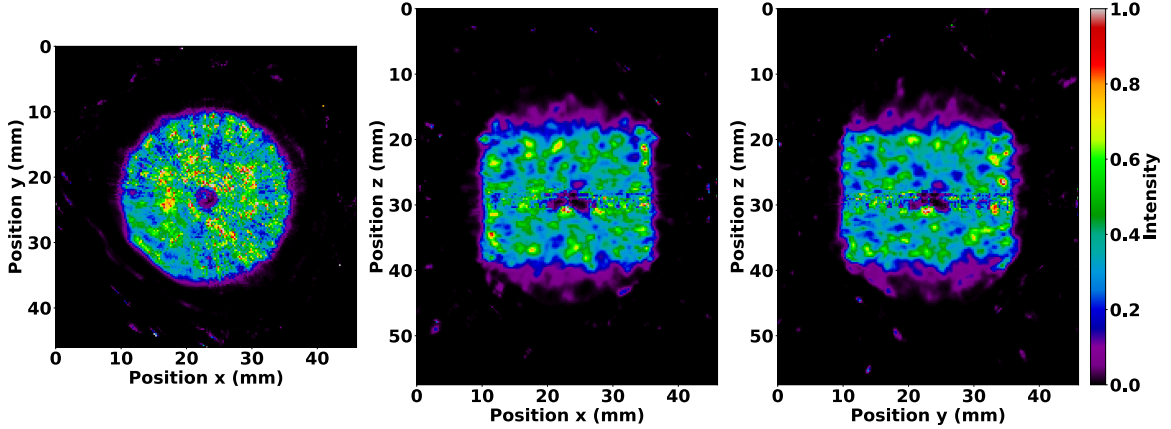


Figure 4.7: Slices of the volumetric cylinder after 35 subiterations of the OSEM algorithm with DOI correction enabled. Image values were thresholded between 0 and 1. The effects from the software bug are visible in the central transverse (left), coronal (middle), and sagittal (right) planes. The bug affects voxels within a small angle from the pinhole axis, as seen along the pinhole trajectory in a 270° counter-clockwise acquisition starting at 180° . The transverse view shows the formation of a multi-armed cross or ‘star shot’ artifact, and all views show the compounding effect at the isocenter due to the intersection of LORs affected by the bug.

also be seen in the fused SPECT/CT image, particularly in the posterior direction, where the majority of γ -rays originated from in this acquisition. Counts detected outside the fully sampled FOV are reconstructed with increased uncertainty, but images retain reliable localization despite the extended distribution of radioactivity. Lastly, low-intensity background noise can be observed throughout the tomographic image. Overall, these results demonstrate that the PinholeSPECTUB projector is suitable for *in vivo* data, and tomographic images can be interpreted and analyzed for further conclusions.

4.7 Discussion

The purpose of this study was to demonstrate and test the integration of a pinhole-SPECT library in STIR using simulated and measured data. The aim was not to optimize reconstruction parameters for the gamma camera used in this study. Altogether, the SPH-SPECT images reconstructed with STIR showed appreciable image quality with radioactive source distributions true to their physical geometry. As discussed in the previous SPECTUB publication, reconstruction requires tuning of (sub)iterations for OSEM and MLEM algorithms or penalization factors for OS-OSL-MRP and OS-SPS-QP algorithms based on the object size, activity, and background [128]. In the

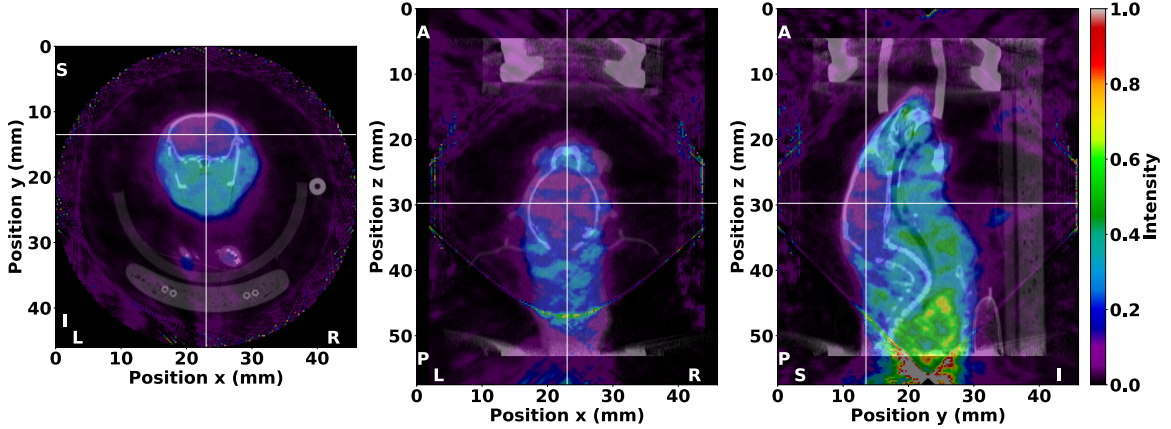


Figure 4.8: Fused SPECT/CT image of the *in vivo* mouse from the investigation of a potential ^{123}I -labelled radiotracer for Alzheimer’s disease diagnosis. SPECT image values were thresholded between 0 and 1. The ^{123}I distribution was clearly localized within the bounds of the body and various organs as illustrated in the transverse (left), coronal (middle), and sagittal (right) planes. Crosshairs are centered in the brain to denote the illustrated planes. The anatomical orientation is also shown with markers where L = left, R = right, A = anterior, P = posterior, S = superior, and I = inferior. The SPECT image was reconstructed with MLEM in nine iterations and no matrix corrections, and the μCT image was reconstructed with FBP and a ramp filter.

present study, PSF correction improved image quality as seen in resolution, uniformity, and variability figures of merit. Although the inclusion of attenuation modelling improves system matrix accuracy, its present application in a preclinical setting shows minimal effects. In general, further improvements to image quality could be achieved with application-specific post-reconstruction image filtering [154].

Apart from the photon energy dependence in attenuation correction, PSF and DOI corrections include energy-specific factors for intrinsic resolution and crystal attenuation, respectively, to improve system matrix accuracy. When DOI correction is disabled, interactions in the scintillator are assumed to occur at half the crystal depth. An energy-dependent modification could apply a corresponding mean or median depth of interaction. This would affect reconstruction quality, and relatively small pinhole acceptance angles and degrees of parallax would be most accurate in the uncorrected case, while DOI correction would be required otherwise.

Unfortunately, DOI correction degrades image quality due to a software bug affecting small angles from the pinhole axis. This results in a loss of counts where pinhole axes intersect rather than a distortion of the reconstructed radioactivity dis-

tribution, as illustrated in Fig. 4.7. In our results, this caused a significant separation between maximum and minimum intensity values and resulted in uniformity quickly approaching 100%. When calculating CV, this caused an increased standard deviation and reduced mean, corresponding to greater variability in the cylindrical volume. However, the resolution calculated with DOI correction and reported in Fig. 4.5 was negligibly affected since the resolution was reported as the average of all x and y FWHM, and the axial line source was only affected in a fraction of the 3.5 mm-thick slice at the isocenter. More specifically, the mean relative standard error from all subiterations calculated with Eq. 4.2 was 9% for DOI-corrected matrices and 8% otherwise, which shows consistent resolution with minor variations throughout the tomographic FOV. Future work aims to correct the DOI bug.

Computational costs were comparable to STIR’s parallel- and converging-hole SPECTUB projector class. Matrices were chosen to be similar in size to those in the previous SPECTUB publication in [128] where projection and reconstruction matrix sizes were 1.1% and 3.2% larger, respectively. When storing the pinhole-SPECT matrix in memory, computations required up to $3\times$ more RAM and $4.7\times$ more CPU time than the parallel-hole SPECT case, except for PSF correction which required $1.7\times$ less RAM and $1.2\times$ less CPU time. When calculating the matrix per projection, memory requirements were nearly identical and computations took up to $6\times$ longer using the `PinholeSPECTUB` projector, except for PSF correction which required $1.3\times$ less RAM and $1.1\times$ less CPU time. The general increase in computation cost can be attributed to pinhole-SPECT LORs that intersect more voxels at non-orthogonal angles than a parallel-hole collimator, and the differences in PSF correction can be attributed to the correction applied in detector space for the `PinholeSPECTUB` projector versus object space for the `SPECTUB` projector.

The integrated software is included in STIR release 5.1.0. Further extensions could expand the software to support non-circular orbits, improve energy dependence, model keel-edge or lofthole pinholes, enable parallel computing, and correct knife-edge penetration. In addition, camera designs can be readily explored with the `PinholeSPECTUB` projector for single- and multi-pinhole collimators in terms of magnification, detector coverage, multiplexing, and pinhole geometry for optimal FOV, sensitivity, and detection efficiency without degrading spatial resolution [48]. The Synergistic Image Reconstruction Framework (SIRF) [14] has also been extended to use these new STIR capabilities, allowing the use of SIRF’s advanced optimization algorithms. Additional possibilities with the software include scatter correction,

motion-compensated image reconstruction, synergistic image reconstruction, dynamic imaging, and multi-tracer protocols. Ongoing work aims to utilize the pinhole-SPECT SIRF extension for multi-tracer protocols. The method under development requires multiple energy-dependent system matrices to simultaneously reconstruct distributions from a multi-radionuclide SPECT acquisition. However, this is currently not possible with STIR's SPECT projectors, as the weight matrix is defined as a global variable that only allows for one unique matrix during reconstruction. Therefore, the next steps will replace any global variables with local ones.

4.8 Conclusion

Pinhole-SPECT is becoming increasingly important in clinical and preclinical investigations of molecular imaging agents. We have demonstrated the pinhole-SPECT modelling tool capabilities in the open-source STIR package. Tomographic image quality was evaluated qualitatively and quantitatively using several figures of merit and iterative reconstruction algorithms with and without system matrix corrections. Our results showed measurable and indicative image quality suitable for *in vivo* applications. This shows that STIR can be configured for complex pinhole-SPECT scanner geometries and used with many reconstruction algorithms.

Chapter 5

Spectral Unmixing of Multi-Radionuclide SPECT Acquisitions using the Open-Source SIRF and CIL Frameworks

5.1 Prologue

The final thesis objective was to develop a novel and robust crosstalk correction method for multi-radionuclide single-photon emission computed tomography (SPECT) that would provide superior quantitative accuracy and image quality compared to conventional methods, namely the triple energy window (TEW) method. The novel method is independent of energy and spatial resolution, which is a key factor in overcoming the TEW method's shortcomings. It demonstrates superior consistency and accuracy in activity quantification and image quality with a variety of radionuclide combinations. Furthermore, it requires no pre-corrections to input data while utilizing advanced image reconstruction software to exploit the synergy between radionuclide distributions during their simultaneous reconstruction. Its open-source construction allows for express implementation with existing preclinical and clinical SPECT systems using a variety of collimators modelled in the Software for Tomographic Image Reconstruction (STIR). This offers considerable opportunities for enhancing our comprehension of underlying pathophysiology while fostering the practice of precision medicine through novel imaging techniques and therapies.

Previously, STIR's SPECT projectors were limited to one instance of the system matrix due to the use of global variables in the source code [126]. Ongoing improvements have replaced the global variables with class members to enable multiple instances of the system matrix. Building upon this, the extension of the pinhole-SPECT library from STIR to the Synergistic Image Reconstruction Framework (SIRF) established the framework for the spectral unmixing method presented here. This work was conducted in collaboration with researchers at University College London (UCL). Professor Kris Thielemans proposed the mixing matrix, and Sam Porter extended multichannel SPECT reconstruction software to allow for synergistic reconstruction of multiple images from hyperspectral data. Its implementation is tested here with the Spark preclinical SPECT scanner, and a publication is pending submission.

5.2 Abstract

Background: Crosstalk is the primary challenge in multi-radionuclide single-photon emission computed tomography (SPECT) where γ -rays from one radionuclide become incorrectly attributed to the competing radionuclide(s). The triple energy window (TEW) method is widely accepted for crosstalk correction, however, its effectiveness is closely tied to the gamma camera’s energy resolution and statistical counts on a pixel-by-pixel basis. Furthermore, methods that pre-correct data by subtracting the crosstalk component, including the TEW method, risk compromising the Poisson distribution of detected events. This directly impacts the accuracy and quality of images reconstructed with statistical algorithms. This work overcomes those challenges by introducing a novel spectral unmixing crosstalk correction technique using the open-source Synergistic Image Reconstruction Framework (SIRF) and Core Imaging Library (CIL), in which a mixing matrix aids in optimizing detected events across multiple radionuclide distributions during their synergistic reconstruction.

Methods: Multi-radionuclide SPECT data were acquired with $^{99m}\text{Tc}/^{123}\text{I}$ in measurement and simulation, and $^{99m}\text{Tc}/^{111}\text{In}$ in simulation, using the Cubresa Spark silicon photomultiplier (SiPM)-based preclinical SPECT scanner. Mixing matrix values were determined from the gamma camera’s sensitivity to each radionuclide. A mouse phantom was assembled with line sources containing 4 MBq mixtures of $\{0,1,2,3,4\}$ MBq of ^{99m}Tc and $\{4,3,2,1,0\}$ MBq of ^{123}I or ^{111}In . Images were reconstructed with varying degrees of crosstalk correction using primary energy windows, the TEW method, spectral unmixing, and gold standard simulation data, and crosstalk correction performance was assessed from quantitative accuracy and image contrast using the root-mean-square error (RMSE), as well as from image noise.

Results: The quantitative accuracy for ^{99m}Tc and ^{123}I according to the mean RMSE in simulation was 0.44 using primary energy windows, and the TEW, spectral unmixing, and gold standard methods provided increasingly accurate quantification according to 51%, 83%, and 95% improvements in the RMSE, respectively. Measured results were in good agreement. The mean RMSE when quantifying ^{99m}Tc and ^{111}In activity was 0.15 using primary windows, and the TEW, spectral unmixing, and gold standard methods provided a 57%, 57%, and 84% improvement in quantitation, respectively. Similar trends were observed in the RMSE of contrast between radionuclides, with spectral unmixing showing superior contrast and the best overall crosstalk correction performance. Compared to primary energy windows, the TEW method yielded in-

creased image noise, while spectral unmixing yielded decreased image noise for ^{99m}Tc and increased image noise for ^{123}I and ^{111}In .

Conclusion: The spectral unmixing method shows excellent crosstalk correction performance in multi-radionuclide SPECT. Simultaneous acquisitions of $^{99m}\text{Tc}/^{123}\text{I}$ separate from $^{99m}\text{Tc}/^{111}\text{In}$ were explored in a preclinical application, and measured and simulated results demonstrated superior and consistent quantitative accuracy and image quality with spectral unmixing compared to conventional methods. Its implementation with SIRF and CIL allows for express configuration of any number of SPECT radionuclides, and can readily accept additional terms to increase model accuracy. The software can be configured for a variety of SPECT systems using pinhole, parallel-hole, and converging hole collimators, enabling its use in several preclinical and clinical settings.

5.3 Introduction

Multi-radionuclide single-photon emission computed tomography (SPECT) is becoming increasingly important in nuclear medicine investigations for radiopharmaceutical drug development and procedural advancement, as it provides enhanced functional and molecular information. The ability of SPECT scanners to discriminate between photons of different energies makes them well-suited for the simultaneous acquisition of multiple radiotracers, such as those previously explored in preclinical and clinical cardiac imaging [18–25], neuroimaging [26–33], lung function assessment [34, 35], and hyperparathyroidism [36–39]. The possibility of generating two or more functional images from a single acquisition can provide several benefits including, but not limited to, multi-functional diagnosis and/or treatment, reduced patient discomfort, reduced overall acquisition time, higher throughput of subjects and studies, perfect co-registration of nuclear medicine images, and improved patient outcomes [2]. Altogether, multi-radionuclide SPECT holds substantial untapped potential for enhancing our comprehension of underlying pathophysiology while facilitating the development of novel and personalized treatment strategies.

Crosstalk is the primary challenge in multi-radionuclide SPECT where γ -rays from one radionuclide become incorrectly attributed to the competing radionuclide(s), leading to a mixing of acquired signals. This transference can occur from downscattered photons from higher energies, or by direct photopeak overlap. The inclusion of crosstalk during tomographic image reconstruction can degrade image quality and

accuracy through false reconstruction of activity location and incorrect quantification of absolute activity. This can negatively impact the interpretation of nuclear medicine images and studies through calculations involving radiation exposure, standardized uptake values, and time-activity curves, for example.

In most corrective approaches, crosstalk is directly estimated and subtracted from the data before, during, or after reconstruction. When applied before or during reconstruction, subtractive methods risk compromising the Poisson distribution of data, which can directly impact the accuracy of statistical algorithms like maximum likelihood expectation maximization (MLEM) [100]. Furthermore, crosstalk corrections that interject during reconstruction are not always available to researchers when SPECT systems utilize proprietary scanner geometry and reconstruction algorithms protected by the manufacturer.

The conventional approach to SPECT image reconstruction uses a primary energy window centered on a photopeak to obtain projection images for input into a reconstruction algorithm. The primary window discriminates photons according to their energy to aid in radionuclide selection while suppressing events deemed as noise. Gamma cameras with superior energy resolution, such as those utilizing cadmium zinc telluride (CZT) or high-purity germanium (HPGe) technology, can more-readily discriminate between photon energies compared to typical scintillation detectors using cesium iodide (CsI) or sodium iodide (NaI) [8]. This makes them theoretically more suitable for multi-radionuclide SPECT [155]. In most cases, however, primary energy windows do not suffice to address crosstalk.

Numerous window-based methods have been developed for scatter correction and extended to crosstalk correction in multi-radionuclide SPECT using dual energy windows [69], triple energy windows (TEWs) [9], dual photopeak windows [75, 81], five energy windows [41], and spectral factor analysis [30]. In general, these methods discriminate photons by their energy, then subtract the crosstalk component prior to image reconstruction. They typically involve scalable or tunable parameters that are acquisition-specific, and the presence of an adjustable parameter yields a fragile method for crosstalk correction that is ineffective at blindly processing multi-radionuclide SPECT acquisitions ranging from simple to complex. Their performance can also differ greatly when considering the type of gamma camera being used and its inherent energy and spatial resolution.

Model-based corrections apply mathematical models during or after image recon-

struction to account for the behaviour of γ -rays and their interactions in the SPECT system. This accounts for crosstalk through modelling of the physical properties of the subject, radionuclides, collimators, and detectors. Such methods include an analytical photon distribution calculated with the Klein-Nishina (K-N) formula [39, 82], dual system matrices using unmatched forward and backprojectors [83], convolution kernel subtraction [86–88], and Monte Carlo techniques such as the effective source scatter estimate (ESSE) method [31]. Model-based corrections are generally more accurate, but have seen limited clinical adoption due to their complexity and computational demands [156].

In closer relation to the approach introduced in this work, Chang et al. [72] and later Yang et al. [73] explored the use of spectral unmixing with independent component analysis (ICA) using several energy windows. Their formalisms solved for mixing matrix values that equated the acquired energy spectrum to a weighted linear combination of independent components associated with technetium-99m ($^{99\text{m}}\text{Tc}$) and iodine-123 (^{123}I). Both groups reported that images could be well-separated, for which Chang et al. used 26 energy windows and Yang et al. used seven energy windows. Xu et al. also formulated an unmixing strategy based on the makeup of signals in each energy window [74]. Their work relied on the calculation of crosstalk contamination factors and detector efficiencies for iodine-125 (^{125}I) and indium-111 (^{111}In) to scale linear combinations of projection images.

The sheer number of correction methods demonstrate that crosstalk problems are not easily solved, nor have they been adequately solved. Ljungberg et al. [80] compared activity quantification of dual-energy, dual-photopeak, and TEW scatter correction in $^{99\text{m}}\text{Tc}$ brain perfusion imaging and found minimal differences, stating that “a user may select a correction method that is easy to implement on a particular system.” In a simultaneous $^{99\text{m}}\text{Tc}/^{123}\text{I}$ brain SPECT study by Du and Frey, the effects of crosstalk contamination reduced image contrast and overestimated absolute activity in all structures by up to 66% [32]. After applying the Monte Carlo-based ESSE approach, image contrast was improved and the errors in absolute activity quantitation were reduced to less than $\pm 5\%$. Farncombe et al. also explored the use of the ESSE method in comparison to perfect scatter rejection, TEW scatter estimation, and no correction for multi-energy SPECT using gallium-67 (^{67}Ga) [85]. They found both methods yielded significant improvements in quantitative accuracy compared to conventional primary energy windows, although the ESSE and TEW results were not significantly different. While past efforts indicate that crosstalk

correction is beneficial for image contrast and quantitative accuracy, the methods in question leave room for improvement due to their widely varying performance, particularly in cases where photopeaks overlap in the energy spectrum.

This work introduces a novel spectral unmixing approach to crosstalk correction. It aims to be robust, generalized, and applicable to any multi-radionuclide SPECT acquisition using primary γ -ray emissions. Following acquisition, hyperspectral data is synergistically reconstructed by separating detected events into their respective images based on a mixing matrix with pre-calculated acquisition-independent weights. The novel application was built with the open-source Synergistic Image Reconstruction Framework (SIRF) [14] and Core Imaging Library (CIL) [102], which enable efficient implementation and validation of novel reconstruction algorithms. SIRF incorporates the Software for Tomographic Image Reconstruction (STIR) for nuclear medicine imaging, and CIL is interoperable with SIRF's data structures to provide a flexible and modular block framework supporting multichannel tomographic data, e.g., dynamic and spectral. Thus, SIRF and CIL together can readily reconstruct multi-radionuclide SPECT data using multiple channels, and this work exploits that feature by introducing a mixing matrix to separate detected events into their respective radionuclide distributions during synergistic reconstruction.

The primary objective of this study was to evaluate the efficacy of spectral unmixing crosstalk correction for multi-radionuclide SPECT. Its implementation was tested with the Cubresa Spark silicon photomultiplier (SiPM)-based preclinical SPECT scanner (Cubresa Inc., Winnipeg, Canada). Complex simultaneous multi-radionuclide SPECT acquisitions were measured and simulated with the Spark using a mouse phantom containing $^{99m}\text{Tc}/^{123}\text{I}$ —a notoriously challenging combination due to their comparable γ -ray energies—and $^{99m}\text{Tc}/^{111}\text{In}$. Tomographic images were reconstructed with varying degrees of crosstalk correction according to different algorithms, and crosstalk correction efficacy was assessed according to image quality metrics and quantitative accuracy.

5.4 Methods and Materials

The following section describes the hardware and software used to develop and test spectral unmixing crosstalk correction. The objective function for spectral unmixing is then defined, followed by the determination of global equation parameters. Lastly, a multi-radionuclide SPECT experiment is presented to test crosstalk correction efficacy

using metrics of image quality and accuracy. The experiment in measurement used $^{99m}\text{Tc}/^{123}\text{I}$, whereas simulations used $^{99m}\text{Tc}/^{123}\text{I}$ and $^{99m}\text{Tc}/^{111}\text{In}$ as ^{111}In could not be procured for this study due to logistical and technical reasons.

5.4.1 Description of Hardware and Software

To utilize the characteristic energy spectrum from each radionuclide during image reconstruction, acquired data were sampled over multiple channels with energy windows and incorporated into the reconstruction process. This was achieved using CIL’s flexible library for regularized reconstruction algorithms supporting multichannel tomographic data, in combination with SIRF’s support for nuclear medicine images. The recent extension of SIRF to utilize STIR’s SPECT libraries enables CIL to reconstruct complex multi-radionuclide SPECT datasets acquired with pinhole, parallel-hole, and converging-hole collimators [126, 128].

To test the spectral unmixing method, the Spark SiPM-based preclinical SPECT scanner was used with a single-pinhole collimator. Previous work characterized the system with the National Electrical Manufacturers Association (NEMA) NU 1-2018 Standards for Performance Measurements of Gamma Cameras, and a corresponding Geant4 Application for Tomographic Emission (GATE) Monte Carlo model was validated [107]. In tandem, STIR’s pinhole-SPECT library was successfully tested with the Spark [126]. Past studies showed excellent agreement between measurement and simulation with differences amounting to a few percent, and the pinhole-SPECT library was shown to provide measurable and indicative image quality, altogether supporting the accuracy and detailed analysis of data in the current study.

Computations were executed on an HP Z820 workstation operating Ubuntu 18.04.5 LTS with two Intel Xeon E5-2630 2.3 GHz hexa-core CPUs and 64 GB of 1600 MHz DDR3 memory. Single-pinhole SPECT data were simulated with GATE v9.0 distributed over 12 cores, and tomographic images were reconstructed with STIR v5.1.0, SIRF v3.4.0, and CIL v21.3.1. Tomographic images were reconstructed on a single CPU core, as STIR’s `PinholeSPECTUB` projector class has not yet been configured for parallel computations. Given that pre-corrected projection data are expected as input into the projection matrix, the SPECT system was calibrated for gain, linearity, center of rotation, and aperture-to-detector distance prior to measurement [129, 130], and measured data were corrected for uniformity prior to reconstruction. No corrections were applied to simulated data at any stage.

5.4.2 Objective Function Defined with the Core Imaging Library

In setting up the objective function for minimization, a data fidelity term allowed for the calculation of the difference between acquired data and forward-projected image estimates, and a regularization term penalized unlikely or undesirable solutions [102]. For acquired data following a Poisson distribution, the Kullback-Leibler (K–L) divergence was the most suitable choice for a data fidelity term. Denoted $\mathcal{D}(f, (\mathcal{A}u + \eta))$, the K–L divergence function can be calculated by summing over all lines-of-response (LORs) j using

$$\mathcal{D}(f, (\mathcal{A}u + \eta)) = \sum_j f_j \log \left(\frac{f_j}{(\mathcal{A}u + \eta)_j} \right) - f_j + (\mathcal{A}u + \eta)_j \quad (5.1)$$

where f is the acquired data, $\mathcal{A}u$ is the forward-projection of the reconstructed image u using an acquisition model \mathcal{A} , and η is a term for background noise such as scatter.

To extend the data fidelity term to handle the simultaneous reconstruction of N radionuclide distributions, a square mixing matrix \mathbf{M} was defined as

$$\mathbf{M} = \begin{bmatrix} m_{11} & \cdots & m_{1L} \\ \vdots & \ddots & \vdots \\ m_{K1} & \cdots & m_{KL} \end{bmatrix} \quad (5.2)$$

where K is the number of energy windows which must be non-overlapping, L is the total number of photopeaks in the acquisition, and m_{kl} denotes the probability of a photon from photopeak l being detected in energy window k . The mixing matrix weights can be calculated using

$$m_{kl} = \frac{\sum_j f_{k,j}}{\sum_j (\mathcal{A}_{ln} u_n)_j} \quad (5.3)$$

where \mathcal{A}_{ln} is the forward projection operator that maps the n^{th} radionuclide image to photopeak l . Eq. 5.3 yields a global calibration factor used in reconstruction that influences both the spectral unmixing process and the image values so that output images can be obtained in units of activity. This requires prior knowledge of an accurate image relating detected counts to radioactivity. For practicality, this work assigned gamma camera system sensitivities as mixing matrix weights, and reconstructed images were subsequently converted to units of radioactivity.

In order to target primary γ -ray emissions, the objective function \mathcal{L} for minimiza-

tion was constructed as

$$\mathcal{L} = \mathcal{D} \left(\mathbf{f}, \begin{bmatrix} m_{11}\mathcal{I} & \dots & m_{1L}\mathcal{I} \\ \vdots & \ddots & \vdots \\ m_{K1}\mathcal{I} & \dots & m_{KL}\mathcal{I} \end{bmatrix} \begin{bmatrix} \mathcal{A}_n & & \\ & \ddots & \\ & & \mathcal{A}_N \end{bmatrix} \mathbf{u} + \boldsymbol{\eta} \right) + \mathcal{R}(\mathbf{u}) \quad (5.4)$$

where \mathcal{I} is the identity operator and $\mathcal{R}(\mathbf{u})$ is the regularization term. A block diagonal matrix defines the acquisition model with column vectors of system matrices accounting for the photopeaks associated with each radionuclide, i.e., $\mathcal{A}_n = [\mathcal{A}_{1n}, \dots, \mathcal{A}_{ln}]^\top$. Variables shown in bold indicate vectors of projection data $\mathbf{f} = [f_1, \dots, f_K]^\top$, discrete image estimates of radionuclide distributions $\mathbf{u} = [u_1, \dots, u_N]^\top$, and noise estimates $\boldsymbol{\eta} = [\eta_1, \dots, \eta_K]^\top$. As defined in CIL, the objective function includes a `BlockFunction` containing K data fidelity K–L divergence terms, a `BlockOperator` containing $K \times L$ scaled identity operators, a `BlockOperator` containing the $L \times N$ projection operators defined here with SIRF’s `PinholeSPECTUBMatrix` acquisition model, a `BlockDataContainer` with N current image estimates, and `BlockDataContainers` with K projection images and noise estimates, plus a prior term (if necessary).

To incorporate prior information, CIL offers a number of regularization methods. Total variation (TV) penalizes large differences between neighbouring pixels in an image, which acts as a noise-reducing and edge-preserving regularizer [157]. This work applied joint TV to encourage smoothness and similarity among reconstructed images [158]. It was calculated using

$$\mathcal{R}(\mathbf{u}) = \beta \sqrt{\sum_n \alpha_n (\nabla u_n)^\top (\nabla u_n) + \epsilon^2} \quad (5.5)$$

where β is a hyperparameter that controls the tradeoff between fitting the data fidelity and imposing the regularization constraint, α_n are hyperparameters that control the tradeoff between penalties imposed on each reconstructed image such that $\sum_n \alpha_n = 1$, ∇ is the finite (forward) difference operator, and ϵ refers to a small positive constant added to ensure differentiability. The above equation assigns complementing weights to the coupled terms, while an uncoupled TV could enforce different and independent penalties on each image estimate. This work assigned $\beta = 1$, $\alpha = 1/N$, and $\epsilon = 0.001$, which may require tuning for optimal results.

In the simplest case of a dual-radionuclide acquisition where each emits one pri-

mary γ -ray, such as $^{99m}\text{Tc}/^{123}\text{I}$, the objective function can be expressed as

$$\mathcal{L} = \mathcal{D} \left(\begin{Bmatrix} f_1 \\ f_2 \end{Bmatrix}, \begin{bmatrix} m_{11}\mathcal{I} & m_{12}\mathcal{I} \\ m_{21}\mathcal{I} & m_{22}\mathcal{I} \end{bmatrix} \begin{bmatrix} \mathcal{A}_{11} & \mathbf{0} \\ \mathbf{0} & \mathcal{A}_{22} \end{bmatrix} \begin{Bmatrix} u_1 \\ u_2 \end{Bmatrix} + \begin{Bmatrix} \eta_1(u_1, u_2) \\ \eta_2(u_1, u_2) \end{Bmatrix} \right) + \mathcal{R}(u_1, u_2) \quad (5.6)$$

Similarly, when one radionuclide has one primary emission and the other has two, such as $^{99m}\text{Tc}/^{111}\text{In}$, the objective function can be expressed as

$$\mathcal{L} = \mathcal{D} \left(\begin{Bmatrix} f_1 \\ f_2 \\ f_3 \end{Bmatrix}, \begin{bmatrix} m_{11}\mathcal{I} & m_{12}\mathcal{I} & m_{13}\mathcal{I} \\ m_{21}\mathcal{I} & m_{22}\mathcal{I} & m_{23}\mathcal{I} \\ m_{31}\mathcal{I} & m_{32}\mathcal{I} & m_{33}\mathcal{I} \end{bmatrix} \begin{bmatrix} \mathcal{A}_{11} & \mathbf{0} \\ \mathbf{0} & \mathcal{A}_{22} \\ \mathbf{0} & \mathcal{A}_{32} \end{bmatrix} \begin{Bmatrix} u_1 \\ u_2 \end{Bmatrix} + \begin{Bmatrix} \eta_1(u_1, u_2) \\ \eta_2(u_1, u_2) \\ \eta_3(u_1, u_2) \end{Bmatrix} \right) + \mathcal{R}(u_1, u_2). \quad (5.7)$$

If the high-energy photopeak from ^{111}In is not used during reconstruction, then Eq. 5.6 is used. To briefly elaborate on the terms in the objective function, the mixing matrix effectively handles the photopeak overlap component of crosstalk, while the background term η effectively handles the scatter component. The current study ignores η due to minimal scatter in preclinical SPECT.

5.4.2.1 Objective Function Optimization

Given the ill-posed nature of the problem at hand [159], the objective function must be minimized to obtain meaningful and stable image estimates that closely approximate the true radiopharmaceutical distributions. The optimization algorithm used in this introductory work was preconditioned projected gradient descent (PPGD) using an expectation maximization (EM)-type preconditioner (see Algo. 1) [160]. Uniform images were initialized with ones, then backprojected to create sensitivity images for preconditioning. A step size of $\lambda = 0.01$ was chosen, and the image estimates were iteratively updated with the preconditioned gradient of the objective function before imposing a positivity constraint to project the solution onto the feasible set.

Algorithm 1 Preconditioned projected gradient descent (PPGD).

- | | |
|---|--|
| 1: $\mathbf{u}^0 = [u_1, \dots, u_N]$ | ▷ Uniform images or warm start (e.g., MLEM) |
| 2: $\mathbf{s} = [\mathcal{A}_{11}^\top \mathbf{1}, \dots, \mathcal{A}_{LN}^\top \mathbf{1}]$ | ▷ Create sensitivity images for preconditioning |
| 3: $\lambda \leftarrow$ choose step size | |
| 4: for i iterations do | |
| 5: $\mathbf{p}^i \leftarrow \mathbf{u}^i / \mathbf{s}$ | ▷ EM-type preconditioner - element-wise division |
| 6: $\bar{\mathbf{u}}^{i+1} \leftarrow \mathbf{u}^i - \lambda \mathbf{p}^i \nabla \mathcal{L}(\mathbf{u}^i)$ | ▷ Gradient step |
| 7: $\mathbf{u}^{i+1} \leftarrow \text{Proj}_{\{\geq 0\}}(\bar{\mathbf{u}}^{i+1})$ | ▷ Positivity constraint |
-

5.4.3 Determination of Equation Parameters

Measured data were corrected for uniformity using a uniformity correction table (UCT) calculated from primary energy windows for each radionuclide, which was obtained with a flood field acquisition of 100 million counts using an 8 MBq point source. Radionuclide activity was assayed with a Capintec CRC-55tR dose calibrator (Mirion Technologies, Florham Park, USA).

5.4.3.1 Energy Windows

Primary energy windows were defined with a width of 30% centered on each photopeak. Considering NEMA’s specification of the maximum bin width when analyzing energy spectra, i.e., $0.1 \times$ the full width at half maximum (FWHM) [124], the TEW method used 2 keV-wide secondary windows centered on the limits of the primary windows [9]. This was based on the Spark’s 14.7% energy resolution measured with ^{99m}Tc in a previous study [107]. Lastly, spectral unmixing used primary energy windows for each photopeak unless the photopeaks were overlapping, in which case the outermost limits of overlapping primary windows were used to define the upper and lower limits of two equally sized abutting energy windows. To illustrate this, Table 5.1 presents the $^{99m}\text{Tc}/^{123}\text{I}$ energy window characteristics used in this study.

Table 5.1: Energy window characteristics for $^{99m}\text{Tc}/^{123}\text{I}$.

Description	Lower limit (keV)	Upper limit (keV)
Primary window ^{99m}Tc	119.45	161.58
TEW lower window ^{99m}Tc	118.45	120.45
TEW upper window ^{99m}Tc	160.58	162.58
Primary window ^{123}I	135.15	182.85
TEW lower window ^{123}I	134.15	136.15
TEW upper window ^{123}I	181.85	183.85
Spectral unmixing lower window	119.45	151.15
Spectral unmixing upper window	151.15	182.85

5.4.3.2 System Matrix

System matrices were configured for emissions of interest from each radionuclide according to the subsections immediately below. Configurable parameters include the intrinsic resolution for point spread function (PSF) corrections, scintillation crystal attenuation coefficient for depth of interaction (DOI) corrections, and an attenuation map for attenuation corrections. DOI corrections were not performed in this study due to a bug in STIR’s pinhole-SPECT software, nor was attenuation correction applied due to its demand on computational resources [126].

5.4.3.2.1 Intrinsic Spatial Resolution

The intrinsic spatial resolution was determined from PSF measurements using a pencil beam emitted from a tungsten line source holder having a tunnel 0.4 mm in diameter, 10.0 mm in length, and centered 1.0 mm above the middle of the detector with a 1.0 cm-thick aluminum plate. A total of 100,000 counts were acquired from a 100 MBq line source established in a glass capillary tube (inner diameter $\varnothing_{ID} = 1.15$ mm, outer diameter $\varnothing_{OD} = 1.50$ mm, length $L = 75$ mm) and secured in the line source holder. Projection images with 0.1 mm pixels were generated with primary energy windows, and the PSF was integrated along detector axes then analyzed in terms of the FWHM according to procedures defined by the NEMA NU 1-2018 protocol [124]. Assuming a Gaussian PSF, the standard deviation σ of the distribution was calculated from the average FWHM for a given radionuclide using the equation

$$\sigma = \frac{\text{FWHM}}{2\sqrt{2\ln 2}} \quad (5.8)$$

for configuration in STIR's detector parameter file. Note that PSF corrections were only explored with $^{99m}\text{Tc}/^{123}\text{I}$.

5.4.3.2.2 Scintillation Crystal Attenuation Coefficient

The attenuation coefficients for sodium-activated cesium iodide (CsI(Na)) housed in the Spark were calculated from the National Institute of Standards and Technology (NIST) database [161]. According to photon energies of 140.5 keV for ^{99m}Tc , 159.0 keV for ^{123}I , and 171.3 keV and 245.4 keV for ^{111}In , the linearly interpolated attenuation coefficients were 4.406 cm^{-1} , 3.005 cm^{-1} , and 2.619 cm^{-1} and 1.310 cm^{-1} , respectively. They are included here for completeness, but were unused due to the DOI correction bug in STIR's pinhole-SPECT library.

5.4.3.3 Mixing Matrix Weights

At the time of writing, the Spark did not have a quantitative SPECT protocol implemented, so mixing matrix values could not be determined with Eq. 5.3. For practicality, this work assigned sensitivities for each mixing value, and images were converted to units of radioactivity after reconstruction. Mixing matrix weights were separately determined between measurement and simulation to account for any differences in the imaging systems and to ensure validity of parameters applied during reconstruction. Weights for simulated data were simply approximated as the system

sensitivity from the main experiment's simulation using

$$m_{kl} = \frac{B_{kl}}{A_{\text{mid},n}} \quad (5.9)$$

where B_{kl} is the average count rate of gold standard data free of scatter (total primary counts divided by total elapsed time) from photopeak l in energy window k , and $A_{\text{mid},n}$ is the activity midway through the acquisition for radionuclide n . Note that index l depends on n .

Mixing matrix weights for measurement of $^{99\text{m}}\text{Tc}/^{123}\text{I}$ were determined from gamma camera planar sensitivity according to the NEMA NU 1-2018 protocol [124]. A 35.0 mm-diameter petri dish was filled with 2 ml of water and injected with a calibrated activity of $A_{\text{cal}} = 25$ MBq. The internal base of the radioactive solution was placed at the center of rotation, i.e., 23.0 mm from the face of the collimator, and 4 million counts were acquired. Projection images were generated for each energy window and corrected for uniformity. The decay-corrected count rate R_{kl} was then calculated as

$$R_{kl} = \lambda_n C_{kl} e^{\lambda_n(T_n - T_{\text{cal},n})} \times (1 - e^{-\lambda_n T_{\text{acq},n}})^{-1} \quad (5.10)$$

where λ_n is the decay constant for radionuclide n , C_{kl} is the summed counts from photopeak l in energy window k , T_n is the acquisition start time, $T_{\text{acq},n}$ is the acquisition duration, and $T_{\text{cal},n}$ is the time of activity calibration. The total system sensitivity was then calculated and assigned to mixing matrix weights as

$$m_{kl} = \frac{R_{kl}}{A_{\text{cal},n}}. \quad (5.11)$$

5.4.4 Experimental Test of Crosstalk Correction Efficacy

5.4.4.1 Multi-Radionuclide Acquisition with Five Capillary Tubes

A mouse-sized quintuple line source scatter phantom was fabricated from an acrylic cylinder ($\varnothing = 25.4$ mm, $L = 60$ mm) with five 0.8 mm-diameter bores accepting precision capillary tubes: one at the center and four separated by 90° with a 10 mm radial offset. Capillary tubes were prepared with $\{0,1,2,3,4\}$ MBq of $^{99\text{m}}\text{Tc}$ and $\{4,3,2,1,0\}$ MBq of ^{123}I (or ^{111}In in simulation) resulting in a 4 MBq mixture in each tube at the beginning of acquisition. Capillary tubes containing the isolated radionuclides were assayed to verify mixture concentrations and calculate a normalization factor for converting tomographic image units to activity. The ^{111}In datasets

were reconstructed using the low-energy photopeak, as well as the combined low- and high-energy photopeaks to further assess crosstalk correction performance.

The phantom was centered along the central axis in the field of view (FOV), and SPECT data were acquired in 3° increments over 270° for a total acquisition time of 60 min. Projection images with 0.5 mm bins were generated in a 208×208 matrix, and measured data were corrected for uniformity. Tomographic images were then reconstructed with 0.25 mm voxels in a $230 \times 184 \times 184$ matrix and masked with a 30.0 mm-diameter cylindrical mask for each method of crosstalk correction.

5.4.4.2 Reconstruction Methods and Crosstalk Correction Algorithms

Data were reconstructed with four approaches applying varying degrees of crosstalk correction:

1. Conventional primary energy windows reconstructed with MLEM,
2. Triple energy window (TEW) method reconstructed with MLEM,
3. Spectral unmixing reconstructed with PPGD, and
4. Gold standard Monte Carlo data reconstructed with MLEM and PPGD.

Note here that gold standard refers to data separated by parent source which includes scatter, whereas mixing weights in simulation were calculated with gold standard data excluding scatter. The number of iterations were chosen as the iteration yielding the greatest contrast in reconstructed images, corresponding to 13 MLEM iterations and 50 PPGD iterations.

Primary energy windows offer no crosstalk correction capabilities. This served as the worst-case-scenario to compare improvements offered by crosstalk correction, for which images were reconstructed with MLEM and no system matrix corrections.

The triple energy window (TEW) method is commonly applied in multi-radionuclide SPECT due to its effectiveness at eliminating downscattered counts from photon crosstalk in planar images [2, 9]. The crosstalk estimate S was calculated on a pixel-by-pixel basis using

$$S = \left(\frac{C_l}{w_l} + \frac{C_u}{w_u} \right) \times \frac{w_p}{2}. \quad (5.12)$$

where C_l and C_u are the counts in the lower and upper energy windows, and w_l , w_u , and w_p are the widths of the lower, upper, and primary energy windows. The crosstalk estimate from all pixels was subtracted directly from the primary photopeak

projection image, then reconstructed with MLEM and no system matrix corrections.

Spectral unmixing has not been previously characterized in multi-radionuclide SPECT. Comparable photon energies of commonly used SPECT radionuclides yield minimal differences between collimator-detector response functions, and reconstruction may not benefit considerably from independent system matrices. Therefore, spectral unmixing was tested with and without PSF corrections for $^{99m}\text{Tc}/^{123}\text{I}$. If no matrix corrections were applied, one system matrix was used for all photopeaks to save on computation cost. If system matrices were PSF-corrected, independent system matrices were calculated for each emission of interest. PSF corrections were not considered for $^{99m}\text{Tc}/^{111}\text{In}$ due to the demand on computational resources. Line source resolution was calculated for spectral unmixing to assess the effects of PSF correction. More specifically, using NEMA’s methodology, the average in-plane resolution was calculated from the FWHM in x and y directions in three 3.5 mm-thick transverse slices: one at the center and two at ± 14.5 mm [124].

Gold standard data were generated with GATE by separating detected events according to their parent source. Gold standard images were reconstructed from the separated spectra in two ways. First, conventional primary energy windows were used to obtain projection images for each radionuclide that were reconstructed with MLEM and no system matrix corrections. Second, projection images were obtained from abutting energy windows where photopeaks would be otherwise overlapping, then reconstructed with PPGD using mixing values set to zero for the competing radionuclide.

5.4.4.3 Analysis of Crosstalk Correction Performance

Prior to analyzing any data, reconstructed images were normalized to convert to units of activity. A normalization factor F was calculated for each image using

$$F = \frac{A_{\text{assay}} L_{\text{ROI}}}{I_{\text{ROI}} L_{\text{src}}} \quad (5.13)$$

where A_{assay} is the assayed activity of the capillary tube containing the isolated radionuclide, I_{ROI} is the integrated intensity in a region of interest (ROI) centered on the corresponding capillary tube, $L_{\text{ROI}} = 28.0$ mm is the length of the ROI, and $L_{\text{src}} = 59.0$ mm is the active length of the capillary tube assuming 1.0 mm of sealing clay at one end.

To calculate line source activity and contrast, capillary tube ROIs were defined around each line source in the fully sampled FOV using 6.0 mm-diameter cylinders with a length of 28.0 mm (see Fig. 5.1. The ROI diameter was based on NEMA’s recommendation of $4 \times \text{FWHM}$ in tomographic analysis, for which the average in-plane spatial resolution was previously found to be on the order of 1.4 mm [107]. A 28.0 mm-long cylindrical ROI was defined with inner and outer radii of 3.0 mm and 7.0 mm to calculate the coefficient of variation (CV), i.e., noise, in a region central to the capillary tubes. Smaller CV values indicate better noise performance.

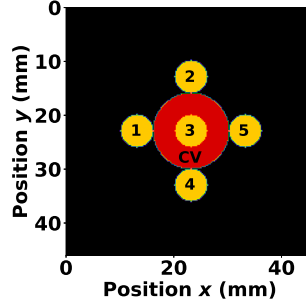


Figure 5.1: Illustration of the 28.0 mm-long ROIs used in the analysis of crosstalk correction performance. Capillary tube ROIs are shown in yellow and numbered by source identification, and the ROI for calculation of image noise is shown in red and labelled ‘CV’. ROI number 1 contains the 4 MBq ^{123}I or ^{111}In line source and ROI number 5 contains the 4 MBq $^{99\text{m}}\text{Tc}$ line source.

The quantitative accuracy of reconstructed images was assessed from the relative line source activity A_{rel} in the fully sampled FOV using

$$A_{\text{rel},i} = \frac{A_i}{A_r}. \quad (5.14)$$

Here, A_i is the total apparent activity in the i^{th} capillary tube ROI, $i = 1, \dots, 5$ is the source identification (ID), and $A_r = 4 \text{ MBq} \times (L_{\text{ROI}}/L_{\text{src}})$ is the nominal activity in the reference line source. Source $i = 1$ corresponds to the ^{123}I - or ^{111}In -only capillary tube and source $i = 5$ corresponds to the $^{99\text{m}}\text{Tc}$ -only capillary tube. To assess quantitative accuracy, the relative activity was plotted against the source ID for each radionuclide, and root-mean-square errors (RMSEs) were calculated using

$$\text{RMSE} = \sqrt{\frac{\sum_{i=1}^5 |A_{\text{rel},i} - A_{r,i}|^2}{5}} \quad (5.15)$$

where $A_{r,i}$ is the nominal reference activity of the i^{th} capillary tube for a given radionuclide. A smaller RMSE indicates superior accuracy.

Image quality metrics were calculated in terms of capillary tube contrast and background noise. Contrast was calculated between image pairs using

$$C_i = \frac{A_{1,i} - A_{2,i}}{A_{1,i} + A_{2,i}} \quad (5.16)$$

where $A_{1,i}$ and $A_{2,i}$ are the total activities in the i^{th} ROI for radionuclides one and two, i.e., $^{99\text{m}}\text{Tc}$ and ^{123}I or ^{111}In , respectively. Note that the absolute value was not considered in the numerator in order to compare the complementing activities between radionuclide distributions. The RMSE was also calculated for contrast using Eq. 5.15. Lastly, the CV was calculated for each image using

$$\text{CV} = \frac{\sigma}{\mu} \quad (5.17)$$

where σ and μ are the standard deviation and mean voxel values, respectively, in the ROI central to the capillary tubes. The CV was tabulated to assess the effect of crosstalk correction on image noise.

5.5 Results

5.5.1 Determination of Equation Parameters

5.5.1.1 Intrinsic Spatial Resolution

The limiting intrinsic spatial resolution in terms of the PSF FWHM was 0.839 ± 0.024 mm for $^{99\text{m}}\text{Tc}$ and 0.845 ± 0.023 mm for ^{123}I . This yielded a standard deviation of 0.0354 cm for $^{99\text{m}}\text{Tc}$ and 0.0359 cm for ^{123}I , which were configured in STIR's pinhole-SPECT detector parameter files. Note that ^{111}In was not procured for this study, so the limiting intrinsic spatial resolution was not measured, nor was it required since PSF corrections were only explored for $^{99\text{m}}\text{Tc}/^{123}\text{I}$.

5.5.1.2 Mixing Matrix Weights

Projection images obtained from system planar sensitivity measurements are presented in Fig. 5.2 along with corresponding energy spectra for $^{99\text{m}}\text{Tc}$ and ^{123}I . According to the energy window characteristics presented earlier in Table 5.1, the primary energy windows are shaded red, and black lines denote the limits of abutting energy windows used in spectral unmixing. The measured system planar sensitivities in the primary windows were 32.9 cps/MBq for $^{99\text{m}}\text{Tc}$ and 27.4 cps/MBq for ^{123}I . Ta-

bles 5.2 and 5.3 present the mixing weight sensitivities calculated for $^{99m}\text{Tc}/^{123}\text{I}$ and $^{99m}\text{Tc}/^{111}\text{In}$, respectively. Sensitivities obtained from measurement and simulation in Table 5.2 are highly agreeable, which supports their use as a global mixing matrix value independent of the acquisition. It also supports the accuracy of the simulation model in testing multi-radionuclide crosstalk correction efficacy.

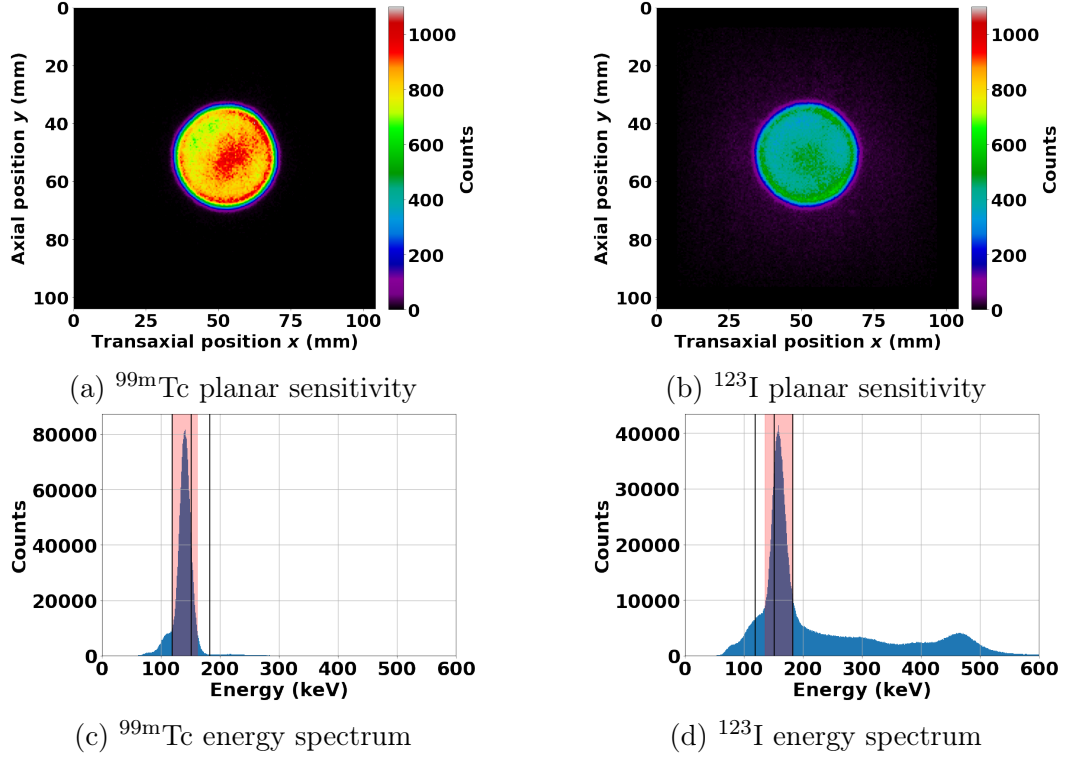


Figure 5.2: System planar sensitivity projection images (top) and energy spectra (bottom) measured for ^{99m}Tc (left) and ^{123}I (right). Images were obtained from the primary energy window in the red shaded region, then corrected for uniformity. Abutting energy windows denoted by vertical black lines were used to calculate the window-specific sensitivities for definition of the mixing matrix weights.

Table 5.2: Sensitivity mixing weights for $^{99m}\text{Tc}/^{123}\text{I}$ in measurement (simulation).

Energy window (keV)	^{99m}Tc sensitivity (cps/MBq)	^{123}I sensitivity (cps/MBq)
135.30 ± 15.85	$m_{11} = 27.9$ (24.9)	$m_{12} = 10.5$ (10.1)
167.00 ± 15.85	$m_{21} = 5.22$ (2.74)	$m_{22} = 19.9$ (19.9)

Table 5.3: Sensitivity mixing weights for $^{99m}\text{Tc}/^{111}\text{In}$ in simulation.

Energy window (keV)	^{99m}Tc sensitivity (cps/MBq)	^{111}In sensitivity (cps/MBq)
138.80 ± 19.40	$m_{11} = 26.9$	$m_{12} = 11.3$ $m_{13} = 0.00$
177.60 ± 19.40	$m_{21} = 0.513$	$m_{22} = 25.2$ $m_{23} = 0.00$
$245.40 \pm 15\%$	$m_{31} = 0.00$	$m_{32} = 0.00$ $m_{33} = 30.5$

5.5.2 Experimental Test of Crosstalk Correction Efficacy using $^{99m}\text{Tc}/^{123}\text{I}$

Results from $^{99m}\text{Tc}/^{123}\text{I}$ spectral unmixing crosstalk correction were obtained without and with PSF corrections. These are distinguished by “spectral unmixing 1” and “spectral unmixing 2”, respectively.

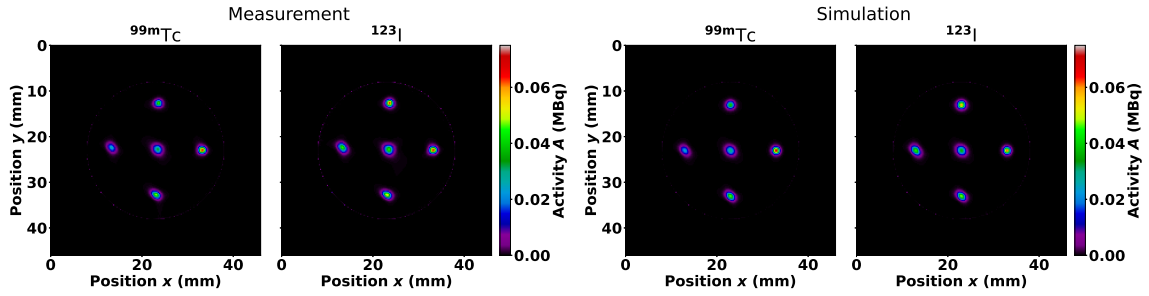
5.5.2.1 $^{99m}\text{Tc}/^{123}\text{I}$ Acquisition with Five Capillary Tubes

The measured activities in the ^{99m}Tc -only and ^{123}I -only capillary tubes were 4.04 MBq and 3.80 MBq, respectively, at the start of the acquisition. This indicates a potential uncertainty in line source activities upwards of $\sim 5.1\%$ in measurement.

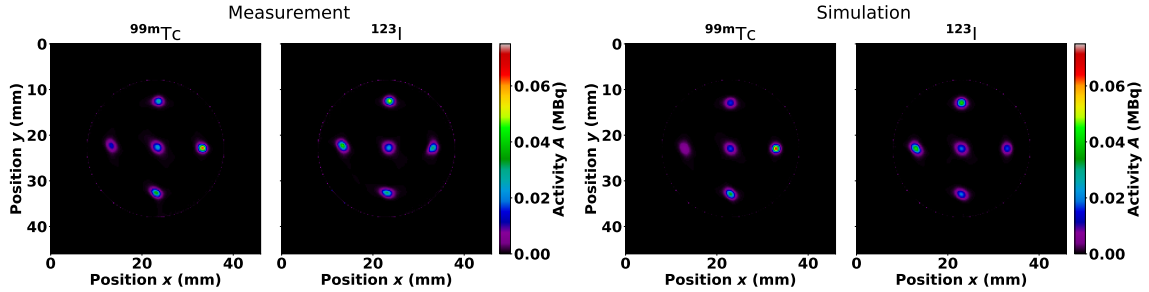
Reconstructed distributions of ^{99m}Tc and ^{123}I were summed over the 28.0 mm axial extent for display of measured and simulated data in Fig. 5.3, and gold standard data in Fig. 5.4. Initial observations comparing measurement and simulation show excellent visual agreement. Similar activity levels can be observed in all capillary tubes reconstructed from primary energy windows. The different amounts of radioactivity become increasingly apparent after applying crosstalk correction as seen from the TEW, spectral unmixing, and gold standard methods. Gold standard MLEM and PPGD images free of crosstalk are nearly indistinguishable, and their comparison amongst all methods shows the best visual agreement with spectral unmixing.

When quantifying crosstalk in measurement, the TEW method estimated that 23% and 28% of events in the ^{99m}Tc and ^{123}I primary windows were due to crosstalk, respectively. Comparably in simulation, the TEW estimated that 26% and 29% of events were due to crosstalk, whereas the actual crosstalk amounts were 43% and 41% in simulation. This highlights the inaccuracy of the TEW method when photopeaks are unresolved in multi-radionuclide SPECT.

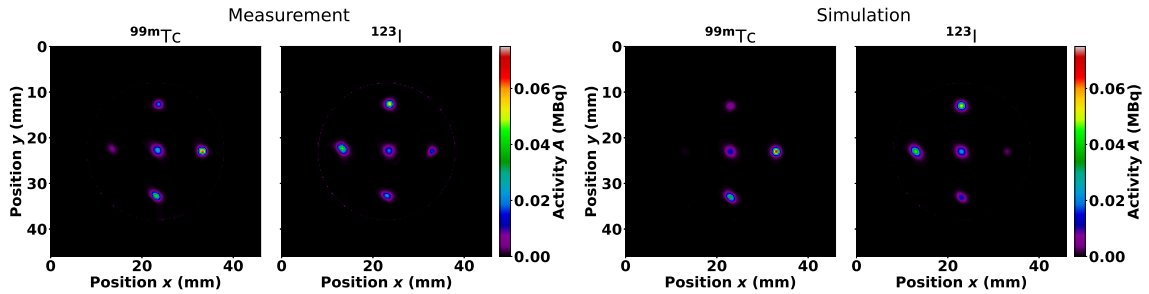
To briefly assess the effect of PSF correction in spectral unmixing, the average in-plane resolution without PSF correction was 1.40 ± 0.19 mm for ^{99m}Tc and 1.41 ± 0.14 mm for ^{123}I . The resolution did not improve when applying PSF correction, as indicated by corresponding FWHM of 1.46 ± 0.22 mm and 1.43 ± 0.15 mm. To further compare to gold standard images, the combined resolution of gold standard MLEM and PPGD results was 1.27 ± 0.20 mm for ^{99m}Tc and 1.48 ± 0.23 mm for ^{123}I . Resolution comparisons were not made with primary and triple energy windows due to the amount of crosstalk remaining after image reconstruction.



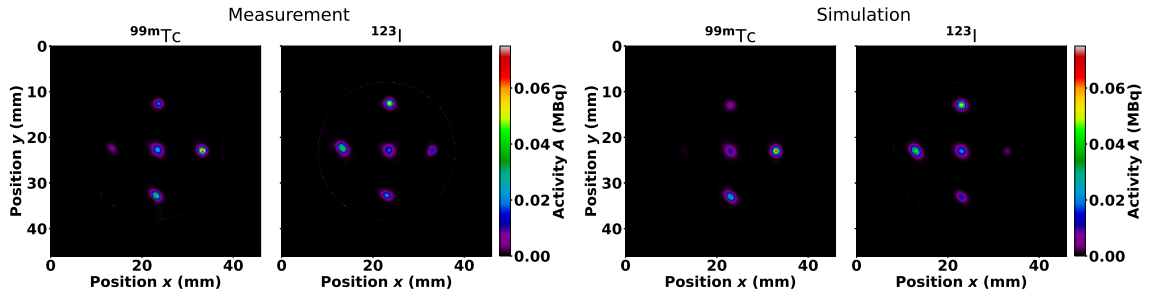
(a) Primary energy window



(b) Triple energy window



(c) Spectral unmixing 1



(d) Spectral unmixing 2

Figure 5.3: Reconstructed images for ^{99m}Tc and ^{123}I demonstrating crosstalk correction in measurement (left) and simulation (right). In each image set, ^{99m}Tc is displayed on the left and ^{123}I on the right. Primary windows contain maximal crosstalk (row one) which is commonly corrected using the TEW method (row two). The spectral unmixing technique shows improved quantitative accuracy and contrast when using one system matrix (row three) and two system matrices, allowing system matrix corrections for PSF effects (row four).

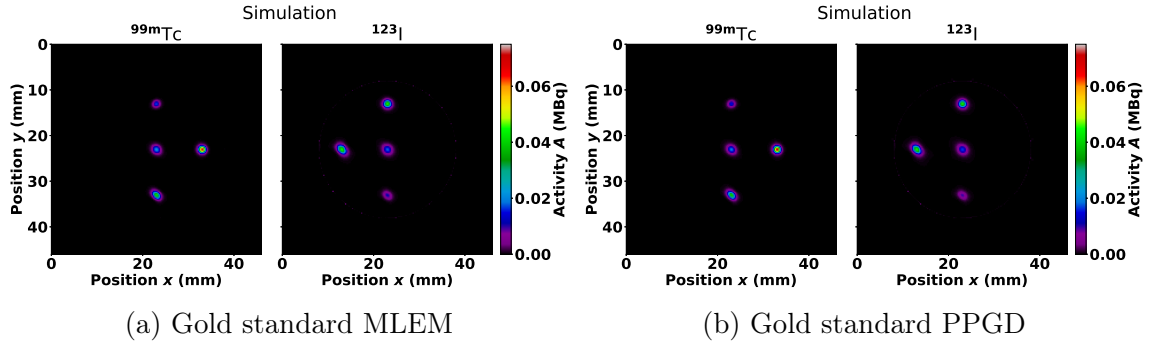


Figure 5.4: Gold standard images for ^{99m}Tc and ^{123}I reconstructed with MLEM (left) and PPGD (right) demonstrating perfect crosstalk correction. In each image set, ^{99m}Tc is displayed on the left and ^{123}I on the right.

5.5.2.2 Analysis of $^{99m}\text{Tc}/^{123}\text{I}$ Crosstalk Correction Performance

Reconstructed images were analyzed in terms of quantitative accuracy and image quality metrics, for which Fig. 5.5 shows the relative activity obtained for each capillary tube of ^{99m}Tc and ^{123}I . Measured and simulated results are in good agreement. Overall, spectral unmixing provided the most accurate quantification, although activity was slightly underestimated for ^{99m}Tc and overestimated for ^{123}I in regions of mixed radioactivity in simulation. Spectral unmixing shows excellent separation of radionuclides in regions of isolated activity in simulation. Furthermore, spectral unmixing results with and without PSF corrections were nearly indistinguishable. Table 5.4 presents the RMSE results that confirm the superior quantitative accuracy of spectral unmixing compared to conventional methods. More specifically, in simulation, primary energy windows yielded an average quantitation RMSE of 0.44, and the TEW, spectral unmixing, and gold standard methods provided improvements of 51%, 83%, and 95%, respectively. Measured results were in good agreement where primary energy windows yielded an average quantitation RMSE of 0.49, and the TEW and spectral unmixing methods provided improvements of 32%, 74%.

Table 5.4: Quantitative accuracy of $^{99m}\text{Tc}/^{123}\text{I}$ using RMSE in measurement (simulation).

Reconstruction method	^{99m}Tc RMSE	^{123}I RMSE
Primary energy window	0.35 (0.35)	0.62 (0.53)
Triple energy window	0.26 (0.17)	0.40 (0.26)
Spectral unmixing 1	0.097 (0.055)	0.16 (0.095)
Spectral unmixing 2	0.10 (0.057)	0.16 (0.098)
Gold standard MLEM	n.d. (0.019)	n.d. (0.026)
Gold standard PPGD	n.d. (0.023)	n.d. (0.026)

n.d.: no data

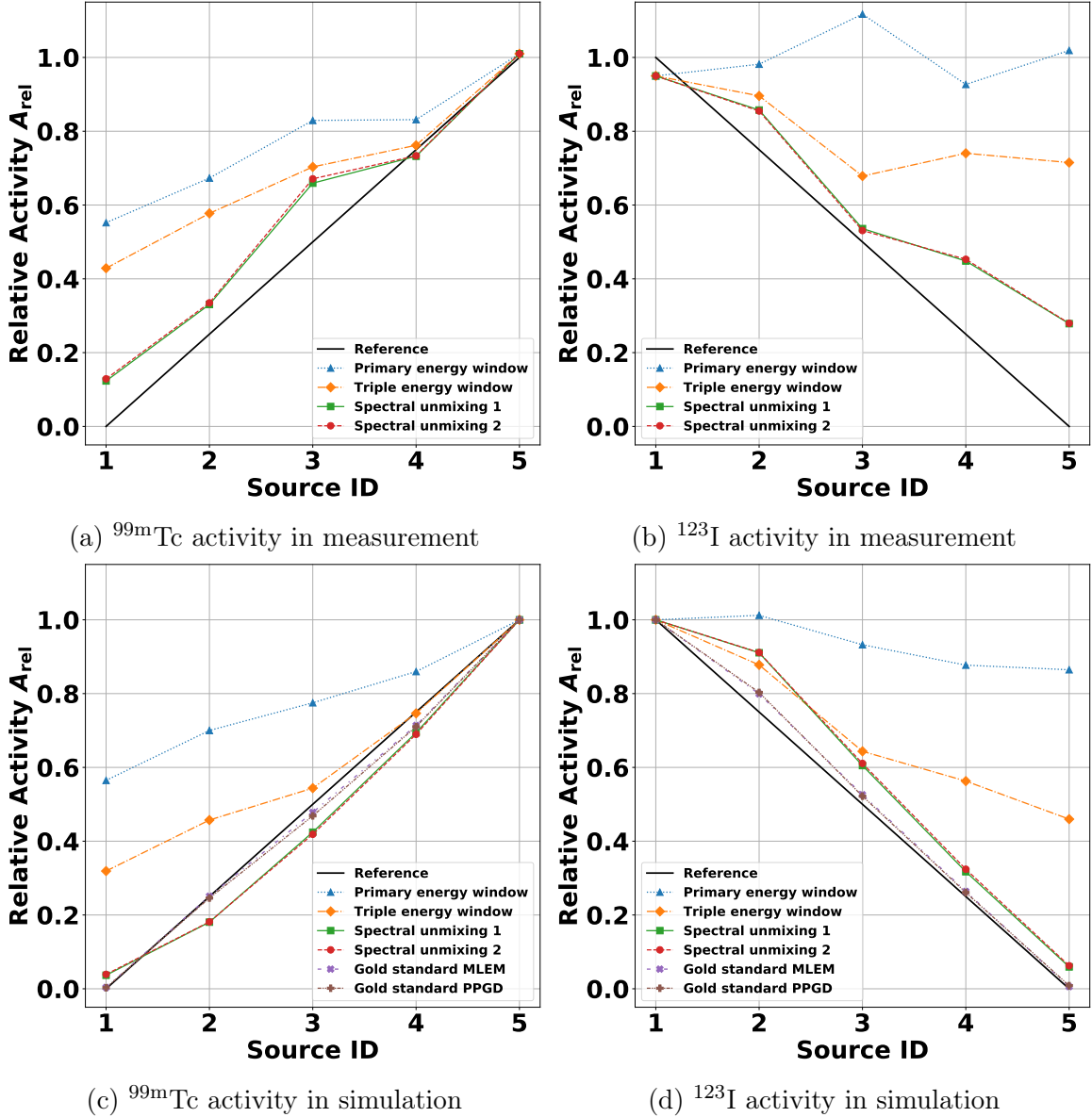


Figure 5.5: Relative activity of reconstructed line sources for ^{99m}Tc (left) and ^{123}I (right) in measurement (top) and simulation (bottom). Primary energy windows yielded the greatest quantitative error in comparison to the reference line, whereas spectral unmixing yielded the least error overall, next to gold standard results.

Plots of radionuclide contrast are shown in Fig. 5.6. As expected, crosstalk correction improved contrast, while spectral unmixing showed the best agreement with gold standard results. Primary energy windows offered poor contrast between radionuclides, as indicated by the large RMSE values in Table 5.5. In simulation, the primary energy window contrast RMSE was 0.59, and the TEW, spectral unmixing, and gold standard methods offered a 32%, 76%, and 95% improvement, respectively.

Comparably in measurement, the primary window contrast RMSE was 0.63, and the TEW and spectral unmixing methods offered a 16% and 60% improvement. Table 5.6 presents image noise, which was lowest for ^{99m}Tc in spectral unmixing and greatest with the TEW method. ^{123}I image noise was lowest with primary windows and comparable between the TEW method and spectral unmixing without PSF correction. Spectral unmixing yielded greater image noise with PSF corrections than without.

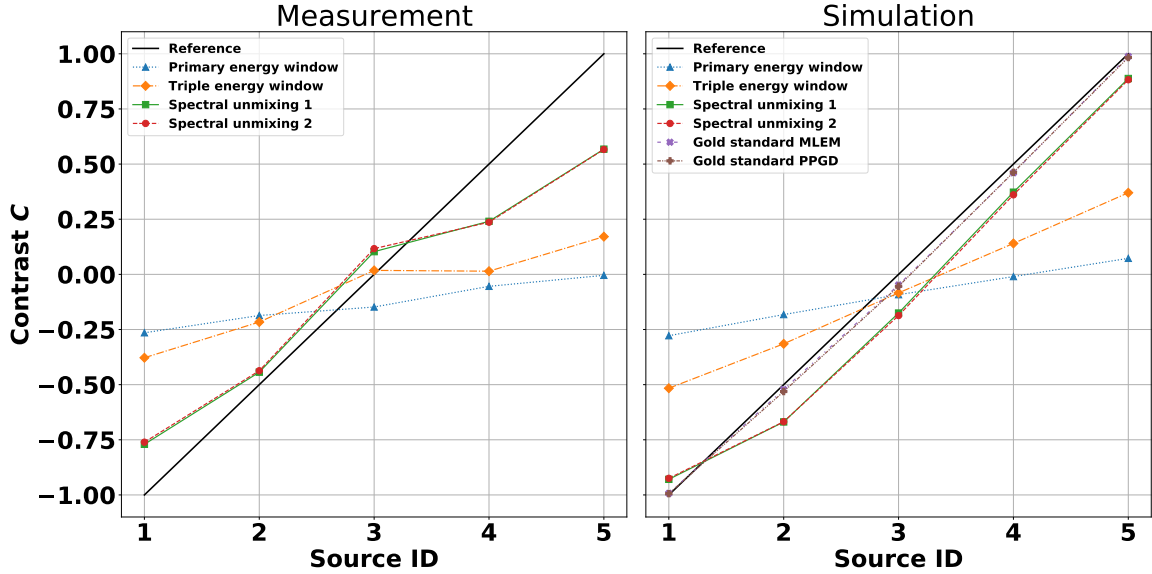


Figure 5.6: Contrast of reconstructed $^{99m}\text{Tc}/^{123}\text{I}$ line sources in measurement (left) and simulation (right). The reference line is included to show the nominal contrast between capillary tubes with perfect crosstalk correction.

Table 5.5: Contrast of $^{99m}\text{Tc}/^{123}\text{I}$ using RMSE in measurement (simulation).

Reconstruction method	RMSE
Primary energy window	0.63 (0.59)
Triple energy window	0.53 (0.40)
Spectral unmixing 1	0.25 (0.14)
Spectral unmixing 2	0.26 (0.14)
Gold standard MLEM	n.d. (0.030)
Gold standard PPGD	n.d. (0.033)

Table 5.6: Image noise of $^{99m}\text{Tc}/^{123}\text{I}$ using CV in measurement (simulation).

Reconstruction method	^{99m}Tc CV	^{123}I CV
Primary energy window	0.55 (0.42)	0.89 (0.53)
Triple energy window	0.70 (0.59)	0.92 (0.73)
Spectral unmixing 1	0.56 (0.39)	1.0 (0.73)
Spectral unmixing 2	0.60 (0.44)	1.1 (0.89)
Gold standard MLEM	n.d. (0.52)	n.d. (0.56)
Gold standard PPGD	n.d. (0.60)	n.d. (0.52)

5.5.3 Experimental Test of Crosstalk Correction Efficacy using $^{99m}\text{Tc}/^{111}\text{In}$

Comparisons between ^{99m}Tc and ^{111}In were made using the low-energy ^{111}In photopeak, as well as the combined low- and high-energy photopeaks. These are distinguished in the results by “1 Peak” and “2 Peaks” accordingly.

5.5.3.1 $^{99m}\text{Tc}/^{111}\text{In}$ Acquisition with Five Capillary Tubes

Reconstructed images of ^{99m}Tc and ^{111}In distributions were summed over the 28.0 mm axial extent for display of simulated and gold standard data in Figs. 5.7 and 5.8, respectively. Initial observations of images reconstructed from primary energy windows show line source activities closer to the expected amounts with greater contrast than observed for the simultaneous acquisition of $^{99m}\text{Tc}/^{123}\text{I}$. While the different amounts of radioactivity become increasingly apparent after applying crosstalk correction, the differences are not as profound as $^{99m}\text{Tc}/^{123}\text{I}$. This was due to the greater separation between ^{99m}Tc and ^{111}In photopeaks, resulting in less crosstalk and less energy window overlap. Spectral unmixing also appears to have underestimated ^{99m}Tc activity and overestimated ^{111}In activity in regions of mixed radionuclides. In all cases, the inclusion of the high-energy photopeak during reconstruction shows improved quantitative accuracy and contrast, notably in the spectral unmixing case, at the expense of degraded spatial resolution in the ^{111}In image. For example, the average in-plane line source resolution in ^{111}In images reconstructed with spectral unmixing was 1.47 ± 0.16 mm using the low-energy photopeak and 1.82 ± 0.25 mm using the combined low- and high-energy photopeaks.

The TEW method estimated that 24% of events in the ^{99m}Tc primary window were due to crosstalk, and 28% and 5.0% of events were due to crosstalk in the lower and upper windows of ^{111}In , respectively. The actual crosstalk amounts were 36% for ^{99m}Tc , and 18% and 0.15% for the low- and high-energy primary windows for ^{111}In . Although the photopeaks were better-resolved between ^{99m}Tc and ^{111}In , optimal TEW estimates require optimization of energy window characteristics, which were not considered in this study and may vary in complexity depending on the imaging system and radionuclides being used [162].

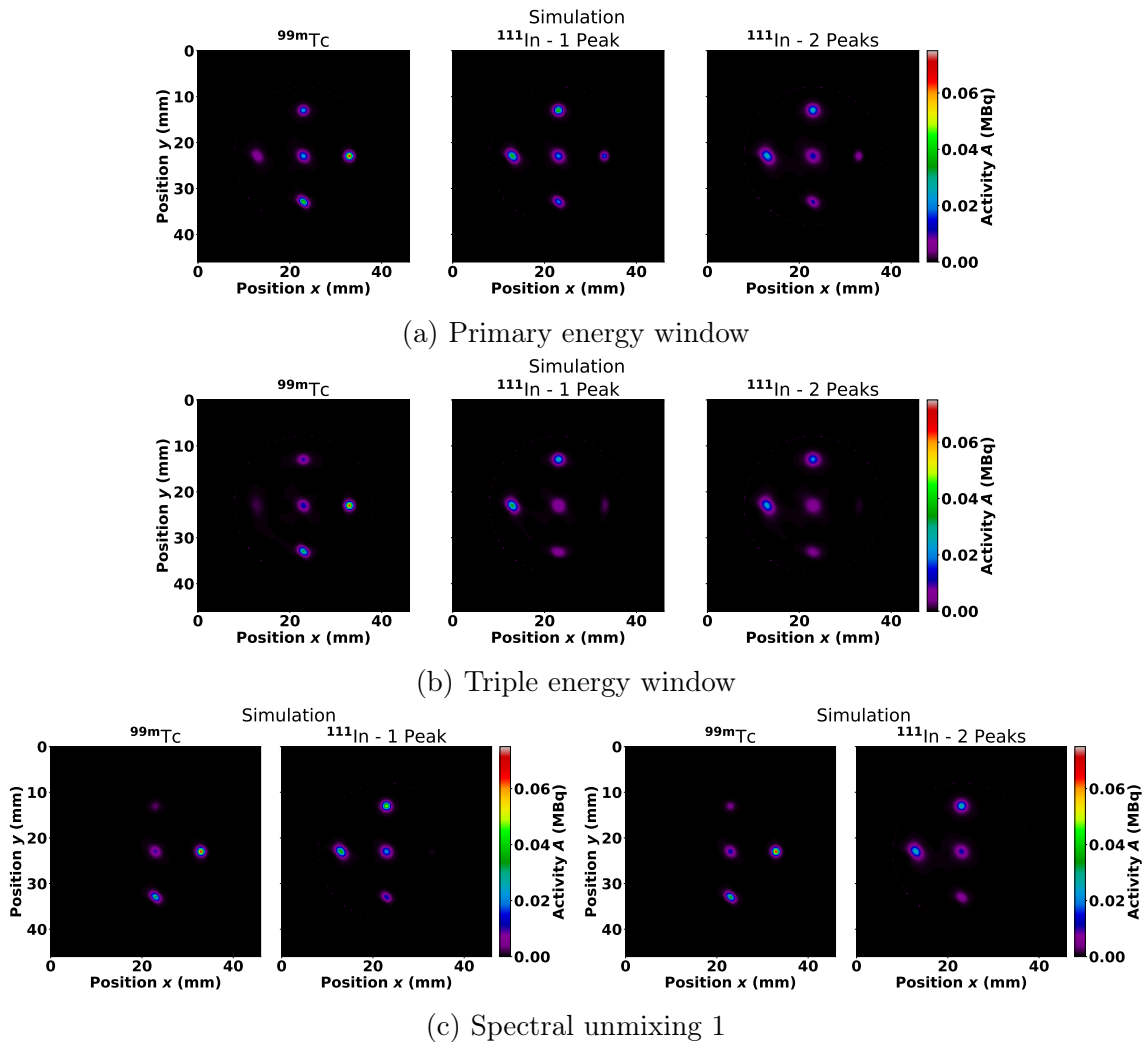


Figure 5.7: Reconstructed images for ^{99m}Tc and ^{111}In demonstrating crosstalk correction in simulation. In each image set, ^{99m}Tc is displayed on the left. In rows one and two, the middle image pertains to the ^{111}In low-energy photopeak, and the rightmost image combines the ^{111}In low- and high-energy photopeaks. In row three, column two pertains to the ^{111}In low-energy photopeak and column four combines the ^{111}In low- and high-energy photopeaks. Primary windows contain maximal crosstalk (row one) which is commonly corrected using the TEW method (row two). The spectral unmixing method (row three) shows comparable quantitative accuracy and contrast to the TEW method. In spectral unmixing's synergistic approach to image reconstruction, the ^{99m}Tc distribution is directly affected by the ^{111}In distribution.

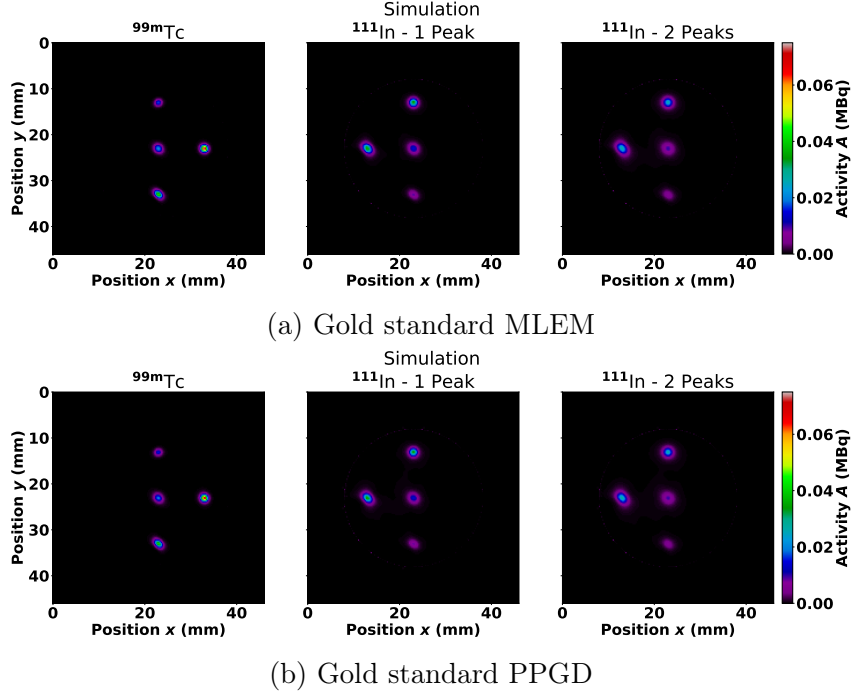
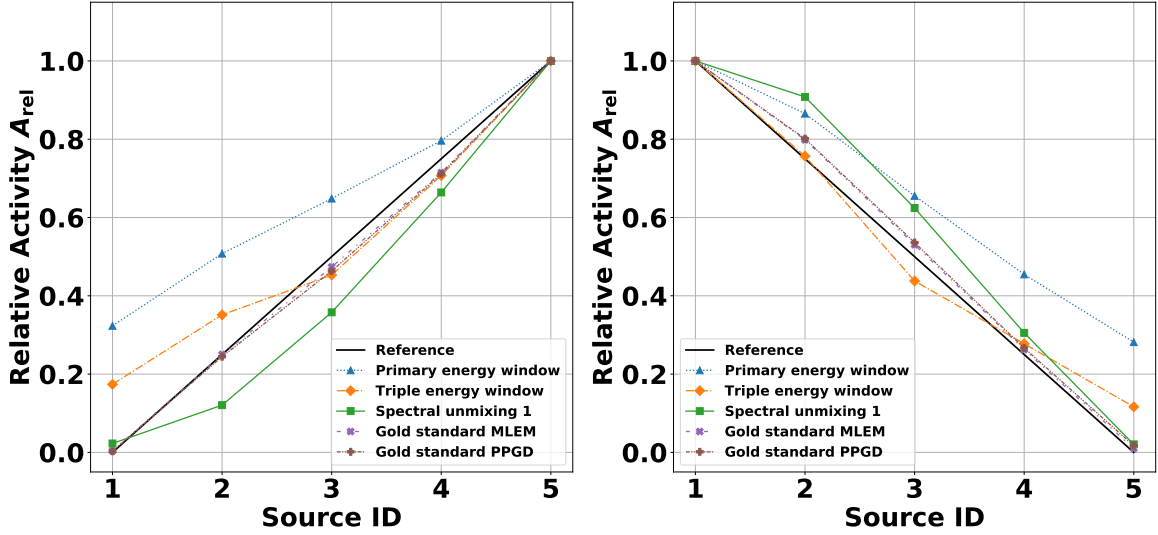


Figure 5.8: Gold standard images for ^{99m}Tc and ^{111}In reconstructed with MLEM (top) and PPGD (bottom) demonstrating perfect crosstalk correction. In each image set, ^{99m}Tc is displayed on the left, the middle image pertains to the ^{111}In low-energy photopeak, and the rightmost image combines the ^{111}In low- and high-energy photopeaks.

5.5.3.2 Analysis of $^{99m}\text{Tc}/^{111}\text{In}$ Crosstalk Correction Performance

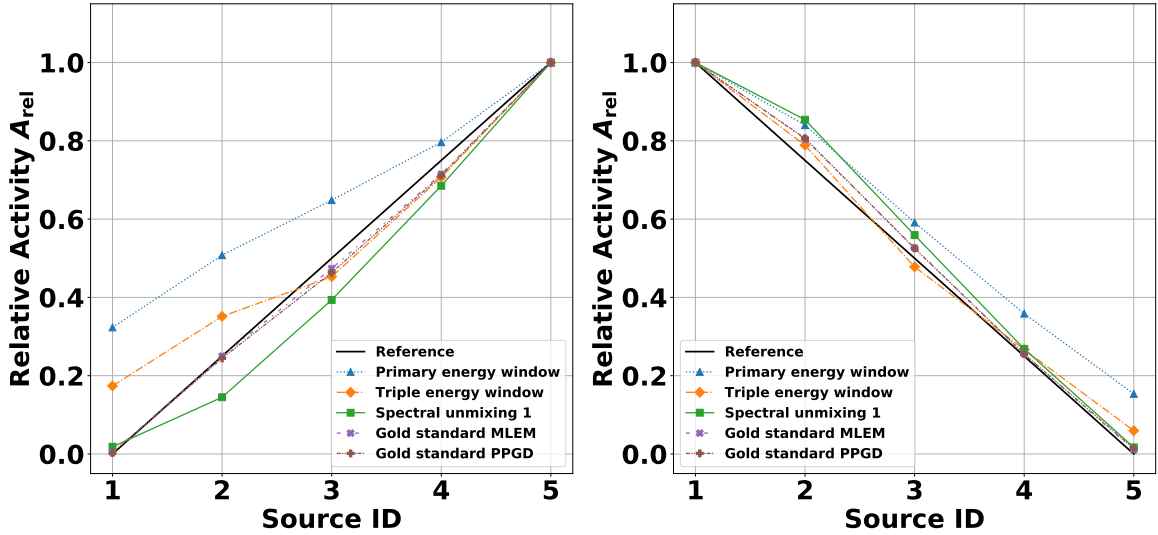
Plots of the relative activity obtained for each capillary tube of ^{99m}Tc and ^{111}In are presented in Fig. 5.9. As expected, the relative activity obtained with primary energy windows shows the greatest discrepancy compared to reference. The TEW method appears to provide the most accurate quantification, although ^{99m}Tc is overestimated in low-activity regions. Similar to the $^{99m}\text{Tc}/^{123}\text{I}$ experiment, spectral unmixing slightly underestimated ^{99m}Tc activity and slightly overestimated ^{111}In activity in regions of mixed radionuclides. This could indicate a systematic error in the spectral unmixing method, possibly due to the exclusion of the scatter term or limitations in using sensitivities as mixing weights. Nonetheless, the inclusion of the high-energy photopeak for ^{111}In improves quantification accuracy for all reconstructed distributions of ^{111}In , as well as for ^{99m}Tc in spectral unmixing due to its synergistic reconstruction.

To directly compare the quantitative accuracy of each reconstruction and crosstalk method, the RMSE of relative activity is presented in Table 5.7. The tabulated values confirm the observations made from the plots of relative activity. When considering



(a) ^{99m}Tc activity in simulation - 1 peak

(b) ^{111}In activity in simulation - 1 peak



(c) ^{99m}Tc activity in simulation - 2 peaks

(d) ^{111}In activity in simulation - 2 peaks

Figure 5.9: Relative activity of reconstructed line sources in measurement and simulation for ^{99m}Tc (left) and ^{111}In (right) using the ^{111}In low-energy window (top) and low- and high-energy windows (bottom). Note that the plots for ^{99m}Tc in the 1 and 2 peak cases are identical for all reconstruction methods except spectral unmixing, in which ^{99m}Tc benefits from the additional ^{111}In photopeak during synergistic reconstruction. The primary energy windows yielded the greatest quantification error in comparison to the reference line. In all ^{111}In images, the inclusion of the additional photopeak improves quantitative accuracy.

the low-energy photopeak of ^{111}In , primary energy windows provided the least accurate quantification as indicated by a mean RMSE of 0.19, and the TEW, spectral unmixing, and gold standard methods provided a 59%, 50%, and 88% improvement,

respectively. Quantitative accuracy improved when combining the low- and high-energy photopeaks as indicated by a mean RMSE of 0.15 in primary windows, with TEW, spectral unmixing, and gold standard methods providing a 57%, 57%, and 84% improvement in quantitation. The inclusion of the high-energy photopeak provided the greatest benefit in spectral unmixing due to the synergistic reconstruction of the ^{99m}Tc and ^{111}In distributions. Furthermore, the quantitative accuracy of $^{99m}\text{Tc}/^{111}\text{In}$ multi-radionuclide SPECT exceeds that of $^{99m}\text{Tc}/^{123}\text{I}$ for primary and triple energy windows due to the increased energy separation between photopeaks, while spectral unmixing shows consistent and comparable quantitation performance.

Table 5.7: Quantitative accuracy of $^{99m}\text{Tc}/^{111}\text{In}$ using RMSE in simulation.

Reconstruction method	1 peak		2 peaks	
	^{99m}Tc RMSE	^{111}In RMSE	^{99m}Tc RMSE	^{111}In RMSE
Primary energy window	0.20	0.18	-	0.10
Triple energy window	0.094	0.060	-	0.034
Spectral unmixing 1	0.095	0.094	0.073	0.055
Gold standard MLEM	0.020	0.027	-	0.028
Gold standard PPGD	0.024	0.030	-	0.028

The contrast between radionuclides is plotted for each capillary tube in Fig. 5.10. Again, primary energy windows offered the worst contrast, and crosstalk correction improved contrast. The spectral unmixing data points for mixed radionuclides (source IDs 2–4) fall under the reference line, illustrating that a greater degree of crosstalk remained in the ^{111}In image than in the ^{99m}Tc image. This discrepancy is reduced when including the high-energy photopeak for ^{111}In . To quantify these discrepancies, Table 5.8 presents the contrast RMSE. When considering the low-energy photopeak for ^{111}In , the contrast RMSE in the primary energy was 0.33, and the TEW, spectral unmixing, and gold standard methods offered an improvement of 45%, 45%, and 90%, respectively. The combined low- and high-energy photopeaks yielded a contrast RMSE of 0.28 in the primary window, and the TEW, spectral unmixing, and gold standard methods improved contrast by 46%, 54%, and 89%.

Table 5.8: Contrast of $^{99m}\text{Tc}/^{111}\text{In}$ using RMSE in simulation.

Reconstruction method	1 peak	2 peaks
	RMSE	RMSE
Primary energy window	0.33	0.28
Triple energy window	0.18	0.15
Spectral unmixing 1	0.18	0.13
Gold standard MLEM	0.033	0.030
Gold standard PPGD	0.044	0.036

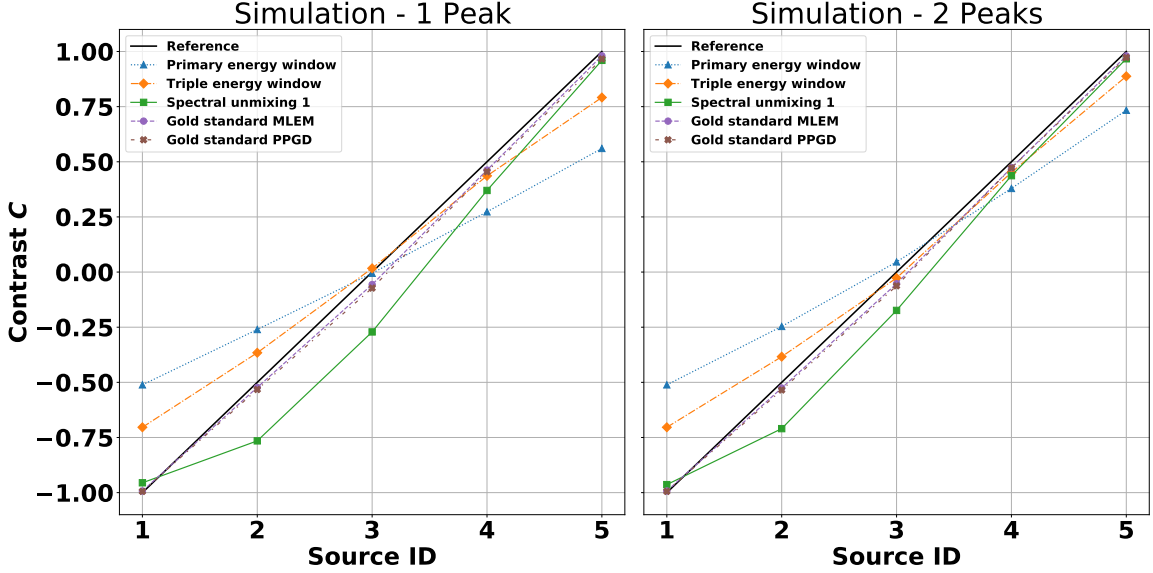


Figure 5.10: Contrast of reconstructed $^{99\text{m}}\text{Tc}/^{111}\text{In}$ line sources in simulation using the ^{111}In low-energy photopeak (left) and low- and high-energy photopeaks (right). The reference line is included to show the nominal contrast between capillary tubes with perfect crosstalk correction.

Image noise is presented in Table 5.6. Upon comparison of reconstruction methods, $^{99\text{m}}\text{Tc}$ images had the most noise with the TEW method and least noise with spectral unmixing, whereas ^{111}In images had the most noise with the TEW method and least noise with primary energy windows. The noise levels were lower and more comparable between $^{99\text{m}}\text{Tc}$ and ^{111}In than $^{99\text{m}}\text{Tc}$ and ^{123}I , and $^{99\text{m}}\text{Tc}$ images were generally less noisy than their high-energy counterparts. Thus, the spectral unmixing method arguably provided superior crosstalk correction performance when considering all aspects of quantitative accuracy and image quality.

Table 5.9: Image noise of $^{99\text{m}}\text{Tc}/^{111}\text{In}$ using CV in simulation.

Reconstruction method	1 peak		2 peaks	
	$^{99\text{m}}\text{Tc}$ CV	^{111}In CV	$^{99\text{m}}\text{Tc}$ CV	^{111}In CV
Primary energy window	0.35	0.49	-	0.51
Triple energy window	0.48	0.67	-	0.56
Spectral unmixing 1	0.31	0.56	0.35	0.53
Gold standard MLEM	0.54	0.49	-	0.52
Gold standard PPGD	0.62	0.43	-	0.48

5.6 Discussion

In this study, a novel spectral unmixing crosstalk correction method for multi-radionuclide SPECT was tested with the Cubresa Spark SiPM-based preclinical

SPECT scanner in measurement and simulation. Spectral unmixing is capable of using the entire energy spectrum to produce multiple radionuclide distributions through simultaneous synergistic reconstruction. This ensures that all detected events are accounted for during reconstruction, while conventional primary and triple energy windows may contain duplicate events between reconstructed images. This feature of spectral unmixing was found to provide superior image quality and quantitative accuracy.

To verify expected gamma camera performance when configuring mixing matrix weights, the $^{99\text{m}}\text{Tc}$ system planar sensitivity was measured as 32.9 cps/MBq, and its comparison with a previous study was found to be less than 2.7% different [107]. The absolute differences between measured and simulated sensitivities were less than 3 cps/MBq, which reflects the difficulty in fine-tuning the simulation model. Altogether, the previously validated Monte Carlo model and agreement between measured and simulated mixing weights show that simulated results are reliable and can be used to draw meaningful conclusions from spectral unmixing crosstalk correction.

The TEW method showed improved quantitation and contrast compared to primary energy windows. However, it underestimated $^{99\text{m}}\text{Tc}/^{123}\text{I}$ crosstalk by up to 17%, while $^{99\text{m}}\text{Tc}/^{111}\text{In}$ crosstalk was underestimated by 12% for $^{99\text{m}}\text{Tc}$ and overestimated by up to 10% for ^{111}In . Line source activity was also considerably overestimated for $^{99\text{m}}\text{Tc}/^{123}\text{I}$ using the TEW method in measurement and simulation, but showed improved performance with $^{99\text{m}}\text{Tc}/^{111}\text{In}$ due to the separately resolved photopeaks. Spectral unmixing provided superior quantitation and contrast to the TEW method, and was most comparable to gold standard results free of crosstalk. There appears to be some residual crosstalk from $^{99\text{m}}\text{Tc}$ in the ^{123}I and ^{111}In images in regions of mixed radionuclides, while regions of isolated activity showed excellent quantitation and contrast with spectral unmixing. The consistency of residual crosstalk could indicate a potential systematic error, perhaps due to the exclusion of the scatter term in the objective function or limitations in using sensitivities as mixing weights. Possible corrections will be explored in future work, and acquisitions with $^{99\text{m}}\text{Tc}$ and a lower-energy radionuclide may help illuminate any underlying systematic errors.

When comparing image noise with primary windows, the TEW method yielded increased image noise, while spectral unmixing images were less noisy for $^{99\text{m}}\text{Tc}$ and slightly more noisy for ^{123}I and ^{111}In . Images in measurement were also noisier than those in simulation, which was traced back to non-uniformities in measured projec-

tion images. Upon closer inspection of measured data, regions of the detector had non-uniform signal when splitting the $^{99m}\text{Tc}/^{123}\text{I}$ photopeaks with abutting energy windows. Previous challenges with the Spark identified faulty cables causing gain fluctuations between and during acquisitions, which directly impacts the system’s calibration. More specifically, random errors causing gain fluctuations can affect the position and width of photopeaks in different SiPMs, which can decouple the projection data from the mixing values. The fluctuations in local photopeak characteristics are typically not a problem when considering projection images from the entire photopeak. However, an energy window that intersects the photopeak may variably and non-uniformly split counts between projection sets that become incorrectly amplified with uniformity correction. This effect is more pronounced with significant photopeak overlap between radionuclides. Given that STIR expects fully corrected and uniform projection images as input, any non-uniformities will introduce artifacts and errors during reconstruction. This issue was not present in simulation, since the Monte Carlo model does not have local variations in the energy spectrum throughout the detector. Successful implementation of spectral unmixing with the Spark will require replacement of the problematic cables, and potential revision of the gain correction algorithm to ensure consistent photopeak characteristics throughout the detector.

An additional correction factor that is potentially problematic in quantitative multi-radionuclide SPECT images is decay correction. Decay correction ensures that reconstructed images accurately reflect the radioactive distribution at a specific time-point [163]. The radionuclides used in this study have relatively long half-lives compared to the scan duration, and decay correction was not applied. However, short-lived radionuclides may require decay correction to yield meaningful results. At this time, it is unclear how to apply decay correction to a single projection dataset containing data from multiple decay rates, although a potential solution may require correction in the image domain rather than the projection domain.

The mixing matrix plays a crucial role in optimizing the radionuclide distributions in reconstructed images. Therefore, it is important that these values are accurately determined in the absence of scatter and crosstalk. Ideally, Eq. 5.3 would provide mixing values that readily translate output images into units of radioactivity. For practicality, this work assigned system sensitivities as mixing values, then images were normalized after reconstruction. Pre-calculating sensitivities could be challenging for radionuclides with multiple γ -ray emissions having comparable energies, such as the three primary emissions from ^{67}Ga . In this case, Monte Carlo simulations would

allow for the determination of sensitivity with respect to one emission of interest in the absence of downscatter and crosstalk from other emissions. Post-reconstruction normalization can also be problematic, since discrepancies in voxel values from the reconstructed set of images can become masked and unapparent if projection data and mixing values become decoupled. Nonetheless, comparable sensitivities were calculated between measurement and simulation, as expected, and their successful application as mixing weights emphasizes the applicability of the mixing matrix as an acquisition-independent global constant.

To improve spectral unmixing accuracy, it is expected that inclusion of the background scatter term in the objective function and attenuation correction in the system matrix would improve quantitative accuracy and image quality. While the background term would be more suitable in clinical applications where scatter can account for 30–40% of photons detected in the photopeak energy window [2], this study excluded η due to minimal scatter in preclinical SPECT. According to simulation results, the $^{99\text{m}}\text{Tc}/^{123}\text{I}$ scatter estimates were 2.2% and 1.2% in primary windows for $^{99\text{m}}\text{Tc}$ and ^{123}I , respectively. Similarly, the $^{99\text{m}}\text{Tc}/^{111}\text{In}$ scatter estimates were 3.5% in the $^{99\text{m}}\text{Tc}$ primary window and 2.1% and 0.77% in the low- and high-energy windows for ^{111}In . An appropriate scatter term for the objective function could potentially be obtained from TEW estimates when photopeaks are fully resolved. Furthermore, while scatter typically leads to a slight overestimation of activity concentrations, attenuation tends to cause a considerable underestimation [164]. While attenuation corrections were not applied due to their demand on computational resources, the acrylic cylinder attenuates $\sim 20\%$ of $^{99\text{m}}\text{Tc}$ γ -rays travelling radially outwards from the central line source [161]. Therefore, further work needs to be done to assess the quantitative accuracy of spectral unmixing with scatter and attenuation correction.

When inspecting computation costs, each spectral unmixing iteration for $^{99\text{m}}\text{Tc}/^{123}\text{I}$ required ~ 30 minutes for one matrix without PSF correction and ~ 180 minutes for two matrices with PSF correction. This increased to ~ 72 minutes for $^{99\text{m}}\text{Tc}/^{111}\text{In}$ without PSF correction. Taking that into consideration, calculations with one system matrix may be suitable in cases where photons have comparable energies. Further investigation is required to identify the effects of system matrix corrections, or seemingly lack thereof, in preclinical and clinical multi-radionuclide SPECT applications of spectral unmixing crosstalk correction. To improve computational efficiency, future work could explore the use of different optimization algorithms that are more advanced than gradient descent, such as the primal dual-hybrid gradient (PDHG)

algorithm [165, 166]. This could improve computational speed with superior quantitation and image quality. Additional enhancements can also be made by enabling parallel computations of the system matrix with STIR's SPECT projectors.

5.7 Conclusion

Spectral unmixing crosstalk correction shows excellent performance in multi-radionuclide SPECT through the synergistic reconstruction of multiple radionuclide distributions. The objective function setup with SIRF and CIL provides a straightforward, generalized, and robust approach to crosstalk correction, in which the mixing matrix effectively targets photopeak overlap, and the background term effectively accounts for downscatter. The modular construction of the objective function lends itself to more advancements with SIRF and CIL, allowing spectral unmixing to be readily implemented, configured, and explored in a variety of settings with other radionuclides, gamma cameras, and collimator combinations using STIR's SPECTUB and PinholeSPECTUB projectors. Multi-radionuclide SPECT is becoming increasingly common in preclinical and clinical nuclear medicine applications to explore physiological and pathological processes. The improvements in quantitative accuracy and image quality due to the novel spectral unmixing crosstalk correction technique will benefit the exploration of a number of diseases and biological processes, and advance the practice of precision medicine through multi-radionuclide SPECT.

Chapter 6

Conclusion

The overarching aim of this thesis was to implement a simultaneous multi-radionuclide single-photon emission computed tomography (SPECT) protocol using a novel silicon photomultiplier (SiPM)-based preclinical SPECT scanner—the Cubresa Spark. A novel spectral unmixing crosstalk correction technique was successfully developed and tested, in which a mixing matrix aids in synergistically reconstructing multiple radionuclide distributions from hyperspectral data. Experimental multi-radionuclide acquisitions were measured and simulated with technetium-99m (^{99m}Tc)/iodine-123 (^{123}I) and ^{99m}Tc /indium-111 (^{111}In). The formulation of the novel spectral unmixing methodology set forth the first hypothesis:

- **Spectral unmixing can be applied to multi-radionuclide SPECT acquisitions, so long as the γ -ray emissions are unique, and the gamma camera sensitivity is known for the primary emissions.**

Each radionuclide enabled the calculation of gamma camera sensitivity across several energy windows for determining mixing matrix weights, and the emission profiles of each radionuclide provided a characteristic row of weights in the mixing matrix. This proves the first hypothesis, which is further supported by the fact that every radionuclide possesses a distinctive emission spectrum defined by specific γ -ray energies, branching ratios, half-lives, and other factors. The second hypothesis stated:

- **Spectral unmixing can allow for any multi-radionuclide SPECT acquisition to be reconstructed with a considerable improvement in quantitative accuracy and image quality compared to conventional primary and triple energy window methods.**

In proof of this hypothesis, spectral unmixing was shown to provide superior quantitative accuracy and image quality compared to conventional image reconstruction methods. Consistent performance was observed in the radionuclide combinations explored in this work, with excellent separation of radionuclides in regions of isolated activity, and good separation in regions of mixed activity.

Multi-radionuclide imaging is becoming increasingly important in modern nuclear medicine practice due to its ability to provide enhanced functional and molecular information. The utility of multi-radionuclide SPECT has already been proven in several applications, including cardiac imaging [18–25], lung function assessment [34, 35], hyperparathyroidism [36–39], and cancer imaging [40, 74]. In neuroimaging, multi-radionuclide SPECT enables diagnosis and assessment of brain function and debilitating conditions like dementia and epilepsy [26–33, 41], and numerous conditions and neurodegenerative diseases without cures are awaiting intervention. In most cases, past studies have been restricted by a gamma camera’s energy and spatial resolution, limiting the exploration of solutions with radionuclide combinations like $^{99m}\text{Tc}/^{123}\text{I}$. While past attempts at crosstalk correction claim to accurately quantify radioactivity with acceptable image quality, their methods are convoluted. They often use tunable acquisition-specific parameters with inconsistent results between radionuclides and gamma cameras, and their methods break the assumptions of the statistical model used for image reconstruction, particularly the Poisson distribution, which may not accurately represent the data characteristics. These are problems that are inherently avoided with spectral unmixing crosstalk correction.

Spectral unmixing can provide immense benefits in multi-radionuclide SPECT for comprehension of physiological, pathophysiological, and pathological processes, making it a valuable tool in both clinical and preclinical settings. This encompasses a wide range of bodily functions and conditions, as well as the mechanisms underlying disease progression. A thorough understanding of these factors is essential for healthcare professionals, researchers, and clinicians, as it plays a pivotal role in diagnosing, treating, and managing diseases. This knowledge guides the development of appropriate interventions to restore or maintain normal physiology in the presence of pathology. Complex medical research and procedures become viable options with robust and precise technology, and this thesis offers significant potential for advancing biomedical research to address a variety of health conditions.

By using open-source software and contributing back to the medical imaging community, others will benefit from the advancements of this thesis. The pioneering integration of the first open-source software for pinhole-SPECT image reconstruction could greatly benefit the research community given the recent advancements in imaging technology, especially in the preclinical setting. The software’s utility is already being explored with a clinical SPECT system for dose monitoring in boron capture neutron therapy [167, 168]. Furthermore, the spectral unmixing multi-radionuclide

SPECT software can provide unique information with respect to dynamic and temporal biological disease processes, while accelerating biomedical research. These tools can be readily implemented in clinical and preclinical settings, thereby enhancing the accuracy and versatility of diagnostic imaging and therapeutic interventions to ultimately improve patient care.

Returning to the thesis objectives, the first objective was to characterize the Cubresa Spark preclinical SPECT scanner using ^{99m}Tc according to standards defined by the National Electrical Manufacturers Association (NEMA). Results were published in the article “NEMA NU 1-2018 performance characterization and Monte Carlo model validation of the Cubresa Spark SiPM-based preclinical SPECT scanner” in *EJNMMI Physics* [107]. This work showed that a SiPM detector mitigates the need for highly magnifying pinhole collimators while preserving detailed information in projection images. The Spark offers an appreciable intrinsic spatial resolution on the order of 0.85 mm, as well as energy resolution below 15%, tomographic resolution near 1.4 mm, and a 34 cps/MBq planar sensitivity when imaging ^{99m}Tc with the single-pinhole collimator. The single-pinhole collimator investigated in this work enables high-resolution whole-body imaging of small animals, and the multi-pinhole collimator offers increased spatial resolution and sensitivity for organ-specific imaging of small animals. In simulation, the Geant4 Application for Tomographic Emission (GATE) Monte Carlo model showed excellent agreement in performance characteristics. Thus, the Spark’s performance was successfully evaluated in measurement and simulation for single-radionuclide SPECT acquisitions, and the Monte Carlo model was validated for subsequent use in nuclear medicine studies.

The second thesis objective was to integrate and test open-source pinhole-SPECT image reconstruction software in the Software for Tomographic Image Reconstruction (STIR). This objective was achieved in tandem with the NEMA study, and the Spark’s single-pinhole collimator utility was effectively extended beyond planar scintigraphy to include SPECT acquisitions. The pinhole-SPECT software was demonstrated in the publication “Integration of advanced 3D SPECT modelling for pinhole collimators into the open-source STIR framework” in *Front. Nucl. Med.* [126]. This marks the first open-source reconstruction platform configurable for pinhole collimators. Measured and simulated data were utilized to test the pinhole-SPECT system matrix modelling library, which allows corrections for attenuation, point spread function (PSF), and depth of interaction (DOI) effects. Tomographic image quality was evaluated qualitatively and quantitatively, and results showed measurable and indicative

image quality suitable for *in vivo* applications. Having benchmarked STIR’s pinhole-SPECT library, the Spark’s single-pinhole collimator could be reliably used with several reconstruction algorithms.

The final thesis objective was to develop a crosstalk correction technique that would overcome typical multi-radionuclide SPECT challenges in low-energy-resolution, high-spatial-resolution, and count-deprived settings. This objective was successfully completed by extending the pinhole-SPECT library from STIR to the Synergistic Image Reconstruction Framework (SIRF), in order to utilize the interoperable modular optimization framework of the Core Imaging Library (CIL). Altogether, this established the basis for the spectral unmixing method, which was found to have superior image quality and quantitative accuracy compared to conventional methods. The third manuscript, titled “Spectral unmixing of multi-radionuclide SPECT acquisitions using the open-source SIRF and CIL frameworks”, was achieved in collaboration with researchers at University College London (UCL). The results presented in this thesis are intended for publication in the very near future. The modular construction of the spectral unmixing objective function enables further advancements with SIRF and CIL, allowing its express implementation and exploration in several preclinical and clinical settings using a variety of radionuclides, gamma cameras, and collimator combinations modelled with STIR. Furthermore, this work revealed the importance of image uniformity when splitting a photopeak across multiple energy windows—a current issue with the Spark.

Several improvements can be made to the software and hardware discussed in this thesis. This research was performed with Ubuntu 18.04.5 LTS, which reached end of life on May 31, 2023, and newer versions have since been released. Similarly, the GATE and Geometry and Tracking (Geant4) packages are under constant development. Although the Monte Carlo model of the Spark has been validated with GATE v9.0, newer versions of the software may offer improved computational speed and accuracy by addressing any bugs and recent software developments. For example, this thesis used Geant4 version 10.06.p01, which has a bug when defining multiple radioactive sources with the general particle source. While this did not affect simulation accuracy, it did result in approximately 10% of simulations failing to run to completion, thereby requiring supervision to restart failed jobs. This bug may have been addressed in a more recent release of Geant4. When considering the pinhole-SPECT library in STIR, the DOI bug needs to be addressed to enable accurate depth of interaction corrections. Furthermore, the current pinhole-SPECT source code only allows

for SPECT acquisitions with circular orbits, but this can be readily changed to allow user-defined positions for non-circular orbits. Lastly, STIR’s SPECT libraries would benefit from parallel computations of the system matrix to improve reconstruction time.

Future work using spectral unmixing crosstalk correction with the Spark will require replacement of the Spark’s cables. Once replaced, gain and uniformity can be reassessed to ensure system stability and image uniformity when splitting photopeaks amongst energy windows. From there, *in vivo* testing can be performed, and acquisitions with three or more radionuclides could be explored for viability. The performance of all software could also be explored with the Spark’s multi-pinhole collimator following determination of the pinhole geometry. Having successfully advanced the tomographic capabilities of the Spark using the single-pinhole collimator for single- and multi-radionuclide imaging, the next most useful tool would arguably be a quantitative SPECT protocol.

Quantitative SPECT with parallel-hole collimators can be performed with STIR by converting reconstructed images from arbitrary units to activity using

$$I = I_{\text{out}} \frac{N}{S T V} \tag{6.1}$$

where I is the quantitative image, I_{out} is the output image from STIR following attenuation, scatter, and decay correction, N is the number of projections, S is the gamma camera sensitivity, T is the acquisition duration, and V is the voxel volume [169]. This will require verification for single-radionuclide pinhole-SPECT and comparisons with existing quantitative protocols [163]. As mentioned in Ch. 5, a quantitative multi-radionuclide SPECT protocol with spectral unmixing could be achieved with well-calibrated mixing matrix weights. Although the output image units are unknown and arbitrary, the mixing matrix weights scale the output intensity accordingly, and this may need to be accounted for when subsequently converting to units of activity. Therefore, it may be beneficial to use weights that represent the fraction of counts in an energy window with respect to the total counts from the radionuclide, i.e., by normalizing the weights by their sum. This might have less of an impact on the scaled output, thereby allowing a more straightforward conversion to units of activity for quantitative multi-radionuclide SPECT.

As implemented, the spectral unmixing crosstalk correction software targets photopeaks for each radionuclide. Considerations are also being made regarding the appli-

cability of the software for multi-radionuclide imaging with bremsstrahlung SPECT. This may require a different form of the acquisition model matrix that uses a dense matrix instead of a sparse block diagonal matrix. Further exploration and optimization of hyperparameters can also be pursued, including a comparison of maximum likelihood expectation maximization (MLEM) and preconditioned projected gradient descent (PPGD) results excluding regularization. Lastly, improvements could be made with more sophisticated optimization algorithms that outperform gradient descent.

Altogether, this thesis formed the basis for understanding the performance of the Cubresa Spark preclinical SPECT scanner when imaging one or more radionuclides. The spectral unmixing crosstalk correction methodology can be readily implemented with different SPECT systems, and its modular construction is suitable for more versatile advancements. Such advancements are leading to fast developments of new compounds in biomedicine for diagnostics, therapeutics, and theranostics. Successful implementation of multi-radionuclide SPECT crosstalk correction using spectral unmixing has the potential to lead to novel molecular imaging abilities and technologies, as well as accelerated studies offering unprecedented insight into the complexities of human physiology and disease progression.

Bibliography

- [1] Bushberg JT. *The essential physics of medical imaging*. 3rd. Philadelphia: Wolters Kluwer Health/Lippincott Williams & Wilkins, 2012. 1030 pp. ISBN: 978-0-7817-8057-5.
- [2] Hutton BF, Buvat I, and Beekman FJ. “Review and current status of SPECT scatter correction”. In: *Physics in Medicine & Biology* 56.14 (June 2011), R85. ISSN: 0031-9155. DOI: 10.1088/0031-9155/56/14/R01.
- [3] O’Malley JP and Ziessman HA. *Nuclear medicine and molecular imaging: the requisites*. Fifth edition. OCLC: 1329022376. Amsterdam: Elsevier, 2021. ISBN: 978-0-323-55074-1.
- [4] Alves RRN and Policarpo IdS. “Animals and Human Health: Where Do They Meet?” In: *Ethnozoology*. London: Elsevier, 2018, pp. 233–259. ISBN: 978-0-12-809913-1.
- [5] Jaszczak RJ, Coleman RE, and Whitehead FR. “Physical Factors Affecting Quantitative Measurements Using Camera-Based Single Photon Emission Computed Tomography (SPECT)”. In: *IEEE Transactions on Nuclear Science* 28.1 (Feb. 1981), pp. 69–80. ISSN: 0018-9499, 1558-1578. DOI: 10.1109/TNS.1981.4331143.
- [6] Beck JW, Jaszczak RJ, Coleman RE, Starmer CF, and Nolte LW. “Analysis of SPECT including Scatter and Attenuation Using Sophisticated Monte Carlo Modeling Methods”. In: *IEEE Transactions on Nuclear Science* 29.1 (1982), pp. 506–511. ISSN: 0018-9499. DOI: 10.1109/TNS.1982.4335896.
- [7] Vries DJ de, King MA, Soares EJ, Tsui BM, and Metz CE. “Effects of scatter subtraction on detection and quantitation in hepatic SPECT”. In: *Journal of Nuclear Medicine: Official Publication, Society of Nuclear Medicine* 40.6 (June 1999), pp. 1011–1023. ISSN: 0161-5505.
- [8] Johnson LC, Campbell DL, Hull EL, and Peterson TE. “Characterization of a high-purity germanium detector for small-animal SPECT”. In: *Physics in Medicine & Biology* 56.18 (Sept. 21, 2011), pp. 5877–5888. ISSN: 0031-9155, 1361-6560. DOI: 10.1088/0031-9155/56/18/007.
- [9] Ogawa K, Harata Y, Ichihara T, Kubo A, and Hashimoto S. “A practical method for position-dependent Compton-scatter correction in single photon emission CT”. In: *IEEE transactions on medical imaging* 10.3 (1991), pp. 408–412. ISSN: 0278-0062. DOI: 10.1109/42.97591.

- [10] Bé MM, Chisté V, Dulieu C, Kellett M, Mougeot X, Arzu A, Chechev V, Kuzmenko N, Kibédi T, Luca A, and Nichols A. *Table of Radionuclides*. Vol. 8. Monographie BIPM 5. Pavillon de Breteuil, F-92310 Sèvres, France: Bureau International des Poids et Mesures, 2016. 258 pp. ISBN: 978-92-822-2264-5.
- [11] Cunha L, Horvath I, Ferreira S, Lemos J, Costa P, Vieira D, Veres DS, Szigeti K, Summavielle T, Máthé D, and Metello LF. “Preclinical imaging: an essential ally in modern biosciences”. In: *Molecular Diagnosis & Therapy* 18.2 (Apr. 2014), pp. 153–173. ISSN: 1179-2000. DOI: 10.1007/s40291-013-0062-3.
- [12] Blower PJ. “A nuclear chocolate box: the periodic table of nuclear medicine”. In: *Dalton Transactions* 44.11 (2015), pp. 4819–4844. ISSN: 1477-9226, 1477-9234. DOI: 10.1039/C4DT02846E.
- [13] Weinstein L. *Medical Imaging: CT, PET, SPECT, and MRI*. Toronto Public Library, 2018. URL: <https://torontopl.kanopy.com/video/medical-imaging-ct-pet-spect-and-mri>.
- [14] Ovtchinnikov E, Brown R, Kolbitsch C, Pasca E, Costa-Luis C da, Gillman AG, Thomas BA, Efthimiou N, Mayer J, Wadhwa P, Ehrhardt MJ, Ellis S, Jørgensen JS, Matthews J, Prieto C, Reader AJ, Tsoumpas C, Turner M, Atkinson D, and Thielemans K. “SIRF: Synergistic Image Reconstruction Framework”. In: *Computer Physics Communications* 249 (Apr. 2020). ISSN: 00104655. DOI: 10.1016/j.cpc.2019.107087.
- [15] Wu M and Shu J. “Multimodal Molecular Imaging: Current Status and Future Directions”. In: *Contrast Media & Molecular Imaging* 2018 (2018), p. 1382183. ISSN: 1555-4317. DOI: 10.1155/2018/1382183.
- [16] Schillaci O, Danieli R, Manni C, and Simonetti G. “Is SPECT/CT with a hybrid camera useful to improve scintigraphic imaging interpretation?” In: *Nuclear Medicine Communications* 25.7 (July 2004), pp. 705–710. ISSN: 0143-3636. DOI: 10.1097/01.mmm.0000130240.83949.54.
- [17] Lim MMD, Gnerre J, and Gerard P. “Mechanisms of Uptake of Common Radiopharmaceuticals”. In: *RadioGraphics* 38.5 (Sept. 2018), pp. 1550–1551. ISSN: 0271-5333, 1527-1323. DOI: 10.1148/rg.2018180072.
- [18] Kadrmas DJ, Frey EC, and Tsui BMW. “Simultaneous technetium-99m/thallium-201 SPECT imaging with model-based compensation for cross-contaminating effects”. In: *Physics in Medicine & Biology* 44.7 (July 1, 1999), pp. 1843–1860. ISSN: 0031-9155, 1361-6560. DOI: 10.1088/0031-9155/44/7/319.
- [19] Ouyang J, Zhu X, Trott CM, and El Fakhri G. “Quantitative simultaneous $^{99m}\text{Tc}/^{123}\text{I}$ cardiac SPECT using MC-JOSEM”. In: *Medical Physics* 36.2 (Feb. 2009), pp. 602–611. ISSN: 0094-2405. DOI: 10.1118/1.3063544.

- [20] Kacperski K, Erlandsson K, Ben-Haim S, and Hutton BF. “Iterative deconvolution of simultaneous ^{99m}Tc and ^{201}Tl projection data measured on a CdZnTe-based cardiac SPECT scanner”. In: *Physics in Medicine & Biology* 56.5 (Mar. 7, 2011), pp. 1397–1414. ISSN: 0031-9155, 1361-6560. DOI: 10.1088/0031-9155/56/5/012.
- [21] Du Y, Links JM, Becker L, DiPaula AF, Frank T, Schuleri KH, Lardo AC, and Frey EC. “Evaluation of simultaneous $^{201}\text{Tl}/^{99m}\text{Tc}$ dual-isotope cardiac SPECT imaging with model-based crosstalk compensation using canine studies”. In: *Journal of Nuclear Cardiology* 21.2 (Apr. 2014), pp. 329–340. ISSN: 1071-3581, 1532-6551. DOI: 10.1007/s12350-013-9842-8.
- [22] Du Y, Bhattacharya M, and Frey EC. “Simultaneous Tc-99m/I-123 dual-radionuclide myocardial perfusion/innervation imaging using Siemens IQ-SPECT with SMARTZOOM collimator”. In: *Physics in Medicine & Biology* 59.11 (June 7, 2014), pp. 2813–2828. ISSN: 1361-6560. DOI: 10.1088/0031-9155/59/11/2813.
- [23] Holstensson M, Erlandsson K, Poludniowski G, Ben-Haim S, and Hutton BF. “Model-based correction for scatter and tailing effects in simultaneous ^{99m}Tc and ^{123}I imaging for a CdZnTe cardiac SPECT camera”. In: *Physics in Medicine & Biology* 60.8 (Mar. 2015). Publisher: IOP Publishing, p. 3045. ISSN: 0031-9155. DOI: 10.1088/0031-9155/60/8/3045.
- [24] Fan P, Hutton BF, Holstensson M, Ljungberg M, Hendrik Pretorius P, Prasad R, Ma T, Liu Y, Wang S, Thorn SL, Stacy MR, Sinusas AJ, and Liu C. “Scatter and crosstalk corrections for $^{99m}\text{Tc}/^{123}\text{I}$ dual-radionuclide imaging using a CZT SPECT system with pinhole collimators”. In: *Medical Physics* 42.12 (Nov. 11, 2015), pp. 6895–6911. ISSN: 00942405. DOI: 10.1118/1.4934830.
- [25] Ko T, Utanohara Y, Suzuki Y, Kurihara M, Iguchi N, Umemura J, Sumiyoshi T, and Tomoike H. “A preliminary feasibility study of simultaneous dual-isotope imaging with a solid-state dedicated cardiac camera for evaluating myocardial perfusion and fatty acid metabolism”. In: *Heart and Vessels* 31.1 (Jan. 2016), pp. 38–45. ISSN: 0910-8327, 1615-2573. DOI: 10.1007/s00380-014-0578-4.
- [26] Devous MD, Lowe JL, and Payne JK. “Dual-isotope brain SPECT imaging with technetium-99m and iodine-123: validation by phantom studies”. In: *Journal of Nuclear Medicine: Official Publication, Society of Nuclear Medicine* 33.11 (Nov. 1992), pp. 2030–2035. ISSN: 0161-5505.
- [27] Brinkmann BH, O’Connor MK, O’Brien TJ, Mullan BP, So EL, and Robb RA. “Dual-isotope SPECT using simultaneous acquisition of ^{99m}Tc and ^{123}I radioisotopes: a double-injection technique for peri-ictal functional neuroimaging”. In: *Journal of Nuclear Medicine: Official Publication, Society of Nuclear Medicine* 40.4 (Apr. 1999), pp. 677–684. ISSN: 0161-5505.

- [28] El Fakhri G, Moore SC, Maksud P, Aurengo A, and Kijewski MF. “Absolute activity quantitation in simultaneous $^{123}\text{I}/^{99\text{m}}\text{Tc}$ brain SPECT”. In: *Journal of Nuclear Medicine: Official Publication, Society of Nuclear Medicine* 42.2 (Feb. 2001), pp. 300–308. ISSN: 0161-5505.
- [29] Du Y, Frey EC, Wang WT, and Tsui BMW. “Optimization of acquisition energy windows in simultaneous $^{99\text{m}}\text{Tc}/^{123}\text{I}$ brain SPECT”. In: *IEEE Transactions on Nuclear Science* 50.5 (Oct. 2003), pp. 1556–1561. ISSN: 0018-9499. DOI: 10.1109/TNS.2003.817404.
- [30] Hapdey S, Soret M, and Buvat I. “Quantification in simultaneous $^{99\text{m}}\text{Tc}/^{123}\text{I}$ brain SPECT using generalized spectral factor analysis: a Monte Carlo study”. In: *Physics in Medicine & Biology* 51.23 (Nov. 2006), p. 6157. ISSN: 0031-9155. DOI: 10.1088/0031-9155/51/23/015.
- [31] Du Y, Tsui BMW, and Frey EC. “Model-based crosstalk compensation for simultaneous $^{99\text{m}}\text{Tc}/^{123}\text{I}$ dual-isotope brain SPECT imaging”. In: *Medical Physics* 34.9 (Aug. 14, 2007), pp. 3530–3543. ISSN: 00942405. DOI: 10.1118/1.2768863.
- [32] Du Y and Frey EC. “Quantitative evaluation of simultaneous reconstruction with model-based crosstalk compensation for $^{99\text{m}}\text{Tc}/^{123}\text{I}$ dual-isotope simultaneous acquisition brain SPECT”. In: *Medical Physics* 36.6 (May 5, 2009), pp. 2021–2033. ISSN: 00942405. DOI: 10.1118/1.3120411.
- [33] Tsartsalis S, Tournier BB, Habiby S, Ben Hamadi M, Barca C, Ginovart N, and Millet P. “Dual-radiotracer translational SPECT neuroimaging. Comparison of three methods for the simultaneous brain imaging of $\text{D}_{2/3}$ and 5-HT_{2A} receptors”. In: *NeuroImage* 176 (Aug. 2018), pp. 528–540. ISSN: 10538119. DOI: 10.1016/j.neuroimage.2018.04.063.
- [34] Klumper A and Zwijnenburg A. “Dual isotope ($^{81\text{m}}\text{Kr}$ and $^{99\text{m}}\text{Tc}$) SPECT in lung function diagnosis”. In: *Physics in Medicine & Biology* 31.7 (July 1, 1986), pp. 751–761. ISSN: 0031-9155, 1361-6560. DOI: 10.1088/0031-9155/31/7/005.
- [35] Hopkins SR. “Ventilation/Perfusion Relationships and Gas Exchange: Measurement Approaches”. In: *Comprehensive Physiology*. Ed. by Terjung R. 1st ed. Wiley, July 8, 2020, pp. 1155–1205. ISBN: 978-0-470-65071-4. DOI: 10.1002/cphy.c180042.
- [36] Sandrock D, Merino MJ, Norton JA, and Neumann RD. “Parathyroid imaging by Tc/Tl scintigraphy”. In: *European Journal of Nuclear Medicine* 16.8 (1990), pp. 607–613. ISSN: 0340-6997. DOI: 10.1007/BF00998157.
- [37] Neumann DR. “Simultaneous dual-isotope SPECT imaging for the detection and characterization of parathyroid pathology”. In: *Journal of Nuclear Medicine: Official Publication, Society of Nuclear Medicine* 33.1 (Jan. 1992), pp. 131–134. ISSN: 0161-5505.

- [38] Neumann DR, Obuchowski NA, and DiFilippo FP. “Preoperative $^{123}\text{I}/^{99\text{m}}\text{Tc}$ -Sestamibi Subtraction SPECT and SPECT/CT in Primary Hyperparathyroidism”. In: *Journal of Nuclear Medicine* 49.12 (Nov. 7, 2008), pp. 2012–2017. ISSN: 0161-5505. DOI: 10.2967/jnumed.108.054858.
- [39] Shcherbinin S, Chamoiseau S, and Celler A. “Quantitative image reconstruction for dual-isotope parathyroid SPECT/CT: phantom experiments and sample patient studies”. In: *Physics in Medicine & Biology* 57.15 (July 2012). Publisher: IOP Publishing, p. 4755. ISSN: 0031-9155. DOI: 10.1088/0031-9155/57/15/4755.
- [40] Guo Z, Gao M, Zhang D, Li Y, Song M, Zhuang R, Su X, Chen G, Liu T, Liu P, Wu H, Du J, and Zhang X. “Simultaneous SPECT imaging of multi-targets to assist in identifying hepatic lesions”. In: *Scientific Reports* 6.1 (Sept. 2016). ISSN: 2045-2322. DOI: 10.1038/srep28812.
- [41] Takeuchi W, Suzuki A, Shiga T, Kubo N, Morimoto Y, Ueno Y, Kobashi K, Umegaki K, and Tamaki N. “Simultaneous Tc-99m and I-123 dual-radionuclide imaging with a solid-state detector-based brain-SPECT system and energy-based scatter correction”. In: *EJNMMI Physics* 3.1 (Dec. 2016), p. 10. ISSN: 2197-7364. DOI: 10.1186/s40658-016-0147-2.
- [42] Könik A, O’Donoghue JA, Wahl RL, Graham MM, and Van Den Abbeele AD. “Theranostics: The Role of Quantitative Nuclear Medicine Imaging”. In: *Seminars in Radiation Oncology* 31.1 (Jan. 2021), pp. 28–36. ISSN: 10534296. DOI: 10.1016/j.semradonc.2020.07.003.
- [43] Suzuki A, Takeuchi W, Ueno Y, Kobashi K, Toyonaga T, Shiga T, and Tamaki N. “Monte Carlo-based scatter correction considering the tailing effect of a CdTe detector for dual-isotope brain SPECT imaging”. In: *Biomedical Physics & Engineering Express* 2.4 (July 29, 2016), p. 045010. ISSN: 2057-1976. DOI: 10.1088/2057-1976/2/4/045010.
- [44] Shiga T, Suzuki A, Sakurai K, Kurita T, Takeuchi W, Toyonaga T, Hirata K, Kobashi K, Katoh C, Kubo N, and Tamaki N. “Dual Isotope SPECT Study With Epilepsy Patients Using Semiconductor SPECT System”. In: *Clinical Nuclear Medicine* 42.9 (Sept. 2017), pp. 663–668. ISSN: 0363-9762. DOI: 10.1097/RLU.0000000000001732.
- [45] Kijewski MF. “Positron Emission Tomography (PET) and Single-Photon Emission Computed Tomography (SPECT) Physics”. In: *Handbook of Neuro-Oncology Neuroimaging*. Elsevier, 2016, pp. 353–358. ISBN: 978-0-12-800945-1. DOI: 10.1016/B978-0-12-800945-1.00032-X.
- [46] Cherry SR, Sorenson JA, and Phelps ME. *Physics in nuclear medicine*. 4th ed. Philadelphia: Elsevier/Saunders, 2012. 523 pp. ISBN: 978-1-4160-5198-5.

- [47] Van Mullekom Group. *Collimators for Nuclear Medicine*. Nuclear Fields. 2021. URL: <https://nuclearfields.com/collimators-nuclear-medicine.htm> (visited on 12/15/2022).
- [48] Van Audenhaege K, Van Holen R, Vandenberghe S, Vanhove C, Metzler SD, and Moore SC. “Review of SPECT collimator selection, optimization, and fabrication for clinical and preclinical imaging”. In: *Medical Physics* 42.8 (Aug. 2015), pp. 4796–4813. ISSN: 2473-4209. DOI: 10.1118/1.4927061.
- [49] Jaszczak RJ, Li J, Wang H, Zalutsky MR, and Coleman RE. “Pinhole collimation for ultra-high-resolution, small-field-of-view SPECT”. In: *Physics in Medicine & Biology* 39.3 (Mar. 1, 1994), pp. 425–437. ISSN: 0031-9155, 1361-6560. DOI: 10.1088/0031-9155/39/3/010.
- [50] Floyd JL, Mann RB, and Shaw A. “Changes in quantitative SPECT thallium-201 results associated with the use of energy-weighted acquisition”. In: *Journal of Nuclear Medicine: Official Publication, Society of Nuclear Medicine* 32.5 (May 1991), pp. 805–807. ISSN: 0161-5505.
- [51] Jiang W, Chalich Y, and Deen MJ. “Sensors for Positron Emission Tomography Applications”. In: *Sensors (Basel, Switzerland)* 19.22 (Nov. 17, 2019). ISSN: 1424-8220. DOI: 10.3390/s19225019.
- [52] Bernsen MR, Vaissier PEB, Van Holen R, Booij J, Beekman FJ, and Jong M de. “The role of preclinical SPECT in oncological and neurological research in combination with either CT or MRI”. In: *European Journal of Nuclear Medicine and Molecular Imaging* 41 (S1 May 2014), pp. 36–49. ISSN: 1619-7070, 1619-7089. DOI: 10.1007/s00259-013-2685-3.
- [53] Aguiar P, Iglesias A, Couce B, and Lois C. “A feasibility study on the use of arrays of discrete SiPMs for MR compatible LYSO readout using Monte Carlo simulation”. In: *Journal of Instrumentation* 7.6 (June 6, 2012), P06002–P06002. ISSN: 1748-0221. DOI: 10.1088/1748-0221/7/06/P06002.
- [54] Carminati M, Baratelli FM, Massara M, Occhipinti M, Nagy K, Nyitrai Z, Czeller M, Kuhne A, Niendorf T, Valtorta S, Belloli S, Moresco RM, Savi A, Iadanza A, Falini A, Politi LS, Cadioli M, and Fiorini C. “Simultaneous SPECT/MR Imaging with a SiPM-Based Preclinical Insert”. In: *2018 IEEE Nuclear Science Symposium and Medical Imaging Conference Proceedings (NSS/MIC)*. 2018 IEEE Nuclear Science Symposium and Medical Imaging Conference (NSS/MIC). Sydney, Australia: IEEE, Nov. 2018, pp. 1–3. ISBN: 978-1-5386-8494-8. DOI: 10.1109/NSSMIC.2018.8824631.
- [55] D’Adda I, Morahan AJ, Carminati M, Erlandsson K, Ljungberg M, Hutton BF, and Fiorini C. “A Statistical DOI Estimation Algorithm for a SiPM-Based Clinical SPECT Insert”. In: *IEEE Transactions on Radiation and Plasma Medical Sciences* 6.7 (Sept. 2022), pp. 771–777. ISSN: 2469-7311, 2469-7303. DOI: 10.1109/TRPMS.2022.3140411.

- [56] Dillenseger JP, Choquet P, Snay ER, and Fragoso Costa P. “Why the preclinical imaging field needs nuclear medicine technologists and radiographers?” In: *European Journal of Hybrid Imaging* 4.1 (July 20, 2020), p. 12. ISSN: 2510-3636. DOI: 10.1186/s41824-020-00081-z.
- [57] Franc BL, Acton PD, Mari C, and Hasegawa BH. “Small-Animal SPECT and SPECT/CT: Important Tools for Preclinical Investigation”. In: *Journal of Nuclear Medicine* 49.10 (Sept. 15, 2008), pp. 1651–1663. ISSN: 0161-5505. DOI: 10.2967/jnumed.108.055442.
- [58] DeBay DR, Reid GA, Pottie IR, Martin E, Bowen CV, and Darvesh S. “Targeting butyrylcholinesterase for preclinical single photon emission computed tomography (SPECT) imaging of Alzheimer’s disease”. In: *Alzheimer’s & Dementia: Translational Research & Clinical Interventions* 3.2 (June 2017), pp. 166–176. ISSN: 23528737. DOI: 10.1016/j.trci.2017.01.005.
- [59] Bryda EC. “The Mighty Mouse: the impact of rodents on advances in biomedical research”. In: *Missouri Medicine* 110.3 (2013), pp. 207–211. ISSN: 0026-6620.
- [60] Hume SP, Gunn RN, and Jones T. “Pharmacological constraints associated with positron emission tomographic scanning of small laboratory animals”. In: *European Journal of Nuclear Medicine* 25.2 (Feb. 1998), pp. 173–176. ISSN: 0340-6997. DOI: 10.1007/s002590050211.
- [61] Acton PD and Kung HF. “Small animal imaging with high resolution single photon emission tomography”. In: *Nuclear Medicine and Biology* 30.8 (Nov. 2003), pp. 889–895. ISSN: 0969-8051. DOI: 10.1016/s0969-8051(03)00112-4.
- [62] Stout D, Berr SS, LeBlanc A, Kalen JD, Osborne D, Price J, Schiffer W, Kuntner C, and Wall J. “Guidance for Methods Descriptions Used in Preclinical Imaging Papers”. In: *Molecular Imaging* 12.7 (Oct. 1, 2013), p. 7290.2013.00055. ISSN: 1536-0121. DOI: 10.2310/7290.2013.00055.
- [63] Austin DW, Paulus MJ, Gleason SS, Mintzer RA, Siegel SB, Figueroa SD, Hoffman TJ, and Wall JS. “Design and Performance of a New SPECT Detector for Multimodality Small Animal Imaging Platforms”. In: *2006 IEEE Nuclear Science Symposium Conference Record*. 2006 IEEE Nuclear Science Symposium Conference Record. San Diego, CA, USA: IEEE, 2006, pp. 3008–3011. ISBN: 978-1-4244-0560-2. DOI: 10.1109/NSSMIC.2006.356508.
- [64] Deleye S, Van Holen R, Verhaeghe J, Vandenberghe S, Stroobants S, and Staelens S. “Performance evaluation of small-animal multipinhole μ SPECT scanners for mouse imaging”. In: *European Journal of Nuclear Medicine and Molecular Imaging* 40.5 (May 2013), pp. 744–758. ISSN: 1619-7070, 1619-7089. DOI: 10.1007/s00259-012-2326-2.

- [65] Magota K, Kubo N, Kuge Y, Nishijima Ki, Zhao S, and Tamaki N. “Performance characterization of the Inveon preclinical small-animal PET/SPECT/CT system for multimodality imaging”. In: *European Journal of Nuclear Medicine and Molecular Imaging* 38.4 (Apr. 2011), pp. 742–752. ISSN: 1619-7070, 1619-7089. DOI: 10.1007/s00259-010-1683-y.
- [66] McElroy DP, MacDonald LR, Beekman FJ, Yuchuan Wang, Patt BE, Iwanczyk JS, Tsui BMW, and Hoffman EJ. “Performance evaluation of A-SPECT: a high resolution desktop pinhole SPECT system for imaging small animals”. In: *IEEE Transactions on Nuclear Science* 49.5 (Oct. 2002), pp. 2139–2147. ISSN: 0018-9499. DOI: 10.1109/TNS.2002.803801.
- [67] Have F van der, Vastenhouw B, Ramakers RM, Branderhorst W, Krah JO, Ji C, Staelens SG, and Beekman FJ. “U-SPECT-II: An Ultra-High-Resolution Device for Molecular Small-Animal Imaging”. In: *Journal of Nuclear Medicine* 50.4 (Mar. 16, 2009), pp. 599–605. ISSN: 0161-5505. DOI: 10.2967/jnumed.108.056606.
- [68] Ljungberg M, Strand SE, and King MA. *Monte Carlo calculations in nuclear medicine: applications in diagnostic imaging*. OCLC: 818750107. Boca Raton: CRC Press, 2013. ISBN: 978-1-4398-4110-5. URL: <http://www.crcnetbase.com/isbn/9781439841099>.
- [69] Jaszczak RJ, Greer KL, Floyd CE, Harris CC, and Coleman RE. “Improved SPECT quantification using compensation for scattered photons”. In: *Journal of Nuclear Medicine: Official Publication, Society of Nuclear Medicine* 25.8 (Aug. 1984), pp. 893–900. ISSN: 0161-5505.
- [70] Cot A, Falcón C, Crespo C, Sempau J, Pareto D, Bullich S, Lomeña F, Calviño F, Pavía J, and Ros D. “Absolute quantification in dopaminergic neurotransmission SPECT using a Monte Carlo-based scatter correction and fully 3-dimensional reconstruction”. In: *Journal of Nuclear Medicine: Official Publication, Society of Nuclear Medicine* 46.9 (Sept. 2005), pp. 1497–1504. ISSN: 0161-5505.
- [71] Tharwat A. “Independent component analysis: An introduction”. In: *Applied Computing and Informatics* 17.2 (Apr. 29, 2021), pp. 222–249. ISSN: 2634-1964, 2210-8327. DOI: 10.1016/j.aci.2018.08.006.
- [72] Chang CJ, Huang WS, Su KH, and Chen JC. “Separation of two radionuclides in simultaneous dual-isotope imaging with independent component analysis”. In: *Biomedical Engineering: Applications, Basis and Communications* 18.5 (Oct. 25, 2006), pp. 264–269. ISSN: 1016-2372, 1793-7132. DOI: 10.4015/S1016237206000403.

- [73] Yang BH, Wang SJ, Chou YH, and Chen JC. “Simultaneous Dual-Isotope SPECT Imaging Using Independent Component Analysis Based on Wavelet Transformation: Wavelet Based Dual-Isotope SPECT Imaging Using ICA Analysis”. In: *2009 2nd International Congress on Image and Signal Processing*. 2009 2nd International Congress on Image and Signal Processing (CISP). Tianjin, China: IEEE, Oct. 2009, pp. 1–3. ISBN: 978-1-4244-4129-7. DOI: 10.1109/CISP.2009.5304064.
- [74] Xu B, Shokeen M, Sudlow GP, Harpstrite SE, Liang K, Cheney PP, Edwards WB, Sharma V, Laforest R, Akers WJ, and Achilefu S. “Utilizing the Multiradionuclide Resolving Power of SPECT and Dual Radiolabeled Single Molecules to Assess Treatment Response of Tumors”. In: *Molecular Imaging and Biology* 17.5 (Oct. 2015), pp. 671–679. ISSN: 1860-2002. DOI: 10.1007/s11307-015-0842-8.
- [75] King MA, Hademenos GJ, and Glick SJ. “A dual-photopeak window method for scatter correction”. In: *Journal of Nuclear Medicine: Official Publication, Society of Nuclear Medicine* 33.4 (Apr. 1992), pp. 605–612. ISSN: 0161-5505.
- [76] Pretorius PH, Rensburg AJ van, Aswegen A van, Lötter MG, Serfontein DE, and Herbst CP. “The channel ratio method of scatter correction for radionuclide image quantitation”. In: *Journal of Nuclear Medicine: Official Publication, Society of Nuclear Medicine* 34.2 (Feb. 1993), pp. 330–335. ISSN: 0161-5505.
- [77] Vija H, Kaplan MS, and Haynor DR. “Simultaneous estimation of SPECT activity and attenuation distributions from measured phantom data using a differential attenuation method”. In: *1999 IEEE Nuclear Science Symposium. Conference Record. 1999 Nuclear Science Symposium and Medical Imaging Conference (Cat. No.99CH37019)*. 1999 IEEE Nuclear Science Symposium. Conference Record. 1999 IEEE Nuclear Science Symposium and Medical Imaging Conference. Vol. 2. Seattle, WA, USA: IEEE, 1999, pp. 884–888. ISBN: 978-0-7803-5696-2. DOI: 10.1109/NSSMIC.1999.845805.
- [78] Buvat I, Hapdey S, Benali H, Todd-Pokropek A, and Paola R. “Spectral Factor Analysis for Multi-isotope Imaging in Nuclear Medicine”. In: *Lecture Notes in Computer Science. Information Processing in Medical Imaging*. Vol. 1613. Visegrád, Hungary: Springer-Verlag Berlin Heidelberg, Jan. 1999, pp. 442–447. DOI: 10.1007/3-540-48714-X_43.
- [79] El Fakhri G, Buvat I, Benali H, Todd-Pokropek A, and Di Paola R. “Relative impact of scatter, collimator response, attenuation, and finite spatial resolution corrections in cardiac SPECT”. In: *Journal of Nuclear Medicine: Official Publication, Society of Nuclear Medicine* 41.8 (Aug. 2000), pp. 1400–1408. ISSN: 0161-5505.

- [80] Ljungberg M, King MA, Hademenos GJ, and Strand SE. “Comparison of four scatter correction methods using Monte Carlo simulated source distributions”. In: *Journal of Nuclear Medicine: Official Publication, Society of Nuclear Medicine* 35.1 (Jan. 1994), pp. 143–151. ISSN: 0161-5505.
- [81] King MA, deVries DJ, Pan TS, Pretorius P, and Case JA. “An investigation of the filtering of TEW scatter estimates used to compensate for scatter with ordered subset reconstructions”. In: *IEEE Transactions on Nuclear Science* 44.3 (June 1997), pp. 1140–1145. ISSN: 00189499. DOI: 10.1109/23.596978.
- [82] Shcherbinin S, Celler A, Trummer M, and Humphries T. “An APD-based iterative reconstruction method for simultaneous technetium-99m/iodine-123 SPECT imaging”. In: *Physica Medica* 25.4 (Dec. 2009), pp. 192–200. ISSN: 11201797. DOI: 10.1016/j.ejmp.2009.01.003.
- [83] Kamphuis C, Beekman FJ, Rijk PP van, and Viergever MA. “Dual matrix ordered subsets reconstruction for accelerated 3D scatter compensation in single-photon emission tomography”. In: *European Journal of Nuclear Medicine* 25.1 (Jan. 1998), pp. 8–18. ISSN: 0340-6997. DOI: 10.1007/s002590050188.
- [84] Zeng GL and Gullberg GT. “Unmatched projector/backprojector pairs in an iterative reconstruction algorithm”. In: *IEEE transactions on medical imaging* 19.5 (May 2000), pp. 548–555. ISSN: 0278-0062. DOI: 10.1109/42.870265.
- [85] Farncombe TH, Gifford HC, Narayanan MV, Pretorius PH, Frey EC, and King MA. “Assessment of scatter compensation strategies for ^{67}Ga SPECT using numerical observers and human LROC studies”. In: *Journal of Nuclear Medicine: Official Publication, Society of Nuclear Medicine* 45.5 (May 2004), pp. 802–812. ISSN: 0161-5505.
- [86] Axelsson B, Msaki P, and Israelsson A. “Subtraction of Compton-scattered photons in single-photon emission computerized tomography”. In: *Journal of Nuclear Medicine: Official Publication, Society of Nuclear Medicine* 25.4 (Apr. 1984), pp. 490–494. ISSN: 0161-5505.
- [87] Feng J, Penney BC, and Pan X. “Convolution estimation of spill-down and scatter in dual isotope ($^{99\text{m}}\text{Tc}/^{111}\text{In}$) SPECT”. In: *Medical Imaging 2002*. Ed. by Antonuk LE and Yaffe MJ. San Diego, CA, May 2, 2002, pp. 73–81. DOI: 10.1117/12.465618.
- [88] Larsson A, Ljungberg M, Mo SJ, Riklund K, and Johansson L. “Correction for scatter and septal penetration using convolution subtraction methods and model-based compensation in ^{123}I brain SPECT imaging—a Monte Carlo study”. In: *Physics in Medicine & Biology* 51.22 (Nov. 21, 2006), pp. 5753–5767. ISSN: 0031-9155. DOI: 10.1088/0031-9155/51/22/003.

- [89] Welsh JS. “Physics of Novel Radiation Modalities: Radionuclides”. Education. Education. 2015 ASTRO Annual Refresher Course. New Orleans, USA, Mar. 6, 2015. URL: https://www.astro.org/uploadedFiles/Main_Site/Meetings_and_Events/2015_Annual_Refresher_Course/Meeting_Program/Welsh.pdf (visited on 05/08/2023).
- [90] Tipler PA and Llewellyn RA. *Modern physics*. 6th ed. New York: W. H. Freeman and Co, 2012. 1 p. ISBN: 978-1-4292-5078-8.
- [91] Attix FH. *Introduction to radiological physics and radiation dosimetry*. New York: Wiley, 1986. 607 pp. ISBN: 978-0-471-01146-0.
- [92] Turner JE. *Atoms, Radiation, and Radiation Protection*. 1st ed. Wiley, May 11, 2007. ISBN: 978-3-527-61697-8. DOI: 10.1002/9783527616978.
- [93] Krane KS and Halliday D. *Introductory nuclear physics*. New York: Wiley, 1987. 845 pp. ISBN: 978-0-471-80553-3.
- [94] Sundaresan MK. *Handbook of particle physics*. CRC series in pure and applied physics. Boca Raton, Fla: CRC Press, 2001. 446 pp. ISBN: 978-0-8493-0215-2.
- [95] Compton AH. “A Quantum Theory of the Scattering of X-rays by Light Elements”. In: *Physical Review* 21.5 (May 1, 1923), pp. 483–502. ISSN: 0031-899X. DOI: 10.1103/PhysRev.21.483.
- [96] Knoll GF. *Radiation detection and measurement*. 4th. Hoboken, N.J: John Wiley, 2010. 830 pp. ISBN: 978-0-470-13148-0.
- [97] Anger HO. “Scintillation Camera”. In: *Review of Scientific Instruments* 29.1 (Jan. 1958), pp. 27–33. ISSN: 0034-6748, 1089-7623. DOI: 10.1063/1.1715998.
- [98] Murayama H and Hasegawa T. “Hal Oscar Anger, D.Sc. (hon.) (1920–2005): a pioneer in nuclear medicine instrumentation”. In: *Radiological Physics and Technology* 7.1 (Jan. 2014), pp. 1–4. ISSN: 1865-0333, 1865-0341. DOI: 10.1007/s12194-013-0252-z.
- [99] Bruyant PP. “Analytic and iterative reconstruction algorithms in SPECT”. In: *Journal of Nuclear Medicine: Official Publication, Society of Nuclear Medicine* 43.10 (Oct. 2002), pp. 1343–1358. ISSN: 0161-5505.
- [100] Shepp LA and Vardi Y. “Maximum likelihood reconstruction for emission tomography”. In: *IEEE transactions on medical imaging* 1.2 (1982), pp. 113–122. ISSN: 0278-0062. DOI: 10.1109/TMI.1982.4307558.
- [101] Hudson HM and Larkin RS. “Accelerated image reconstruction using ordered subsets of projection data”. In: *IEEE transactions on medical imaging* 13.4 (1994), pp. 601–609. ISSN: 0278-0062. DOI: 10.1109/42.363108.

- [102] Papoutsellis E, Ametova E, Delplancke C, Fardell G, Jørgensen JS, Pasca E, Turner M, Warr R, Lionheart WRB, and Withers PJ. “Core Imaging Library - Part II: multichannel reconstruction for dynamic and spectral tomography”. In: *Philosophical Transactions of the Royal Society A: Mathematical, Physical and Engineering Sciences* 379.2204 (Aug. 23, 2021), p. 20200193. ISSN: 1364-503X, 1471-2962. DOI: 10.1098/rsta.2020.0193.
- [103] Shao W, Rowe SP, and Du Y. “Artificial intelligence in single photon emission computed tomography (SPECT) imaging: a narrative review”. In: *Annals of Translational Medicine* 9.9 (May 2021), pp. 820–820. ISSN: 23055839, 23055847. DOI: 10.21037/atm-20-5988.
- [104] Arabi H, AkhavanAllaf A, Sanaat A, Shiri I, and Zaidi H. “The promise of artificial intelligence and deep learning in PET and SPECT imaging”. In: *Physica Medica* 83 (Mar. 2021), pp. 122–137. ISSN: 11201797. DOI: 10.1016/j.ejmp.2021.03.008.
- [105] Saboury B, Bradshaw T, Boellaard R, Buvat I, Dutta J, Hatt M, Jha AK, Li Q, Liu C, McMeeKin H, Morris MA, Scott PJ, Siegel E, Sunderland JJ, Pandit-Taskar N, Wahl RL, Zuehlsdorff S, and Rahmim A. “Artificial Intelligence in Nuclear Medicine: Opportunities, Challenges, and Responsibilities Toward a Trustworthy Ecosystem”. In: *Journal of Nuclear Medicine* 64.2 (Feb. 2023), pp. 188–196. ISSN: 0161-5505, 2159-662X. DOI: 10.2967/jnumed.121.263703.
- [106] Reader AJ and Pan B. “AI for PET image reconstruction”. In: *The British Journal of Radiology* 96.1150 (Oct. 2023), p. 20230292. ISSN: 0007-1285, 1748-880X. DOI: 10.1259/bjr.20230292.
- [107] Strugari ME, DeBay DR, Beyea SD, and Brewer KD. “NEMA NU 1-2018 performance characterization and Monte Carlo model validation of the Cubresa Spark SiPM-based preclinical SPECT scanner”. In: *EJNMMI Physics* 10.1 (June 1, 2023), p. 35. ISSN: 2197-7364. DOI: 10.1186/s40658-023-00555-6.
- [108] Herzog H. “*In vivo* functional imaging with SPECT and PET”. In: *Radiochimica Acta* 89.4 (Apr. 1, 2001), pp. 203–214. ISSN: 2193-3405, 0033-8230. DOI: 10.1524/ract.2001.89.4-5.203.
- [109] Weber WA, Czernin J, Anderson CJ, Badawi RD, Barthel H, Bengel F, Bodei L, Buvat I, DiCarli M, Graham MM, Grimm J, Herrmann K, Kostakoglu L, Lewis JS, Mankoff DA, Peterson TE, Schelbert H, Schöder H, Siegel BA, and Strauss HW. “The Future of Nuclear Medicine, Molecular Imaging, and Theranostics”. In: *Journal of Nuclear Medicine* 61 (Supplement 2 Dec. 2020), 263S–272S. ISSN: 0161-5505, 2159-662X. DOI: 10.2967/jnumed.120.254532.

- [110] Gomes Marin JF, Nunes RF, Coutinho AM, Zaniboni EC, Costa LB, Barbosa FG, Queiroz MA, Cerri GG, and Buchpiguel CA. “Theranostics in Nuclear Medicine: Emerging and Re-emerging Integrated Imaging and Therapies in the Era of Precision Oncology”. In: *RadioGraphics* 40.6 (Oct. 2020), pp. 1715–1740. ISSN: 0271-5333, 1527-1323. DOI: 10.1148/rg.2020200021.
- [111] Marquis H, Deidda D, Gillman A, Willowson KP, Gholami Y, Hioki T, Eslick E, Thielemans K, and Bailey DL. “Theranostic SPECT reconstruction for improved resolution: application to radionuclide therapy dosimetry”. In: *EJN-MMI Physics* 8.1 (Dec. 2021), p. 16. ISSN: 2197-7364. DOI: 10.1186/s40658-021-00362-x.
- [112] Demetrius L. “Of mice and men: When it comes to studying ageing and the means to slow it down, mice are not just small humans”. In: *EMBO reports* 6 (S1 July 2005). ISSN: 1469-221X, 1469-3178. DOI: 10.1038/sj.embor.7400422.
- [113] Sarrut D, Bała M, Bardiès M, Bert J, Chauvin M, Chatzipapas K, Dupont M, Etxebeste A, M Fanchon L, Jan S, Kayal G, S Kirov A, Kowalski P, Krzemien W, Labour J, Lenz M, Loudos G, Mehadji B, Ménard L, Morel C, Papadimitroulas P, Rafecas M, Salvadori J, Seiter D, Stockhoff M, Testa E, Trigila C, Pietrzyk U, Vandenberghe S, Verdier MA, Visvikis D, Ziemons K, Zvolský M, and Roncali E. “Advanced Monte Carlo simulations of emission tomography imaging systems with GATE”. In: *Physics in Medicine & Biology* 66.10 (May 21, 2021), 10TR03. ISSN: 0031-9155, 1361-6560. DOI: 10.1088/1361-6560/abf276.
- [114] Allison J, Amako K, Apostolakis J, Arce P, Asai M, Aso T, Bagli E, Bagulya A, Banerjee S, Barrand G, Beck B, Bogdanov A, Brandt D, Brown J, Burkhardt H, Canal P, Cano-Ott D, Chauvie S, Cho K, Cirrone G, Cooperman G, Cortés-Giraldo M, Cosmo G, Cuttone G, Depaola G, Desorgher L, Dong X, Dotti A, Elvira V, Folger G, Francis Z, Galoyan A, Garnier L, Gayer M, Genser K, Grichine V, Guatelli S, Guèye P, Gumplinger P, Howard A, Hřivnáčová I, Hwang S, Incerti S, Ivanchenko A, Ivanchenko V, Jones F, Jun S, Kaitaniemi P, Karakatsanis N, Karamitros M, Kelsey M, Kimura A, Koi T, Kurashige H, Lechner A, Lee S, Longo F, Maire M, Mancusi D, Mantero A, Mendoza E, Morgan B, Murakami K, Nikitina T, Pandola L, Paprocki P, Perl J, Petrović I, Pia M, Pokorski W, Quesada J, Raine M, Reis M, Ribon A, Ristić Fira A, Romano F, Russo G, Santin G, Sasaki T, Sawkey D, Shin J, Strakovsky I, Taborda A, Tanaka S, Tomé B, Toshito T, Tran H, Truscott P, Urban L, Uzhinsky V, Verbeke J, Verderi M, Wendt B, Wenzel H, Wright D, Wright D, Yamashita T, Yarba J, and Yoshida H. “Recent developments in Geant4”. In: *Nuclear Instruments and Methods in Physics Research Section A: Accelerators, Spectrometers, Detectors and Associated Equipment* 835 (Nov. 2016), pp. 186–225. ISSN: 01689002. DOI: 10.1016/j.nima.2016.06.125.

- [115] Kawrakow I, Rogers DWO, Mainegra-Hing E, Tessier F, Townson RW, and Walters BRB. *EGSnrc toolkit for Monte Carlo simulation of ionizing radiation transport*. 2000. URL: <https://github.com/nrc-cnrc/EGSnrc> (visited on 04/06/2022).
- [116] Werner CJ, Bull JS, Solomon CJ, Brown FB, McKinney GW, Rising ME, Dixon DA, Martz RL, Hughes HG, Cox LJ, Zukaitis AJ, Armstrong JC, Forster RA, and Casswell L. *MCNP Version 6.2 Release Notes*. LA-UR-18-20808, 1419730. Feb. 5, 2018, LA-UR-18-20808, 1419730. URL: <http://www.osti.gov/servlets/purl/1419730/> (visited on 04/06/2022).
- [117] Mok GSP, Du Y, Wang Y, Frey EC, and Tsui BMW. “Development and Validation of a Monte Carlo Simulation Tool for Multi-Pinhole SPECT”. In: *Molecular Imaging and Biology* 12.3 (June 2010), pp. 295–304. ISSN: 1536-1632, 1860-2002. DOI: 10.1007/s11307-009-0263-7.
- [118] Lee Sh, Gregor J, Kennel SJ, Osborne DR, and Wall J. “GATE Validation of Standard Dual Energy Corrections in Small Animal SPECT-CT”. In: *PLOS ONE* 10.4 (Apr. 7, 2015). Ed. by Tian J. ISSN: 1932-6203. DOI: 10.1371/journal.pone.0122780.
- [119] Sadremomtaz A and Telikani Z. “Validation and optimization studies of small animal SPECT using GATE Monte Carlo simulation”. In: *Nuclear Instruments and Methods in Physics Research Section A: Accelerators, Spectrometers, Detectors and Associated Equipment* 915 (Jan. 2019), pp. 94–101. ISSN: 01689002. DOI: 10.1016/j.nima.2018.09.068.
- [120] Lukas M, Kluge A, Beindorff N, and Brenner W. “Accurate Monte Carlo Modeling of Small-Animal Multi-Pinhole SPECT for Non-Standard Multi-Isotope Applications”. In: *IEEE Transactions on Medical Imaging* 40.9 (Sept. 2021), pp. 2208–2220. ISSN: 0278-0062, 1558-254X. DOI: 10.1109/TMI.2021.3073749.
- [121] Wunderlich C, Guberman D, Paoletti R, Rugliancich A, and Passeri A. “Large-Area SiPM Pixels (LASiPs) in SPECT”. In: *Nuclear Instruments and Methods in Physics Research Section A: Accelerators, Spectrometers, Detectors and Associated Equipment* 1048 (Mar. 2023), p. 167963. ISSN: 01689002. DOI: 10.1016/j.nima.2022.167963.
- [122] Strugari M. “Performance characterization and Monte Carlo model validation of the Cubresa Spark SiPM-based preclinical SPECT scanner using NEMA NU 1-2018”. Virtual GATE Scientific Meeting. May 19, 2022. URL: <https://indico.in2p3.fr/event/27057/contributions/> (visited on 03/12/2023).

- [123] Strugari M. “Integration of advanced 3D SPECT modelling for pinhole collimators into the open-source STIR framework”. STIR User’s and Developer’s Meeting at the IEEE Nuclear Science Symposium, Medical Imaging Conference, and Room Temperature Semiconductor Detector Conference. Milan, Italy, Nov. 10, 2022. URL: <https://stir.sourceforge.net/2022UsersMeeting/> (visited on 03/12/2023).
- [124] *NEMA Standards Publication NU 1-2018, Performance Measurements of Gamma Cameras*. 2019.
- [125] Bal G and Acton PD. “Analytical derivation of the point spread function for pinhole collimators”. In: *Physics in Medicine & Biology* 51.19 (Oct. 7, 2006), pp. 4923–4950. ISSN: 0031-9155, 1361-6560. DOI: 10.1088/0031-9155/51/19/013.
- [126] Strugari M, Falcon C, Erlandsson K, Hutton BF, Brewer K, and Thielemans K. “Integration of advanced 3D SPECT modelling for pinhole collimators into the open-source STIR framework”. In: *Frontiers in Nuclear Medicine* 3 (Apr. 18, 2023), p. 1134774. ISSN: 2673-8880. DOI: 10.3389/fnume.2023.1134774.
- [127] Thielemans K, Tsoumpas C, Mustafovic S, Beisel T, Aguiar P, Dikaios N, and Jacobson MW. “STIR: software for tomographic image reconstruction release 2”. In: *Physics in Medicine & Biology* 57.4 (Feb. 21, 2012), pp. 867–883. ISSN: 0031-9155, 1361-6560. DOI: 10.1088/0031-9155/57/4/867.
- [128] Marti Fuster B, Falcon C, Tsoumpas C, Livieratos L, Aguiar P, Cot A, Ros D, and Thielemans K. “Integration of advanced 3D SPECT modeling into the open-source STIR framework”. In: *Medical Physics* 40.9 (Aug. 5, 2013), p. 092502. ISSN: 00942405. DOI: 10.1118/1.4816676.
- [129] Beque D, Nuyts J, Bormans G, Suetens P, and Dupont P. “Characterization of pinhole SPECT acquisition geometry”. In: *IEEE Transactions on Medical Imaging* 22.5 (May 2003), pp. 599–612. ISSN: 0278-0062. DOI: 10.1109/TMI.2003.812258.
- [130] Beque D, Nuyts J, Suetens P, and Bormans G. “Optimization of geometrical calibration in pinhole SPECT”. In: *IEEE Transactions on Medical Imaging* 24.2 (Feb. 2005), pp. 180–190. ISSN: 0278-0062. DOI: 10.1109/TMI.2004.839367.
- [131] Brun R and Rademakers F. “ROOT — An object oriented data analysis framework”. In: *Nuclear Instruments and Methods in Physics Research Section A: Accelerators, Spectrometers, Detectors and Associated Equipment* 389.1 (Apr. 1997), pp. 81–86. ISSN: 01689002. DOI: 10.1016/S0168-9002(97)00048-X.
- [132] Radiation Solutions Inc. *Pulse Pile-up and Pile-up Rejection*. Oct. 20, 2021. URL: https://www.radiationsolutions.ca/fileadmin/pdf/Pulse_Pile-up.pdf.

- [133] Saint-Gobain Ceramics and Plastics, Inc. *CsI(Tl), CsI(Na), Cesium Iodide Scintillation Material*. Dec. 2012. URL: <https://www.gammadata.se/assets/Uploads/CsITl-and-Na-data-sheet.pdf> (visited on 01/12/2022).
- [134] Gupta T. *Radiation, ionization, and detection in nuclear medicine*. Heidelberg: Springer, 2013. ISBN: 978-3-642-34076-5.
- [135] Mehadji B. “Modélisation Monte Carlo d’une caméra Compton basée sur l’utilisation de détecteurs à scintillation sensibles à la position couplés à des SiPM”. PhD thesis. Marseille, France: Aix-Marseille University, May 28, 2021. 204 pp. URL: <https://www.theses.fr/2021AIXM0212.pdf> (visited on 02/23/2022).
- [136] Lenz M. “Design and Characterisation of an MRI Compatible Human Brain PET Insert by Means of Simulation and Experimental Studies”. PhD thesis. Wuppertal, Germany: Bergische Universität Wuppertal, 2020. 194 pp. URL: <http://elpub.bib.uni-wuppertal.de/servlets/DocumentServlet?id=11590> (visited on 02/23/2022).
- [137] Larsson Åkerman L. “A technical validation of the PET/SPECT/CT (Triumph) scanner”. PhD thesis. Uppsala, Sweden: Uppsala University, Feb. 2011. 42 pp. URL: <http://www.diva-portal.org/smash/get/diva2:407708/FULLTEXT01.pdf> (visited on 02/24/2022).
- [138] Lee Sh, Gregor J, and Osborne DR. “Initial validation of a complete GATE model of the Siemens Inveon trimodal imaging system”. In: *2012 IEEE Nuclear Science Symposium and Medical Imaging Conference Record (NSS/MIC)*. 2012 IEEE Nuclear Science Symposium and Medical Imaging Conference (2012 NSS/MIC). Anaheim, CA, USA: IEEE, Oct. 2012, pp. 2540–2542. DOI: 10.1109/NSSMIC.2012.6551580.
- [139] Boisson F, Zahra D, Parmar A, Gregoire MC, Meikle SR, Hamse H, and Reilhac A. “Imaging Capabilities of the Inveon SPECT System Using Single- and Multipinhole Collimators”. In: *Journal of Nuclear Medicine* 54.10 (Oct. 2013), pp. 1833–1840. ISSN: 0161-5505, 2159-662X. DOI: 10.2967/jnumed.112.117572.
- [140] Sajedi S, Zeraatkar N, Moji V, Farahani MH, Sarkar S, Arabi H, Teymoorian B, Ghafarian P, Rahmim A, and Reza Ay M. “Design and development of a high resolution animal SPECT scanner dedicated for rat and mouse imaging”. In: *Nuclear Instruments and Methods in Physics Research Section A: Accelerators, Spectrometers, Detectors and Associated Equipment* 741 (Mar. 2014), pp. 169–176. ISSN: 01689002. DOI: 10.1016/j.nima.2014.01.001.

- [141] Moji V, Zeraatkar N, Farahani MH, Aghamiri MR, Sajedi S, Teimourian B, Ghafarian P, Sarkar S, and Ay MR. “Performance evaluation of a newly developed high-resolution, dual-head animal SPECT system based on the NEMA NU1-2007 standard”. In: *Journal of Applied Clinical Medical Physics* 15.6 (Nov. 2014), pp. 267–278. ISSN: 15269914. DOI: 10.1120/jacmp.v15i6.4936.
- [142] Lukas M, Kluge A, Beindorff N, and Brenner W. “Multi-Isotope Capabilities of a Small-Animal Multi-Pinhole SPECT System”. In: *Journal of Nuclear Medicine* 61.1 (Jan. 2020), pp. 152–161. ISSN: 0161-5505, 2159-662X. DOI: 10.2967/jnumed.119.226027.
- [143] Islamian J, Azazrm A, Mahmoudian B, and Gharapapagh E. “Advances in Pin-hole and Multi-Pinhole Collimators For Single Photon Emission Computed Tomography Imaging”. In: *World Journal of Nuclear Medicine* 14.1 (Jan. 2015), pp. 3–9. ISSN: 1450-1147, 1607-3312. DOI: 10.4103/1450-1147.150505.
- [144] Ozsahin I, Chen L, Könik A, King MA, Beekman FJ, and Mok GSP. “The clinical utilities of multi-pinhole single photon emission computed tomography”. In: *Quantitative Imaging in Medicine and Surgery* 10.10 (Oct. 2020), pp. 2006–2029. ISSN: 2223-4292. DOI: 10.21037/qims-19-1036.
- [145] Marti Fuster B, Erlandsson K, Falcon C, Tsoumpas C, Livieratos L, Ros D, and Thielemans K. “Evaluation of the novel 3D SPECT modelling algorithm in the STIR reconstruction framework: Simple vs. full attenuation correction”. In: *2013 IEEE Nuclear Science Symposium and Medical Imaging Conference (2013 NSS/MIC)*. 2013 IEEE Nuclear Science Symposium and Medical Imaging Conference (2013 NSS/MIC). Seoul, Korea (South): IEEE, Oct. 2013, pp. 1–3. ISBN: 978-1-4799-0534-8. DOI: 10.1109/NSSMIC.2013.6829258.
- [146] Falcon CM. “Métodos iterativos de reconstrucción tomográfica en SPECT”. PhD thesis. Universitat de Barcelona, Sept. 2, 1999. URL: <https://www.tdx.cat/handle/10803/1785> (visited on 12/15/2022).
- [147] Pareto D, Cot A, Falcon C, Juvells I, Pavia J, and Ros D. “Geometrical response modeling in fan-beam collimators-a numerical simulation”. In: *IEEE Transactions on Nuclear Science* 49.1 (Feb. 2002), pp. 17–24. ISSN: 1558-1578. DOI: 10.1109/TNS.2002.998675.
- [148] Pareto D, Cot A, Pavía J, Falcón C, Juvells I, Lomeña F, and Ros D. “Iterative reconstruction with correction of the spatially variant fan-beam collimator response in neurotransmission SPET imaging”. In: *European Journal of Nuclear Medicine and Molecular Imaging* 30.10 (Oct. 1, 2003), pp. 1322–1329. ISSN: 1619-7089. DOI: 10.1007/s00259-003-1229-7.

- [149] Todd-Pokropek A, Craddock TD, and Deconinck F. “A file format for the exchange of nuclear medicine image data: a specification of Interfile version 3.3”. In: *Nuclear Medicine Communications* 13.9 (Sept. 1992), p. 673. ISSN: 0143-3636. URL: https://journals.lww.com/nuclearmedicinecomm/Abstract/1992/09000/A_file_format_for_the_exchange_of_nuclear_medicine.7.aspx.
- [150] Bresenham JE. “Algorithm for computer control of a digital plotter”. In: *IBM Systems Journal* 4.1 (1965), pp. 25–30. ISSN: 0018-8670. DOI: 10.1147/sj.41.0025.
- [151] Green PJ. “On Use of the EM for Penalized Likelihood Estimation”. In: *Journal of the Royal Statistical Society. Series B (Methodological)* 52.3 (1990), pp. 443–452. ISSN: 0035-9246. DOI: 10.1111/j.2517-6161.1990.tb01798.x.
- [152] Ahn S and Fessler JA. “Globally convergent image reconstruction for emission tomography using relaxed ordered subsets algorithms”. In: *IEEE transactions on medical imaging* 22.5 (May 2003), pp. 613–626. ISSN: 0278-0062. DOI: 10.1109/TMI.2003.812251.
- [153] Macdonald IR, DeBay DR, Reid GA, O’Leary TP, Jollymore CT, Mawko G, Burrell S, Martin E, Bowen CV, Brown RE, and Darvesh S. “Early detection of cerebral glucose uptake changes in the 5XFAD mouse”. In: *Current Alzheimer Research* 11.5 (2014), pp. 450–460. ISSN: 1875-5828. DOI: 10.2174/1567205011666140505111354.
- [154] Lyra M and Ploussi A. “Filtering in SPECT Image Reconstruction”. In: *International Journal of Biomedical Imaging* 2011 (2011), pp. 1–14. ISSN: 1687-4188, 1687-4196. DOI: 10.1155/2011/693795.
- [155] Hutton BF, Erlandsson K, and Thielemans K. “Advances in clinical molecular imaging instrumentation”. In: *Clinical and Translational Imaging* 6.1 (Feb. 2018), pp. 31–45. ISSN: 2281-5872, 2281-7565. DOI: 10.1007/s40336-018-0264-0.
- [156] Karamat MI. “Accelerated Monte Carlo Based Simultaneous Dual-isotope SPECT Reconstruction”. Master of Applied Science. Hamilton, Ontario, Canada: McMaster University, Feb. 2012. 112 pp. URL: <http://hdl.handle.net/11375/11969>.
- [157] Rudin LI, Osher S, and Fatemi E. “Nonlinear total variation based noise removal algorithms”. In: *Physica D: Nonlinear Phenomena* 60.1 (Nov. 1992), pp. 259–268. ISSN: 01672789. DOI: 10.1016/0167-2789(92)90242-F.
- [158] Haber E and Holtzman Gazit M. “Model Fusion and Joint Inversion”. In: *Surveys in Geophysics* 34.5 (Sept. 2013), pp. 675–695. ISSN: 0169-3298, 1573-0956. DOI: 10.1007/s10712-013-9232-4.

- [159] Kabanikhin SI. “Definitions and examples of inverse and ill-posed problems”. In: *Journal of Inverse and Ill-posed Problems* 16.4 (Jan. 2008). ISSN: 0928-0219, 1569-3945. DOI: 10.1515/JIIP.2008.019.
- [160] De Pierro AR and Yamagishi MEB. “Fast EM-like methods for maximum "a posteriori" estimates in emission tomography”. In: *IEEE Transactions on Medical Imaging* 20.4 (Apr. 2001), pp. 280–288. ISSN: 02780062. DOI: 10.1109/42.921477.
- [161] Seltzer S. *Tables of X-Ray Mass Attenuation Coefficients and Mass Energy-Absorption Coefficients, NIST Standard Reference Database 126*. 1995. DOI: 10.18434/T4D01F.
- [162] Asmi H, Bentayeb F, and Bouzekraoui Y. “Contrast optimization using triple energy window scatter correction method for In-111 SPECT imaging: A SIMIND Monte Carlo study”. In: *Iranian Journal of Medical Physics* (Online First Aug. 2020). DOI: 10.22038/ijmp.2020.46778.1735.
- [163] Ritt P, Vija H, Hornegger J, and Kuwert T. “Absolute quantification in SPECT”. In: *European Journal of Nuclear Medicine and Molecular Imaging* 38 (S1 May 2011), pp. 69–77. ISSN: 1619-7070, 1619-7089. DOI: 10.1007/s00259-011-1770-8.
- [164] Hwang AB, Franc BL, Gullberg GT, and Hasegawa BH. “Assessment of the sources of error affecting the quantitative accuracy of SPECT imaging in small animals”. In: *Physics in Medicine and Biology* 53.9 (May 7, 2008), pp. 2233–2252. ISSN: 0031-9155, 1361-6560. DOI: 10.1088/0031-9155/53/9/002.
- [165] Chambolle A and Pock T. “A First-Order Primal-Dual Algorithm for Convex Problems with Applications to Imaging”. In: *Journal of Mathematical Imaging and Vision* 40.1 (May 2011), pp. 120–145. ISSN: 0924-9907, 1573-7683. DOI: 10.1007/s10851-010-0251-1.
- [166] Esser E, Zhang X, and Chan TF. “A General Framework for a Class of First Order Primal-Dual Algorithms for Convex Optimization in Imaging Science”. In: *SIAM Journal on Imaging Sciences* 3.4 (Jan. 2010), pp. 1015–1046. ISSN: 1936-4954. DOI: 10.1137/09076934X.
- [167] Caracciolo A, Di Vita D, Buonanno L, Carminati M, Protti N, Altieri S, Pola A, Bortot D, and Fiorini C. “Experimental validation of a spectroscopic gamma-ray detector based on a LaBr₃ scintillator towards real-time dose monitoring in BNCT”. In: *Nuclear Instruments and Methods in Physics Research Section A: Accelerators, Spectrometers, Detectors and Associated Equipment* 1041 (Oct. 2022), p. 167409. ISSN: 01689002. DOI: 10.1016/j.nima.2022.167409.

- [168] Caracciolo A, Di Vita D, Ferri T, Carminati M, Protti N, Altieri S, Camera F, and Fiorini C. “A spectroscopic and imaging gamma-detector prototype towards dose monitoring in BNCT”. In: *Nuclear Instruments and Methods in Physics Research Section A: Accelerators, Spectrometers, Detectors and Associated Equipment* 1048 (Mar. 2023), p. 168019. ISSN: 01689002. DOI: 10.1016/j.nima.2023.168019.
- [169] Marquis H. “Development of a Dosimetry Platform for Theranostic Agents”. PhD thesis. Sydney, Australia: University of Sydney, 2022. 299 pp.

Appendix A

STIR Parameter Files

This section presents part of a STIR parameter file for use with the PinholeSPECTUB projector. Sample detector and collimator files are also given below. Demonstrated parameters were configured for ^{99m}Tc acquisitions using the Cubresa Spark. The STIR User's Guide provides a detailed description of each parameter.

Sample Parameter File

```
projector pair type := Matrix
Projector Pair Using Matrix Parameters :=
  Matrix type := Pinhole SPECT UB
  Projection Matrix By Bin Pinhole SPECT UB Parameters:=

    maximum number of sigmas := 2.0
    spatial resolution PSF := 0.01
    subsampling factor PSF := 1

    detector file := detector.txt
    collimator file := collimator.txt

    ; PSF and DOI correction { Yes // No }
    psf correction := no
    doi correction := no

    ; Attenuation correction { Simple // Full // No }
    attenuation type := no
    attenuation map :=

    object radius (cm) := 2.3
    mask file :=
    ; If no mask file set, compute it from attenuation map or object radius
    mask from attenuation map := 0

    keep all views in cache := 0

  End Projection Matrix By Bin Pinhole SPECT UB Parameters:=
End Projector Pair Using Matrix Parameters :=
```

Sample Detector File

```
Number of rings: 1
#intrinsic PSF#
Sigma (cm): 0.0361
Crystal thickness (cm): 0.3
Crystal attenuation coefficient (cm -1): 4.407
\#.....repeat for each ring.....\#
Nangles: 91
ang0 (deg): 180.
incr (deg): 3.0
z0 (cm): 0.
\#.....until here.....\#
```

Sample Collimator File

```
Model (cyl/pol): pol
Collimator radius (cm): 2.8
Wall thickness (cm): 1.
#holes#
Number of holes: 91
nh: ind x(cm) y(cm) z(cm) shape(rect-round) sizex(cm) sizez(cm) angx(deg) angz(deg) accx(deg) accz(deg)
h1: 1 0. 0. 0. round 0.1 0.1 0. 0. 45. 45.
:
h91: 91 0. 0. 0. round 0.1 0.1 0. 0. 45. 45.
```


Appendix B

Copyright License Agreements

The articles presented in this thesis were published under the terms of a Creative Commons Attribution 4.0 International Public License (CC BY 4.0). This license affirms that copyright ownership resides with the author. Therefore, additional permissions were not required to share or adapt the articles “NEMA NU 1-2018 performance characterization and Monte Carlo model validation of the Cubresa Spark SiPM-based preclinical SPECT scanner” and “Integration of advanced 3D SPECT modelling for pinhole collimators into the open-source STIR framework” in this thesis.

Copyright license agreements were obtained for figures. They are presented on the preceding pages in order of appearance in the Bibliography.



PARTIES:

1. **Wolters Kluwer Health (P&E) Limited** (Licensor); and
2. **Matthew Strugari** (Licensee).

Thank you for your recent permission request. Some permission requests for use of material published by the Licensor, such as this one, are now being facilitated by PLSclear.

Set out in this licence cover sheet (the **Licence Cover Sheet**) are the principal commercial terms under which Licensor has agreed to license certain Licensed Material (as defined below) to Licensee. The terms in this Licence Cover Sheet are subject to the attached General Terms and Conditions, which together with this Licence Cover Sheet constitute the licence agreement (the **Licence**) between Licensor and Licensee as regards the Licensed Material. The terms set out in this Licence Cover Sheet take precedence over any conflicting provision in the General Terms and Conditions.


Licence Terms

Licence Date: 25/10/2023
PLSclear Ref No: 87571

The Licensor

Company name: Wolters Kluwer Health (P&E) Limited
Address: Floor 41
25 Canada Square
London
E14 5LQ
GB

The Licensee

Licensee Contact Name: Matthew Strugari
Licensee Address: 

Licensed Material

title: Essential Physics of Medical Imaging
ISBN/ISSN: 9780781780575
publisher: Wolters Kluwer Health (P&E) Limited

Are you requesting permission to reuse the cover of the publication?	No
Figure number & title	Figure 17-1 Interaction rate
Page numbers	635
Are you the author of the content that you are requesting to reuse?	No
Will you be changing or editing the image?	No

For Use In Licensee's Publication(s)

usage type	Book, Journal, Magazine or Academic Paper-Thesis or Dissertation
Will your dissertation be placed in an online repository?	Yes
Author	Matthew Strugari
Language	English
Title of dissertation/thesis	Development of Simultaneous Multi-Radionuclide Imaging with a Novel SiPM-based Preclinical SPECT Scanner
University or institution	Dalhousie University
Unlimited circulation?	Yes

Rights Granted

Exclusivity:	Non-Exclusive
Format:	Thesis/Dissertation
Language:	English
Territory:	World
Duration:	Lifetime of Licensee's edition
Maximum Circulation:	Maximum print circulation: Unlimited copies

Payment Details

Fee Payable:	£0.00 [+ VAT if applicable]
Payment Terms:	Strictly 30 days from date of Licence

This is a License Agreement between Matthew Strugari ("User") and Copyright Clearance Center, Inc. ("CCC") on behalf of the Rightsholder identified in the order details below. The license consists of the order details, the Marketplace Permissions General Terms and Conditions below, and any Rightsholder Terms and Conditions which are included below.

All payments must be made in full to CCC in accordance with the Marketplace Permissions General Terms and Conditions below.

Order Date	02-Oct-2023	Type of Use	Republish in a thesis/dissertation
Order License ID	1402570-1	Publisher	IOP Publishing
ISSN	1361-6560	Portion	Image/photo/illustration

LICENSED CONTENT

Publication Title	Physics in Medicine & Biology	Publication Type	e-Journal
Article Title	Characterization of a high-purity germanium detector for small-animal SPECT.	Start Page	5877
Author/Editor	Institute of Physics (Great Britain), American Association of Physicists in Medicine, Canadian Association of Physicists, Medical and Biological Physics Division, Deutsche Gesellschaft für Medizinische Physik, Hospital Physicists' Association, International Organization for Medical Physics, Institute of Physics and Engineering in Medicine (Great Britain)	End Page	5888
Date	01/01/1956	Issue	18
Language	English	Volume	56
Country	United Kingdom of Great Britain and Northern Ireland	URL	http://iopscience.iop.org/0031-9155/
Rightsholder	IOP Publishing, Ltd		

REQUEST DETAILS

Portion Type	Image/photo/illustration	Distribution	Worldwide
Number of Images / Photos / Illustrations	1	Translation	Original language of publication
Format (select all that apply)	Print, Electronic	Copies for the Disabled?	No
Who Will Republish the Content?	Academic institution	Minor Editing Privileges?	Yes

Duration of Use	Life of current edition	Incidental Promotional Use?	No
Lifetime Unit Quantity	More than 2,000,000	Currency	CAD
Rights Requested	Main product		

NEW WORK DETAILS

Title	Development of Simultaneous Multi-Radionuclide Imaging with a Novel SiPM-based Preclinical SPECT Scanner	Institution Name	Dalhousie University
Instructor Name	Dr. Kimberly Brewer	Expected Presentation Date	2023-12-01

ADDITIONAL DETAILS

Order Reference Number	N/A	The Requesting Person/Organization to Appear on the License	Matthew Strugari
------------------------	-----	---	------------------

REQUESTED CONTENT DETAILS

Title, Description or Numeric Reference of the Portion(s)	Figure 3	Title of the Article/Chapter the Portion Is From	Characterization of a high-purity germanium detector for small-animal SPECT.
Editor of Portion(s)	Johnson, Lindsay C; Campbell, Desmond L; Hull, Ethan L; Peterson, Todd E	Author of Portion(s)	Johnson, Lindsay C; Campbell, Desmond L; Hull, Ethan L; Peterson, Todd E
Volume / Edition	56	Issue, if Republishing an Article From a Serial	18
Page or Page Range of Portion	5877-5888	Publication Date of Portion	2011-09-21

This is a License Agreement between Matthew Strugari ("User") and Copyright Clearance Center, Inc. ("CCC") on behalf of the Rightsholder identified in the order details below. The license consists of the order details, the Marketplace Permissions General Terms and Conditions below, and any Rightsholder Terms and Conditions which are included below.

All payments must be made in full to CCC in accordance with the Marketplace Permissions General Terms and Conditions below.

Order Date	02-Oct-2023	Type of Use	Republish in a thesis/dissertation
Order License ID	1402576-1	Publisher	INSTITUTE OF ELECTRICAL AND ELECTRONICS ENGINEERS,
ISSN	0278-0062	Portion	Chart/graph/table/figure

LICENSED CONTENT

Publication Title	IEEE transactions on medical imaging	Rightsholder	The Institute of Electrical and Electronics Engineers, Incorporated (IEEE)
Article Title	A practical method for position-dependent Compton-scatter correction in single photon emission CT.	Publication Type	Journal
Author/Editor	INSTITUTE OF ELECTRICAL AND ELECTRONICS ENGINEERS., IEEE ACOUSTICS, SPEECH, AND SIGNAL PROCESSING SOCI	Start Page	408
Date	01/01/1982	End Page	412
Language	English	Issue	3
Country	United States of America	Volume	10

REQUEST DETAILS

Portion Type	Chart/graph/table/figure	Distribution	Worldwide
Number of Charts / Graphs / Tables / Figures Requested	1	Translation	Original language of publication
Format (select all that apply)	Print, Electronic	Copies for the Disabled?	No
Who Will Republish the Content?	Academic institution	Minor Editing Privileges?	No
Duration of Use	Life of current edition	Incidental Promotional Use?	No
Lifetime Unit Quantity	Up to 250,000	Currency	CAD
Rights Requested	Main product		

NEW WORK DETAILS

Institution Name	Dalhousie University
-------------------------	----------------------

Title	Development of Simultaneous Multi-Radionuclide Imaging with a Novel SiPM-based Preclinical SPECT Scanner	Expected Presentation Date	2023-12-01
Instructor Name	Dr. Kimberly Brewer		

ADDITIONAL DETAILS

Order Reference Number	N/A	The Requesting Person/Organization to Appear on the License	Matthew Strugari
-------------------------------	-----	--	------------------

REQUESTED CONTENT DETAILS

Title, Description or Numeric Reference of the Portion(s)	Figure 2	Title of the Article/Chapter the Portion Is From	A practical method for position-dependent Compton-scatter correction in single photon emission CT.
Editor of Portion(s)	Ogawa, K; Harata, Y; Ichihara, T; Kubo, A; Hashimoto, S	Author of Portion(s)	Ogawa, K; Harata, Y; Ichihara, T; Kubo, A; Hashimoto, S
Volume / Edition	10	Issue, if Republishing an Article From a Serial	3
Page or Page Range of Portion	408-412	Publication Date of Portion	1991-09-01

This is a License Agreement between Matthew Strugari ("User") and Copyright Clearance Center, Inc. ("CCC") on behalf of the Rightsholder identified in the order details below. The license consists of the order details, the Marketplace Permissions General Terms and Conditions below, and any Rightsholder Terms and Conditions which are included below.

All payments must be made in full to CCC in accordance with the Marketplace Permissions General Terms and Conditions below.

Order Date	02-Oct-2023	Type of Use	Republish in a thesis/dissertation
Order License ID	1402575-1	Publisher	ROYAL SOCIETY OF CHEMISTRY
ISSN	1477-9234	Portion	Image/photo/illustration

LICENSED CONTENT

Publication Title	Dalton transactions	Rightsholder	Royal Society of Chemistry
Article Title	A nuclear chocolate box: the periodic table of nuclear medicine.	Publication Type	e-Journal
Author/Editor	Royal Society of Chemistry (Great Britain)	Start Page	4819
Date	01/01/2003	End Page	4844
Language	English	Issue	11
Country	United Kingdom of Great Britain and Northern Ireland	Volume	44

REQUEST DETAILS

Portion Type	Image/photo/illustration	Distribution	Worldwide
Number of Images / Photos / Illustrations	1	Translation	Original language of publication
Format (select all that apply)	Print, Electronic	Copies for the Disabled?	No
Who Will Republish the Content?	Academic institution	Minor Editing Privileges?	No
Duration of Use	Life of current edition	Incidental Promotional Use?	No
Lifetime Unit Quantity	Up to 750,000	Currency	CAD
Rights Requested	Main product		

NEW WORK DETAILS

Title	Development of Simultaneous Multi-Radionuclide Imaging with a Novel SiPM-based Preclinical SPECT Scanner	Institution Name	Dalhousie University
Instructor Name	Dr. Kimberly Brewer	Expected Presentation Date	2023-12-01

ADDITIONAL DETAILS

Order Reference Number	N/A	The Requesting Person/Organization to Appear on the License	Matthew Strugari
-------------------------------	-----	--	------------------

REQUESTED CONTENT DETAILS

Title, Description or Numeric Reference of the Portion(s)	Figure 1	Title of the Article/Chapter the Portion Is From	A nuclear chocolate box: the periodic table of nuclear medicine.
Editor of Portion(s)	Blower, Philip J	Author of Portion(s)	Blower, Philip J
Volume / Edition	44	Issue, if Republishing an Article From a Serial	11
Page or Page Range of Portion	4819-4844	Publication Date of Portion	2015-03-21

WOLTERS KLUWER HEALTH, INC. LICENSE TERMS AND CONDITIONS

Oct 22, 2023

This Agreement between Matthew Strugari ("You") and Wolters Kluwer Health, Inc. ("Wolters Kluwer Health, Inc.") consists of your license details and the terms and conditions provided by Wolters Kluwer Health, Inc. and Copyright Clearance Center.

License Number	5641111485343
License date	Oct 02, 2023
Licensed Content Publisher	Wolters Kluwer Health, Inc.
Licensed Content Publication	Nuclear Medicine Communications
Licensed Content Title	Is SPECT/CT with a hybrid camera useful to improve scintigraphic imaging interpretation?
Licensed Content Author	Orazio Schillaci, Roberta Danieli, Carlo Manni, et al
Licensed Content Date	Jul 1, 2004
Licensed Content Volume	25
Licensed Content Issue	7
Type of Use	Dissertation/Thesis
Requestor type	University/College
Sponsorship	No Sponsorship
Format	Print and electronic
Will this be posted online?	Yes, on a secure website
Portion	Figures/tables/illustrations
Number of figures/tables /illustrations	1
Author of this Wolters Kluwer article	No
Will you be translating?	No
Intend to modify/change the content	No
Title	Development of Simultaneous Multi-Radionuclide Imaging with a Novel SiPM-based Preclinical SPECT Scanner
Institution name	Dalhousie University
Expected presentation date	Dec 2023
Portions	Figure 1
Requestor Location	Matthew Strugari ██████████ ████████████████████ ██████████ Attn: Mr. Matthew Strugari
Publisher Tax ID	895524239 RT0001
Total	0.00 CAD

ELSEVIER LICENSE TERMS AND CONDITIONS

Oct 22, 2023

This Agreement between Matthew Strugari ("You") and Elsevier ("Elsevier") consists of your license details and the terms and conditions provided by Elsevier and Copyright Clearance Center.

License Number	5641060625431
License date	Oct 02, 2023
Licensed Content Publisher	Elsevier
Licensed Content Publication	Elsevier Books
Licensed Content Title	Handbook of Neuro-Oncology Neuroimaging
Licensed Content Author	Marie Foley Kijewski
Licensed Content Date	Jan 1, 2022
Licensed Content Pages	7
Start Page	415
End Page	421
Type of Use	reuse in a thesis/dissertation
Portion	figures/tables/illustrations
Number of figures/tables /illustrations	1
Format	both print and electronic
Are you the author of this Elsevier chapter?	No
Will you be translating?	No
Title	Development of Simultaneous Multi-Radionuclide Imaging with a Novel SiPM-based Preclinical SPECT Scanner
Institution name	Dalhousie University
Expected presentation date	Dec 2023
Portions	Figure 33.3
Requestor Location	Mr. Matthew Strugari ██████████
	██████████ ██████████ Attn: Mr. Matthew Strugari
Publisher Tax ID	GB 494 6272 12
Total	0.00 CAD

This is a License Agreement between Matthew Strugari ("User") and Copyright Clearance Center, Inc. ("CCC") on behalf of the Rightsholder identified in the order details below. The license consists of the order details, the Marketplace Permissions General Terms and Conditions below, and any Rightsholder Terms and Conditions which are included below.

All payments must be made in full to CCC in accordance with the Marketplace Permissions General Terms and Conditions below.

Order Date	24-Oct-2023	Type of Use	Republish in a thesis/dissertation
Order License ID	1409945-1	Publisher	Elsevier Health Sciences
ISBN-13	9781416051985	Portion	Image/photo/illustration

LICENSED CONTENT

Publication Title	Physics in Nuclear Medicine	Country	United States of America
Author/Editor	Cherry, Simon R., Sorenson, James A., Phelps, Michael E.	Rightsholder	Elsevier Science & Technology Journals
Date	04/12/2012	Publication Type	Book
Language	English		

REQUEST DETAILS

Portion Type	Image/photo/illustration	Distribution	Worldwide
Number of Images / Photos / Illustrations	8	Translation	Original language of publication
Format (select all that apply)	Print, Electronic	Copies for the Disabled?	No
Who Will Republish the Content?	Academic institution	Minor Editing Privileges?	Yes
Duration of Use	Life of current edition	Incidental Promotional Use?	No
Lifetime Unit Quantity	Up to 499	Currency	CAD
Rights Requested	Main product		

NEW WORK DETAILS

Title	Development of Simultaneous Multi-Radionuclide Imaging with a Novel SiPM-based Preclinical SPECT Scanner	Institution Name	Dalhousie University
Instructor Name	Dr. Kimberly Brewer	Expected Presentation Date	2023-12-01

ADDITIONAL DETAILS

Order Reference Number	N/A	The Requesting Person / Organization to Appear on the License	Matthew Strugari
-------------------------------	-----	--	------------------

REQUESTED CONTENT DETAILS

Title, Description or Numeric Reference of the Portion(s)	Figs. 7-1, 7-13, 11-14, 13-7, 16-3, 16-4, 16-5, 16-9	Title of the Article / Chapter the Portion Is From	N/A
Editor of Portion(s)	N/A	Author of Portion(s)	Cherry, Simon R.; Sorenson, James A.; Phelps, Michael E.
Volume / Edition	4	Issue, if Republishing an Article From a Serial	N/A
Page or Page Range of Portion	88, 98, 168, 202, 256-261	Publication Date of Portion	2012-04-12

JOHN WILEY AND SONS LICENSE TERMS AND CONDITIONS

Oct 22, 2023

This Agreement between Matthew Strugari ("You") and John Wiley and Sons ("John Wiley and Sons") consists of your license details and the terms and conditions provided by John Wiley and Sons and Copyright Clearance Center.

License Number	5653070779974
License date	Oct 20, 2023
Licensed Content Publisher	John Wiley and Sons
Licensed Content Publication	Wiley Books
Licensed Content Title	Charged-Particle Interactions in Matter
Licensed Content Date	Dec 29, 2007
Licensed Content Pages	43
Type of Use	Dissertation/Thesis
Requestor type	University/Academic
Format	Print and electronic
Portion	Figure/table
Number of figures/tables	1
Will you be translating?	No
Title of new work	Development of Simultaneous Multi-Radionuclide Imaging with a Novel SiPM-based Preclinical SPECT Scanner
Institution name	Dalhousie University
Expected presentation date	Dec 2023
Portions	Figure 8.1
Requestor Location	Matthew Strugari ██████████ ████████████████████ ██████████ Attn: Mr. Matthew Strugari
Publisher Tax ID	EU826007151
Total	0.00 CAD

JOHN WILEY AND SONS LICENSE TERMS AND CONDITIONS

Oct 22, 2023

This Agreement between Matthew Strugari ("You") and John Wiley and Sons ("John Wiley and Sons") consists of your license details and the terms and conditions provided by John Wiley and Sons and Copyright Clearance Center.

License Number	5653071207685
License date	Oct 20, 2023
Licensed Content Publisher	John Wiley and Sons
Licensed Content Publication	Wiley Books
Licensed Content Title	Interaction of Heavy Charged Particles with Matter
Licensed Content Date	Oct 18, 2007
Licensed Content Pages	29
Type of Use	Dissertation/Thesis
Requestor type	University/Academic
Format	Print and electronic
Portion	Figure/table
Number of figures/tables	1
Will you be translating?	No
Title of new work	Development of Simultaneous Multi-Radionuclide Imaging with a Novel SiPM-based Preclinical SPECT Scanner
Institution name	Dalhousie University
Expected presentation date	Dec 2023
Portions	Figure 5.6
Requestor Location	Matthew Strugari ██████████ ████████████████████ ██████████ Attn: Mr. Matthew Strugari
Publisher Tax ID	EU826007151
Total	0.00 CAD

JOHN WILEY AND SONS LICENSE TERMS AND CONDITIONS

Oct 24, 2023

This Agreement between Matthew Strugari ("You") and John Wiley and Sons ("John Wiley and Sons") consists of your license details and the terms and conditions provided by John Wiley and Sons and Copyright Clearance Center.

License Number	5655540101224
License date	Oct 24, 2023
Licensed Content Publisher	John Wiley and Sons
Licensed Content Publication	Wiley Books
Licensed Content Title	Introductory Nuclear Physics, 3rd Edition
Licensed Content Author	Kenneth S. Krane
Licensed Content Date	Jan 1, 1991
Licensed Content Pages	1
Type of Use	Dissertation/Thesis
Requestor type	University/Academic
Format	Print and electronic
Portion	Figure/table
Number of figures/tables	4
Will you be translating?	No
Title of new work	Development of Simultaneous Multi-Radionuclide Imaging with a Novel SiPM-based Preclinical SPECT Scanner
Institution name	Dalhousie University
Expected presentation date	Dec 2023
Portions	Figs. 7.8, 7.10, 7.11, and 7.13
Requestor Location	Matthew Strugari [REDACTED]
	[REDACTED]
	[REDACTED]
Publisher Tax ID	Attn: Mr. Matthew Strugari EU826007151
Billing Type	Invoice
Billing Address	Matthew Strugari [REDACTED]
	Canada
	Attn: Matthew Strugari
Total	0.00 CAD

This is a License Agreement between Matthew Strugari ("User") and Copyright Clearance Center, Inc. ("CCC") on behalf of the Rightsholder identified in the order details below. The license consists of the order details, the Marketplace Permissions General Terms and Conditions below, and any Rightsholder Terms and Conditions which are included below.

All payments must be made in full to CCC in accordance with the Marketplace Permissions General Terms and Conditions below.

Order Date	20-Oct-2023	Type of Use	Republish in a thesis/dissertation
Order License ID	1408774-1	Publisher	John Wiley & Sons
ISBN-13	9780470131480	Portion	Chart/graph/table/figure

LICENSED CONTENT

Publication Title	Radiation Detection and Measurement	Country	United States of America
Author/Editor	Knoll, Glenn F.	Rightsholder	John Wiley & Sons - Books
Date	08/16/2010	Publication Type	Book
Language	English		

REQUEST DETAILS

Portion Type	Chart/graph/table/figure	Distribution	Worldwide
Number of Charts / Graphs / Tables / Figures Requested	4	Translation	Original language of publication
Format (select all that apply)	Print, Electronic	Copies for the Disabled?	No
Who Will Republish the Content?	Academic institution	Minor Editing Privileges?	Yes
Duration of Use	Life of current edition	Incidental Promotional Use?	No
Lifetime Unit Quantity	Up to 499	Currency	CAD
Rights Requested	Main product		

NEW WORK DETAILS

Title	Development of Simultaneous Multi-Radionuclide Imaging with a Novel SiPM-based Preclinical SPECT Scanner	Institution Name	Dalhousie University
Instructor Name	Dr. Kimberly Brewer	Expected Presentation Date	2023-12-01

ADDITIONAL DETAILS

The Requesting Person / Organization to Appear on the License	Matthew Strugari
--	------------------

REQUESTED CONTENT DETAILS

Title, Description or Numeric Reference of the Portion(s)	Figs. 10.2, 10.3, 10.4, and 10.6	Title of the Article / Chapter the Portion Is From	Radiation Spectroscopy with Scintillators
Editor of Portion(s)	N/A	Author of Portion(s)	Knoll, Glenn F.
Volume / Edition	4	Publication Date of Portion	2010-08-16
Page or Page Range of Portion	327-333		